Investigation of Limit Cycle Behavior in BWRs with Time-Domain Analysis

by

Aaron John Wysocki

A dissertation submitted in partial fulfillment
of the requirements for the degree of
Doctor of Philosophy
(Nuclear Engineering and Radiological Sciences)
in the University of Michigan
2015

Doctoral Committee:

Professor Thomas J. Downar, Co-Chair
Associate Professor Annalisa Manera, Co-Chair
Associate Professor Krzysztof J. Fidkowski
Professor John C. Lee
José March-Leuba, Oak Ridge National Laboratory
Yunlin Xu, Argonne National Laboratory

Table of Contents

List of Figures

List of Tables

Abstract

This thesis investigates the use of time-domain codes for boiling water reactor (BWR) stability analysis, with emphasis on out-of-phase limit cycle behavior. A detailed validation of the TRACE/PARCS coupled thermal hydraulic (TH)/neutronic code system was performed for both in- and out-of-phase instabilities using operating BWR data. Additional studies under hypothetical operating conditions indicated the possibility of a "rotating mode" limit cycle behavior, in which the line of symmetry exhibited a steadily-rotating behavior. This occurred even when the first two azimuthal neutronic modes had different (linear) natural frequencies, indicating that a nonlinear coupling mechanism was causing the steady rotation over time. The principal original contribution of this thesis is the characterization of this rotating mode behavior, prediction of the conditions under which it is expected to occur, and an explanation for this behavior based on physical principles governing BWR dynamics. This was achieved through the use of two simplified models: a four-channel TRACE model with a fixed total flow rate, and a multi-channel, multi-modal reduced-order model. Attention was given to the TH boundary conditions used for these models, which were found to play a critical role in determining the in- or out-of-phase behavior as well as the behavior of the out-of-phase limit cycle line of symmetry. For all standalone TH cases performed, a preference for rotating behavior was observed; however, for coupled TH/neutronic cases, it was found that strengthening the TH coupling between channels favored the rotating mode, while strengthening the neutronic coupling between channels favored the side-to-side mode with a stationary symmetry line. A physical explanation was put forth to explain why the rotating symmetry line behavior is preferred from a thermal hydraulic standpoint. This explanation examines the time-dependent variation in total flow rate for general (nonlinear) oscillations, and demonstrates that (1) this variation is typically minimized under a rotating mode pattern and (2) this yields the most unstable configuration for out-of-phase unstable cases. Additionally, it was found that larger-amplitude limit cycles converged to the rotating behavior more quickly than smaller-amplitude limit cycles under similar conditions.

Chapter 1. Introduction

There are currently more than 80 boiling water reactors (BWRs) in operation around the world. These plants make use of the large heat removal capability of boiling water due to the high latent heat of vaporization, as well as the simplicity of generating steam directly in the heating process to feed to the turbines for conversion to electric power.

However, due to the nature of the two-phase flow characteristics and the coupling between coolant density and neutronic power in BWR channels, there exist certain conditions under which the reactor may become unstable, leading to growing oscillations in state parameters (power, flow, etc.). The conditions under which the BWR core may become unstable are typically expressed in terms of the power-flow diagram for the specific reactor of interest. In general, the reactor becomes more unstable as one moves towards lower flow and higher power, and typically a small region exists below the 100 % rod line which may be unstable and thus must be avoided at all times. This region, the so-called "exclusion region," is of relevance most frequently during reactor startup; however, certain events, including some anticipated transient without SCRAM (ATWS) events, are possible which may cause the reactor to enter the exclusion region starting from normal operating conditions.

Few if any stability events occurred in the early years of nuclear power; however, over the years, several trends such as increased power and increased reliance on natural circulation core cooling have increased the size of the exclusion region and contributed to the emergence of a variety of stability events that have occurred in operating reactors [1]. Table 1-1 gives a summary of events reported in BWRs, all within the last 35 years. The most common type of instability has been the coupled neutronic-thermohydraulic instability, which can be understood as density-wave oscillations coupled to the neutron kinetics via temperature and moderator density feedback [2]. These will be discussed in greater detail in Chapter 2.

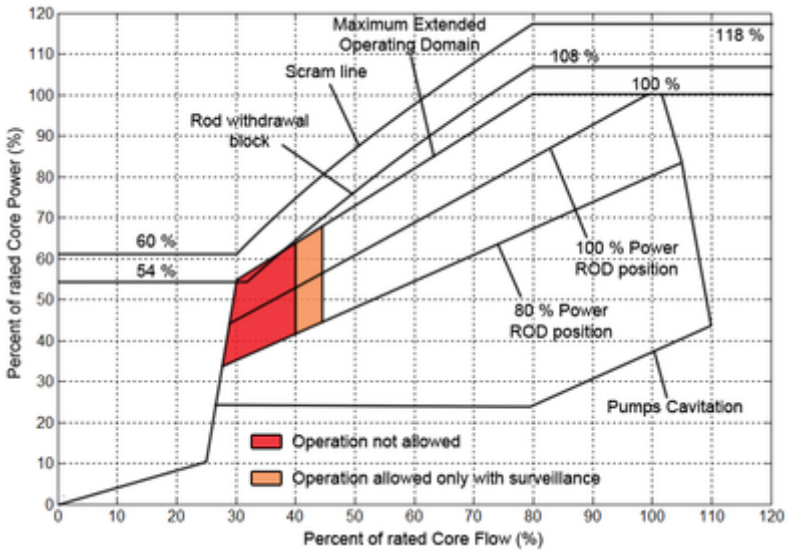

Figure 1-1 – Typical Power-Flow Diagram for a BWR [3].

In many of these events, the oscillations were allowed to grow until the power (measured via the average power range monitor, or APRM) exceeded the level for automatic SCRAM (typically around 120% power). In the context of an ATWS (*i.e.* if SCRAM is not available) then these events can pose a serious safety concern as power levels can reach well above that needed for cladding failure and fuel melting. In addition, the occurrence of instability events, particularly the rapid thermal and mechanical cycling it can cause, may pose significant concerns for the long-term reliability of the fuel as well.

Instabilities in BWRs can be classified into one of the following three types, based on their spatial behavior: in-phase (or core wide) oscillations, in which all channels oscillate in-phase with each other; out-of-phase (or regional) oscillations, in which the power in one half of the core increases at the same time as the power in the opposite half decreases, and vice versa; and local oscillations, in which the instability is restricted to a single channel or small group of channels, for example due to mechanical vibration of a single poorly-seated assembly in the core.

Table 1-1. Summary of Reported BWR Stability Events [1].

Date	NPP, Country, Manufacturer	Event
30.06.1982	Caorso, Italy, GE (General Electric)	It occurred during startup of the reactor. The reactor thermal power was 53.5% and the recirculation flow 38%. The operating point of the reactor entered the unstable region, the oscillations diverged and the reactor scrammed on high-high APRM signal (120% power).
13.01.1984	Caorso, Italy, GE	The second event occurred after trip of a recirculation pump and following loss of some preheater trains. The cold feed water and the strongly peaked axial power distribution led to neutron flux oscillations.
23.02.1987	TVO-I, Finland, ABB Atom	A power oscillation event took place when the plant was brought back to power after a short shutdown period. The reactor power was about 60% with a recirculation flow of 30% when increased APRM signal oscillations started to appear.
09.03.1988	LaSalle 2, USA, GE	Underwent a dual recirculation pump trip following which the unit experienced excessive neutron flux oscillations while it was in natural circulation. The resulting perturbation on the switches for anticipated transient without scram resulted in a trip of both recirculation pumps.
15.01.1989	Forsmark 1, Sweden, ABB Atom	After having carried out tests in several of the selected operating points, the stability boundary was very close. Moving from one point to another, the operator chose to switch from the pump speed control mode to the power control mode. This was done at 71% power and 4700 kg/s. A remaining control mismatch led to a small decrease in core flow. The combined effect of the power control system, caused power oscillations with an amplitude that increased to about ±20% after 20 s, enough the initiate a pump run-down.
26.10.1989	Ringhals 1, Sweden, ABB Atom	In 1989 these NPP was starting up for a new cycle, power oscillations were observed in the core. During the oscillation, several LPRMs gave a high level alarm, indicating that the local power in those positions had exceeded 118 %. The core was stabilized about 30 seconds after the partial scram.
08.01.1990	Oskarshamn 2, Sweden, ABB Atom	A planned power reduction from 106% to 65% was performed. The power was reduced by reducing pump speed to minimum. After about 1 minute, power oscillations had developed, having peak-to-peak amplitudes of ±10%. The APRM signals showed the oscillations to be in phase. A manual partial scram was performed which completely quenched the oscillations.
29.01.1991	Cofrentes, Spain, GE	Oscillations appeared after the operator withdraw control rods and reduced core flow in order to transfer the recirculation pumps from low to high speed.
03.07.1991	Isar 1, Germany, Siemens	The Isar 1 NPP had a trip of four internal recirculation pumps, due to a reduction in seal water flow to the 8 recirculation pumps. The power reduction due to the control rod insertion proved to be too slow to prevent the reactor from entering the unstable region of the power-flow map. Neutron flux oscillations with increasing amplitude appeared at about 50 % power and 30% core flow. When the oscillations reached peak-to-peak amplitude of 30 %, corresponding to a peak power of 67.5 % at 30 % flow, the reactor scrammed on the undelayed setpoint of neutron flux to core flow ratio. This occurred 44 seconds after the trip of the four recirculation pumps.
15.08.1992	WNP 2, USA, GE	The WNP 2 experienced power oscillations during startup. The event occurred early in cycle 8 operation. Upon recognizing the power oscillations, the operators manually initiated a reactor scram. Post event review indicated that the oscillations were in-phase and had grown to peak-to-peak amplitude of about 25 % of rated power.
09.07.1993	Perry, USA, GE	Entry into a region of core instability.
01.1995	Laguna Verde 1, Mexico, GE	During startup of the reactor, at 34% power, the operator was waiting to increase pump recirculation speed. Power was increased to 37% by control rod withdrawal and closure of the control valves of the pumps was initiated, thus leading to power reduction. During these operations the operator observed power oscillations with a tendency to diverge and he stopped the closure of the valves. At this time the peak-to-peak amplitude in the oscillations was 6%.
17.07.1996	Forsmark 1, Sweden, ABB Atom	Local oscillations due to a bad seated fuel assembly.
08.02.1998	Oskarshamn 3, Sweden, ABB Atom	Power oscillations due to a bad combination of core design and control-rod pattern during start up.
25.02.1999	Oskarshamn 2, Sweden,	Power oscillations after a turbine trip with pump runback.

Historically, out-of-phase oscillations have been less common than in-phase oscillations; however, the out-of-phase mode presents an additional safety concern as they typically will not be detected based on the APRM signal alone. This is because the total core power remains relatively constant as the oscillations in the two halves of the core effectively cancel each other out. This mode therefore requires more specific signal processing on the level of local power range monitors (LPRMs) to detect regional changes in power level that would otherwise be missed under normal APRM monitoring.

In principle, for out-of-phase oscillations, the line of symmetry (*i.e.* the imaginary line separating the "positive" and "negative" halves of the oscillation at any given time) may remain stationary throughout the event. However, in some cases a non-stationary (time-dependent) line of symmetry has been observed, as in the Leibstadt (KKL) stability test performed in September, 1990 [4]. In addition, a space-dependent decay ratio was observed in the Forsmark-1 instability event of 1996/1997, which has since been explained analytically as a consequence of multiple spatial oscillation modes being active in the core [5]. As multiple authors have pointed out [6] [7], for small-amplitude (linear) oscillations, a time-dependent line of symmetry is the result of a linear superposition of the first and second azimuthal modes of the neutron flux excited at slightly different frequencies or phase shifts with respect to each other. For example, two azimuthal modes with exactly the same frequency and a 90° phase shift would combine to create a power profile that appears to rotate in the azimuthal direction with a constant angular velocity.

However, for larger-amplitude oscillations, the neutronic modes are not strictly independent from each other due to the nonlinear interaction between the neutronic and thermohydraulic fields [8]. One effect of this nonlinear coupling is the existence of so-called "limit cycles," in which growing oscillations will eventually become "saturated" at some amplitude due to nonlinear effects [9].

A primary goal of this thesis is to understand the behavior of a BWR in situations where both azimuthal modes are unstable, including the possibility of them interacting in such a way as to produce a "rotating mode" limit cycle in which the two modes evolve into a 90° phase

shift (hence a rotating symmetry line) due to particular nonlinear effects which may be inherent in the underlying equations.

Such a rotating mode would have significant implications in terms of safety and fuel performance. For example, one would expect the peak clad temperature (PCT) attained for the case of a rotating mode limit cycle to be approximately equal to the PCT attained if the oscillations were characterized by a stationary line of symmetry; however, for the case of a rotating mode, the PCT would be attained in an entire ring of channels around the core, rather than in two individual channels on opposite sides of the core as would be expected for the case of a stationary symmetry line.

Chapter 2 provides a more in-depth discussion of the physical mechanisms leading to instabilities, with emphasis on density-wave oscillations and coupled neutronic-TH oscillations. In addition, some important techniques for understanding and analyzing BWR oscillations based on neutronic modal decomposition and modal feedback reactivity analysis are presented. Finally, the chapter gives an overview of general stability concepts such as the decay ratio (DR) and natural frequency (NF) of a system, and presents a more rigorous mathematical understanding of system stability in general terms.

Chapter 3 gives an introduction to the TRACE/PARCS code and the numerical methods used. The code is then applied to two different stability benchmark problems based on the Ringhals-1 and Oskarshamn-2 BWRs, which include analysis of both in-phase and out-of-phase stability test points (Ringhals) as well as simulation of a real instability event with growing in-phase power oscillations (Oskarshamn). Model development and important numerical considerations for TRACE/PARCS stability analysis are discussed, and final results are compared to measured plant data.

Chapter 4 presents the results of an additional study using a modified form of the full-core model used for the Ringhals benchmark, adjusted to give unstable out-of-phase oscillations to permit detailed study of the full-core limit cycle behavior. Limit cycle results, including rotating mode behavior, were analyzed for several cases, and the potential implications of this behavior on the safety performance of a BWR in terms of possible fuel failure were briefly discussed.

Chapter 5 focuses on a smaller four-channel TRACE/PARCS model in an attempt to understand and reproduce the behavior, specifically the rotating-mode behavior, seen in the full-core model. Multi-channel TRACE models with fixed power (*i.e.* no neutronic feedback) and fixed total flow rate were created and run until asymptotic limit cycles were reached, and results were analyzed and compared across cases. Neutronic coupling was added via an appropriate four-channel PARCS model, and conclusions were drawn as to the ordering of channels in terms of phase shifts during out-of-phase limit cycle oscillations.

Chapter 6 presents a similar analysis except with a reduced-order model which used a simplified physical treatment in order to gain basic physical insights into the behavior of out-of-phase limit cycles in systems of parallel channels. A detailed investigation of boundary conditions and treatment of the inlet and outlet plena was made, with respect to their effect on the oscillatory behavior. Both standalone TH and coupled TH/neutronic calculations were performed and analyzed for a variety of conditions.

Chapter 7 gives an explanation for the rotating mode limit cycle behavior in terms of the fundamental physical behavior of the out-of-phase unstable system. A Fourier expansion approach is used to characterize the total core flow rate over time, and connections are made to out-of-phase unstable systems which point to the rotating mode being the most unstable oscillation pattern from the standpoint of TH.

Finally, Chapter 8 gives an overview of the conclusions gained from this thesis and a series of recommendations for future work on these topics.

Chapter 2. Background

2.1 Physical Mechanisms for BWR Instabilities

Thermal Hydraulic Instabilities

Several types of thermal hydraulic instabilities can occur in BWR channels [10]. Boure et al. [11] have classified these instabilities into two main categories: static instabilities and dynamic instabilities. Static instabilities occur when a small perturbation from a given steady-state condition leads to new conditions where no steady state solution can exist; the flow behavior then "jumps" to a nearby condition where a steady state can exist. This can lead to either a new steady state condition or to periodic switching between the two possible steady state conditions. Some examples of static instabilities include flow excursion instability, boiling crisis instability, geysering, or chugging. All of these can be analyzed solely through the use of steady state laws.

Dynamic instabilities are instabilities in which feedback effects such as inertia play an active role, and the time-dependent solution depends on the solution of the dynamic conservation equations. Acoustic or pressure-wave oscillations have been noticed by several researchers in a wide range of frequencies, some as low as the 10-100 Hz range (*e.g.* [12]) and some in the range of 1000-10,000 Hz (*e.g.* [13]). Such oscillations are typically small in amplitude and may lead to undesirable mechanical vibration of the flow channel.

However, the primary type of dynamic instability of interest in terms of operating BWR plants is the density wave instability [2]. This type of instability is caused under certain conditions by the feedback between channel flow rate and channel pressure drop under two-phase flow conditions. Consider a single thermal hydraulic channel which experiences a positive flow perturbation. An enthalpy "wave" of decreasing enthalpy will result, which travels through the single-phase region at the liquid velocity. Once the enthalpy wave reaches the

two-phase region, it will cause a negative perturbation in local void fraction which propagates upwards at approximately the mixture velocity of the two-phase fluid. This in general will cause an increase in local pressure drops throughout the channel, except with an increasing delay with respect to the inlet flow perturbation as a function of height.

Now consider a sinusoidal variation in inlet flow rate. As depicted in Figure 2-1, this will result in a series of delayed sinusoids (assuming linearity holds) for the local pressures drops which, when summed together, yield a sinusoidally-varying total channel pressure drop with some particular phase shift compared with the inlet perturbation. If this phase shift is approximately 180°, the total channel pressure drop decreases at the same time as the flow rate increases.

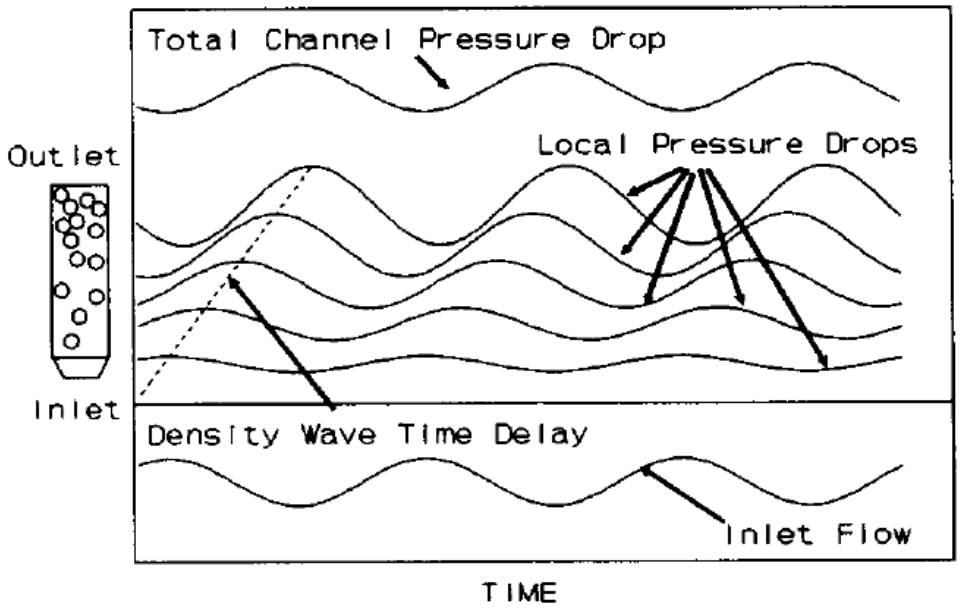

Figure 2-1 – Illustration of the local pressure drop delay introduced by the density wave mechanism [2].

However, if, for example, the inlet flow rate was not imposed externally but was allowed to adjust itself based on the channel pressure drop (as is the case, *e.g.*, for fixed pressure drop boundary conditions) then the 180° phase shift would mean that an increase in inlet flow rate would be combined with a further increase due to feedback from the total pressure drop, and self-reinforcing oscillations would result.

The frequency of inlet flow rate oscillation which leads to this 180° phase shift is known as the "fundamental" or "natural" frequency (NF) of density wave oscillation for the given channel and flow conditions, as it is the frequency at which the density wave mechanism is most unstable. The NF is typically on the order of 1-2 times the transit time of the fluid through the channel [11].

An important quantity for closely tied to the stability of the channel is the ratio of the pressure drop in the two-phase region to the pressure drop in the single-phase region within a channel. The single-phase pressure drop has essentially zero phase delay with respect to inlet flow perturbations, due to the incompressibility of single-phase flow; therefore, the phase delay in the pressure drop response is due almost entirely to the two-phase pressure drop (*i.e.* the pressure drop in the two-phase region). Since this delay is needed to give unstable conditions, increasing the steady-state two-phase pressure drop relative to the steady-state single-phase pressure drop (*i.e.* by changing the steady-state flow rate, power shape, pressure loss factors, etc.) is always expected to yield more unstable conditions. This is confirmed in numerous previous studies (*e.g.* March-Leuba et al. [2] [14]).

Coupled Neutronic-Thermal Hydraulic Instabilities

Coupled neutronic-thermal hydraulic oscillations can be viewed as thermal hydraulic (*i.e.* density wave) oscillations reinforced by neutronic feedback. The coupling between these two fields arises from the relationship between coolant (*i.e.* moderator) density and neutronic reactivity, as well as the feedback of neutronic power generation on the thermal state of the fuel which in turn affects the heat flux to the coolant itself.

The neutronic feedback typically has a destabilizing effect on the system, as compared to a similar system in which the heat flux remains constant over time (as is the case for pure thermal hydraulic instability). The time constant for heat transfer in the fuel is an important parameter for stability; typical values are between 6 and 10 seconds, which is slow enough compared to the density wave oscillation period (typically about 2-3 s) that the fuel adds an almost 90° phase delay to the feedback, which has a destabilizing effect. However, the large time constant also serves to filter out high frequency oscillations, which has a stabilizing effect

at the density wave frequency of 0.3-0.5 Hz. This results in a competition between the two effects, but overall it has been found that increasing the time constant of the fuel has a destabilizing effect in general [2].

As described in Chapter 1, there are mainly two types of oscillations that can occur in operating BWRs: in-phase and out-of-phase oscillations. A third type is local or single-channel oscillations, but these are less common and will not be investigated further in this thesis.

2.2 Analysis of System Behavior Based on Neutronics

Neutron Diffusion Equation and Modal Decomposition Method

There is a well-established connection between the oscillation modes of a BWR core and the static modes of the neutron flux [6] [7] [15]. In-phase oscillations correspond to an excitation of the fundamental neutronic mode, while out-of-phase oscillations correspond to an excitation of one (or both) of the first two azimuthal modes of the neutron flux.

The neutron diffusion equation can be expressed as

$$\bar{\bar{M}}(\vec{r})\bar{\phi}_n(\vec{r}) = \frac{1}{k_n}\bar{\bar{F}}(\vec{r})\bar{\phi}_n(\vec{r}) \tag{2.1}$$

where $\vec{r}$ is the spatial vector, k_n is the eigenvalue for the n-th mode, $\bar{\phi}_n(\vec{r})$ is the two-group neutron flux (with subscripts 1 and 2 corresponding to the fast and thermal neutron group, respectively) given by

$$\bar{\phi}_n(\vec{r}) = \begin{bmatrix}\phi_{1,n}(\vec{r})\\ \phi_{2,n}(\vec{r})\end{bmatrix} \tag{2.2}$$

and the migration, diffusion, absorption, and fission operators are given in terms of standard cross section definitions as

$$\bar{\bar{M}}(\vec{r}) = \nabla\cdot\bar{\bar{D}}(\vec{r})\nabla + \bar{\bar{\Sigma}}(\vec{r}) \tag{2.3}$$

$$\bar{\bar{D}}(\vec{r}) = \begin{bmatrix}D_1(\vec{r}) & 0\\ 0 & D_2(\vec{r})\end{bmatrix} \tag{2.4}$$

$$\bar{\bar{\Sigma}}(\vec{r}) = \begin{bmatrix}-\Sigma_{a,1}(\vec{r}) - \Sigma_{rem}(\vec{r}) & 0\\ \Sigma_{rem}(\vec{r}) & -\Sigma_{a,2}(\vec{r})\end{bmatrix} \tag{2.5}$$

and

$$\bar{\bar{F}}(\vec{r}) = \begin{bmatrix}-\nu\Sigma_{f,1}(\vec{r}) & -\nu\Sigma_{f,2}(\vec{r})\\ 0 & 0\end{bmatrix} \tag{2.6}$$

The adjoint diffusion equation can likewise be given as

$$\bar{\bar{M}}^T\bar{\phi}_n^*(\vec{r}) = \frac{1}{k_n}\bar{\bar{F}}^T(\vec{r})\bar{\phi}_n^*(\vec{r}) \tag{2.7}$$

where the adjoint flux $\bar{\phi}_n^*(\vec{r})$ is expressed as

$$\bar{\phi}_n^*(\vec{r}) = \begin{bmatrix} \bar{\phi}_{1,n}^*(\vec{r}) \\ \bar{\phi}_{2,n}^*(\vec{r}) \end{bmatrix} \tag{2.8}$$

It may be assumed that Eqs. (2.1) and (2.2) have been spatially discretized using an appropriate method. Thus, the solution vectors $\bar{\phi}_n^*(\vec{r})$ and $\bar{\phi}_n(\vec{r})$ are vectors of length $2N$, where N is the number of spatial meshes in the problem. Each eigenvector $\bar{\phi}_n^*(\vec{r})$ and $\bar{\phi}_n(\vec{r})$ has a corresponding eigenvalue k_n; it can be shown that the forward and adjoint eigenvalues for each mode n are the same [7].

These eigenvectors form a complete set in $\mathbb{R}^N$, and can be seen as the forward or adjoint "static" modes of the neutron flux, as they correspond to some steady-state condition of the BWR system.

Typically, when performing transient simulations of BWR behavior, one begins from a converged steady state calculation and then initiates some transient behavior to model the dynamic response of the system over time. In the case of stability analysis, it is often useful to express the time-dependent flux vector $\bar{\phi}(\vec{r},t)$ (or $\bar{\phi}^*(\vec{r},t)$) during a transient as a linear combination of the static modes, which is permissible since the static modes $\bar{\phi}_n(\vec{r})$ (and $\bar{\phi}_n^*(\vec{r})$) form a complete set in $\mathbb{R}^N$ and therefore can be used to express any vector in that space. This linear combination can be written as

$$\bar{\phi}(\vec{r},t) = \sum_{n=0}^{\infty} a_n(t)\bar{\phi}_n(\vec{r}) \tag{2.9}$$

The functions $a_n(t)$ can be viewed as time-dependent amplitudes of each mode.

It is possible (and often useful, for stability analysis) to decompose the time dependent three-dimensional two-group flux (*i.e.* the left-hand side of Eq. (2.9)) – for example, calculated during a transient code simulation – based on the constituent eigenmodes and their amplitudes. This can be done by making use of the so-called "biorthogonality" relationship of the flux modes. It can be shown by manipulation of Eqs. (2.1) and (2.7) and by use of the properties of the adjoint operator that the following relation holds:

$$\langle \bar{\phi}_m^*(\vec{r}) \, , \bar{\bar{F}}\bar{\phi}_n(\vec{r}) \rangle = \langle \bar{\phi}_n(\vec{r}) \, , \bar{\bar{F}}^T\bar{\phi}_m^*(\vec{r}) \rangle = 0, \;\; m \neq n \, , \tag{2.10}$$

where the brackets denote the inner product of the matrices on either side of the comma (analogous to integrating over the entire spatial domain and both energy groups).

Applying the orthogonality condition of Eq. (2.10) to Eq. (2.9) for a given mode n, one may obtain the following expression for $a_n(t)$:

$$a_n(t) = \frac{\langle \bar{\phi}_n^*(\vec{r}) \, , \bar{\bar{F}} \bar{\phi}(\vec{r}, t) \rangle}{\langle \bar{\phi}_n^*(\vec{r}) \, , \bar{\bar{F}} \bar{\phi}_n(\vec{r}) \rangle} \tag{2.11}$$

Thus, the mode amplitudes may be determined using the three dimensional flux vector calculated at each timestep in the calculation as well as the static modes of the neutron flux obtained from the steady-state conditions preceding the transient.

To understand what type of spatial shape each mode might represent, consider the case of a simplified homogeneous cylindrical reactor (assuming one energy group for now), whose first three flux modes are given by

$$\begin{aligned} \phi(r, \varphi, t) &= \sum_{n=0}^{\infty} a_n(t) \Phi_n(r) \Psi_n(\varphi) \\ &= a_0(t) \Phi_0(r) \\ &\quad + \Phi_1(r) \left[a_1^{(1)}(t) \cos(\varphi) + a_1^{(2)}(t) \sin(\varphi) \right] + \cdots \end{aligned} \tag{2.12}$$

where $\Phi_n(r)$ are Bessel's functions of the first kind of order n, r is the radius, and ϕ is the azimuthal angle. These three modes are depicted in Figure 2-2. A typical BWR reactor will not have the exact same mode shapes as for the simplified homogeneous reactor described in (2.12); for example, the fundamental mode follows the steady-state flux shape which is often depressed in the radial center of the core by control rods. However, experience has shown that, after this fundamental mode which is always the dominant one, the next two flux modes in a realistic BWR core (in order of decreasing eigenvalue k_n) generally correspond to the first and second azimuthal modes similar to those depicted in Figure 2-2, with additional modes having some combination of higher harmonic behavior in the azimuthal angle and/or the axial direction as well.

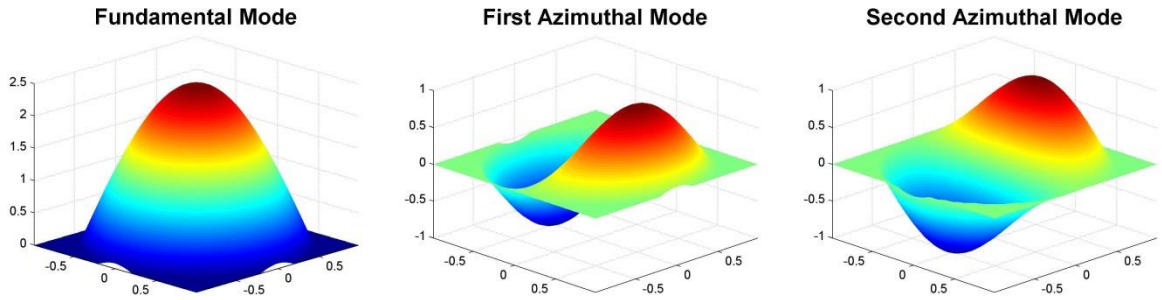

Figure 2-2 – Fundamental and first two azimuthal modes for a homogeneous cylindrical reactor.

If the reactor core is azimuthally homogeneous in terms of fuel loading, geometry, control rod positions, etc., then the first and second azimuthal modes would be expected to be identical and if one mode is unstable then the other one would be unstable as well. However, if the core is azimuthally non-heterogeneous, it is not guaranteed that the second azimuthal modes would be unstable if the first one is.

From the figure, it is readily apparent that in-phase oscillations would correspond to an excitation of the fundamental mode and out-of-phase oscillations would correspond to an excitation of the first and second azimuthal modes. This excitation would manifest itself as a time-dependent periodic oscillation of the mode amplitude function $a_n(t)$ for the corresponding mode n.

Furthermore, if one considers the out-of-phase oscillation case where both the first and second azimuthal modes are unstable, then both will oscillate with some (approximately) sinusoidal amplitude function in time. For a simple illustration of how the core might behave, assume that the amplitude function for the fundamental mode is constant ($a_o(t) = c_0$), the amplitude functions for the first two azimuthal modes are sinusoidal given by $a_1(t) = c_1 \sin(\omega t)$ and $a_2(t) = c_1 \sin(\omega t + \phi)$, and the amplitudes of all other modes are zero. In other words, in this scenario both azimuthal modes oscillate with the same characteristic frequency and amplitude but with a phase shift separating the two sinusoidal oscillations.

For the case of $\phi = 0°$ (or $\phi = 180°$), the overall behavior (*i.e.* the sum of all modes given by $\phi(r, \varphi, t)$ in Eq. (2.12)) is a "side-to-side" oscillatory behavior, where the line of symmetry is at a $45°$ angle to the lines of symmetry for each of the two azimuthal modes separately.

However, for the case of $\phi = 90°$ (or $\phi = 270°$), the summation of the two azimuthal modes gives a "rotating" behavior where the location of the peak power changes as a function of time in a "ring" around the core at some constant radius from the center. Furthermore, the line of symmetry rotates with a constant angular velocity, returning to its original value once each period. The direction can be either clockwise or counterclockwise, depending on the value of ϕ ($90°$ or $270°$) and the orientation of the azimuthal mode shapes.

For any other value of ϕ (*i.e.* not a multiple of $90°$) the line of symmetry rotates with a non-constant angular velocity. For example, if ϕ is close to $0°$, the line of symmetry remains very nearly steady (*i.e.* nearly side-to-side rotation) except for a very rapid rotation twice per period as the peak power switches quickly to the opposite side of the core. If ϕ is close to $90°$, on the other hand, the behavior is very nearly a steady rotation except for a sometimes accelerated or sometimes decelerated angular velocity for the line of symmetry.

This basic discussion of rotating versus side-to-side behavior as it relates to the phase shift between azimuthal modes will become important in later chapters which investigate out-of-phase limit cycle oscillations in which both azimuthal modes are oscillating with different relative phase shifts (usually either preferring pure side-to-side or pure rotating oscillation modes).

In terms of reactor safety, the practical relevance of the out-of-phase behavior (*e.g.* side-to-side versus rotating behavior) can be visualized in Figure 2-3, which shows the maximum local power achieved over each oscillation period for each oscillation mode. It is expected that the overall maximum local power achieved in each case will be the same (or nearly so) for limit cycle oscillations; however, in the side-to-side case, the maximum power is confined to two particular locations on opposite sides of the core, while for the rotating case the maximum power occurs in a ring around the entire core. Thus, it is expected that the rotating mode would give a greater number of channels reaching the maximum power, which increases the overall number of expected fuel failures due to fuel melting, clad melting, pellet-clad interaction, or other transient failure mechanisms.

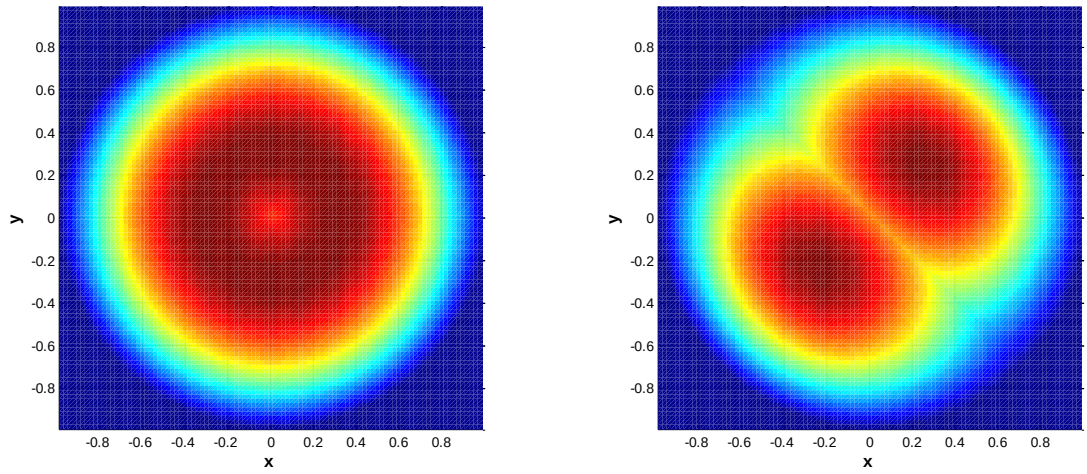

Figure 2-3 – Maximum local power achieved over each oscillation period for the case of rotating oscillations (left) and side-to-side oscillations (right) based on the simple homogeneous cylindrical reactor representation.

Neutron Kinetics and Mode Reactivities

The previous section discussed the static neutron flux equation, *i.e.* Eq. (2.1). This equation can be seen as an extension of the more general neutron kinetics equations given by

$$[v^{-1}]\frac{d}{dt}\bar{\phi}(\vec{r},t) + \bar{\bar{M}}(\vec{r})\bar{\phi}(\vec{r},t) = (1-\beta)\bar{\bar{F}}(\vec{r})\bar{\phi}(\vec{r},t) + \sum_{k=1}^{K}\lambda_k C_k(t)\bar{\bar{X}} \tag{2.13}$$

and

$$\dot{C}_k(t) = \beta_k[\nu\Sigma_{f1} \quad \nu\Sigma_{f2}]\bar{\phi}(\vec{r},t) - \lambda_k C_k(t) \tag{2.14}$$

with C_k being defined as the precursor concentration of delayed group k (with some total number of delayed groups K), β_k the delayed neutron fraction for group k,

$$[v^{-1}] = \begin{bmatrix} \frac{1}{v_1} & 0 \\ 0 & \frac{1}{v_2} \end{bmatrix} \tag{2.15}$$

$$\bar{\bar{X}} = \begin{bmatrix} 1 \\ 0 \end{bmatrix} \tag{2.16}$$

and

$$\beta = \sum_{k=1}^{K} \beta_k \tag{2.17}$$

By applying the modal expansion shown in Eq. (2.9), multiplying both sides by $\bar{\phi}_m^*(\vec{r})$, and integrating (or summing, in the discrete case) over all spatial locations and energy groups (denoted by $\langle \cdot,\cdot \rangle$), Eqs. (2.13) and (2.14) can be written as

$$\begin{aligned} &\sum_{n=0}^{\infty} \langle \bar{\phi}_m^* , [v^{-1}] \bar{\phi}_n \rangle \frac{da_n}{dt} \\ &\qquad = -\sum_{n=0}^{\infty} \langle \bar{\phi}_m^* , \bar{\bar{M}} \bar{\phi}_n \rangle a_n + (1-\beta) \sum_{n=0}^{\infty} \langle \bar{\phi}_m^* , \bar{\bar{F}} \bar{\phi}_n \rangle a_n \\ &\qquad + \sum_{k=1}^{6} \lambda_k \langle \bar{\phi}_m^* , C_k \bar{\bar{X}} \rangle \end{aligned} \tag{2.18}$$

and

$$\frac{d}{dt} \langle \bar{\phi}_m^* , C_k \bar{\bar{X}} \rangle = \beta_k \sum_{n=0}^{\infty} \langle \bar{\phi}_m^* , \bar{\bar{F}} \bar{\phi}_n \rangle a_n - \lambda_k \langle \bar{\phi}_m^* , C_k \bar{\bar{X}} \rangle \tag{2.19}$$

One may consider the migration and fission operators as consisting of steady-state and time-varying components according to $\bar{\bar{M}} = \bar{\bar{M}}_0 + \delta\bar{\bar{M}}$ and $\bar{\bar{F}} = \bar{\bar{F}}_0 + \delta\bar{\bar{F}}$, respectively. If one applies these relations to Eqs. (2.18) and (2.19), as well as the biorthogonality relation given by Eq. (2.10) and the steady-state equation given by (2.1), the resulting equations are

$$\sum_{n=0}^{\infty} \Lambda_{mn} \frac{da_n}{dt} = (\rho_m^s - \beta) a_m + \sum_{n=0}^{\infty} \rho_{mn}^F a_n - \sum_{n=0}^{\infty} \rho_{mn}^D a_n + \sum_{k=1}^{K} \lambda_k C_{mk} \tag{2.20}$$

$$\frac{d}{dt} C_{mk} = \beta_k a_m + \sum_{n=0}^{\infty} \rho_{mn}^{D_k} a_n - \lambda_k C_{mk} \tag{2.21}$$

where the following definitions have been used:

$$N_m = \langle \bar{\phi}_m^* , F \bar{\phi}_m \rangle \tag{2.22}$$

$$\Lambda_{mn} = \frac{1}{N_m} \langle \bar{\phi}_m^* , [v^{-1}] \bar{\phi}_n \rangle \tag{2.23}$$

$$C_{mk} = \frac{1}{N_m} \langle \bar{\phi}_m^* , C_k \bar{\bar{X}} \rangle \tag{2.24}$$

$$\rho_m^S = 1 - \frac{1}{k_m} \tag{2.25}$$

$$\rho_{mn}^F = \frac{1}{N_m}\langle \bar{\phi}_m^* , \left(\delta\bar{\bar{F}} - \delta\bar{\bar{M}}\right)\bar{\phi}_n\rangle \tag{2.26}$$

$$\rho_{mn}^{D_k} = \beta_k \frac{1}{N_m}\langle \bar{\phi}_m^* , \delta\bar{\bar{F}}\bar{\phi}_n\rangle \tag{2.27}$$

$$\rho_{mn}^{D} = \beta \frac{1}{N_m}\langle \bar{\phi}_m^* , \delta\bar{\bar{F}}\bar{\phi}_n\rangle \tag{2.28}$$

In practice, rather than summing the terms in Eq. (2.20) from $n = 0$ to ∞, one uses some finite upper bound N and ignores contributions from all modes $n > N$.

An additional approximation can be made, using the fact that the off-diagonal terms in the $N \times N$ matrix Λ_{mn} (*i.e.* the $m \neq n$ terms) are typically several orders of magnitude less than the diagonal terms (*i.e.* the $m = n$ terms), as has been reported by several authors (*e.g.* [6] [16]). This allows one to reduce the term

$$\sum_{n=0}^{\infty} \Lambda_{mn} \frac{da_n}{dt}$$

in Eq. (2.20) to

$$\Lambda_{mm} \frac{da_m}{dt}$$

which allows the system to be reduced to the following set of first-order nonlinear ordinary differential equations:

$$\frac{da_m}{dt} = \frac{1}{\Lambda_{mm}}\left[(\rho_m^S - \beta)a_m + \sum_{n=0}^{N} \rho_{mn}^F a_n - \sum_{n=0}^{N} \rho_{mn}^D a_n + \sum_{k=1}^{K} \lambda_k C_{mk}\right] \tag{2.29}$$

$$\frac{d}{dt} C_{mk} = \beta_k a_m + \sum_{n=0}^{N} \rho_{mn}^{D_k} a_n - \lambda_k C_{mk} \tag{2.30}$$

for $m = 1, \ldots, N$ and $k = 1, \ldots, K$.

Eqs. (2.29) and (2.30) may be used as a starting point to derive various reduced-order models which describe reactor behavior through the use of simplifying assumptions. An alternative application of the equations is in extracting useful information from, for example, a detailed three-dimensional full-core simulation such as that provided by TRACE/PARCS or other coupled systems codes.

Eqs. (2.25)-(2.28) can each be understood in physical terms as different types of "feedback reactivities" [17] [18]. Specifically, ρ_{mn}^{F} represents simply the feedback reactivity between mode m and mode n, while $\rho_{mn}^{D_k}$ and ρ_{mn}^{D} represent the delayed feedback reactivities between mode m and mode n for delayed group k and for all delayed groups combined, respectively.

Eqs. (2.29) and (2.30), and the corresponding definitions in Eqs. (2.23)-(2.28), are an extension of what are sometimes called the "exact point kinetics" equations as described, *e.g.*, by Ott [19], which typically only deal with the fundamental ($m = 0$) mode. For example, the term ρ_{00}^{F} using (2.26) is simply the reactivity (or "dynamic reactivity") using the standard exact point kinetics formulation.

The expression for fundamental reactivity, $\rho_{00}^{F} = \frac{1}{N_0}\langle \bar{\phi}_0^*, \left(\delta\bar{\bar{F}} - \delta\bar{\bar{M}}\right)\bar{\phi}_0\rangle$, can be understood in the following physical terms. $\left(\delta\bar{\bar{F}} - \delta\bar{\bar{M}}\right)\bar{\phi}_0$ is a vector representing the space- and energy-dependent change in the neutron flux levels (with the shape of $\bar{\phi}_0$ in space and energy) due to changes in the operators $\bar{\bar{F}}$ and $\bar{\bar{M}}$. These are weighted by $\bar{\phi}_m^*$ (representing the "importance" of each point in space and energy in terms of the multiplication factor k_0) and summed over all points in space and energy to find the total impact of the changes in the operators $\bar{\bar{F}}$ and $\bar{\bar{M}}$ on the overall multiplication of neutrons (after properly weighting by the total neutron flux level N_0).

Analogously, the modal reactivity terms $\rho_{mn}^{F} = \frac{1}{N_m}\langle \bar{\phi}_m^*, \left(\delta\bar{\bar{F}} - \delta\bar{\bar{M}}\right)\bar{\phi}_n\rangle$ represent the space- and energy-dependent changes in flux levels (now based on the shape of $\bar{\phi}_n$) weighted by their space- and energy-dependent "importance" in terms of the m-th flux mode $\bar{\phi}_m^*$, which determines the overall effect on the multiplication factor for that mode, k_m.

Therefore, ρ_{mn}^{F} can be seen as a mode coupling term which modifies the mode amplitude a_n by an appropriate factor accounting for the spatial and energy shape of $\left(\delta\bar{\bar{F}} - \delta\bar{\bar{M}}\right)$ in terms of $\bar{\phi}_n$ and $\bar{\phi}_m^*$. These are then summed over all n (*i.e.* all components of the neutron flux shape) to find the total impact on the multiplication (or, similarly, the reactivity) of mode m caused by changes in $\bar{\bar{F}}$ and $\bar{\bar{M}}$. This explains the form of the terms

$\sum_{n=0}^{N} \rho_{mn}^{F} a_n$ and $\sum_{n=0}^{N} \rho_{mn}^{D} a_n$ in Eq. (2.29), which account for changes in prompt and delayed neutron levels, respectively.

Unsurprisingly, a significant amount of useful information can be gained by calculating the values of ρ_{mn}^{F} as functions of time based on the results of a full three-dimensional time-dependent simulation (or, in principle, from measured data such as LPRM signals). For example, Miro et al. [6] have compared the behavior of the ρ_{00}^{F}, ρ_{01}^{F}, ρ_{10}^{F}, and ρ_{11}^{F} terms for different cases and found that for in-phase oscillations the ρ_{00}^{F} and ρ_{11}^{F} terms dominate while the mode coupling terms ρ_{01}^{F} and ρ_{10}^{F} are weak, while the opposite is true for out-of-phase oscillations.

For the case of oscillations in which the both azimuthal modes (*i.e.* $n = 1,2$) are active and interact with each other, it is the author's belief that examination of the corresponding mode reactivity terms can provide insights into the causes and nature of interaction and help to explain some of the behavior that is witnessed.

2.3 Analysis of the Complete System Behavior

Linear Stability Characteristics

The previous section discussed a method to find certain information on the stability behavior of a system by examination of the static modes of the neutron flux and the decomposition of the transient flux into these modes. However, this approach has one serious limitation: it does not directly account for the entire equation set governing the dynamic behavior of the reactor – namely, it does not take into account the equations for thermal hydraulics.

The neutronic modes by themselves cannot, for example, indicate with certainty what oscillation mode (in-phase or out-of-phase) will occur. From a purely neutronic perspective, the fundamental mode has an eigenvalue of 1.0 (*i.e.* "neutral" stability) and the higher modes are all subcritical, meaning that these higher modes would all decay away over time naturally (in the absence of TH feedback).

Clearly, the TH feedback must be accounted for in determining the overall system stability. One could perhaps think of the TH feedback as a "destabilizing" force under certain conditions, driving the system into, for example, an out-of-phase instability mode even though the corresponding azimuthal flux modes are subcritical by themselves.

It is common in the literature to find discussions of instability modes in terms of the "eigenvalue separation," which is typically defined as the difference between k_0 and the eigenvalues k_n, or some related quantity [6]. Often, one finds a general trend that as the eigenvalue separation decreases (*e.g.* due to changes in core geometry or operating conditions), the likelihood of out-of-phase oscillation as opposed to in-phase oscillation increases, with the interpretation that it becomes easier for the TH feedback to overcome the subcriticality of the azimuthal mode(s) if the eigenvalue separation is small.

Additionally, some researchers have looked at various parameters characterizing the radial and/or axial power distributions of the core under steady state conditions, for instance finding that a "bowl shape" radial power profile (*i.e.* relatively low power in the radial center

and high power in the periphery) and a bottom peaked axially averaged power profile both favor the out-of-phase mode over the in-phase.

However, in general, these parameters appear to provide more of a general "rule of thumb" than an actual, precise prediction of stability behavior. There are more variables at play than can be expressed in any one simple parameter and the methods described here, while oftentimes helpful, have limited use in actually determining the most unstable mode of oscillation (*e.g.* in-phase versus out-of-phase) [6].

To obtain a true, definitive, and mathematically rigorous prescription for the stability states of a system, one must consider the entire system of equations including both the neutronics and TH equations together. For complex systems codes, especially ones in which the neutronics and TH are coupled explicitly as is often the case (*e.g.* with TRACE/PARCS), assembling the entire equation set and finding the true eigendecomposition of the system is essentially impossible, or at least impractical.

However, the theoretical basis for understanding the behavior of the overall system in described here nonetheless, partly because it provides an important understanding of the combined system dynamics including an introduction to important concepts such as the decay ratio (DR) and natural frequency (NF).

Additionally, for the case of reduced-order models, one can in fact actually find the overall behavior of the system in terms of eigenmodes, and so the following discussion will prove essential when reduced-order models are discussed later.

In general, BWRs behave nonlinearly, with significant nonlinearities present in the underlying equations themselves (*i.e.* the neutron kinetics equations and the two-phase mass-momentum-energy fluid equations) as well as in the coupling between these two fields, expressed through nonlinear feedback terms. Not surprisingly, then, a full description of BWR stability behavior must account for nonlinear effects. Such effects will be treated in part in the next section.

However, while the behavior of a BWR is nonlinear in general, the Hartman-Grossman theorem [20] guarantees that the system will behave linearly in the neighborhood of a hyperbolic fixed point. That is to say, the stability of the system may be described by linearized

forms of the governing equations provided that the deviation from steady-state conditions remains sufficiently small.

The linearized system can be written as a series of first-order, homogeneous[1] ordinary differential equations for that fixed point, of the form

$$\frac{d\left(\underline{x}(t)\right)}{dt} = \frac{d\left(\delta\underline{x}(t)\right)}{dt} = \underline{\underline{A}}\,\delta\underline{x}(t) \tag{2.31}$$

where $\underline{x}(t)$ is the solution vector containing the entire problem domain (*i.e.* all variables for all spatial nodes), $\delta\underline{x}(t)$ is the deviation of $\underline{x}(t)$ from the fixed point $\underline{x}_0$ (*i.e.* $\delta\underline{x}(t) = \underline{x}(t) - \underline{x}_0$) and the matrix $\underline{\underline{A}}$ is the Jacobian matrix containing the linear (*i.e.* first derivative) coefficients for the entries in $\underline{x}(t)$ about the point $\underline{x}_0$.

Using the relation

$$\underline{\underline{A}}\,\underline{v}_n = \lambda_n \underline{v}_n \tag{2.32}$$

where $\underline{v}_n$ is any eigenvector of $\underline{\underline{A}}$, with a corresponding eigenvalue of λ_n, it can be shown by inspection that

$$\delta\underline{x}(t) = \sum_{n=1}^{\infty} c_n e^{\lambda_n t}\underline{v}_n \tag{2.33}$$

is a solution of Eq. (2.31).

For the general case of complex eigenvalues, it is useful to rewrite Eq. (2.33) as

$$\delta\underline{x}(t) = \sum_{n=1}^{\infty} c_n e^{\gamma_n t}\left(\cos(\omega_n t) + i\sin(\omega_n t)\right)\underline{v}_n \tag{2.34}$$

where γ_n and ω_n are the real and imaginary components of the eigenvalue λ_n, respectively.

If λ_n contains an imaginary component, then at least some of the elements of v_n must contain imaginary components as well, in order to satisfy Eq. (2.32). Furthermore, as imaginary eigenvalues must occur in conjugate pairs, the corresponding eigenvectors must occur in conjugate pairs as well, given that the coefficients of $\underline{\underline{A}}$ are all real [21], as is the case here. Assuming that two modes k and k^* form a conjugate pair, the two corresponding $n = k$ and $n = k^*$ terms in Eq. (2.34) can be rewritten with real coefficients as

[1] In the absence of external sources (*e.g.* neutron sources)

$$c_k e^{\gamma_k t}\left(\cos(\omega_k t)\underline{v}_{k,r} - \sin(\omega_k t)\underline{v}_{k,i}\right)$$

and

$$c_k e^{\gamma_k t}\left(\cos(\omega_k t)\underline{v}_{k,i} + \sin(\omega_k t)\underline{v}_{k,r}\right)$$

where $\underline{v}_{k,r}$ and $\underline{v}_{k,i}$ are the real and imaginary components of $\underline{v}_k$, respectively. Thus, when converted to the real domain, the two modes exhibit the same exponential coefficient but with different combinations of spatial vectors weighted by sinusoidal time-dependent components.

Note that if λ_n is a real number, $\omega_n = 0$ and the expression reduces to Eq. (2.33) with λ_n replaced by γ_n. Hence, regardless of the complexity of λ_n, if $\gamma_n > 0$ the nth component will grow unbounded for $\gamma_n > 0$ but will approach zero for $\gamma_n < 0$, either as a simple exponential or as a growing (or decaying) sinusoid if λ_n is real or complex, respectively.

From here on, according to convention, the eigenvalues and eigenvectors will be sorted in order of decreasing real component, *i.e.*

$$\gamma_0 \geq \gamma_1 \geq \gamma_2 \geq \cdots \geq \gamma_{n-1} \geq \gamma_n \geq \cdots \tag{2.35}$$

for all $n > 0$.

From Eq. (2.34) it follows that, after a sufficiently long time, the term corresponding to the largest value of γ_n will dominate the behavior, as all other terms decay away at a faster rate than this term. The overall system stability, which is characterized by the long-term behavior, is therefore determined solely by the leading ($n = 0$) term.

Instead of using the form of Eq. (2.34), it is conventional in the field of BWR stability analysis to work in terms of the "decay ratio" (DR) and "natural frequency" (NF), which are defined formally as

$$DR = e^{2\pi\gamma_0/|\omega_0|} \tag{2.36}$$

and

$$NF = |\omega_0|/2\pi \tag{2.37}$$

However, in most practical applications – such as analyzing plant data or running complicated numerical simulations – the eigenvalues and eigenvectors of a system are not known ahead of time; rather, the oscillatory response of the overall system is fitted via various post-processing techniques to extract the best possible estimate for the DR and NF and hence

the overall stability characteristics of the system. Under this viewpoint, the DR is recognized as the ratio of amplitudes between successive oscillations, while the NF is simply the reciprocal of the period of the oscillations.

In a numerical simulation, for instance, the DR and NF can be evaluated at a given fixed operating point by applying a small perturbation from steady state conditions. In a BWR simulation, for instance, this can be done by, for example, perturbing the pressure in the system or moving a control rod bank, returning back to the original condition or position shortly thereafter. Mathematically, an impulse (*i.e.* delta function) perturbation is ideal, as this ensures that all frequencies are excited. Otherwise, if for example the perturbation had zero excitation at the natural frequency, the most unstable mode (ignoring nonlinear effects) would not be excited at all, and the DR one would calculate would be only the DR of the most unstable remaining mode that was excited, which, according to Eq. (2.35), would be less than or equal to the true DR for the system.

Additionally, as can be expected from Eq. (2.34), if multiple eigenmodes of the system are excited, the initial system response after the perturbation will not be governed only by the most unstable mode, and hence the DR, as determined by comparing amplitudes of successive peaks or by other methods, will not reflect the correct DR value based on the most unstable mode only. Therefore, it is standard practice to begin processing data only after the first 2 to 3 full oscillations have completed, to give sufficient time for the higher (*i.e.* $n > 0$) modes to have decayed away sufficiently so that the true "asymptotic" DR [22] can be found more accurately.

Detailed examination of the dependence of the DR on channel flow and boundary conditions for single and multiple channel systems is given by many sources. For example, Figure 2-4 shows a typical result for the stability boundary (*i.e.* the locus of points for which the DR equals 1.0) as a function of the Zuber number, which is proportional to the power-to-flow ratio, and the subcooling number, proportional to the inlet subcooling, for a single TH channel with fixed power.

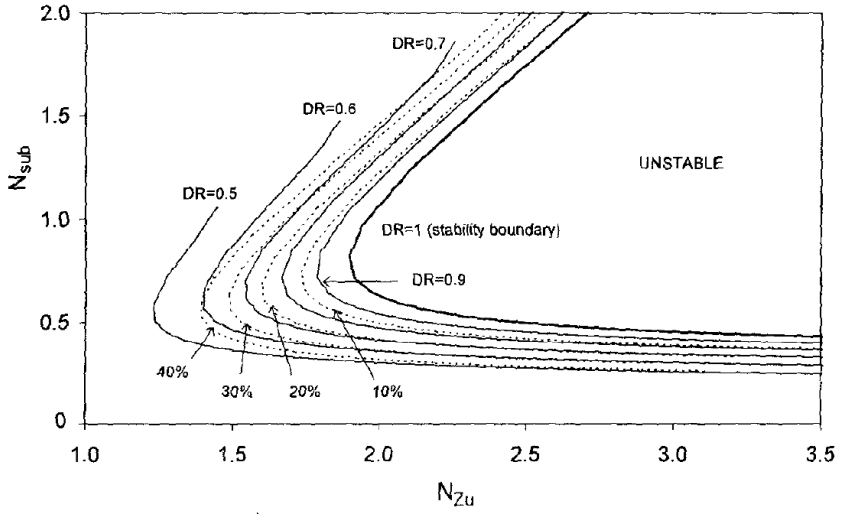

Figure 2-4 – Sample stability map in the Zuber-subcooling plane [23].

Analysis of the Nonlinear Stability Characteristics of a System

Recall that the system being solved, *i.e.* Eq. (2.31), represents only a linearized form of the full equation set which is in general nonlinear. Therefore, the DR and NF should be seen as indicators only of the *linear* stability of the system within a small neighborhood of the hyperbolic fixed point around which the system was linearized. In other words, the DR and NF are valid only while the perturbations away from steady-state conditions are sufficiently small. For larger perturbations, nonlinear effects begin to play an increasingly large role, and the system can no longer be characterized by simply the DR and NF.

In this more general case of larger-amplitude oscillations, bifurcation theory can be used to understand the nonlinear dynamics of the BWR system. The relevant form of bifurcation seen in BWR systems is Poincaré-Andronov-Hopf (PAH) bifurcation [24] [25] [26] [27], in which either bounded or unbounded limit cycle oscillations (corresponding to supercritical and subcritical PAH bifurcation, respectively) can develop depending on the nonlinear characteristics at a given fixed point.

Many researchers have used so-called “reduced order models” which take advantage of various simplifications to the underlying mathematical descriptions of BWR dynamics in order to determine the existence and type of bifurcation across certain ranges of fixed points via analytical or semi-analytical means [16] [28]. This process involves selecting one (or possibly

several) bifurcation parameters, determining the critical value at which the system crosses the stability boundary for the chosen parameter, and using center manifold reduction and reduction to Poincaré normal form to extract additional information about the nature of bifurcation (*i.e.* subcritical versus supercritical PAH bifurcation) that cannot be otherwise obtained via linear analysis.

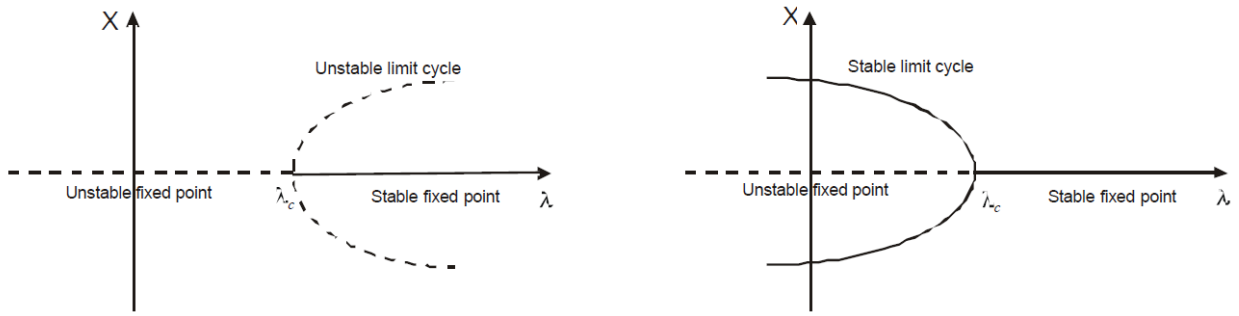

Figure 2-5 – Illustration of limit cycle amplitude and characteristics for subcritical (left) and supercritical (right) PAH bifurcations [16].

Figure 2-5 gives a simple illustration of the characteristic behavior for both sub- and supercritical PAH bifurcations. Suppose that for some parameter (specifically, bifurcation parameter) λ, which represents some particular input variable in the system, there exists a value at which the system crosses the threshold from linear stability to linear instability. If the nature of bifurcation at that point is supercritical, and if the system is operating in the (linearly) stable region, any perturbations will eventually decay away and the system will return to a fixed steady state. If the system is operating within the (linearly) unstable region, the dynamic behavior will gradually evolve to a stable, periodic limit cycle of fixed amplitude. However, for the case of subcritical PAH bifurcation, a perturbation to a system operating in the (linearly) unstable region will result in oscillations of unbounded amplitude[2], while a perturbation to a system operating in the (linearly) stable region will experience decaying oscillations for small enough initial perturbations but unbounded oscillations for perturbations larger than some threshold value. This is contrary to the findings of linear theory, which predicts decaying oscillations in the stable region regardless of perturbation amplitude.

[2] In a realistic BWR system, however, one expects that the amplitude would eventually be bounded due to the onset of additional "nonlinear" effects (such as boiling crisis) not accounted for in the simplified models.

The above has been found to be true in general near the stability boundary. However, farther from the stability boundary, more complex phenomena have been predicted via analytical and numerical means. March-Leuba and Blakeman [24] demonstrated the existence of period-doubling, chaotic behavior far from the stability boundary, and more recently Rizwan-uddin [29] and Lange [30] have reported the existence of a saddle-node bifurcation of cycles (turning point) in which stable fixed points, unstable limit cycles, and stable limit cycles can coexist at some system states away from the stability boundary.

Nonlinear Effects Associated with Out-of-Phase Limit Cycles

In a recent study, Dokhane et al. [31] performed SIMULATE-3K calculations based on the KKL out-of-phase instability event. In one case, the code predicted an out-of-phase limit cycle which appeared to show a "rotating mode" behavior similar to that described in Chapter 1 of this thesis, with the two azimuthal modes oscillating with a roughly 90° phase shift to yield a steadily-rotating symmetry line. In a separate case, a very small-amplitude limit cycle was obtained which showed evidence of not only the first azimuthal mode, but higher (odd-numbered) azimuthal modes as well (*e.g.* mode 3, mode 5, etc.).

Andersson and Stepniewski [32] have examined data from a natural circulation test performed in the Oskarshamn-3 reactor and have reported the appearance of a behavior possibly similar to that observed numerically by Dokhane et al. According to Andersson and Stepniewski, during the tests the core oscillated with a clear "rotating mode" behavior in a clockwise direction. However, at a certain point the rotation suddenly switched into a "side to side" oscillation mode (*i.e.* stationary symmetry line) for a time, until eventually a rotating behavior reappeared traveling in the opposite direction (counterclockwise). The authors provide figures detailing the LPRM signals, their relative magnitudes, and their relative phase shifts at multiple different snapshots during the test, including during the clockwise portion and the counterclockwise portion. Unfortunately, no detailed figures or data are provided to visualize the timescale and manner of transition from a rotating behavior to a side-to-side behavior and back; therefore, it remains uncertain whether or not this behavior was due simply to the superposition of two azimuthal modes oscillating independently with slightly different

natural frequencies. This could plausibly account for the observed behavior in the Oskarshamn-3 test, yielding a gradual transition between the different states as the relative phase shift between azimuthal modes slowly drifts. However, Andersson and Stepniewski do indicate that a "sudden" transition occurred from the rotating behavior to the side-to-side behavior; therefore, it remains plausible that some underlying physical phenomenon was at play driving the oscillations into one pattern or another, as well as the transitions between them.

Similar results to those of Dokhane et al. will be discussed in this thesis. In particular, a similar "rotating-mode" behavior has been obtained for limit cycles calculated using TRACE/PARCS, and an effort will be made first to demonstrate that this behavior is associated with nonlinear mode coupling effects and not merely a chance event due to an arbitrary phase shift between azimuthal modes operating independently. Afterwards, an attempt will be made to understand the causes of this and possibly other behaviors, using various approaches such as analytical or simplified models and/or investigation of the behavior of mode reactivity terms or other insights.

Chapter 3. TRACE/PARCS Methods

3.1 The TRACE Code

All simulations in this chapter were performed in the time domain using the TRACE/PARCS coupled code system [33] [34]. This code system has been successfully applied to the study of BWR instabilities as part of the OECD Ringhals stability benchmark and the OECD Oskarshamn stability benchmark. Numerical and modeling issues associated with TRACE/PARCS for stability applications, such as the role of axial nodalization and numerical diffusion on the decay ratio, have been examined in these works and also in more detail in a separate study [35].

The Ringhals benchmark provided a well-instrumented set of stability tests performed at various power and flow conditions. These points, which included both in-phase and out-of-phase measurements, were useful in demonstrating the TRACE/PARCS code system's ability to predict decay ratios and frequencies at various conditions and in different oscillation modes. With a few exceptions, decay ratios typically agreed with measurements within ±0.1, and natural frequencies within 0.05 s for all points analyzed.

The Oskarshamn benchmark was useful in extending the range of code validation to include nonlinear effects. The event upon which the benchmark was based included large amplitude in-phase oscillations with a decay ratio (DR) greater than one which grew to an amplitude of approximately 80% of nominal power before reactor scram was triggered. For such large, nonlinear oscillations, coupled time domain codes such as TRACE/PARCS provide arguably the most accurate and reliable solutions by taking into account the full three-dimensional core configuration and spatial effects. The TRACE/PARCS code proved successful in matching the measured APRM signal both in the events leading up to oscillations as well as in the growth of the oscillations themselves.

The Semi-Implicit Numerical Method

The TRAC/RELAP5 Advanced Computational Engine (TRACE) is used to study the reactor coolant system under a wide variety of flow conditions including multi-phase thermal hydraulics [36]. There are two main numerical methods available to solve the flow equations in TRACE: the "semi-implicit" (SI) method and the SETS method. As will be shown later, the SI method is best suited for BWR stability applications due to the ability to minimize numerical diffusion with careful axial mesh spacing, as opposed to the SETS method for which the only way to effectively eliminate numerical diffusion is by increasing the total number of axial meshes.

For simplicity, the discretization scheme of the SI method [37] is shown here for single-phase flow only, although the actual implementation in TRACE includes a full two-phase (six equation) representation of the flow. The single-phase mass conservation equation is given by

$$\frac{\left(\rho_j^{n+1}-\rho_j^n\right)}{\Delta t}+\frac{\partial}{\partial x_j}\left(\rho^n V^{n+1}\right)=0 \tag{3.1}$$

while the momentum conservation equation is given by

$$\begin{aligned}\frac{V_{j+1/2}^{n+1}-V_{j+1/2}^n}{\Delta t}+V_{j+1/2}^n\left.\frac{\partial V^n}{\partial x}\right|_{j+1/2}+\frac{1}{\langle\rho\rangle_{j+1/2}^n}\frac{\left(P_{j+1}^{n+1}-P_j^{n+1}\right)}{\Delta x}\\ +K_{j+1/2}^n V_{j+1/2}^{n+1}\left|V_{j+1/2}^n\right|=0\end{aligned} \tag{3.2}$$

and the energy conservation equation by

$$\begin{aligned}\frac{\left(\rho_j^{n+1}e_j^{n+1}-\rho_j^n e_j^n\right)}{\Delta t}+\frac{\partial}{\partial x_j}\left(\rho^n e^n V^{n+1}\right)+P_j^{n+1}\frac{\left(V_{j+1/2}^{n+1}-V_{j-1/2}^{n+1}\right)}{\Delta x}\\ =Q\end{aligned} \tag{3.3}$$

where ρ is the fluid density, V is the fluid velocity, e is the fluid internal energy, K is the local frictional loss coefficient, j is the node index, n is the timestep index, Q is a heat source term,

$$\left.\frac{\partial V}{\partial x}\right|_{j+1/2}=\begin{cases}\dfrac{V_{j+1/2}-V_{j-1/2}}{\Delta x} & \text{if } V_{j+1/2}\geq 0\\ \dfrac{V_{j+3/2}-V_{j+1/2}}{\Delta x} & \text{if } V_{j+1/2}<0\end{cases} \tag{3.4}$$

and, for some quantity Y,

$$\langle Y \rangle_{j+1/2}^{n} = \begin{cases} Y_j & \text{if } V_{j+1/2} \geq 0 \\ Y_{j+1} & \text{if } V_{j+1/2} < 0 \end{cases} \tag{3.5}$$

and

$$\frac{\partial}{\partial x_j}(YV) = \frac{\langle Y \rangle_{j+1/2} V_{j+1/2} - \langle Y \rangle_{j-1/2} V_{j-1/2}}{\Delta x} \tag{3.6}$$

For numerical schemes employing an explicit temporal discretization for flow as in Eq. (3.2), the Courant-Friedrichs-Lewy (CFL) condition applies. This is expressed in terms of the Courant number $C_{j+1/2}$ as

$$C_{j+1/2} = \frac{\left|V_{j+1/2}^{n}\right| \Delta t}{\Delta x_{j+1/2}} \leq C_{max} \tag{3.7}$$

The CFL condition is a necessary but, in general, not sufficient criterion for numerical stability [38]. It has the physical meaning that the fluid traveling with velocity $V_{j+1/2}^{n}$ is not allowed to traverse farther than some fraction of the mesh length $\Delta x_{j+1/2}$ within one timestep Δt.

In the case of the SI method – specifically, Eq. (3.2) – we have the requirement

$$C_{max} = 1$$

or, in other words,

$$\frac{\left|V_{j+1/2}^{n}\right| \Delta t}{\Delta x_{j+1/2}} \leq 1 \tag{3.8}$$

This arises from the first-order spatial discretization of Eqs. (3.1)-(3.3), which contain information from timestep n from only the current $(j + 1/2)$ node and the node immediately upstream of this node (based on Eqs. (3.4) and (3.5)). The equations can thus be seen as an interpolation between the values of the two nodes.

In this light, the CFL condition given by Eq. (3.8) is a simple requirement that an element of fluid with velocity $V_{j+1/2}^{n}$ must not travel farther than one node length $\Delta x_{j+1/2}$ in one timestep Δt – otherwise, the interpolation between the current node and the upstream node is not valid. Due to the hyperbolic nature of the flow equations in which information is propagated at finite velocity, this means that the interpolation between node $(j + 1/2)$ and the upstream node has no way of properly accounting for information that was beyond the upstream node at timestep n, as would be the case if $C_{j+1/2} > 1$.

It is important to note that if the pressure terms in Eq. (3.2) were made explicit, *i.e.* were given a superscript n rather than $n+1$, the CFL condition given by Eq. (3.8) would instead have had the form

$$\frac{\left(\left|V_{j+1/2}^{n}\right| + c_s\right)\Delta t}{\Delta x_{j+1/2}} \leq 1 \tag{3.9}$$

where c_s is the speed of sound in the fluid. The value of c_s for saturated liquid at a typical BWR operating pressure of around 7 MPa is 984 m/s [39]. Based on typical fluid velocities in BWR channels, this would require a timestep reduction by roughly 2-3 orders of magnitude to satisfy the CFL condition as compared to the prescription of Eq. (3.4) without the sound speed term. This is the primary reason why pressures are solved implicitly (*i.e.* at the $n+1$ timestep) in the SI method – to avoid this issue of needing an extremely small timestep size.

3.2 Ringhals

The TRACE/PARCS code has been previously employed to analyze the OECD Ringhals stability benchmark [40] [41]. In these studies, a stability methodology was developed, verified, and validated based on the measured plant data from the Ringhals plant for a series of 10 stability measurements at various operating conditions during startup for Cycle 14. A half-core symmetric TRACE model with 325 TH channels was used for all stability points.

The measured data includes the operating conditions (power, flow rate, inlet temperature, etc.) and the DR and NF value for each point. The DR and NF were calculated at the plant and based on noise analysis of the time-dependent signal data. For the TRACE/PARCS simulations, three different methods were used to excite oscillations. First, a control rod perturbation was simulated, in which the rod positions were changed briefly then returned to their original values. Another method was a pressure perturbation, in which the system outlet pressure was perturbed in a similar manner. For both of these methods, DRs and NFs were calculated from post-processing of the calculated core power level versus time using an ARMA process for curve fitting [42]. A sample power signal and curve fit is shown in Figure 3-1.

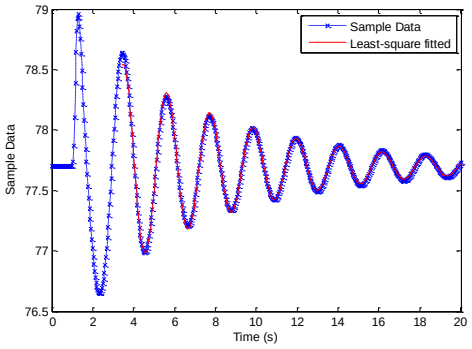

Figure 3-1 – Example of a total core power response calculated with TRACE/PARCS after an induced pressure perturbation at $t = 1$ s, along with a depiction of the curve fitting performed starting around $t = 3.5$ s [41].

A third method used a simulated white noise perturbation of the cross section data in TRACE/PARCS, and the resulting time-dependent response in the power level was analyzed with a different ARMA process [43] to estimate the DR and NF.

Results for the measured DR and NF versus the values calculated using TRACE/PARCS for the ten points are shown in Table 3-1. In general, the three different methods for estimating the DR and NF gave DR results within ~0.03 of each other, with a few notable exceptions. Overall, these results were typically within ~0.10 of the measured DR for all but a couple of cases.

Table 3-1. Summary of stability solutions for all test points at Cycle 14 of Ringhals-1 [41]

Poi-nts	Flow error (%)[a]		Power RMS (%)[a]			Decay ratio				Natural frequency			
	8x8	SVEA	axial	radial	nodal	Ref.	CR[b]	PP[c]	NS[d]	Ref.	CR[b]	PP[c]	NS[d]
P01	2.21	-0.88	6.77	2.73	9.14	0.30	0.377	0.391	0.444	0.43	0.382	0.382	0.395
P03	2.23	-0.42	5.89	2.90	8.19	0.69	0.580	0.582	0.616	0.43	0.391	0.391	0.391
P04	2.34	-0.35	8.45	3.40	9.80	0.79	0.833	0.813	0.677	0.55	0.505	0.505	0.511
P05	2.08	-0.55	6.73	3.14	8.41	0.67	0.741	0.757	0.736	0.51	0.487	0.483	0.484
P06	2.14	-0.81	0.60	3.02	7.95	0.64	0.619	0.622	0.647	0.52	0.481	0.477	0.474
P08	2.07	-0.60	4.85	2.88	6.72	0.78	0.870	0.854	0.851	0.52	0.477	0.476	0.475
P09	2.05	-0.32	13.5	2.25	14.4	0.80	0.896	0.891	0.803	0.56	0.526	0.524	0.532
P10	2.13	-0.87	3.23	2.66	5.68	0.71	0.733	0.724	0.729	0.50	0.476	0.474	0.475

[a]Compared with reference values; [b]Control rod perturbation; [c]Pressure perturbation; [d]Noise simulation

In addition, several parametric studies were performed on Point 10 of Cycle 14. First, a study on the effect of spatial and temporal discretization was performed. Figure 3-2 shows a comparison of decay ratios calculated as a function of timestep size for both the Semi-Implicit and SETS numerical methods in TRACE. As described in the previous section, the Semi-Implicit method behaves as an explicit method for these purposes, and the SETS method as an implicit method. As shown in the paper [41], a Taylor expansion approach can be used to determine the truncation error, and if the problem is represented by a simple one-dimensional wave equation, the Taylor expansion becomes

$$\rho_t + v\rho_x = v\Delta x(1 \mp c) f_{xx} / 2 + O[\Delta x^2, \Delta t^2] \tag{3.10}$$

The main feature to note is the $\Delta x(1 \mp c)$ factor, where Δx is the axial mesh size, c is the Courant number described in the previous section, and the sign is negative for the explicit (*i.e.* Semi-Implicit) method and positive for the implicit (SETS) method. The other terms (v and f_{xx})

in the right hand side expression are determined by the physical conditions and can't be directly adjusted numerically.

Thus, the results of Figure 3-2 can be explained in terms of this leading truncation error term, which corresponds to second-order diffusion. This has a significant dampening effect on the oscillations, which can be seen in the figure. For example, as Δt goes to 0, c goes to 0 as well, and both numerical methods have the same leading truncation error of $v\Delta x f_{xx}/2$, which causes the decay ratio to dampen (decrease) by a certain amount. As Δt is increased (which increases c), the SETS method sees an increase in the numerical diffusion (*i.e.* lower DR) due to the $(1 + c)$ factor; however, the Semi-Implicit method sees a *decrease* in numerical diffusion (higher DR) due to a $(1 - c)$ factor.

The maximum achievable Δt for this case was approximately 19 ms for the Semi-Implicit method with a uniform spatial mesh; this occurred once the maximum Courant number in the entire model reached 1.0; c was not allowed to exceed 1.0 anywhere since this would cause instability, as described in the section above. However, as depicted in Figure 3-3, an additional case was developed which matched the local Δx values to the local vapor velocity values; this ensured a more uniform range of c from the inlet to the exit of each channel, allowing for the average c value across the core to be higher once the maximum Δt giving $c = 1.0$ in any cell was reached. Thus, as seen in Figure 3-2, Δt was now able to reach approximately 38 ms and the overall numerical diffusion was reduced further to yield a DR approximately 0.17 higher than when Δt was zero. A similar nodalization strategy was used for all remaining full-core stability results shown in this thesis, due to the significant effect it has on the calculated DR.

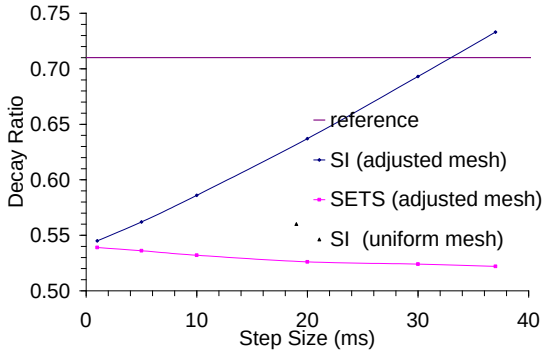

Figure 3-2 – Decay ratio as a function of timestep size for different meshes and numerical methods, for Point 10 of Cycle 14 [41]. The horizontal line at a y-coordinate of 0.71 is the measured reference value.

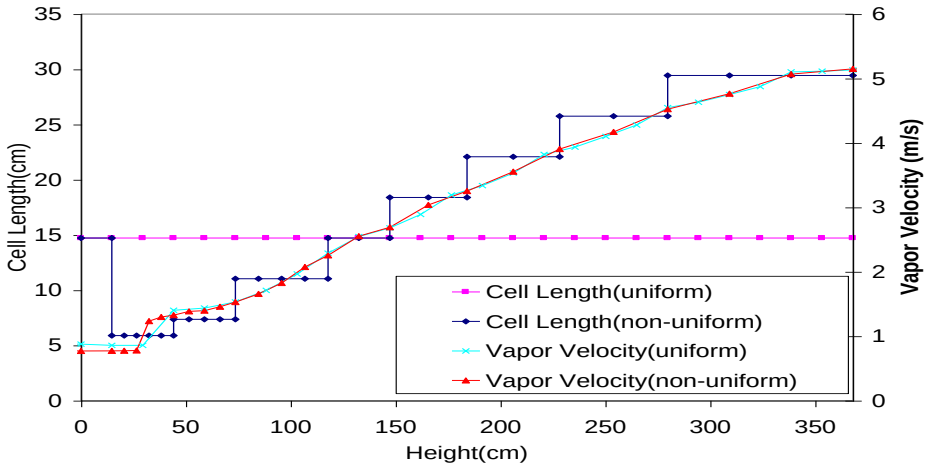

Figure 3-3 – Axial mesh spacing used to minimize the variation in the Courant number by matching Δx to the local velocity [40].

One additional sensitivity study in particular showed a strong effect on the stability characteristics: the decay ratio was found to increase significantly as the gap conductivity was increased, as shown in Figure 3-4. Other parameters were adjusted as well, but the gap conductivity effect was found to be the strongest.

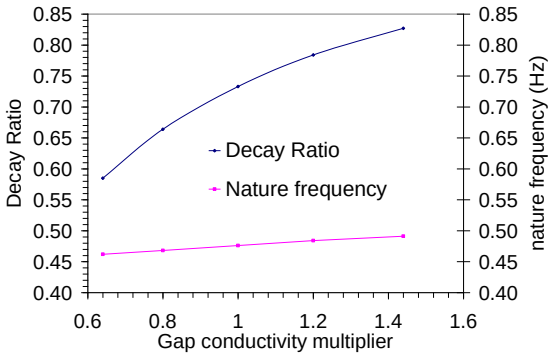

Figure 3-4 – Effect of gap conductivity on the calculated DR and NF [41].

3.3 Oskarshamn

On February 25, 1999, the Oskarshamn-2 NPP experienced a stability event which culminated in diverging power oscillations. The event was successfully modeled by the TRACE/PARCS coupled system code, and further uncertainty analysis of the event is described in the present study. The results show very good agreement with the plant data, capturing the entire behavior of the transient including the onset of instability, growth of the oscillations, and oscillation frequency. This provides confidence in the prediction of other parameters which are not available from the plant records. The event provides coupled code validation for a challenging BWR stability event, which involves the accurate simulation of neutron kinetics (NK), thermal-hydraulics (TH), and TH/NK coupling. The success of this work has demonstrated the ability of the 3-D coupled systems code TRACE/PARCS to capture the complex behavior of BWR stability events. The problem was released as an international OECD/NEA benchmark, and it is the first benchmark based on measured plant data for a stability event with a DR greater than one.

Introduction

Assessment of coupled nuclear-thermal-hydraulic (CNTH) codes has been enhanced since the mid-90s by a series of OECD/NEA coupled code benchmarks based on operating reactor data, including:

- OECD PWR Main Steam Line Break Benchmark (based on TMI-1 Nuclear Power Plant (NPP)) [44]
- OECD BWR Turbine Trip Benchmark (based on Peach Bottom 2 NPP) [45]
- OECD VVER1000 Coolant Transient Benchmark (based on Kozloduy 6 NPP) [46]

The previous OECD benchmarks for CNTH codes have confirmed the codes' capability to model and simulate postulated accidents (PAs) and anticipated operational occurrences (AOOs). The primary objective of the present benchmark is to establish confidence in extending code applications from its original intended use such as PAs and AOOs, to more challenging events such as unstable power oscillations without scram, where non-linear models are necessary.

The previous BWR stability benchmarks, such as the Peach Bottom 2 stability tests [47], OECD Ringhals 1 [48] and Forsmark [49] benchmarks, are based on noise measurements of a stable reactor, where a decay ratio (DR) less than 1.0 was measured for all conditions. The present BWR stability benchmark is the first benchmark based on measured plant data for a stability event with a DR greater than one.

The present benchmark is based on the Oskarshamn-2 NPP and the transient measurements of the February 25, 1999 event. A loss of feedwater (FW) pre-heaters and control system logic failure resulted in a condition with a high feedwater flow and low feedwater temperature without reactor scram. In addition to the initiating event, an interaction of the automatic power and flow control system caused the plant to move into a low flow – high power regime. The combination of the above events culminated in diverging power oscillations with in-phase instability, which triggered an automatic scram at high power. The power evolution for the event is shown in Figure 3-5.

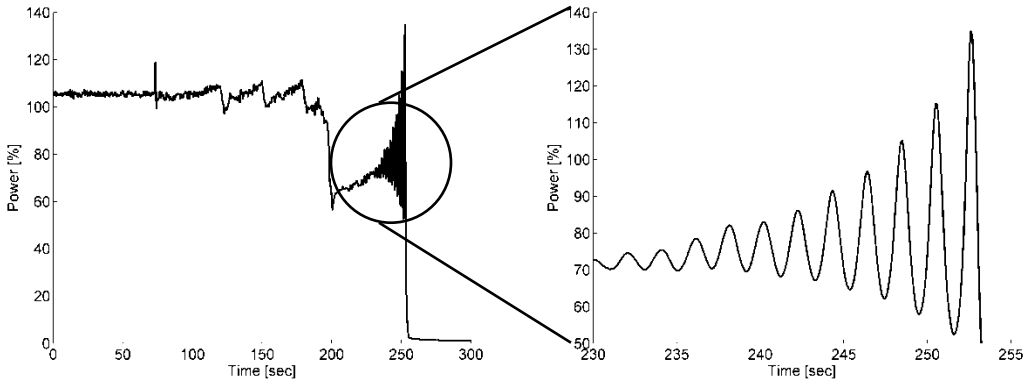

Figure 3-5 – Oskarshamn-2 February 25, 1999 feedwater transient.

This problem is challenging to neutron kinetics (NK), thermal-hydraulics (TH), and TH/NK coupling, where high-fidelity coupled TH/NK is required. The expected benefits of the benchmark are:

- The benchmark provides a framework for coupled code validation for the BWR with both large-amplitude nonlinear power oscillations and challenging plant transients, including changes in subcooling and partial control rod insertions;
- The benchmark challenges the accuracy of the TH solution – numerical methods, model discretization, constitutive relations, flow regime maps;

- The benchmark challenges the accuracy of the NK solution – coolant temperature and density feedback, neutronics and kinetics data;
- The benchmark challenges the accuracy of TH/NK coupling – tightly coupled transient, oscillatory conditions with feedback, fast multi-physics and a strongly coupled problem.

A full-core, three-dimensional coupled neutronics/thermal-hydraulics model was created using the US NRC coupled code system TRACE (TRAC/RELAP Advanced Computational Engine)/PARCS (Purdue Advanced Reactor Core Simulator). The model was successful in reproducing the measured power during the event, including the unstable oscillations.

The following subsection describes in greater detail the events leading to instability in the Oskarshamn-2 plant. Next, details on the plant and a description of the TRACE/PARCS model are provided, followed be a presentation of the results of the TRACE/PARCS simulation and comparison with plant data, as well as the results of a space and time convergence study.

February 1999 Feedwater Event Description

On February 25, 1999, maintenance work was performed on the switchyard outside of Unit 2 of the Oskarshamn power plant. After finishing this task, the normal electric supply was restored, during which the power supply to a bus bar was unexpectedly interrupted for 150 milliseconds. The control logic for the main breaker connecting the unit to the main grid interpreted this as a load rejection. The load rejection signal was transmitted to the turbine and caused a turbine trip. However, due to a failure in the relay circuit, the load reject signal was never transmitted to the reactor (Point 1; see Figure 3-6 and Figure 3-7).

The output power level of the generator decreased from 625 MWe to 585 MWe, and steam line bypass valves opened to allow the excess steam into the main condenser while maintaining full reactor power. As the load rejection signal was never received by the reactor, the expected automatic control such as automatic insertion of control rods and main recirculation pump trips never occurred.

Because of the turbine trip and the opening of the steam line bypass valves, the feedwater pre-heater system was no longer functional and the feedwater temperature decreased by 75 degree Celsius over a period of 150 seconds. The feedwater temperature

decrease caused colder water to enter the reactor vessel and created a positive reactivity feedback, increasing the core power level.

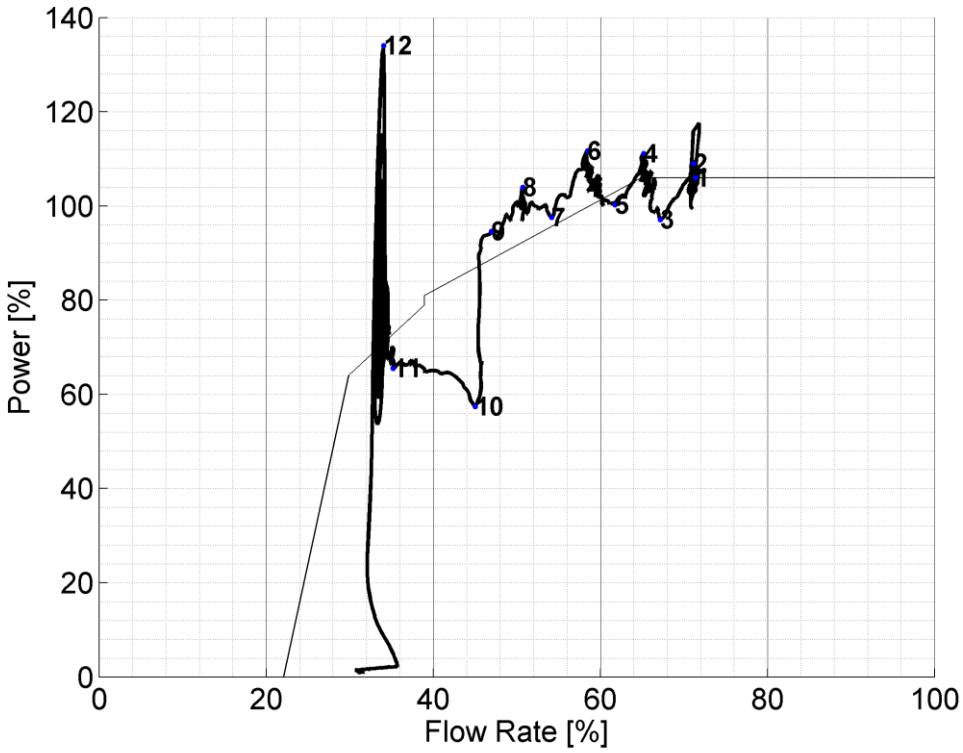

Figure 3-6 – Oskarshamn-2 February 25, 1999 feedwater transient power-flow map.

A pump controller, controlling the rotation speed of the recirculation pumps, reduced the main recirculation flow when the reactor power increased more than 2% above the nominal power, thereby reducing the power. The controller was activated 45 seconds after the turbine trip when the power reached 108% (the nominal power level at the time of the event was 106%), reducing the pump speed at a rate of 640 rpm/min until the power level decreased below 108% (Point 2). However, the cold water continued entering the vessel causing the power level to increase once more above 108% and activating the pump controller (Point 4). This sequence was repeated a third time (Point 6).

Due to the nature of the event involving an increase in reactor power and decrease in reactor flow, the operators partially scrammed the reactor by fully inserting 7 predefined control rods and reducing flow to the minimum at about two minutes after the initiation of the

event (Point 8, Point 9). After the partial scram, the power was reduced to 65% and the flow to 3200 kg/sec. However, the flow of the cold feedwater continued, causing the reactor power to increase and enter the unstable region of the power/flow map (Point 11). The reactor power started to oscillate with successively increasing amplitudes over a period of 20 seconds.

The reactor scrammed due to high power at 3 minutes and 6 seconds after the initial load rejection event, when the power exceeded 132% at 2500 kg/s recirculation flow (Point 12). The scram proceeded according to the design, opening the generator breaker two seconds after the scram, disconnecting it from the main grid and moving the reactor into a hot shutdown state.

The most important thermal-hydraulic parameters (power, pressure, flow, temperature, level) measured during the transient are shown in Figure 3-6 and Figure 3-7.

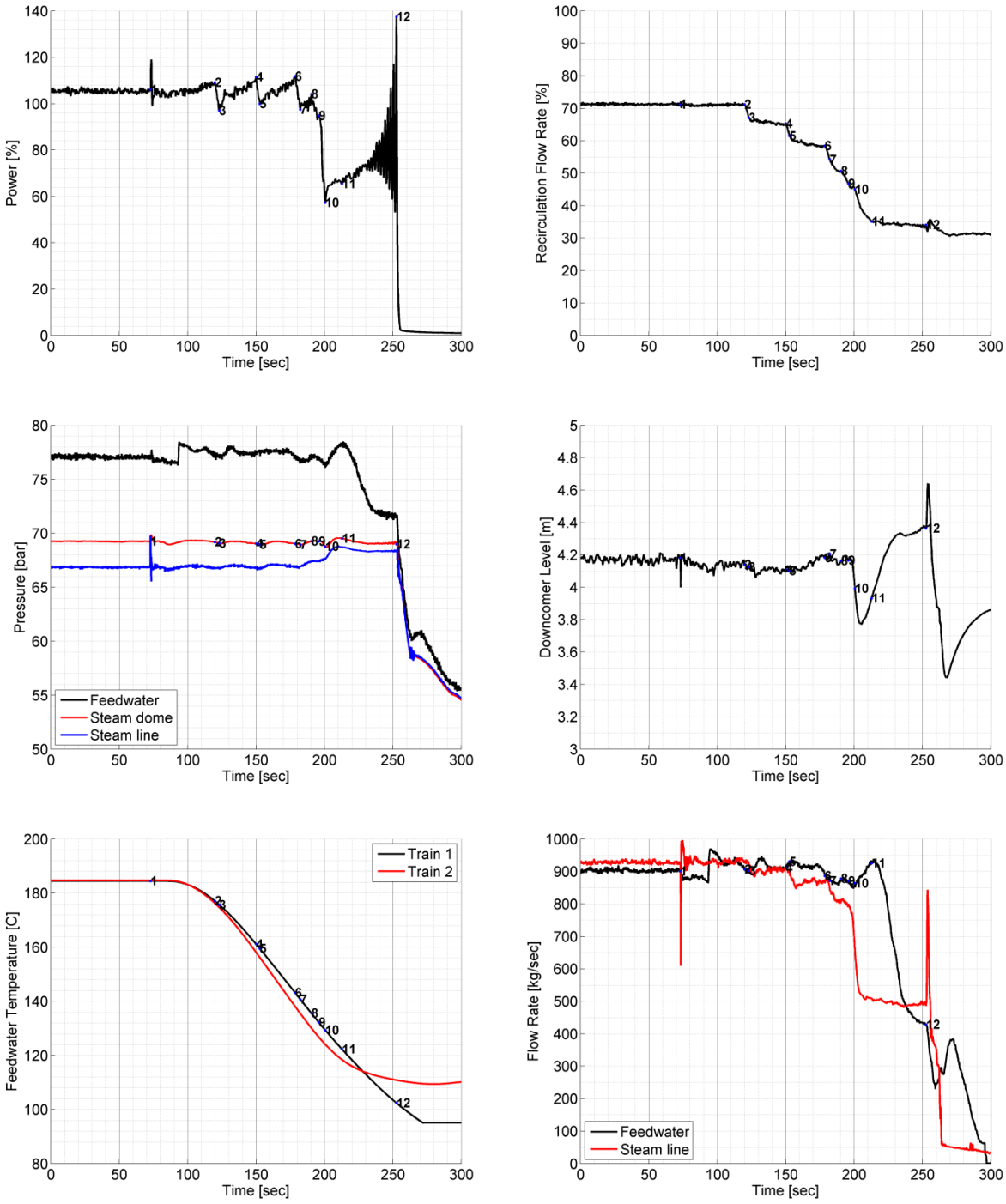

Figure 3-7 – Oskarshamn-2 February 25, 1999 feedwater transient measurements.

Plant and TRACE/PARCS Model Description

Oskarshamn-2 is an external-loop type BWR reactor designed and built by ASEA Atom (currently Westinghouse). The reactor contains four external recirculation loops and the core

consists of 444 bundles. The power was uprated in the early 1980's to 1800 MWth (from the original 1700 MWth), with full power in 1999 denoted as 105.9%. The vessel geometry is shown in Figure 3-8.

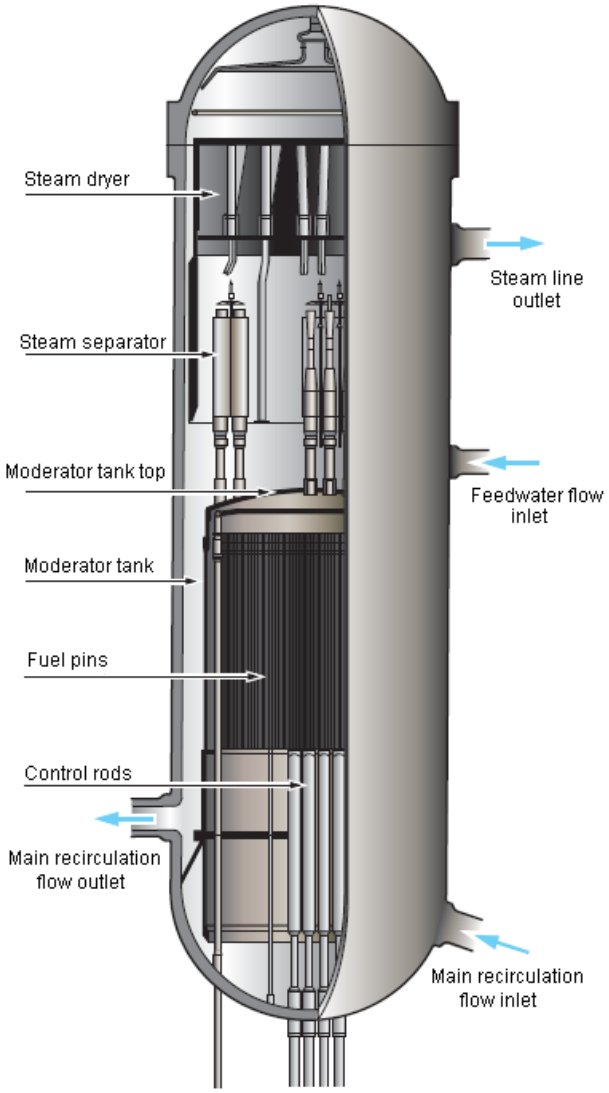

Figure 3-8 – Oskarshamn-2 vessel, system drawing.

The TRACE/PARCS model has been prepared based on the plant documentation and existing plant models. It consists of explicit core, vessel, recirculation loop, separator, feedwater and steam line models. The balance-of-plant was modeled through controllers and boundary conditions. The TRACE base nodalization diagram is shown in Figure 3-9.

Time-dependent FW flow and temperature boundary conditions were taken directly from plant data during the event. The steam line outlet pressure was adjusted to match the measured steam dome pressure. Finally, the recirculation pump speed in the model was adjusted to give the correct recirculation flow rate during the event. The pump speed was prescribed in the model, rather than the pump flow rate itself, in order to more accurately represent the recirculation loop dynamics, in which the changing flow resistance in the primary loop during oscillations can create a significant feedback effect on recirculation flow rate.

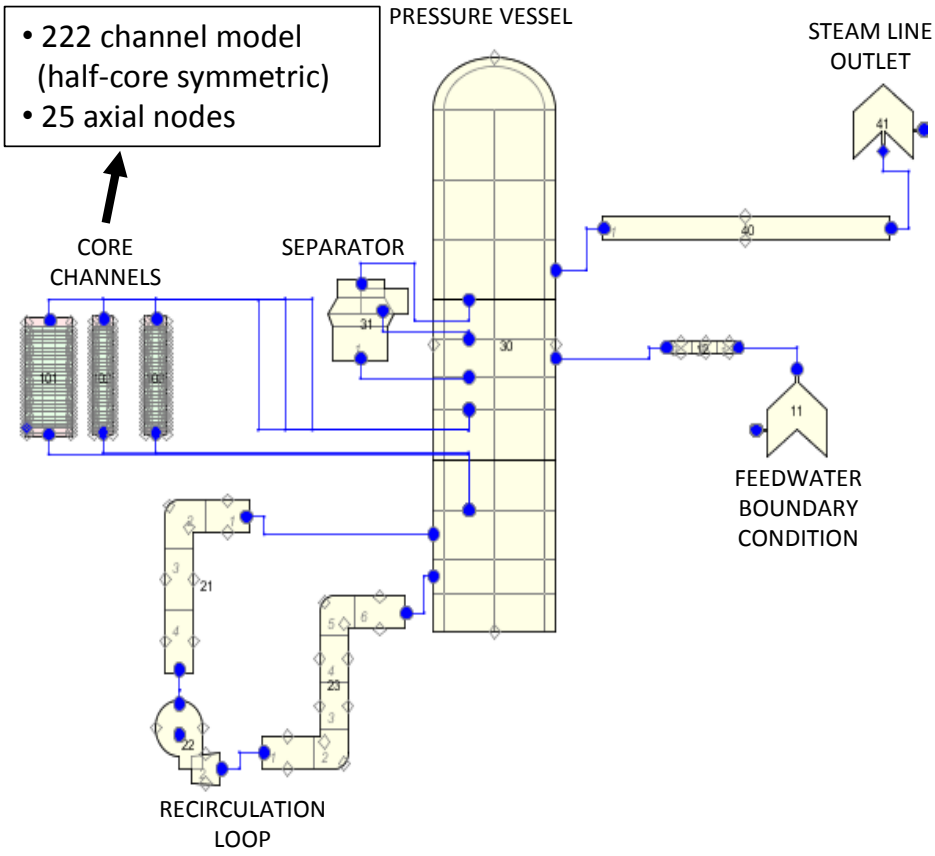

Figure 3-9 – Oskarshamn-2 TRACE nodalization diagram.

The Oskarshamn-2 core at the time of the 1999 event consisted of four main fuel types, arranged in the radial configuration shown in Figure 3-10. The core inlet is divided into three orifice zones with separate frictional loss coefficients for each. Figure 3-11 shows the positions of control rods during normal operation at the time of the event, as well as after partial scram.

Further information on the Oskarshamn-2 core, including bundle geometry, spacer grid configuration, fuel rod configuration and composition, and all other parameters necessary to

create a complete core model, is given in the benchmark specifications [50]. The same material thermal properties (conductivity, heat capacity) were used for all fuel elements.

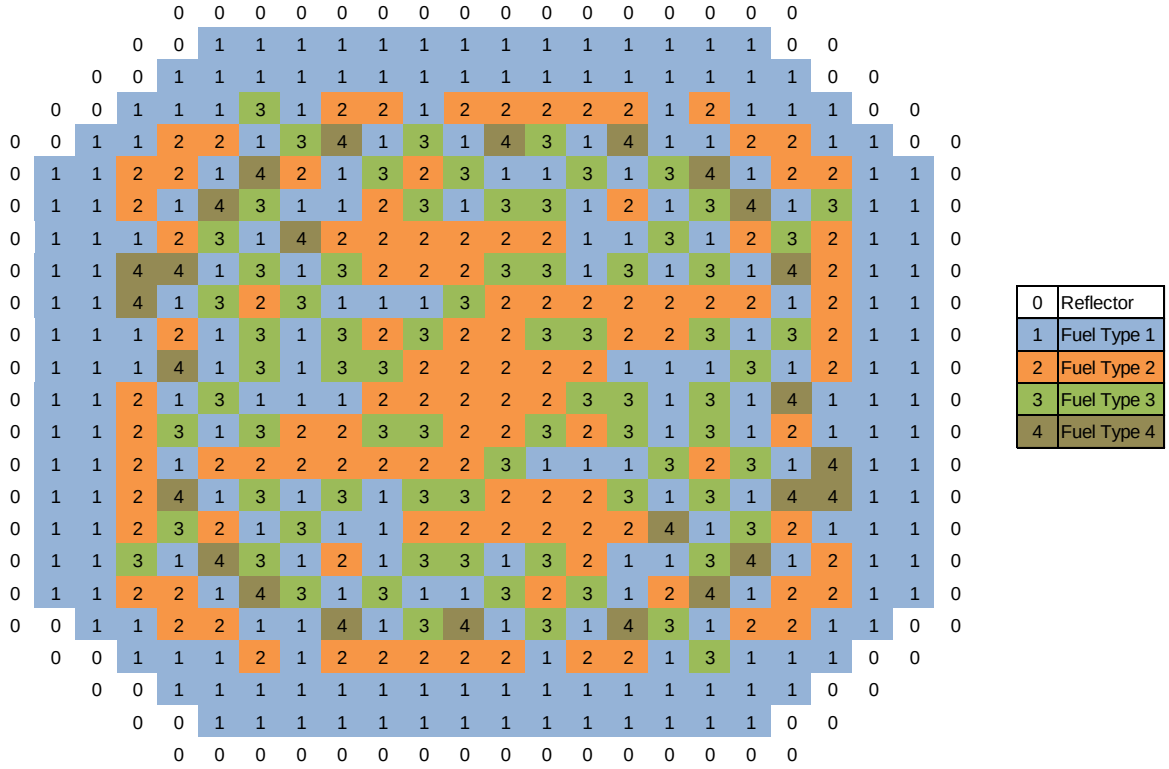

Figure 3-10 – Radial fuel type map used in the PARCS model for the Oskarshamn-2 reactor at the time of the event.

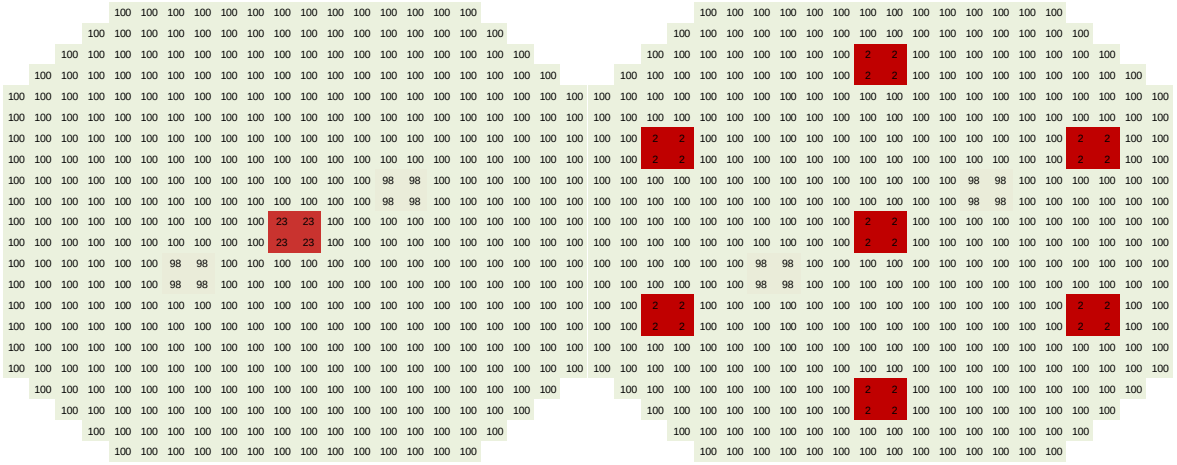

Figure 3-11 – Control rod positions before (left) and after (right) partial scram. A value of 0 indicates the control rod bank is fully inserted, while a value of 100 indicates fully withdrawn.

The core has been modeled in TRACE using 222 core channels, corresponding to half-core symmetry. Axially, the core channels have been divided into 28 axial nodes, with node size proportional to the maximum vapor velocity among all channels (with larger nodes at top of the core) to stay as close as possible to the Courant limit in all cells. The axial channel nodalization is shown on Figure 3-12 (left) and the Courant number is shown on Figure 3-13, where the bundle number correspond to radial location shown on Figure 3-14.

In addition, the Semi-Implicit method was used in TRACE. As shown in previous stability modeling with TRACE/PARCS [41], this procedure helps cancel out the spatial and temporal discretization errors as closely as possible in order to minimize numerical diffusion, which has a strong dampening effect on any oscillations predicted by the codes. The fine meshing at the bottom of the core also has the side benefit of a well-resolved boiling height, which is important for the prediction of BWR stability. In fact, a recent study [51] has indicated that this effect (well-resolved boiling height) could actually be more important in calculating the DR than numerical diffusion itself, and recommends a generic nodalization independent of the specific velocity profile of the model. Regardless, the two nodalization methods are qualitatively similar (finer nodes towards the bottom), so it is expected that either method would have given similar results.

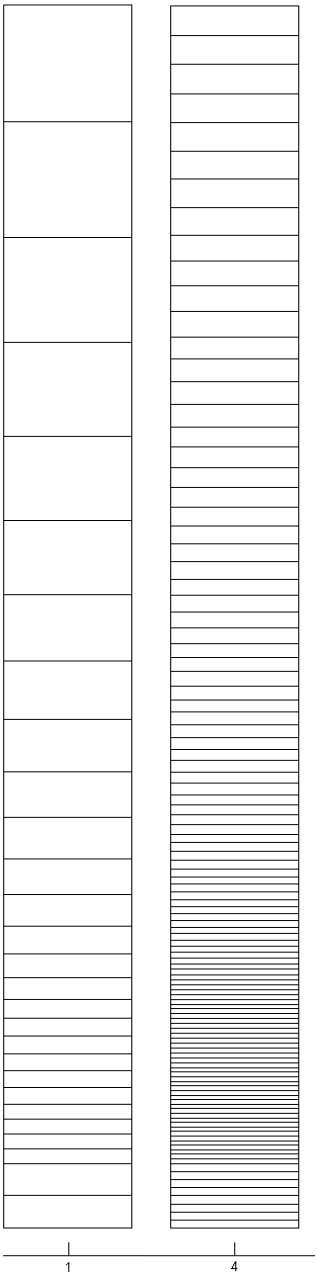

Figure 3-12 – Axial channel nodalization for the Initial (left) and Final (right) Model.

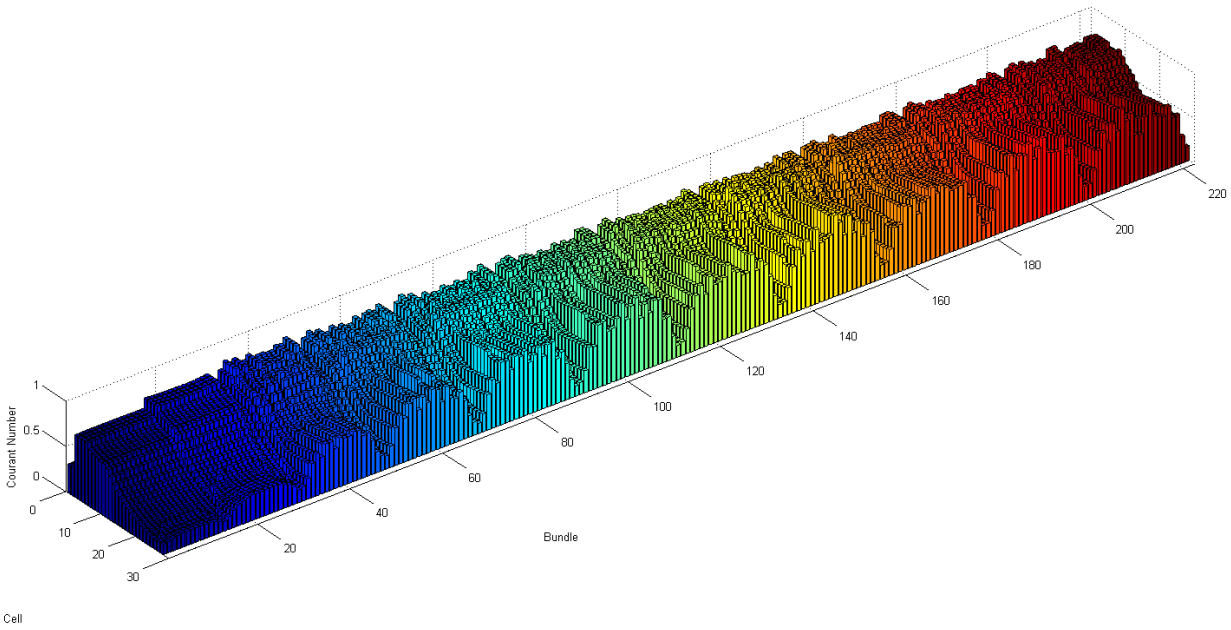

Figure 3-13 – The steady-state Courant number in each channel cell in the core.

PARCS was coupled with TRACE for neutronics calculations. PARCS axial nodalization was uniform (equidistance), so it did not follow the TRACE non-uniform axial nodalization. Two-to-one radial mapping of PARCS neutronic nodes to TRACE thermal-hydraulic channels was used, exploiting the half-core rotational symmetry of the core layout. The radial mapping of TRACE channels to PARCS nodes is shown on Figure 3-14. The plant provided cross-section libraries, and burnup and history distributions were converted to the PMAXS format [52] used in PARCS.

```
                    0   0   0   0   0   0   0   0   0   0   0   0   0   0   0   0
                0   0   1   2   3   4   5   6   7   8   9  10  11  12  13  14   0   0
            0   0  15  16  17  18  19  20  21  22  23  24  25  26  27  28  29  30   0   0
        0   0  31  32  33  34  35  36  37  38  39  40  41  42  43  44  45  46  47  48   0   0
    0   0  49  50  51  52  53  54  55  56  57  58  59  60  61  62  63  64  65  66  67  68   0   0
    0  69  70  71  72  73  74  75  76  77  78  79  80  81  82  83  84  85  86  87  88  89  90   0
    0  91  92  93  94  95  96  97  98  99 100 101 102 103 104 105 106 107 108 109 110 111 112   0
    0 113 114 115 116 117 118 119 120 121 122 123 124 125 126 127 128 129 130 131 132 133 134   0
    0 135 136 137 138 139 140 141 142 143 144 145 146 147 148 149 150 151 152 153 154 155 156   0
    0 157 158 159 160 161 162 163 164 165 166 167 168 169 170 171 172 173 174 175 176 177 178   0
    0 179 180 181 182 183 184 185 186 187 188 189 190 191 192 193 194 195 196 197 198 199 200   0
    0 201 202 203 204 205 206 207 208 209 210 211 212 213 214 215 216 217 218 219 220 221 222   0
    0 222 221 220 219 218 217 216 215 214 213 212 211 210 209 208 207 206 205 204 203 202 201   0
    0 200 199 198 197 196 195 194 193 192 191 190 189 188 187 186 185 184 183 182 181 180 179   0
    0 178 177 176 175 174 173 172 171 170 169 168 167 166 165 164 163 162 161 160 159 158 157   0
    0 156 155 154 153 152 151 150 149 148 147 146 145 144 143 142 141 140 139 138 137 136 135   0
    0 134 133 132 131 130 129 128 127 126 125 124 123 122 121 120 119 118 117 116 115 114 113   0
    0 112 111 110 109 108 107 106 105 104 103 102 101 100  99  98  97  96  95  94  93  92  91   0
    0  90  89  88  87  86  85  84  83  82  81  80  79  78  77  76  75  74  73  72  71  70  69   0
    0   0  68  67  66  65  64  63  62  61  60  59  58  57  56  55  54  53  52  51  50  49   0   0
        0   0  48  47  46  45  44  43  42  41  40  39  38  37  36  35  34  33  32  31   0   0
            0   0  30  29  28  27  26  25  24  23  22  21  20  19  18  17  16  15   0   0
                0   0  14  13  12  11  10   9   8   7   6   5   4   3   2   1   0   0
                    0   0   0   0   0   0   0   0   0   0   0   0   0   0   0   0
```

Figure 3-14 – Radial mapping of TRACE channels to PARCS nodes, each number corresponds to the channel number, which is coupled to one fuel assembly. 0 corresponds to radial reflector.

February 1999 Feedwater Transient TRACE/PARCS Results

The complete initial and boundary conditions necessary for modeling of the February 1999 feedwater transient (stability event) have been made available by the plant. The initial steady-state conditions measured or calculated by the plant were compared with those calculated by TRACE/PARCS.

After optimizing the TH axial nodalization in the core channels based on the Courant number, the average Courant number among all core cells was 0.58 at steady-state conditions. The steady-state conditions calculated by TRACE/PARCS were in excellent agreement with the measured or plant-calculated results. In addition, the model has been validated with two stability measurements performed in December 1998, approximately 3 months before the event. The results have been presented in a previous paper [53].

Once the model had been validated with the December 1998 stability measurements and February 1999 event initial conditions, exactly the same model and nodalization was used for the February 1999 transient, changing only the relevant transient boundary conditions. The measured transient feedwater flow, feedwater temperature, pump speed and steam line

pressure time histories (see Figure 3-7) were used as boundary conditions for the simulation of the February 25, 1999 event.

The TRACE/PARCS calculated power is shown in Figure 3-15. As indicated, the TRACE/PARCS solution is in very good agreement with the plant data. The TRACE/PARCS solution captures the entire behavior of the transient, including power behavior during pump runback, partial scram, onset of instability, growth (decay ratio) and frequency of oscillation, and scram.

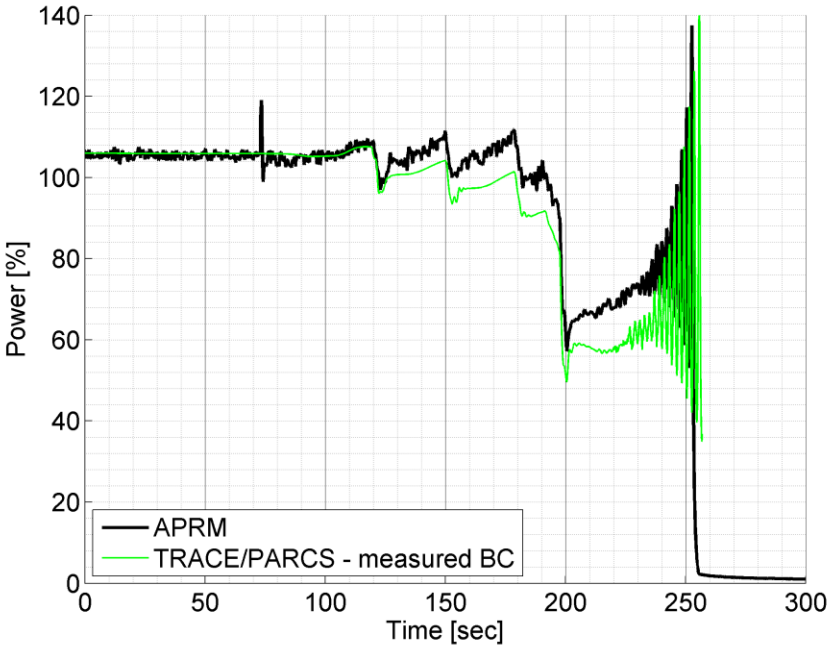

Figure 3-15 – Oskarshamn-2 February 25, 1999 feedwater transient, TRACE/PARCS solution.

Feedwater temperature correction

Even though the instability behavior is predicted qualitatively well, there is a systematic power deviation since 120 sec, well before the onset of instability 220 sec. Deeper investigation of this issue revealed the limitation of the time-dependent feedwater temperature measurement. The FW temperature was measured by resistance temperature detectors (RTD), which are mounted on wells that go inside the FW flow (the RTDs do not penetrate the pipe; they cannot be part of the pressure boundary). The RTDs are very accurate, but the transient response is delayed due to the time required to conduct heat through the

steel separating the flow from the detector. The reactor operator is mainly interested in the steady-state temperature, so it is not a problem for normal operation if the sensor has some delay.

However, for this type of event, an accurate time-dependent FW temperature is necessary. The problem was posed as an inverse heat conduction problem in a one-dimensional semi-infinite slab of steel, in which the time-dependent temperature at a certain depth into the slab was known (using the RTD measurement) and the boundary condition at the wall (assumed equal to the FW fluid temperature) must be determined. An analytic solution to this problem is available [54], and the solution using an assumed steel thickness of 1.27 cm (0.5 inch) is shown in Figure 3-16 in comparison to the original FW temperature measurement. As can be seen, the FW temperature decreases faster and to a lower level than indicated by the plant measurement, compensating for the expected time delay in the measured signal.

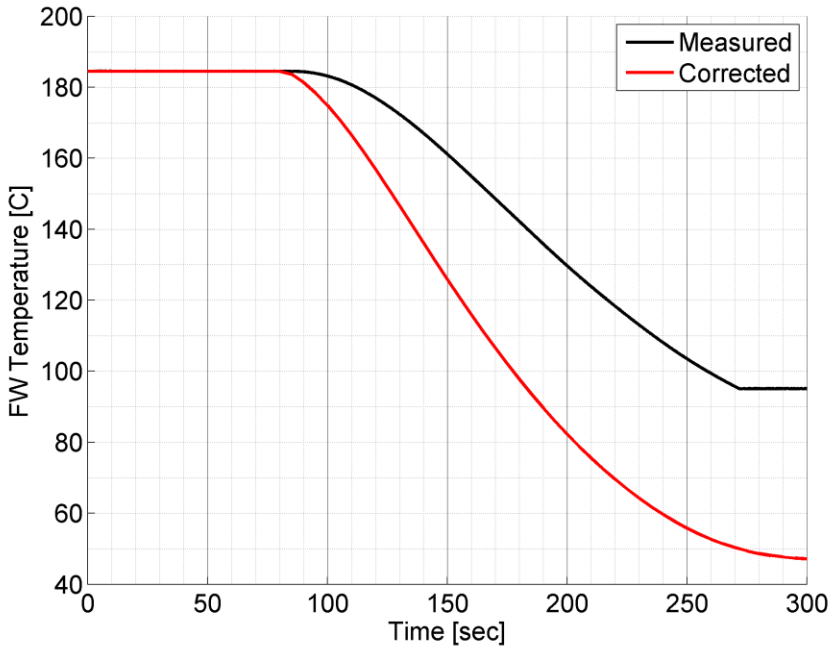

Figure 3-16 – Original and corrected transient FW temperature.

Using the "corrected" FW temperature, the TRACE/PARCS calculated power is shown on Figure 3-17, marked as the "corrected BC" (red line). Due to the close agreement between measured and calculated power in the 120 s to 190 s range (during pump runbacks), 0.5" was

accepted as an appropriate thickness of steel in the absence of more precise information from plant specifications.

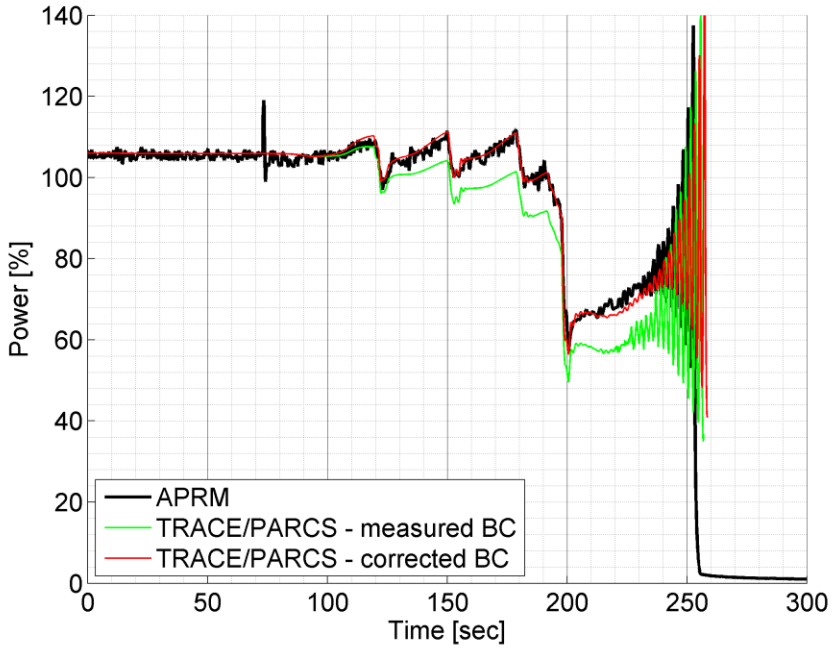

Figure 3-17 – Oskarshamn-2 February 25, 1999 feedwater transient, TRACE/PARCS solution.

With only one corrected parameter (FW temperature), the final TRACE/PARCS solution completely captures the entire behavior of the transient, including power behavior during pump runback, partial scram, onset of instability, growth of oscillation (decay ratio), the oscillation frequency and the scram.

Space/time convergence

The previous result, based on Courant optimization of the spatial and temporal discretization, essentially provides the best solution attainable with the original model which included 28 nodes per TH channel in the core. However, the same nodalization was used in all channels, yet the velocity profile is different in each channel, and also varies as a function of time during flow oscillations. Therefore, since the time step size is restricted by the most limiting cell among all cells in the model, the average Courant number averaged across all cells in the core was observed to be only 0.58 for the steady-state (see Figure 3-13), indicating that significant numerical damping may still exist with the Courant optimization approach.

In order to truly ensure that numerical discretization errors were no longer influencing the results, a full space and time convergence study was carried out for all components in the TRACE model [55], of which a brief summary is provided here. Rather than seeking to "cancel out" the spatial and temporal errors, as was done with the Courant optimization approach, the numerical errors were instead minimized by increasing the number of nodes and decreasing the time step size until further space-time refinement no longer significantly affected the solution, *i.e.* space-time converged model was achieved. Table 3-2 compares the Initial Model (*i.e.* the Courant-optimized model corresponding to Figure 3-9) to the Final Model (the space and time converged model). The axial channel nodalization of the Initial Model was refined by factor of 4 and the vessel nodalization was refined by factor of 3. The axial nodalization of both models is shown on Figure 3-12.

Table 3-2. Differences in discretization between the Initial and Final Models.

	Initial Model	**Final Model**
Nodes in Vessel	15	45
Nodes per Core Channel	28	112
Time step size (sec)	0.008 s - 0.045 (varies)	0.004 (constant)

Figure 3-18 shows the simulation results for core power for both models. Both models show very close agreement with each other in terms of power level during the first 200 sec of simulation time. However, it is once the oscillations begin after 200 sec that the solution becomes highly sensitive to the spatial and temporal discretization. The oscillations in the Final Model were significantly less damped than for the Initial Model, which appears to confirm the fact that numerical diffusion still played a significant role in the Initial Model, despite attempts to minimize this effect.

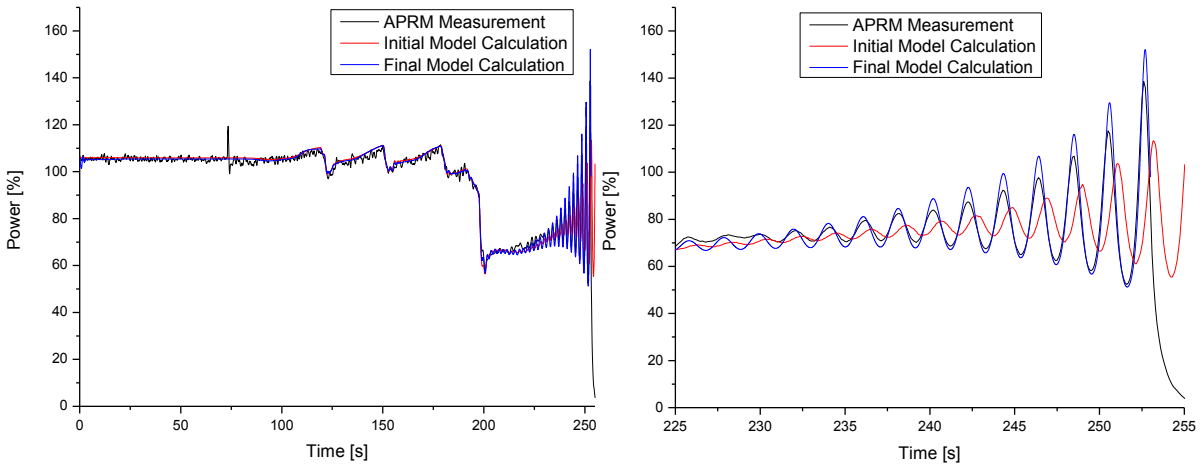

Figure 3-18 – Comparison of the Initial Model using the Courant optimization approach versus the Final Model using the space and time convergence approach.

Table 3-3 compares the calculation time for the two models. Note that the Final Model was terminated at a simulation time of 253 sec, compared to 300 sec for the Initial Model. Despite shorter simulation time, the calculation with the Final Model required approximately 17 times as long to complete compared to the Initial Model, due to the finer spatial nodalization in the core and vessel, and the smaller time step size.

Therefore, there exists a significant tradeoff between accuracy of the solution and computational cost. For the first-order explicit discretization methods, the Courant optimization approach is capable of giving a reasonably accurate prediction of unstable oscillations with a relatively small computational burden. However, if the most accurate and robust solution is desired using the first-order method, space and time converged approach is necessary despite the increased computational burden.

Table 3-3. Runtime comparison for the two models.

	Initial Model	Final Model
Calculation time for the transient (hr)	2.9	49.6
Total simulation time (sec)	300	253

Conclusions

A TRACE/PARCS model has been developed for the Oskarshamn-2 reactor and validated with the February 1999 steady-state and transient conditions. The initial attempt to model the event exposed limitation of RTD well instrumentation to measure and capture dynamic effects. With the correct boundary conditions, the obtained results for the February 1999 event show excellent agreement with the plant data, capturing the entire behavior of the transient including onset of instability, growth of oscillation and oscillation frequency. The results of a time and space convergence study have been presented, showing the significant tradeoff that exists between accuracy and computational cost for the prediction of oscillations. The Final Model (space-time converged) obtains better power amplitudes and signal frequency, compared to the experimental results (APRM), and hence better DR. Both models (Initial and Final) will be used for further studies to scrutinize and delineate their capabilities and limitations.

The success of this work has demonstrated the ability of 3-D coupled code TRACE/PARCS to capture the complex behavior of BWR stability event with a decay ratio larger than unity. The Oskarshamn-2 1999 stability event allows coupled code validation for BWR with a real, challenging stability event, which challenges accuracy of TH solution, NK solution and TH/NK coupling. The problem has been released as an international OECD/NEA benchmark and interested participants are invited to contact authors for more information.

Chapter 4. Investigation of Mode Interactions with a Full-Core TRACE/PARCS Model

The previous chapter has demonstrated a successful application of the TRACE/PARCS code to stability analysis, in the form of two OECD benchmark problems. It is because of the TRACE/PARCS code's success in modeling both in-phase and out-of-phase oscillations, and ability to handle nonlinearities associated with large-amplitude oscillations, that the author feels confident in using the code for the complex out-of-phase limit cycle behavior to be examined in this chapter.

A study of BWR out-of-phase oscillations has been performed with the TRACE/PARCS coupled code system. Unstable power oscillations with a time-dependent, rotating line of symmetry have been successfully simulated using input models from two different BWRs and applying simple anticipated transient without scram (ATWS) scenarios. The λ-modes of the neutron flux were calculated using an implicitly-restarted Arnoldi solver, and the time-dependent amplitudes of the fundamental, first azimuthal, and second azimuthal power modes were determined for each simulation. After progressing in an irregular, sporadic fashion, the oscillations appeared to transition into a clear "rotating mode" that was sustained indefinitely with a fixed phase shift between modes of roughly 90°. Because the phase shift did not gradually change over time, despite each mode having a different natural frequency in the linear range, the conclusion was made that a nonlinear interaction mechanism was active between the first and second subcritical azimuthal modes to maintain the constant phase shift during the limit cycle. However, an additional model, based on the same core but using homogeneous cross sections and channel geometries, gave a "side-to-side" out-of-phase oscillation mode as the final limit cycle behavior, with a phase shift between the two azimtuahl modes of $180°$. The cause for the difference in behavior is uncertain, although it was likely related to the difference in neutronic behavior via the cross sections used.

An additional study was performed which found that a small perturbation is capable of drastically affecting the development of oscillations in a simulation when both modes (in-phase and out-of-phase) are unstable; when one of the models was modified to include a small-amplitude noise source on the first azimuthal mode, purely out-of-phase oscillations were observed, whereas the oscillations had been purely in-phase for the first 55 seconds when no noise signal was included. Because most ATWS event calculations involve mostly in-phase perturbations to the BWR core, it is recommended to add a small out-of-phase perturbation in simulations where both the in-phase and out-of-phase modes may be unstable.

4.1 Methodology

The first model used in this study is a 648-channel model derived from the same model used for the Ringhals benchmark – specifically, cycle 14. However, for this study, the core model was modified to exhibit a fully "north-south" symmetric core loading (where "north" here refers to the radial upper half of the core and "south" to the lower half). This symmetry was attained by projecting all fuel bundle information (including fuel composition, geometry, and burnup distributions) from the north half of the core onto the south half of the core so that the two halves mirrored each other. For example, Figure 1 compares the burnup distribution in the north-south symmetric model versus the original burnup distribution. The original intent of the present study was to compare results using a full-core model versus a half-core model; thus, the full-core model was modified with a fully "north-south" symmetric core loading so that the model was completely analogous to the half-core model and would match it exactly, at least in the steady state.

However, as it turned out, the comparison between the half-core and full-core models for transient limit cycle simulations did not reveal any interesting results. Interestingly, though, when a slight asymmetry was applied to the full-core north-south symmetric model (in the form of an asymmetric burnup distribution), the limit cycle behavior changed and a clear "rotating mode" limit cycle oscillation developed in the transient simulation. This result is the primary focus of this chapter, and for this reason the "modified" north-south symmetric model was used rather than the original (asymmetric) model from the Ringhals benchmark.

The fully north-south symmetric model, including a symmetric burnup distribution, will hereafter be referred to in this chapter as "Model A." The modified north-south symmetric model, identical to Model A except for the burnup distribution, will be referred to as "Model B." To be clear, this model still included fully north-south symmetric fuel composition and geometry information, just with an asymmetric burnup distribution. The burnup distribution for each case, averaged over each assembly, is indicated in Figure 4-1.

Two additional modifications were made to Models A and B which departed from the original TRACE/PARCS Ringhals model. These modifications were added to promote instability in the simulation. First, the core was artificially destabilized by adding a significant pressure

drop at the outlet (K_{out} = 4 velocity heads). In addition, several control rods in the radial center of the core were inserted fully in order to achieve the so-called "bowl shape" in which the power is relatively low in the center and high in the periphery. This control rod pattern is shown in Figure 4-2. This, in addition to the "bottom-peaked" axial power profile in both models, was found to promote the out-of-phase mode over the in-phase mode. This is consistent with results reported from many sources (see, *e.g.*, [6] [18] [56]). In light of the modifications described above, these models were not necessarily intended to represent realistic core conditions; rather, they were developed for illustrative purposes to better understand the phenomenon of out-of-phase oscillations.

For each model used in this study, a coupled neutronic-thermohydraulic steady-state solution was obtained from a stable operating condition, after which a newly-implemented subroutine in the PARCS neutronics code was used to find the higher λ-modes of the static neutron flux via an implicitly-restarted Arnoldi solver. The same subroutine was used during the transient calculations to determine mode amplitudes during the oscillations based on the shapes of the forward and adjoint power modes (found during the steady state) and the three-dimensional power distribution (for a detailed discussion of the method, see [6] and [7]).

For Models A and B, an asymptotically convergent steady state solution was able to be found. Conveniently (for the purposes of this study), the transient solution happened to be unstable in at least one mode without making any changes to the physical conditions (boundary conditions, control rod positions, etc.) compared to the steady state. This was most likely because the steady state calculation used the SETS time discretization method in TRACE, whereas the transient calculation used TRACE's Semi-Implicit method. The Semi-Implicit method in general yields a more unstable solution (*i.e.* higher decay ratio) than the SETS method based on consideration of axial nodalization and numerical diffusion as demonstrated in previous studies [41] [53] [35]. In any case, this circumstance proved convenient in that the eigenvalues and eigenvectors from the steady state were still applicable (at least in the linear range) to the transient oscillations, without needing to change the physical operating conditions externally which would have made the eigenvalues and eigenvectors found from the steady state not strictly applicable.

In the event that a stable out-of-phase limit cycle was attained during the simulation, *e.g.* for Model B, estimates for the oscillation frequency and phase shift between modes were calculated using simple expressions based on the local maxima and minima of each time-dependent mode amplitude. Once the oscillations had converged to a steady limit cycle behavior (*i.e.* the oscillation amplitudes were essentially constant from iteration to iteration), the oscillation frequency was determined by

$$f = \left(\frac{\sum_{n=1}^{N-1} \left(t_{max,i}^{n+1} - t_{max,i}^{n} \right)}{N-1} \right)^{-1} = \left(\frac{t_{max,i}^{N} - t_{max,i}^{1}}{N-1} \right)^{-1} \qquad (4.1)$$

where f is the oscillation frequency in Hz, $t_{max,i}^{n}$ is the time at which the nth local maximum occurs for azimuthal mode i ($i \in \{1,2\}$), starting from a specified point in the simulation after a steady limit cycle has been achieved, and N is the number of time values (*i.e.* number of full oscillation periods plus one) to use for the averaging process. Equivalent results for f will be obtained regardless of which azimuthal mode is chosen for Eq. 1, due to both modes oscillating with the same periodicity.

Similarly, the average phase shift between the two azimuthal modes was found using the formula

$$\phi = \frac{1}{2} \left(\frac{\sum_{n=1}^{N} \left(t_{max,1}^{n} - t_{max,2}^{n} \right)}{N} + \frac{\sum_{n=1}^{N} \left(t_{min,1}^{n} - t_{min,2}^{n} \right)}{N} \right) \left(\frac{360^{\circ}}{f} \right) \qquad (4.2)$$

where ϕ is the average phase shift, in degrees, between mode 2 and mode 1 and $t_{min,i}^{n}$ is the time at which the nth local minimum occurs for azimuthal mode i. For the cases studied in this chapter, the average value of $\left(t_{max,1}^{n} - t_{max,2}^{n} \right)$ was different than the average value of $\left(t_{min,1}^{n} - t_{min,2}^{n} \right)$ due to slight asymmetries in the oscillation patterns as a function of time, likely caused by asymmetries in the model itself. Hence, an approximate "average" phase shift was determined by averaging between the two results based on the minima and maxima, respectively.

For this chapter, a value of N=10 (*i.e.* 10 full oscillation periods) was chosen for both Eq. 1 and Eq. 2 in order to help average out the small variations in f and ϕ that would occur if only a single oscillation were considered (*i.e.* N=1). For example, the value of $\left(t_{max,i}^{n} - t_{max,i}^{n} \right)$ was

found to vary on the order of 1% from one oscillation to the next, mostly due to the error associated with the finite timestep size of the calculation ($\Delta t \approx 10$ ms).

An additional case, called "Model C," was created which was identical to Model B, except that a short perturbation was artificially added to the first and second azimuthal modes at the beginning of the transient. This was accomplished with built-in PARCS functionality which perturbs the moderator cross-sections in PARCS using a user-specified spatial shape – in this case, the shape of the first two azimuthal modes calculated from the Arnoldi subroutine described below. In this manner, the first and second azimuthal modes were excited without introducing any perturbation in the fundamental mode or any higher modes. This perturbation was applied to Model C as a short 0.1 s pulse starting at a simulation time of 1.0 s. To be clear, only the moderator cross-sections in PARCS were modified here; there was no direct perturbation applied to the TRACE thermal-hydraulic solution (with only an indirect effect occurring via neutronics feedback over time).

The amplitude of the artificial PARCS cross-section perturbation was adjusted so that initial the response in terms of relative power was small (on the order of 1%-2%). This created small-amplitude, but growing, oscillations which allowed the linear stability characteristics of each mode (*i.e.* decay ratio and natural frequency) to be determined. The simulated mode amplitudes as functions of time were truncated after approximately 7 unstable periods, ensuring that the oscillations remained small enough that nonlinear effects were negligible, and then these time signals were inputted to the DRARMAX code which calculated decay ratios and frequencies using an ARMA process [41]. Performing this stability analysis in the linear regime (*i.e.* small-amplitude oscillations) ensures that the two azimuthal modes oscillate independently with no nonlinear interaction between them. This information was then used to compare with the fully-developed limit cycle results of Model B to draw conclusions regarding the coupling between modes.

In addition to the two models based on the Ringhals plant, two more models (termed "Model D" and "Model E") were used which were derived from a generic BWR-5 plant model. The model contains 764 fuel assemblies, and the core loading consists of a single fuel type with quarter-core symmetry and a uniform burnup distribution. Control rod positions are shown in

Figure 4-2; note that this core was able to achieve an out-of-phase limit cycle without inserting many rods in the radial center of the core, unlike for Models A and B. Also unlike Models A and B, which developed limit cycle oscillations from the steady-state conditions, a turbine trip event was simulated in Model D and Model E to bring about instability. The turbine trip led to a spike in reactor power and a significant subcooling transient which led to a decreased core flow rate and brought the core to unstable conditions. Model E was identical to Model D except that it also included a simulated white noise perturbation in the PARCS neutronic calculation. This was accomplished by perturbing the moderator cross-section in PARCS for the azimuthal modes only, using the same method as for Model C except that this time it was chosen to use a simulated white noise signal over a specified time interval based on the PARCS built-in functionality. This simulated white noise was used as a means of exciting as many different frequency "modes" as possible.

Realistically, in each case a scram would have been triggered on the average power level alone (without considering regional power levels) since the average power exceeded 150% at some point during each transient calculation that was performed. However, in each case the reactor scram was disabled in order to allow oscillations to develop freely. Therefore these simulations represent an Anticipated Transient Without Scram (ATWS) event.

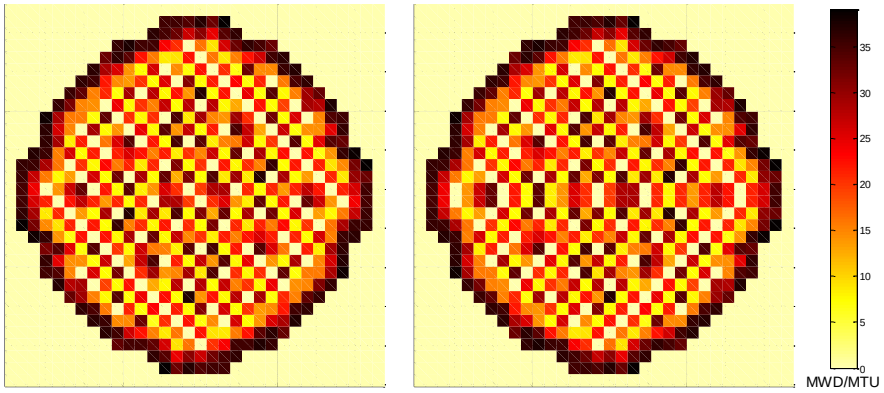

Figure 4-1 – Radial map of the axially averaged assembly burnup distributions for Models A-C. Models B and C (left) used the original asymmetric burnup distribution, while Model A (right) used a north-south symmetric distribution with values from the north half reflected onto the south half.

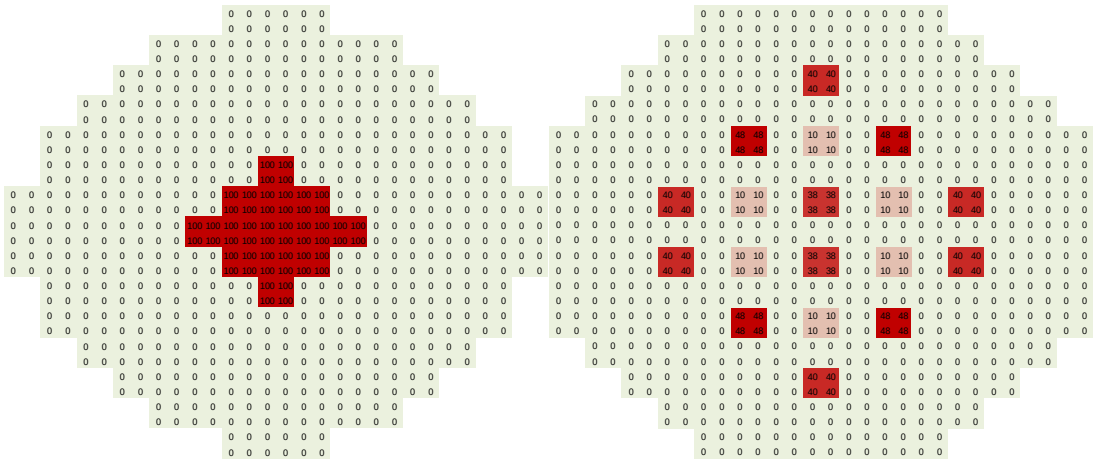

Figure 4-2 – Radial map of control rod positions for Models A, B, and C (left), and Models D and E (right). A value of 100 indicates the control rods are fully inserted; a value of 0 indicates fully withdrawn.

4.2 Results

Out-of-Phase Limit Cycle with No Rotation

The first three power modes calculated from the steady-state solutions of Model A by the Arnoldi subroutine in PARCS are visualized in Figure 4-3. Here, the modes have been averaged in the axial direction for each fuel assembly. Note the highly depressed power in the center of the core for the fundamental mode caused by the control rod pattern. Also note that the north-south symmetry of the model forces the symmetry lines of the azimuthal modes to be aligned perfectly east-to-west and north-to-south, respectively. This would not necessarily be the case for a non-symmetric core configuration.

Eigenvalues for the steady state calculation for Model A are shown in Table 4-1. The fundamental eigenvalue is significantly far from unity (subcritical by 793 pcm); this is likely largely due to the added control rod insertions in the center of the core. The eigenvalue separation, also given in the table, was calculated with respect to the fundamental eigenvalue using the typical reactivity formula $1/k_i - 1/k_0$, where k_i is the eigenvalue of the *i*-th mode.

Figure 4-4 shows the calculated mode amplitudes as a function of time during the simulated transient. As described in the previous section, the transient simulations for Model A developed limit cycle oscillations without any external change (*e.g.* change in boundary conditions) required. The oscillation mode was out-of-phase but only in the north-to-south direction, as Mode 1 was 'active' while Mode 2 was not (*i.e.* the amplitude of Mode 2 was essentially zero throughout). The apparent oscillations in the fundamental mode were not actually indicative of in-phase oscillations; rather, this was a result of the non-sinusoidal time variation in the azimuthal modes due to nonlinear behavior – as one half of the core experienced a sharp "peak," the other experienced a wide "trough" because the power cannot be negative, and the total power (as well as the calculated fundamental amplitude) oscillated as a result.

The simulation results for Model A are rather typical of out-of-phase limit cycle oscillations in which only one azimuthal mode is active. The fact that the core oscillated only in the north-south direction is not especially surprising considering that the Mode 1 eigenvalue

was greater than the Mode 2 eigenvalue; however, this consideration does not always guarantee that only one azimuthal mode will become activated in limit cycle oscillations, as will be demonstrated in the following section. Thus, although the simulation for Model A does not reveal many insights in itself, it is useful for providing a sharp contrast to the results shown later, demonstrating that relatively small changes to the model can give very different results.

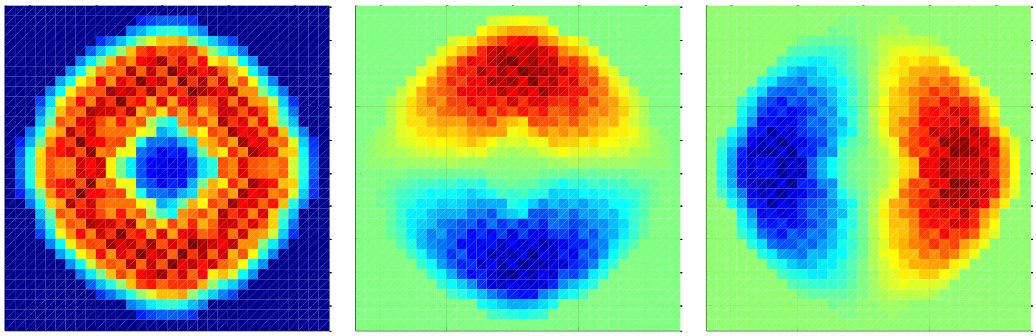

Figure 4-3 – Axially-averaged radial shape of the first three power modes for BWR Model A: the fundamental mode (left), the first azimuthal mode (center), and the second azimuthal mode (right).

Table 4-1. Eigenvalues for the first three modes for Model A

	Mode 0	**Mode 1**	**Mode 2**
Eigenvalues:	0.99207	0.98675	0.98629
Separation:	-	0.00544	0.00591

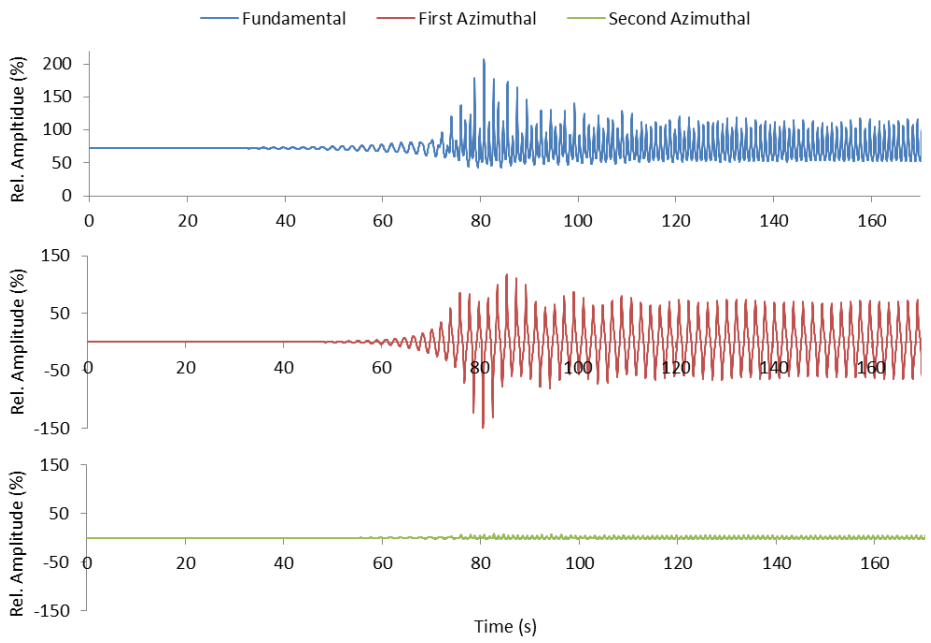

Figure 4-4 – Mode amplitudes during the transient for Model A.

Out-of-Phase Limit Cycle with Rotation

The first three power modes calculated for Model B are visualized in Figure 4-5, which shows the bundle average power for the three modes. Eigenvalues are reported in Table 4-2. Due to the asymmetric burnup distribution applied to Model B, the core was no longer fully north-south symmetric, and therefore was free to have a different angular orientation of the azimuthal mode symmetry lines. Note that the eigenvalues were roughly 200 pcm higher for Model B than for Model A; however, the eigenvalue separation values were very similar in both models.

Figure 4-6 shows the mode amplitudes as a function of time during the simulation for Model B. Unlike for Model A, both azimuthal modes were active, despite very similar values of eigenvalue separation between the two cases. Clearly, the eigenvalue separation is of only limited use in this particular instance; there appears to be no clear way to predict which modes will or will not be active unless an actual coupled simulation is performed.

To further examine the spatial and temporal behavior of the core during the simulation, the radial power profile was plotted as a function of time using animation software (not shown

here). Starting around 40 seconds, the power oscillated out-of-phase with a stationary line of symmetry; but gradually the behavior became more complex and sporadic as the second azimuthal mode came into play, until a fairly steady rotation of the symmetry line was established starting around 95 seconds and continuing through the end of the calculation at 500 seconds. During this period, the oscillation amplitudes of each azimuthal mode changed over time but eventually settled into a stable limit cycle with a clear "rotating mode" behavior.

Several "snapshots" of the radial power during the rotating phase are reproduced in Figure 4-7 for the purpose of illustration. A more detailed view of the two azimuthal mode amplitudes during this time is given in Figure 4-8. Table 4-3 shows the values for frequency and average phase shift calculated according to Eqs. 1 and 2, using N=10 and a starting time of 400 seconds. The mode amplitudes are nearly sinusoidal, and the first mode oscillates with an approximately 92.5° phase lag with respect to the second azimuthal mode. This phase lag, as described above, manifests itself as a very nearly steady rotation of the symmetry line over time.

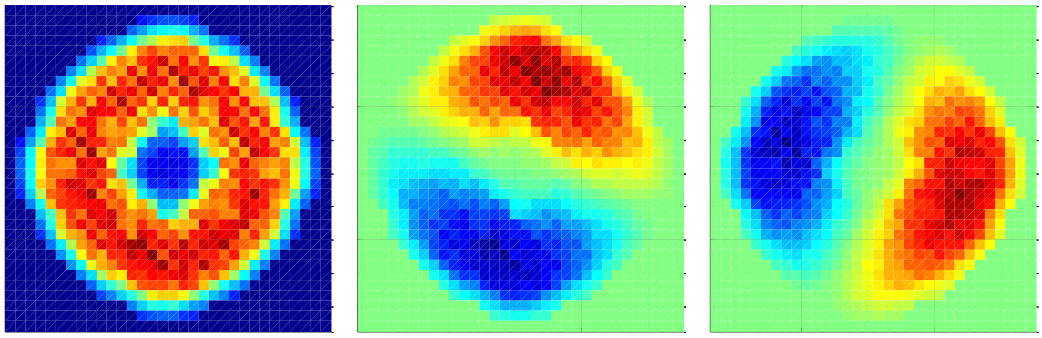

Figure 4-5 – Axially-averaged radial shape of the first three power modes for BWR Model B: the fundamental mode (left), the first azimuthal mode (center), and the second azimuthal mode (right).

Table 4-2. Eigenvalues for the first three modes for Model B

	Mode 0	**Mode 1**	**Mode 2**
Eigenvalues:	0.99413	0.98875	0.98834
Separation:	-	0.00547	0.00589

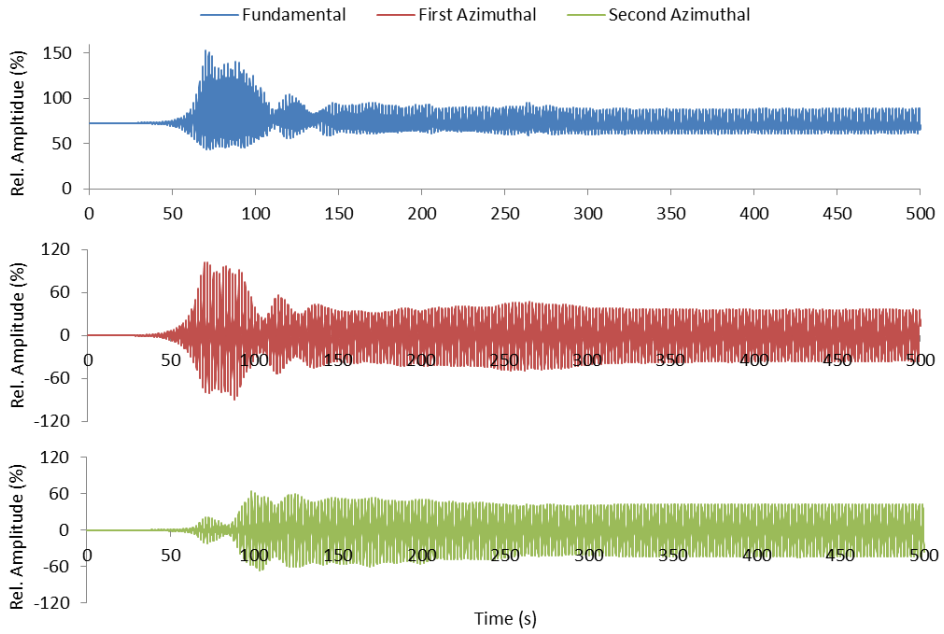

Figure 4-6 – Mode amplitudes during the transient for Model B.

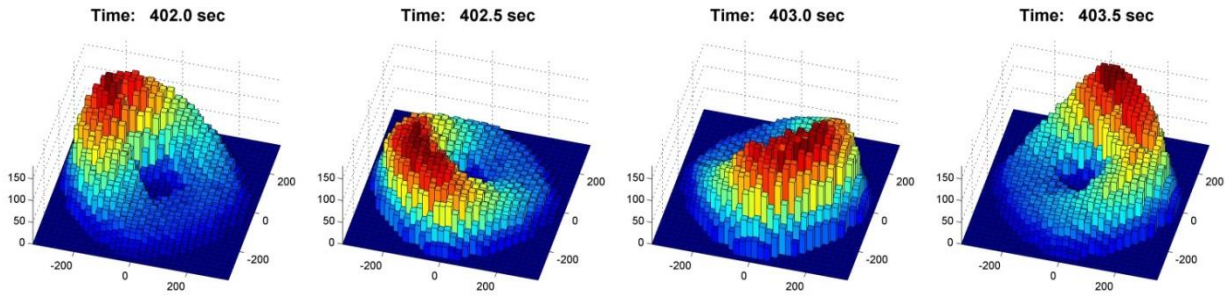

Figure 4-7 - Progression of the radial power over a 1.5-second interval during the rotating-mode portion of the transient for Model A.

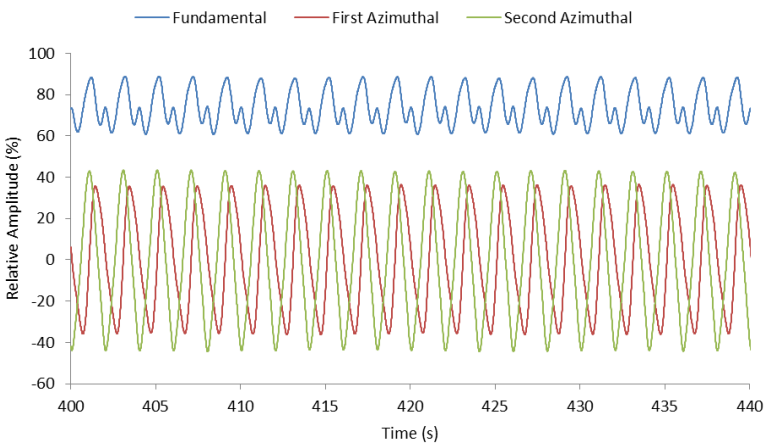

Figure 4-8 – Detailed view of the mode amplitudes during the rotating oscillations for Model B.

Table 4-3. Parameters calculated for Model B during the stable limit cycle oscillations

Parameter	**Value**
f (frequency)	0.500 s^{-1}
ϕ (phase shift)	92.5°

Examination of Mode Frequencies

Although no mathematical proof is given in this paper to understand the physical mechanism (this will be described in detail in Chapter 7), from the current study appears as though the rotating mode behavior described in the previous section is caused by some specific nonlinear coupling mechanism between the two azimuthal modes. In other words, the azimuthal modes were "communicating" with each other and causing this specific rotating behavior. An alternative hypothesis would be that the two modes are actually oscillating independently and that the 90° phase shift between modes happened by chance based on the initial phase shift; however, an additional study (Model C) was performed in an attempt to disprove the latter hypothesis and demonstrate that the constant 90° phase shift was a repeatable phenomenon that appears to be based on physics rather than coincidence.

As described in the Methodology section, Model C was identical to Model B except for a short (0.1 s) perturbation artificially applied to the two azimuthal modes via the moderator density cross-sections at a simulation time of 1.0 s. Figure 4-9 shows how the oscillations for

each azimuthal mode grew over time after this perturbation, while Table 4-4 gives the linear stability parameters for each mode separately, as calculated by the DRARMAX code. The time interval used for decay ratio and frequency calculation was from 2 seconds to 15 seconds; however, it was found that the decay ratio and frequency were insensitive to the choice of time interval, at least out to 20 seconds or possibly further. This implies that the oscillations are indeed still in the linear range in this time interval, and therefore the modes are oscillating independently at this time (as opposed to later in the simulation, where nonlinear effects lead to interaction between modes).

The main significance of Table 4 is to show that Mode 1 has a natural preference to oscillate at a different frequency from Mode 2, due to the asymmetries in the model (these asymmetries can be noticed in the burnup distribution in Figure 4-1 and the fundamental power distribution in Figure 4-5). Therefore, it can be safely concluded that there is a nonlinear coupling mechanism active during the limit cycle portion of Model B that is "forcing" the two azimuthal modes to remain at an approximately 90° phase shift – otherwise, the phase shift would have been expected to slowly "drift" over time as the two modes would have tended to oscillate at slightly different frequencies from each other.

It is also relevant to note that the Model C simulation achieved the same rotating-mode limit cycle behavior as was seen in Model B. Figure 4-10 and Figure 4-11 depict the mode amplitudes as functions of time when the simulation is carried out to 500 seconds. By comparing with Figure 4-6, it can be seen that the Model C oscillations develop rather earlier than the Model B oscillations, due to the "head start" to the oscillations provided by the artificial perturbation. In addition, there are slight differences in the evolution of the mode amplitudes during the "developing" stage around 50 seconds to 100 seconds. Nevertheless, the final asymptotic rotating-mode limit cycle behavior is indistinguishable between Model B and Model C. This furthers the argument that the rotating mode behavior seen in these two models is due to some fundamental physical mode coupling phenomenon that, presumably, could be understood in terms of the underlying mathematical equations. However, for now, this mathematical understanding is left as a topic for future study.

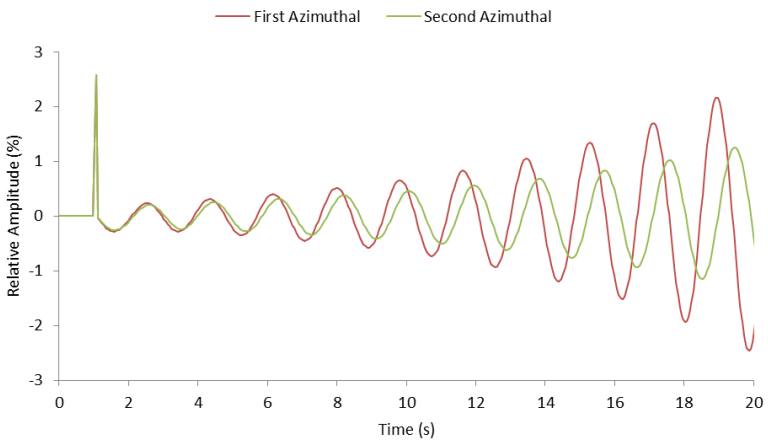

Figure 4-9 – Initial growth of oscillations for Model C after an artificial perturbation was introduced at a simulation time of 1 s.

Table 4-4. Linear stability parameters calculated for Model C for each azimuthal mode

	Decay Ratio	**Frequency**
Mode 1	1.273	0.547 s^{-1}
Mode 2	1.240	0.532 s^{-1}

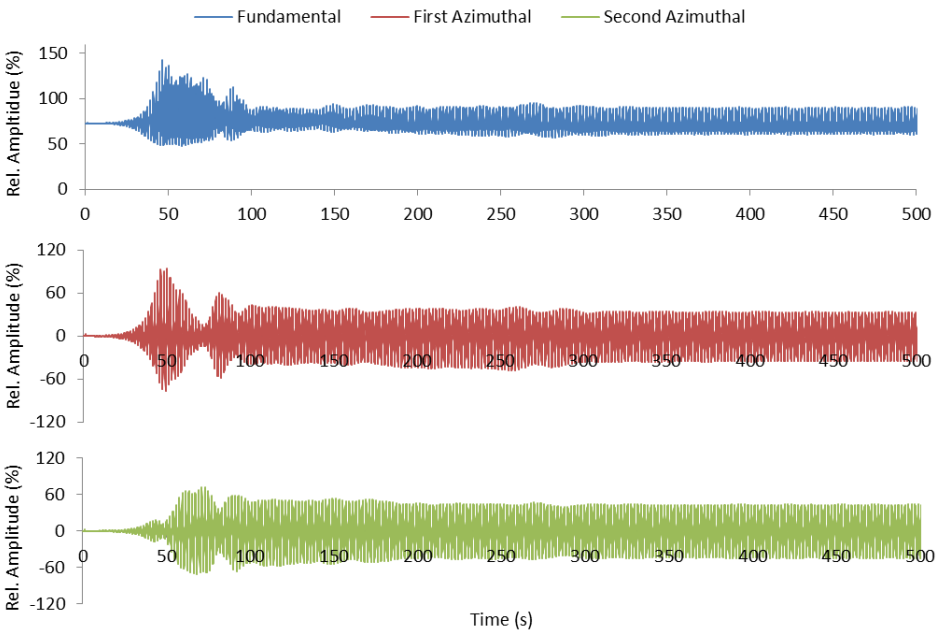

Figure 4-10 – Mode amplitudes during the transient for Model C.

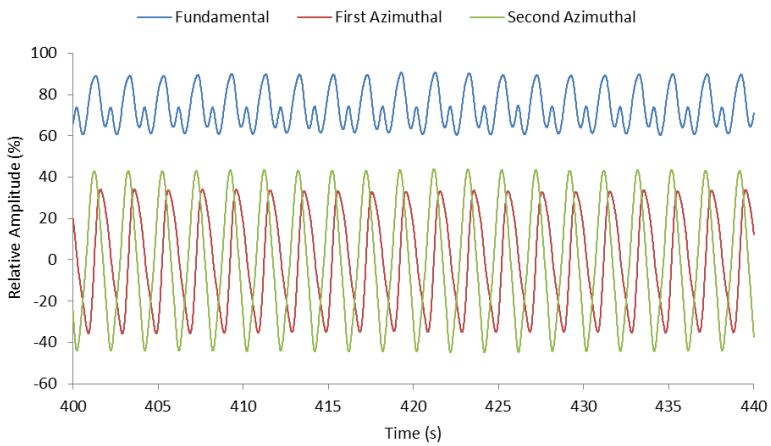

Figure 4-11 – Detailed view of the mode amplitudes during the rotating oscillations for Model C.

Homogeneous Full-Core Model

A modified version of Model B, named Model B-2, was created by selecting one particular channel and copying its inputs (TH channel input, neutronic values, cross sections) to all other channels, such that all channels were identical. This gave a full core model that was homogeneous in the radial direction, except for the control rod pattern which was the same as for Case B (*i.e.* rods inserted in the radial center of the core). Note that the core was not homogeneous in the axial direction since axial-dependent geometry and cross sections were still used.

Figure 4-12 shows the radial shape for each of the first three neutronic modes. Due to the radial homogeneity of the model (except for the central control rods), the fundamental power shape was azimuthally symmetric as well and had a much smoother behavior than for Case B with its heterogeneities. Once again, for Case B-2 the first two azimuthal modes were tilted by $45°$ in either direction (counterclockwise or clockwise).

Eigenvalues for Case B-2 are shown in Table 4-5. The fundamental eigenvalue was unrealistically large, due to the choice of the channel that was duplicated – evidently, this channel had a higher reactivity than average, leading to an unrealistically large fundamental eigenvalue. However, since in the PARCS code the fission cross sections are scaled to give a k_{eff} of unity at the start of a transient, this was not seen as a major issue (since this case did not represent a physically realistic core anyway, *e.g.* due to the control rod pattern).

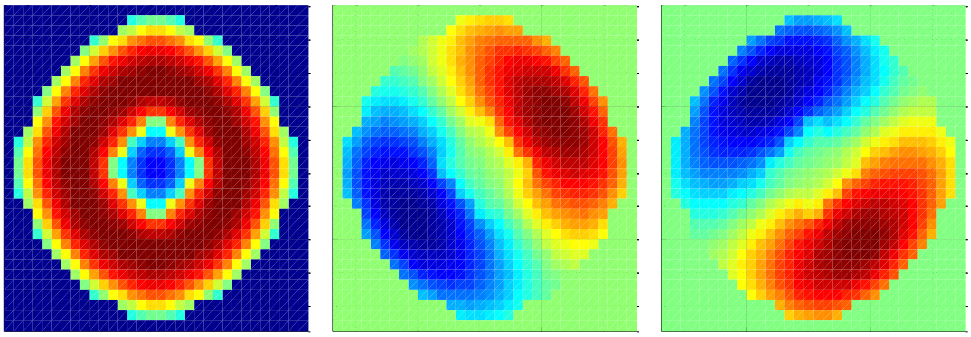

Figure 4-12 – Axially-averaged radial shape of the first three power modes for BWR Model B-2: the fundamental mode (left), the first azimuthal mode (center), and the second azimuthal mode (right).

Table 4-5. Eigenvalues for the first three modes for Model B-2.

	Mode 0	**Mode 1**	**Mode 2**
Eigenvalues:	1.03996	1.03433	1.03433
Separation:	-	0.00523	0.00523

Results for the transient for Model B-2 are shown in Figure 4-13 and Figure 4-14. As for the other models, *e.g.* Model B, no action was taken to bring the core to unstable conditions; the core was started from unstable conditions and a noise perturbation at 20 seconds was used to initiate the oscillations. The transient required approximately 400 seconds of simulation time in order to attain a converged limit cycle; however, in this case a side-to-side out-of-phase behavior was seen, in contrast to the rotating behavior seen in Case B.

The reasons for the difference in behavior are unclear at this time. However, based on results shown later on, in 0 of this thesis, the core may prefer the side-to-side behavior over the rotating behavior if the neutronic coupling is sufficiently strong, *i.e.* relative to the TH channel coupling. It remains a topic of future work to determine, for example, the void and fuel temperature reactivity coefficients for each case (Case B and Case B-2), to determine whether larger feedback coefficients might be associated with the side-to-side mode, and vice versa for the rotating mode, as was found with the reduced order model in 0.

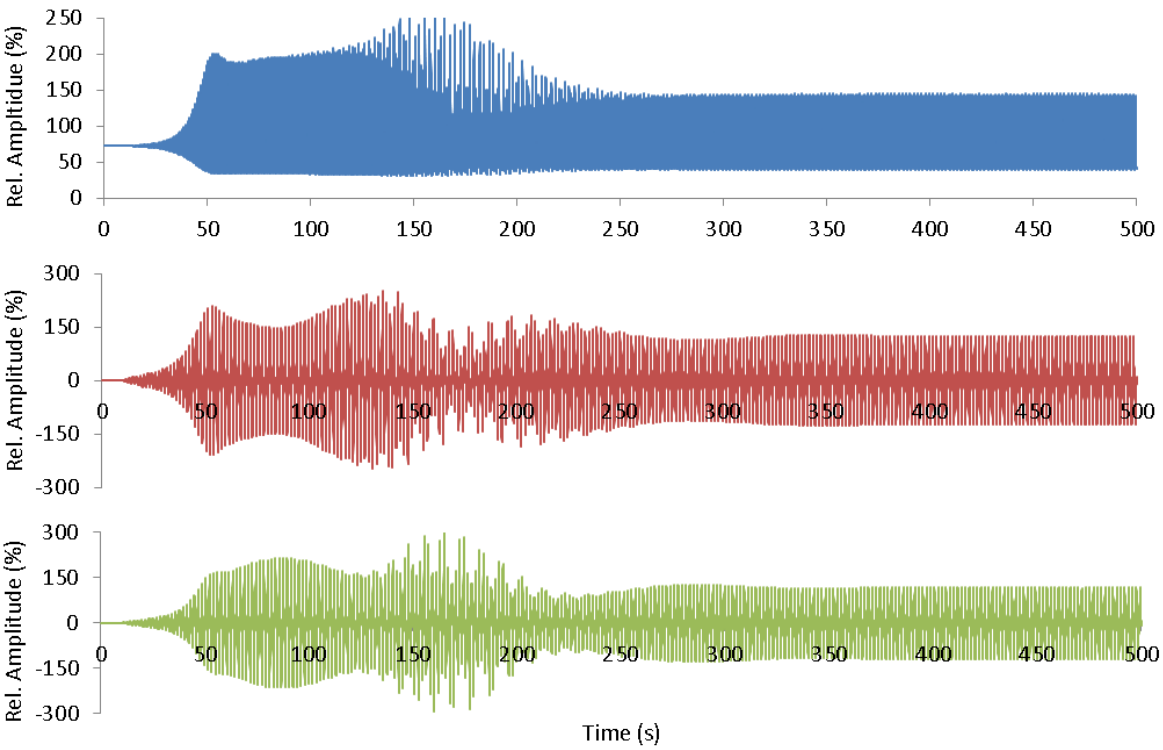

Figure 4-13 – Mode amplitudes during the transient for Model B-2

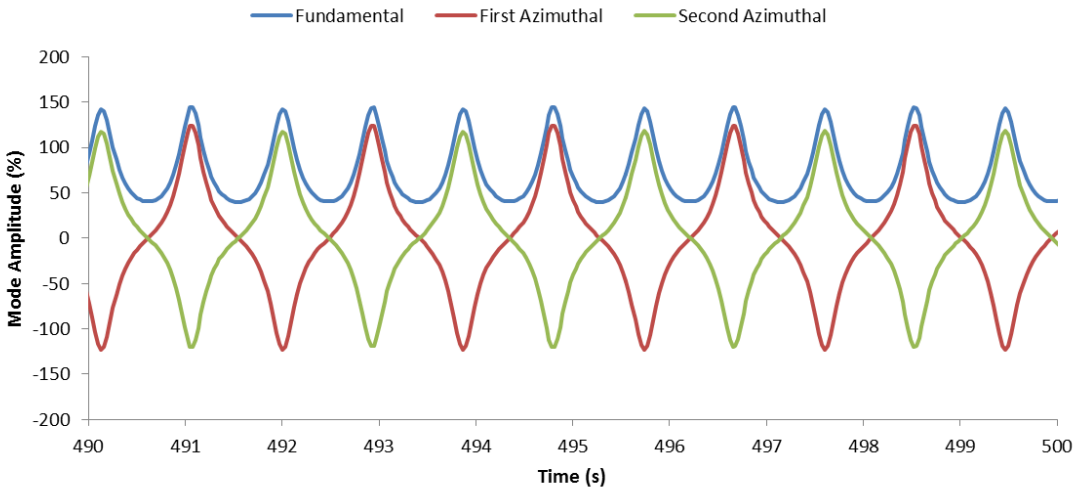

Figure 4-14 – Detailed view of the mode amplitudes during the side-to-side limit cycle oscillations for Model B-2

Half Core Versus Full Core Model Comparison

The first two power modes calculated from the steady-state solution of Model B are shown in Figure 4-15. The bottom half of the core was not part of the actual model, but it is shown here as a reflection of the top half of the core for visualization purposes. Eigenvalues for the fundamental and first harmonic are shown in Table 4-6. Note that in Model B there was no second azimuthal mode corresponding to the one in Model A because only half of the core was modeled. Also note that the orientation of the azimuthal mode was such that out-of-phase oscillations can only occur east-to-west, due to the half-core symmetry of the model.

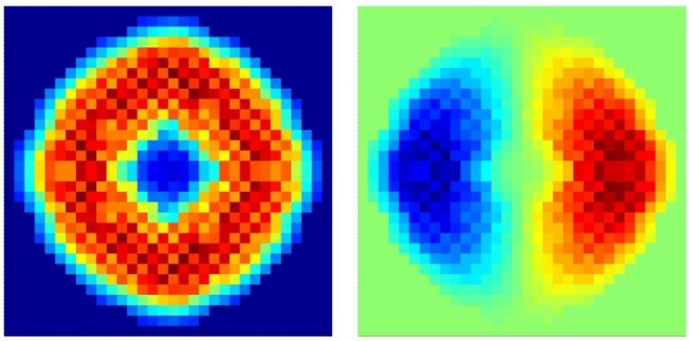

Figure 4-15 – Axially-averaged radial shape of the fundamental mode (left) and first azimuthal mode (right) for BWR Model B.

Table 4-6. Eigenvalues for the fundamental mode (1) and first azimuthal mode (2) of Model B

Mode number	1	2
Eigenvalue	0.99234	0.98668

The same pump trip event was simulated with Model B as was performed with Model A, and the results are shown in Figure 4-16. As before, the oscillations developed in an out-of-phase mode. However, as a rotating mode was established in Model A, the amplitude of oscillation for each azimuthal mode decreased somewhat, possibly related to the rotation; but in Model B this did not occur due to half-core symmetry, leaving only an east-to-west oscillation mode with a comparatively large amplitude.

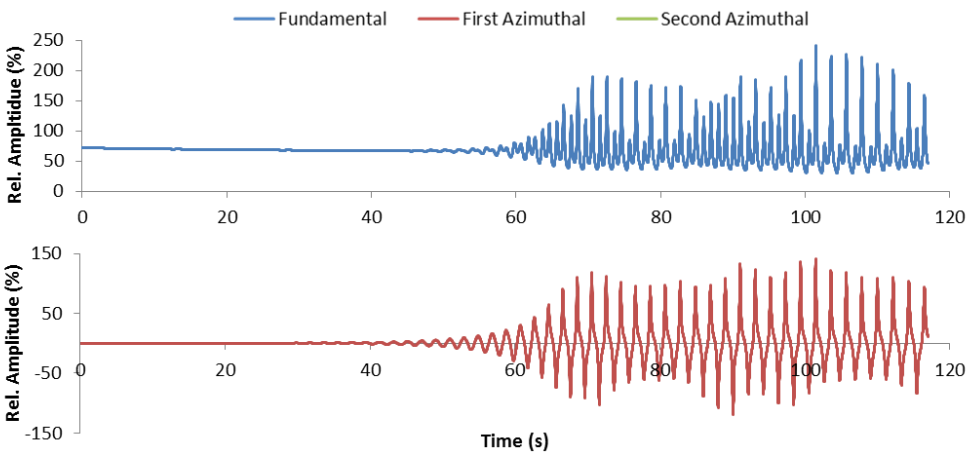

Figure 4-16 – Mode amplitudes for Model B during the simulated pump trip event.

As shown in Figure 4-17, the peak clad temperature (the highest temperature reached by the clad at any location in the core, an important safety performance parameter), evolved similarly for the two models after about 90 seconds. This was most likely because both models predicted a similar average power and therefore the hottest fuel rods (blanketed with steam) were heated at nearly the same rate. It was expected that the overall maximum power would also be similar in both models but that Model A would give a greater number of "hot channels" distributed in a ring about the core due to the rotating mode, versus a single maximum on either side of the core for Model B. This behavior was observed to some extent (Figure 4-18), but asymmetries in the model caused a significant departure from a perfect ring shape (Model A) or an evenly-balanced east-west oscillation (Model B). The highest power achieved by any single fuel assembly during the transient was significantly higher for Model B (563%) than for Model A (468%). While these two models behaved as expected qualitatively, the outcome in terms of maximum assembly power is a somewhat surprising result that merits further attention for its implications for the simulation of out-of-phase oscillations during core safety analysis.

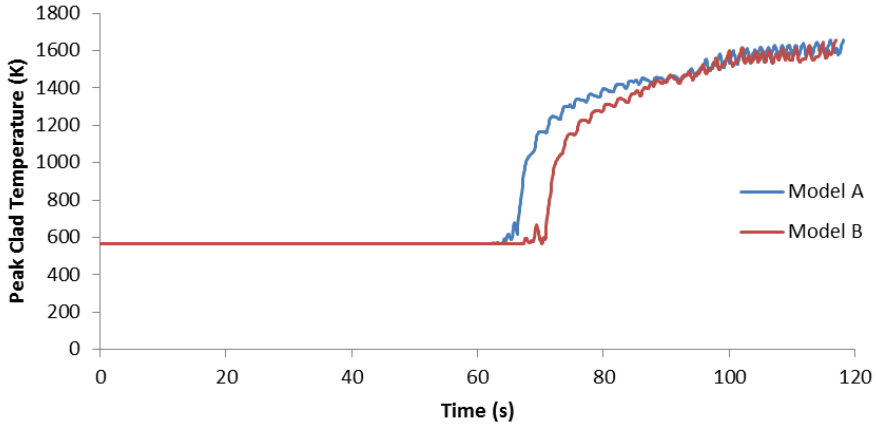

Figure 4-17 – Peak clad temperature versus time during the simulated pump trip event.

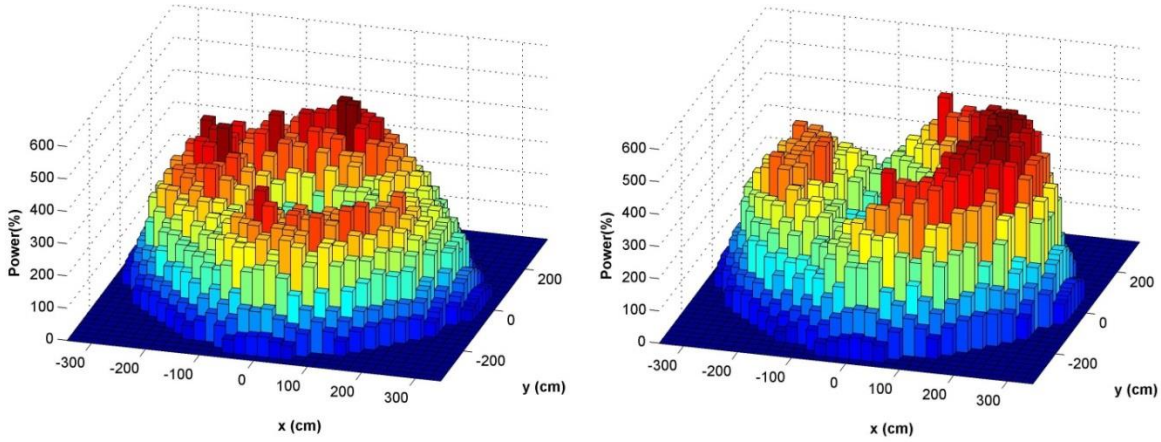

Figure 4-18 – Plot of maximum power experienced by each individual fuel assembly during the pump trip transient for Model A (left) and Model B (right).

Additional Simulation of Out-of-Phase Oscillations

Results for the first three power mode shapes for Model D, depicted in Figure 4-19, are as expected for a quarter-core symmetric model. The eigenvalues for each of the modes are shown in Table 4-7. Note that the Mode 2 and Mode 3 eigenvalues are not quite identical due to a difference in the control rod pattern (shown in Figure 4-2) in the east-west direction compared to the north-south direction.

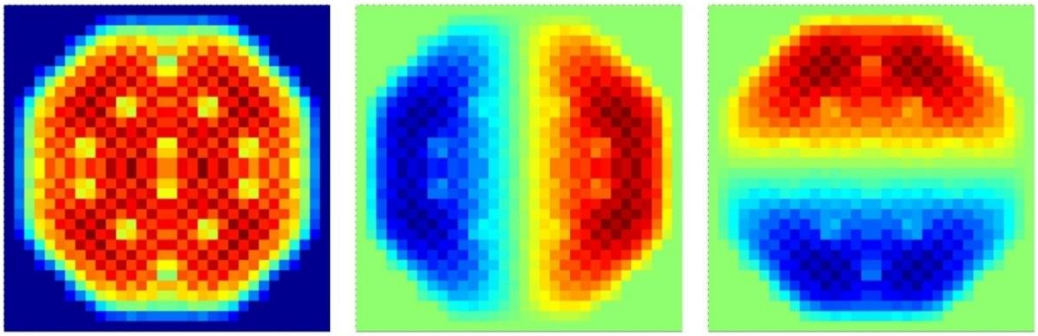

Figure 4-19 – Axially-averaged radial shape of the first three modes for BWR Model D.

Table 4-7. Eigenvalues for the first three modes of Model D

Mode number	1	2	3
Eigenvalue	1.00736	1.00095	1.00060

The time evolution of the mode amplitudes for the simulated turbine trip event is shown in Figure 4-20. The core oscillated in a purely in-phase mode for approximately the first 55 seconds of oscillations (Figure 4-21), until out-of-phase oscillations began to develop starting around 130 seconds. The behavior was "chaotic" in appearance, with all three modes active at once. By around 145 seconds, the core had transitioned into a similar rotating behavior such as was observed in Model B (Figure 4-22), although soon the power in the northeast and southwest quadrants spiked to very high powers (the maximum assembly power reached was 961%). TRACE predicted steam blanketing in some assemblies, after which nucleate boiling was not allowed to occur for the rest of the transient because conditions did not allow for rewet. This caused the oscillations to suddenly die out, and the simulation was terminated manually once this was observed.

It seems plausible that Model D could have eventually settled into a similar rotating-mode limit cycle, based on the qualitative similarities in how the radial power developed in this model as compared to Model B. However, further work will be required to conclusively demonstrate this for the current model.

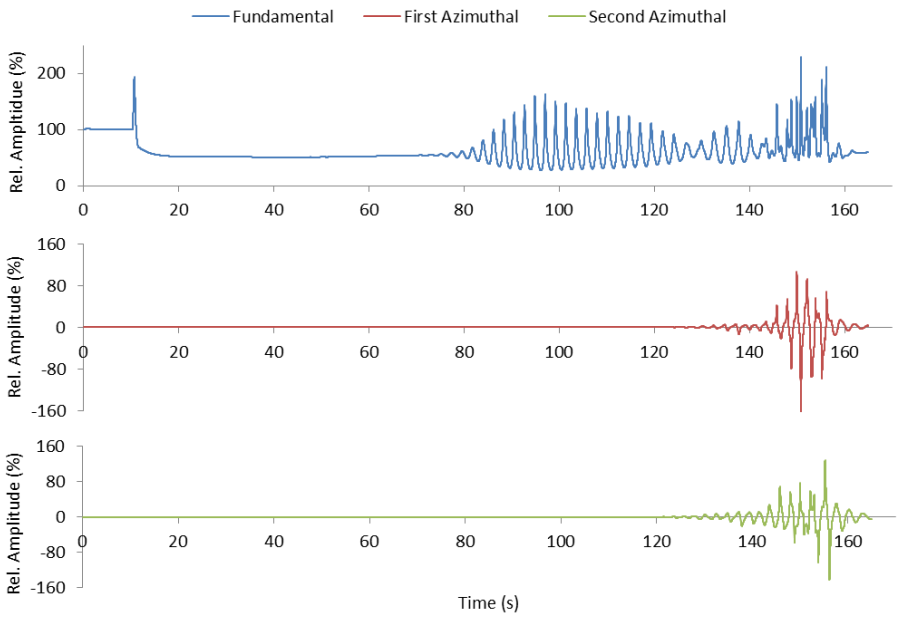

Figure 4-20 – Mode amplitudes for Model D during the simulated turbine trip event.

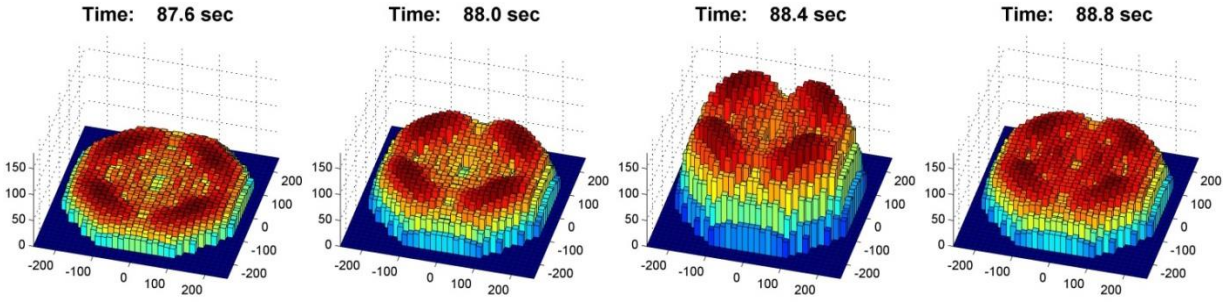

Figure 4-21 – Progression of the radial power during the in-phase oscillation portion of the simulated turbine trip event for Model D.

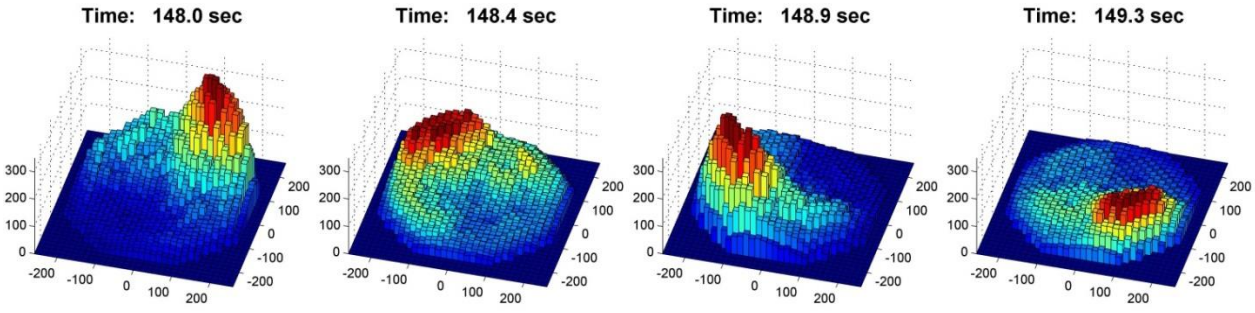

Figure 4-22 – Progression of the radial power during the rotating-mode portion of the simulated turbine trip event for Model D.

Sensitivity to Initial Perturbation

Figure 4-23 show the time-dependent mode amplitudes for Model E, which was identical to Model D except for the addition of out-of-phase noise from 40 seconds to 70 seconds. As opposed to Model D, which began in a purely in-phase oscillation mode (Figure 4-21), Model E oscillated in a purely out-of-phase mode from the beginning (Figure 4-24) and continued to grow even after the out-of-phase noise perturbation was switched off at 70 seconds. The apparent oscillations in the fundamental amplitude were merely an artifact of the nonlinear out-of-phase oscillations as the power in one half of the core rose higher than the other half could fall, as can be inferred from Figure 4-24.

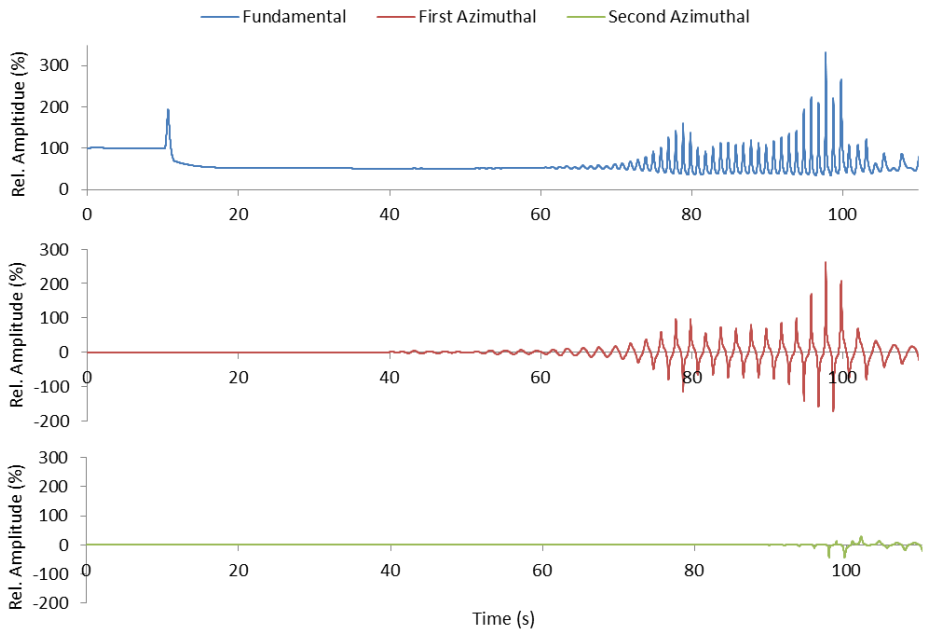

Figure 4-23 – Mode amplitudes for Model E (out-of-phase noise added) during the simulated turbine trip event.

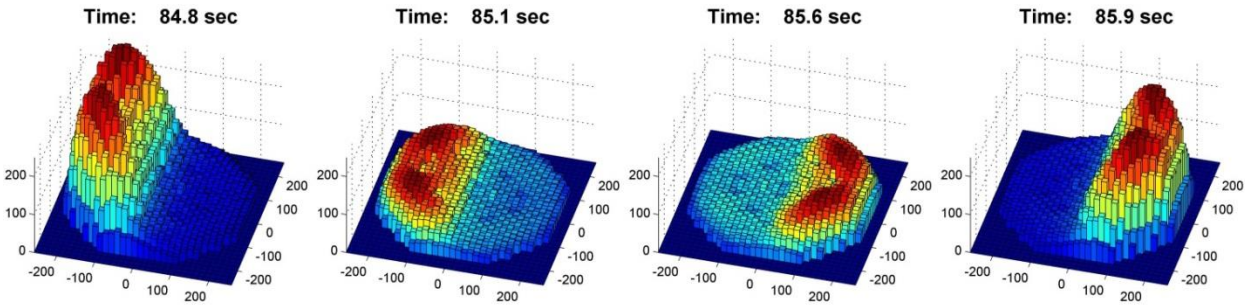

Figure 4-24 – Progression of the radial power during the out-of-phase portion of the simulated turbine trip event for Model E.

This fundamental change of the oscillation mode due to only a small-amplitude perturbation can be explained as follows. After a pump trip or a core inlet temperature perturbation, the fundamental mode is excited preferentially because the perturbation is symmetric across the core. From a strictly linear point of view, a (hypothetically) 100% symmetric perturbation would not excite the out-of-phase mode because the perturbation on one side of the core would cancel the perturbation in the other side, leaving only a perturbation in total core power (*i.e.* the fundamental mode).

Realistically, there may be some small out-of-phase component added to the system (due to numerical error), but the amplitude of this out-of-phase oscillation would initially be very small. Therefore, oscillations might not become visibly apparent if the simulation is run for only a short period of time. For example, imagine a hypothetical reactor with an out-of-phase decay ratio of 1.01 and a core-wide decay ratio of 0.9. If a time-domain simulation were performed and a large core-wide perturbation (*e.g.* a pump trip) was introduced, the result would be a decaying core-wide oscillation superimposed on a growing out-of-phase oscillation. However, if the initial out-of-phase perturbation was very small, it may take a very long time – perhaps on the order of 10 or even 100 periods – for the out-of-phase oscillations to grow to a visible level. Depending on the simulation, the transient may be completed before this ever occurs. There are therefore two solutions to this problem: either run the code for a sufficient period of time so that any incipient unstable oscillations will have enough time to grow; or, alternatively, provide an artificial asymmetric perturbation so that the unstable oscillation will have a larger initial amplitude and become visible much earlier in the simulation.

Model D and Model E present a similar scenario, except that in this case both the core-wide and out-of-phase modes are unstable (after the pump trip). However, in the short term, the conclusion remains the same: which mode dominates is strongly tied to the size of the initial perturbation of each mode.

This result has practical significance for the simulation of BWR limit cycle oscillations. In the long run, both cases (with or without an out-of-phase perturbation) would be expected to converge to the same limit cycle (excluding considerations such as clad melting or dryout). However, both in-phase and out-of-phase noise are present in any operating BWR; and, if both modes are unstable, a model that doesn't properly include some excitation of both of these modes (as many simulations don't) may significantly mispredict the oscillatory behavior, at least in the early stages until a stable limit cycle is achieved.

4.3 Conclusion

This chapter reported a study of BWR out-of-phase oscillations using the TRACE/PARCS coupled code system. Unstable power oscillations with a time-dependent, rotating line of symmetry were successfully simulated using inputs from two different BWRs. The λ-modes of the neutron flux were calculated using an implicitly-restarted Arnoldi solver, and the time-dependent amplitudes of the fundamental, first azimuthal, and second azimuthal power modes were determined for each simulation. After progressing in an irregular, sporadic fashion, the oscillations appeared to transition into a clear "rotating mode" that was sustained indefinitely with a fixed phase shift between modes of roughly 90°. Because the phase shift did not gradually change over time, despite each mode having a different natural frequency in the linear range, the conclusion was made that a nonlinear interaction mechanism was active between the first and second subcritical azimuthal modes to maintain the constant phase shift during the limit cycle. An additional study was performed which found that a small perturbation is capable of drastically affecting the development of oscillations in a simulation when both modes (in-phase and out-of-phase) are unstable; when one of the models was modified to include a small-amplitude noise source on the first azimuthal mode, purely out-of-phase oscillations were observed, whereas the oscillations had been purely in-phase for the first 55 seconds when no noise signal was included. Because most ATWS event calculations involve mostly in-phase perturbations to the BWR core (*e.g.*, pressure perturbations or core flow reductions), it is recommended to add a small out-of-phase perturbation in simulations where both the in-phase and out-of-phase modes may be unstable.

Whether a rotating mode will develop in all cases where both azimuthal modes are unstable, or whether its occurrence depends on the specific core conditions or other considerations, is a question that will be addressed in the remainder of this thesis.

Chapter 5. Investigation of Parallel-Channel TH Oscillations with a 4-Channel TRACE/PARCS Model

5.1 Theory

Boundary Conditions and Oscillation Modes

The behavior of a system of parallel flow channels undergoing oscillations (most commonly, density-wave oscillations) has been the topic of numerous studies, both experimental and analytical. Boundary conditions play an important role in determining the stability characteristics, *e.g.* whether the in-phase or out-of-phase oscillation mode dominates. For the case of in-phase oscillations, the recirculation loop dynamics play a role, and the boundary conditions may reflect this in terms of additional pressure drop terms or other treatment. However, for the case of out-of-phase oscillations, Grandi et al. [57] have shown that recirculation loop dynamics play virtually no role at all, and the results are almost identical if one eliminates the recirculation loop dynamics from the model and imposes a constant total core inlet flow rate and a constant core pressure drop boundary condition instead.

More recently, Munoz-Cobo et al. [57] have argued that a constant pressure drop boundary condition should not be imposed along with a constant total mass flow rate condition, as this leads to an overdetermined system of equations and artificially inhibits the variations in total inlet flow rate.

Alternately, Dokhane [16] was able to impose a fixed pressure drop boundary condition and still obtain in-phase oscillations, provided that the oscillations remained small in amplitude (1%).

The models used in this chapter using TRACE/PARCS use a fixed total flow rate boundary condition. This was chosen to simplify the calculations, eliminating unnecessary complications involved with the VESSEL component and other components, while also forcing out-of-phase

oscillations which were the goal of this study; a fixed total flow rate prevents in-phase oscillations and forces the oscillations to be out-of-phase (or no oscillations at all).

However, as will be shown in 0, a modified fixed pressure drop boundary condition can be applied, by adding separate pressure drop terms applied to the total flow rate entering or leaving all channels. This is an important difference from applying the pressure drop condition across each individual channel only, as the channels cannot interact in this case and behave completely independently from each other. By adding a pressure drop based on the total (or average) flow entering or leaving all channels, the channels can now interact via feedback related to the velocity and pressure fields among the channels. This will be investigated in detail in the next chapter, but in the current chapter only a fixed total flow rate condition will be used.

Sinusoidal Oscillations and Phase Shifts

Considering that the oscillations in a given channel behave sinusoidally for small-amplitude oscillations (based on Eq. (2.34) , for example), it is reasonable to expect the same essentially sinusoidal behavior for limit cycle oscillations, especially for a system operating close to the linear stability boundary in which the oscillation amplitude remains small. In other words, for the general multi-channel case, one expects the individual channel flow rates to follow some fixed pattern in the limit cycle approximately according to

$$\delta\dot{m}_n(t) = A_n \sin(\omega t + \varphi_n), \quad n = 1,2,\dots,N \tag{5.1}$$

where $\delta\dot{m}_i(t)$ is the deviation of the channel inlet flow rate from steady state conditions at time t for channel n, A_n is some constant oscillation amplitude for channel n, ω is a common oscillation frequency among all channels, φ_n is an angular phase shift corresponding to channel n, and N is the total number of channels in the system. Note that ω is a parameter closely related to the geometry and flow characteristics of the individual channels – namely, it is approximately the reciprocal of the transit time for a fluid element to traverse the channel from inlet to outlet – and therefore it is assumed that, since all channels share the same steady-state flow rate and geometry, they will all oscillate with the same characteristic frequency under stable limit cycle conditions of small amplitude as are being analyzed here; and, while

theoretically possible for a channel to oscillate at, say, double this frequency or half this frequency, it is assumed that such modes would be so much less unstable than the fundamental frequency that they need not be considered.

The constraint of constant total flow among all channels imposed by the model gives the condition

$$\sum_{n} \delta\dot{m}_n(t) = 0 \tag{5.2}$$

for all $t > 0$. Eqs. (5.1) and (5.2) have the trivial solution $A_n = 0,\ A \in \{1,2,\dots,N\}$. However, nontrivial solutions also exist and depend on the number of channels involved.

To simplify the notation in the following analysis, the oscillation modes will be expressed in terms of relative amplitudes and phase shifts using the format $\left(\tilde{A}_1 e^{\varphi_1 i}, \tilde{A}_2 e^{\varphi_2 i}, \dots, \tilde{A}_N e^{\varphi_N i}\right)$, where $\tilde{A}_n$ are arbitrarily normalized relative flow perturbation amplitudes. For example, $(1,1,1)$ would indicate a three-channel case with all three channels oscillating in phase with the same amplitude (*i.e.* $\tilde{A}_1 = \tilde{A}_2 = \tilde{A}_3$ and $\varphi_1 = \varphi_2 = \varphi_3 = 0$).

***N*-Channel Systems**

For $N = 2$, only one nontrivial set of solutions exists – namely, $(1,-1)$, or the case where the two channels oscillate 180° out-of-phase with respect to each other with the same amplitude. No other possible oscillation mode exists for this case, assuming that Eqs. (5.1) and (5.2) are valid.

For $N = 3$, several unique oscillatory modes are possible. For this case, Nakanishi et al. [58] described the following oscillation modes which were all obtained experimentally: $(1,-1,0)$, $(1,1,-2)$, and $\left(e^{-(2/3)\pi i}, 1, e^{(2/3)\pi i}\right)$. The first case corresponds to two channels oscillating counter-phase (*i.e.* 180° phase to each other) with the third channel stationary; the second case corresponds to two channels oscillating in-phase with each other while the third oscillates counter-phase with double the amplitude; and the third case corresponds to three channels oscillating with the same amplitude but with phases staggered by 120°.

For the case of four parallel channels, Nakanishi et al. [58] reported experimental results in which two pairs of channels form, with the two channels of each pair oscillating counter-

phase to each other but with an arbitrary phase shift for one pair with respect to the other. Mathematically, this corresponds to the set of modes $(1, -1, e^{ci}, -e^{ci})$, where c is some arbitrary constant between 0 and 2π.

Hypothetically, other modes are possible, such as $(1,1,-2,0)$ which is similar to the case reported for three-channel systems; however, the author could find no experimental occurrence of this or other modes other than $(1, -1, e^{ci}, -e^{ci})$ in the literature.

For the case of five parallel channels, Nakanishi et al. [58] reported the experimental result $(e^{-(4/5)\pi i}, e^{-(2/5)\pi i}, 1, e^{(2/5)\pi i}, e^{(4/5)\pi i})$, which corresponds to five channels oscillating with equal amplitude but with phases staggered by 72°.

The author could find no experimental results for systems of greater than five channels. However, based on the trends shown above, the simplest and perhaps most likely oscillation mode for a system of N channels, when N is even, would be for $N/2$ pairs of counter-oscillating channels to form with equal amplitudes but arbitrary phase shifts between any two pairs of channels from the set. For odd N, the most likely oscillation mode appears to be the case of all channels oscillating with equal amplitude but phases staggered by $(2\pi/N)$ radians.

5.2 TRACE Parallel Channel Model

A four-channel model has been created to investigate the behavior of instabilities in BWR channels with as simple a model as possible. The channels are loosely modeled after a typical BWR assembly in terms of flow area, length, number of fuel pins, etc. However, for simplicity, no loss factors (K-factors) were included in the model. Also for simplicity, and to decrease runtime for this simple case, only 8 axial cells were used, with 5 uniform cells comprising the active fuel length. Although, as discussed in Chapter 3, more axial nodes and a variable mesh spacing would have improved accuracy and reduced numerical diffusion, this approach was not used here because the key goal was to develop a fundamental understanding of the phenomena at work, rather than numerical accuracy, and the choice of mesh size was not expected to affect this understanding.

Table 5-1. Assembly Geometry and TH Conditions for the Multi-Channel TRACE Models

Flow Area	0.01 m^2
Hydraulic Diameter	0.013 m
Number of Fuel Pins	49
Active Length	3.5 m
Total Length	4.0 m
Total Cells	8 (5 active)
Flow Rate (per channel)	12.5 kg/s
Inlet Temperature	548.64 K
Outlet Pressure	7.36 MPa

Table 5-1 gives several key parameters for the geometry and TH conditions used for the multi-channel model. As shown in Figure 5-1, the channels in TRACE were connected to a VESSEL component through which a prescribed total flow rate was provided by a FILL component, while a BREAK component provided a fixed outlet pressure boundary condition. The VESSEL was modeled simply with a single radial node and 12 axial nodes, with connections at cell edges 5 and 9. A flow area restriction was added at cell edge 7 to prevent any flow from bypassing the channels; thus, due to the incompressibility of the liquid water between the FILL

and the channel inlet, the total flow rate was, with negligible numerical error, exactly equal to the flow provided by the FILL component at any point in time.

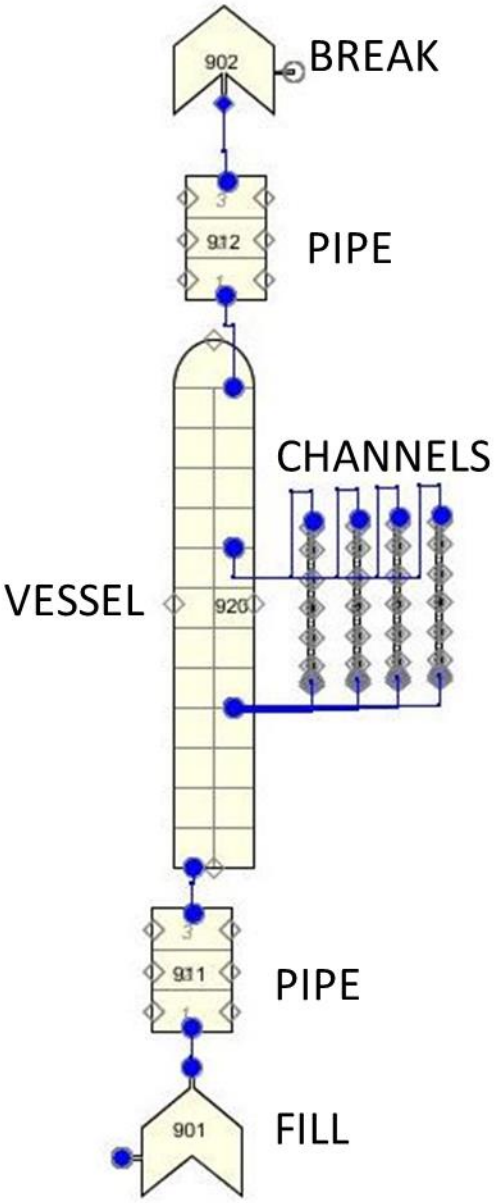

Figure 5-1 – Diagram of the parallel-channel TRACE model.

A uniform axial power distribution was applied among all active channel nodes, with equal power provided to each channel; however, the total power level applied to the channels was adjusted in each case via trial and error to find the onset of instability. Once unstable conditions were reached, calculations were then allowed to run for as long as necessary until

the oscillations became saturated and a stable limit cycle was observed. From there, an incrementally higher power level could be applied in subsequent runs to examine the effect of power level on limit cycle amplitude, for example.

The imposition of a fixed total inlet flow condition places a restriction on the oscillation modes that can occur. In a more realistic BWR model, the flow is driven by recirculation pumps which have characteristic pressure-to-flow curves that allow the total core inlet flow rate to vary depending on the total (net) flow resistance through the core and vessel. This allows the core, under certain conditions, to oscillate in an in-phase mode in which the total inlet flow rate oscillates in time.

However, in the simplified FILL-VESSEL-BREAK model discussed in this section, total inlet flow rate variation is not possible, and therefore a behavior similar to the in-phase oscillations in BWRs cannot occur. As discussed in the previous section, only a discrete number of possibilities exist in which individual channels are allowed to oscillate while ensuring that the total flow rate among channels remains fixed at all times.

***N*-Channel TRACE Models**

Figure 5-2 through Figure 5-5 show the results of TRACE transient simulations for 2, 3, 4, and 8 channels, respectively, including results for time-dependent channel flow rates as well as relative phase shifts between channels over time.

In each case, each channel was given arbitrarily different initial conditions which effectively provided an initial perturbation from which the oscillations could develop over time. The total flow rate in each case was adjusted such that 12.5 kg/s would be provided to each channel on average. The total power level was also adjusted more-or-less proportionally to the number of channels to provide essentially the same power per channel in all cases; however, for some of the cases, it was necessary to adjust the total power slightly up or down to find a point just slightly on the unstable side of the linear stability boundary.

The relative phase shifts were determined as follows. For each channel, the times at which the flow rate crossed the 12.5 kg/s level with a positive slope were recorded; these were found by linearly interpolating between the two closest timesteps on either side of this point.

Then the phase shifts for each of these time points relative to channel 1 were calculated by subtracting from each of these time points the nearest previous time point for channel 1, then scaling by the oscillation period for channel 1 between that point and the next, then (if using units of degrees) multiplying by 360.

In all of the cases performed for this study, regardless of the initial phase shift between channels, the channel flow rates eventually settled into a pattern of equal-amplitude oscillation with phase shifts staggered by $(2\pi/N)$ radians. This is shown in the bottom plots of Figure 5-2 through Figure 5-5, where the phase shift between channels eventually converges to this pattern regardless of initial phase shift.

Unsurprisingly, the two-channel case settled into the expected 180° phase shift pattern essentially instantaneously. Since there were only two channels, any decrease in flow in one channel must be instantly compensated by an equal increase in the other; so, as soon as sinusoidal-type oscillations began, they oscillated immediately with a 180° phase shift.

The three channel case also converged to the expected phase behavior quite quickly (within 200 s), though not quite as fast as the two channel case due to the additional degree of freedom in terms of channel flow rates. However, as described in the previous section, this was still the only possible mode of oscillation that allowed for equal oscillation amplitudes for each channel in the three-channel case – the other possible modes being $(1,-1,0)$ and $(1,1,-2)$, but these perhaps understandably seemed to be disfavored in the limit cycle case where the oscillations were not strictly linear (*i.e.* if one channel were to oscillate with higher amplitude than the others, this channel would experience stronger nonlinear effects that would be expected to drive the amplitude down until equaling that of the other channels).

However, as discussed in the previous section, the case of four channels has an even greater degree of freedom than the three channel case, since two pairs of channels can form in which (at least in the case of linear oscillations) the channels in each pair can balance each other by oscillating 180° apart, therefore allowing the two pairs to have an arbitrary phase shift with respect to each other. This was expressed by the phase notation $\left(1,-1,e^{ci},-e^{ci}\right)$, with c being an arbitrary constant.

The formation of two pairs can clearly be seen in the bottom plot of Figure 5-4, in which channel 4 relatively quickly (within 350 s) converges to a 180° phase shift with respect to channel 1, and channels 2 and 3 also appear to have a 180° phase shift with respect to each other by that time.

However, the key finding of this study was what happened after the 350 s mark: channels 2 and 3, though they oscillated with a roughly 130° phase shift with respect to channels 4 and 1, respectively, at around the 350 s mark, both slowly converged to a final phase shift of precisely 90° with respect to channels 4 and 1, respectively, by the end of the simulation.

As a side note, any deviation from this 90° value was due to discretization error caused by the finite timestep size and plotting interval, causing small errors in the interpolation scheme described above which manifested themselves as very small-amplitude noise-like oscillations in the phase shift upon closer inspection.

The results of the eight channel case also demonstrate a $(2\pi/N)$ phase pattern. Figure 5-5 shows the channels gradually forming into four pairs – channels 1 and 7, channels 8 and 3, channels 5 and 2, and channels 4 and 6, each pair establishing roughly a 180° phase among its two channels with about 300 s or sooner, but requiring another 700 s or so to fall into the $(2\pi/N)$ (*i.e.* 45°) phase pattern which the channels proceeded to oscillate with indefinitely afterwards. It should be noted, however, that the pairing was not quite as precise as in the four channel model – for example, channels 8 and 3 were not precisely 180° out of phase until significantly later in the transient than for the other pairs – and this was likely due to the many degrees of freedom due to the large number of channels, with the coupling between one channel and the rest being relatively less tight that it was with fewer-channel cases.

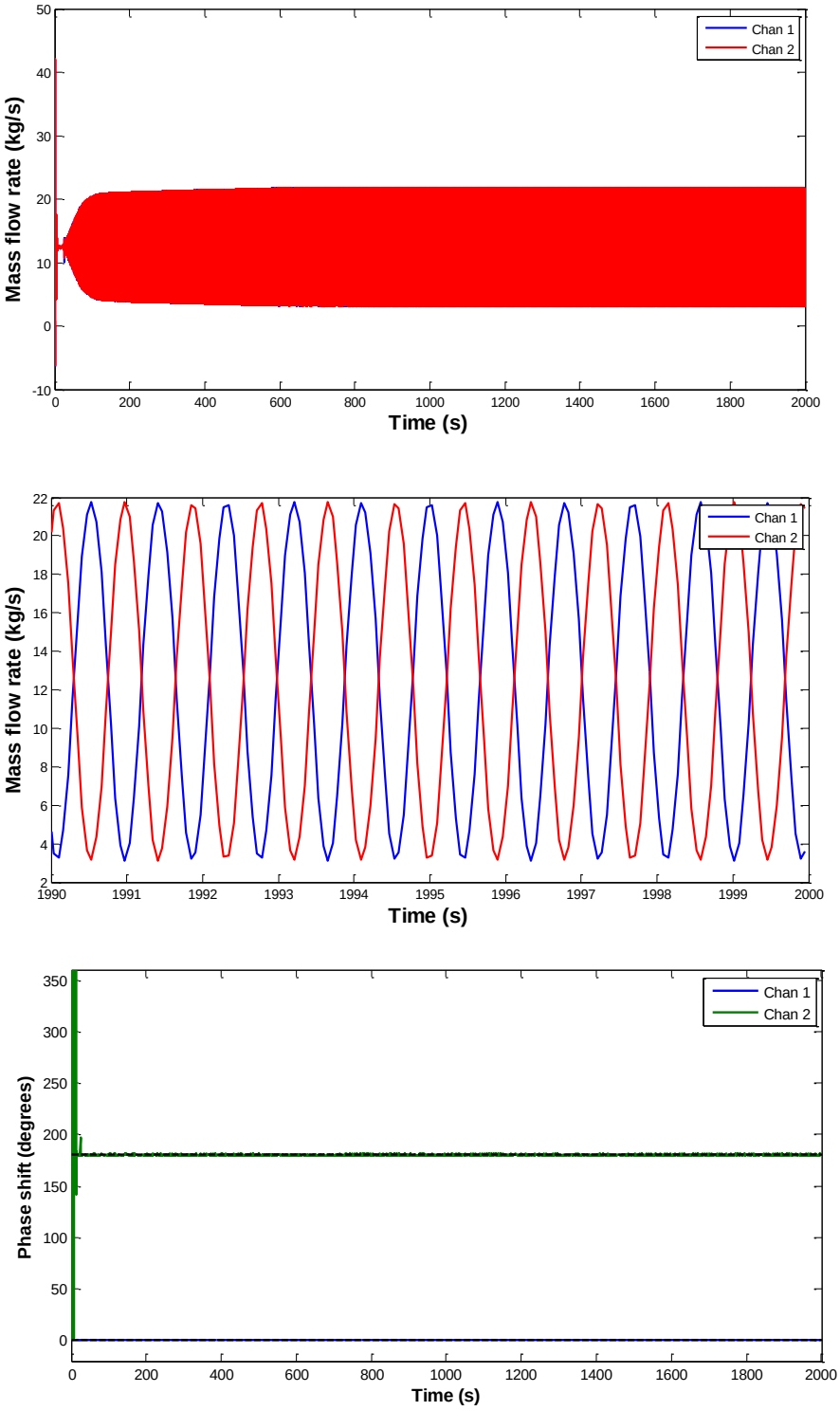

Figure 5-2 – Two-channel TRACE model, showing channel flow rates over the entire problem time (top) and a ten-second interval during the converged limit cycle (middle), as well as the relative phase shift between Channel 1 and Channel 2 (bottom).

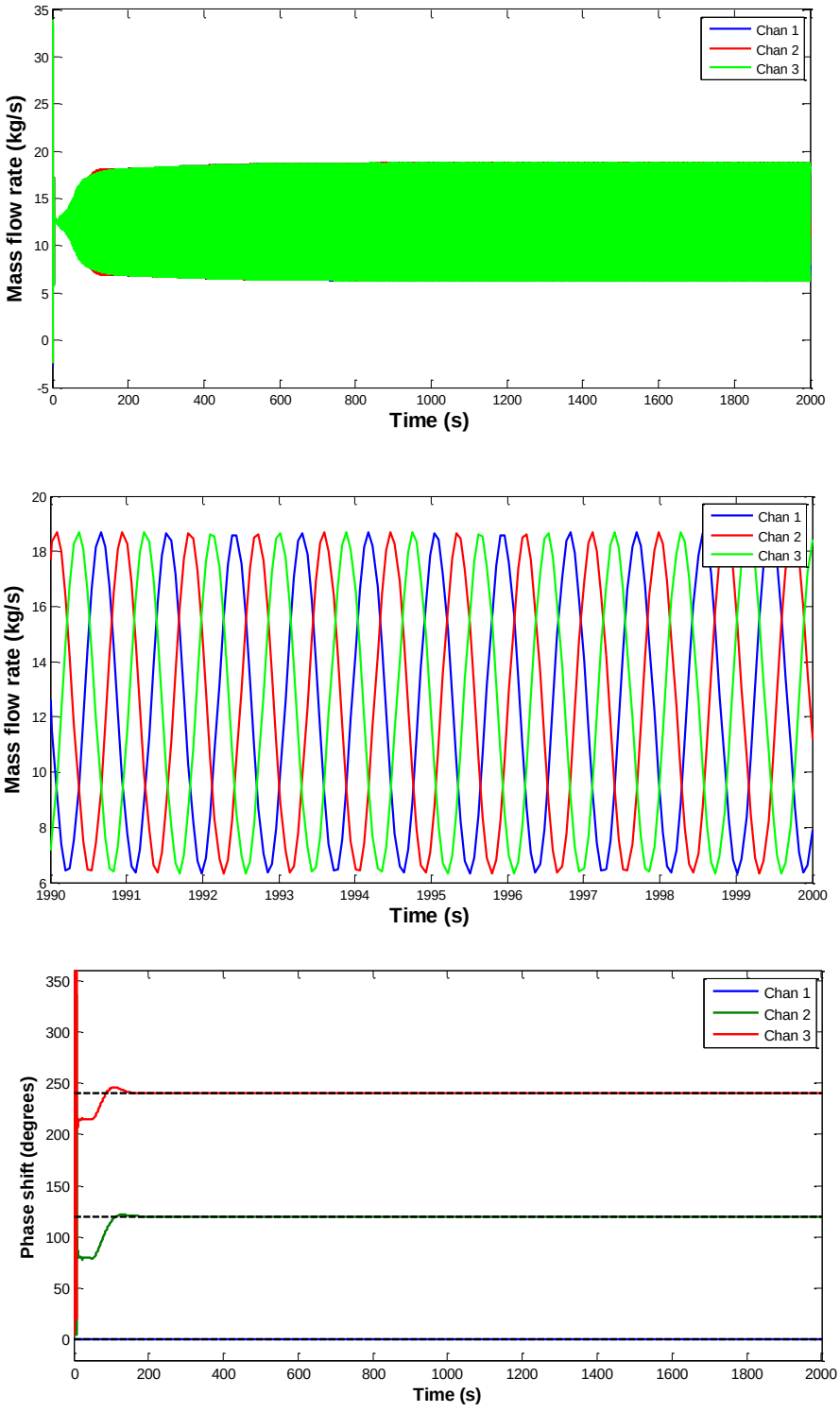

Figure 5-3 – Three-channel TRACE model, showing channel flow rates over the entire problem time (top) and a ten-second interval during the converged limit cycle (middle), as well as the relative phase shift between Channel 1 and Channels 2 and 3 (bottom).

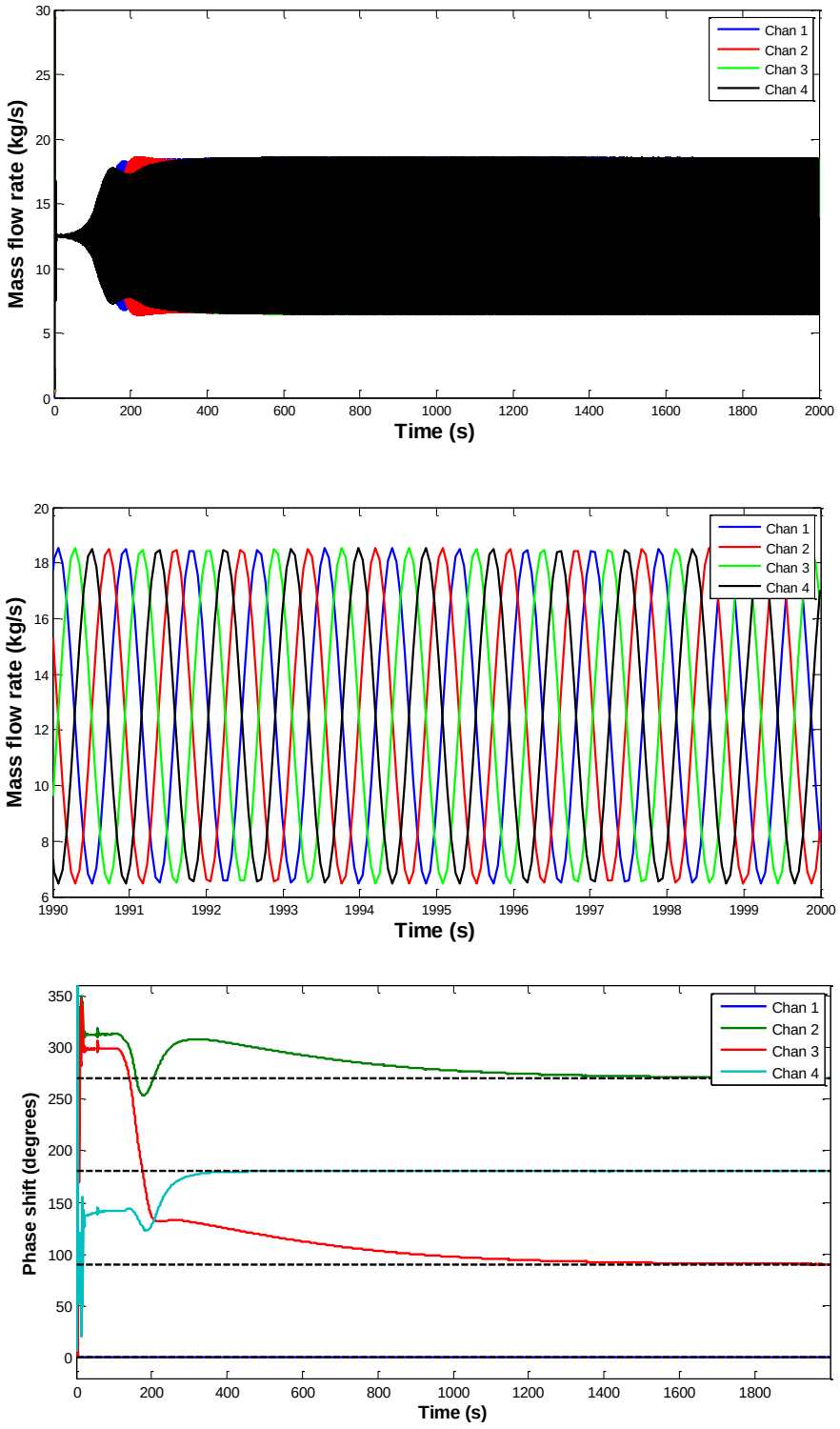

Figure 5-4 – Four-channel TRACE model, showing channel flow rates over the entire problem time (top) and a ten-second interval during the converged limit cycle (middle), as well as the relative phase shift between Channel 1 and Channels 2-4 (bottom).

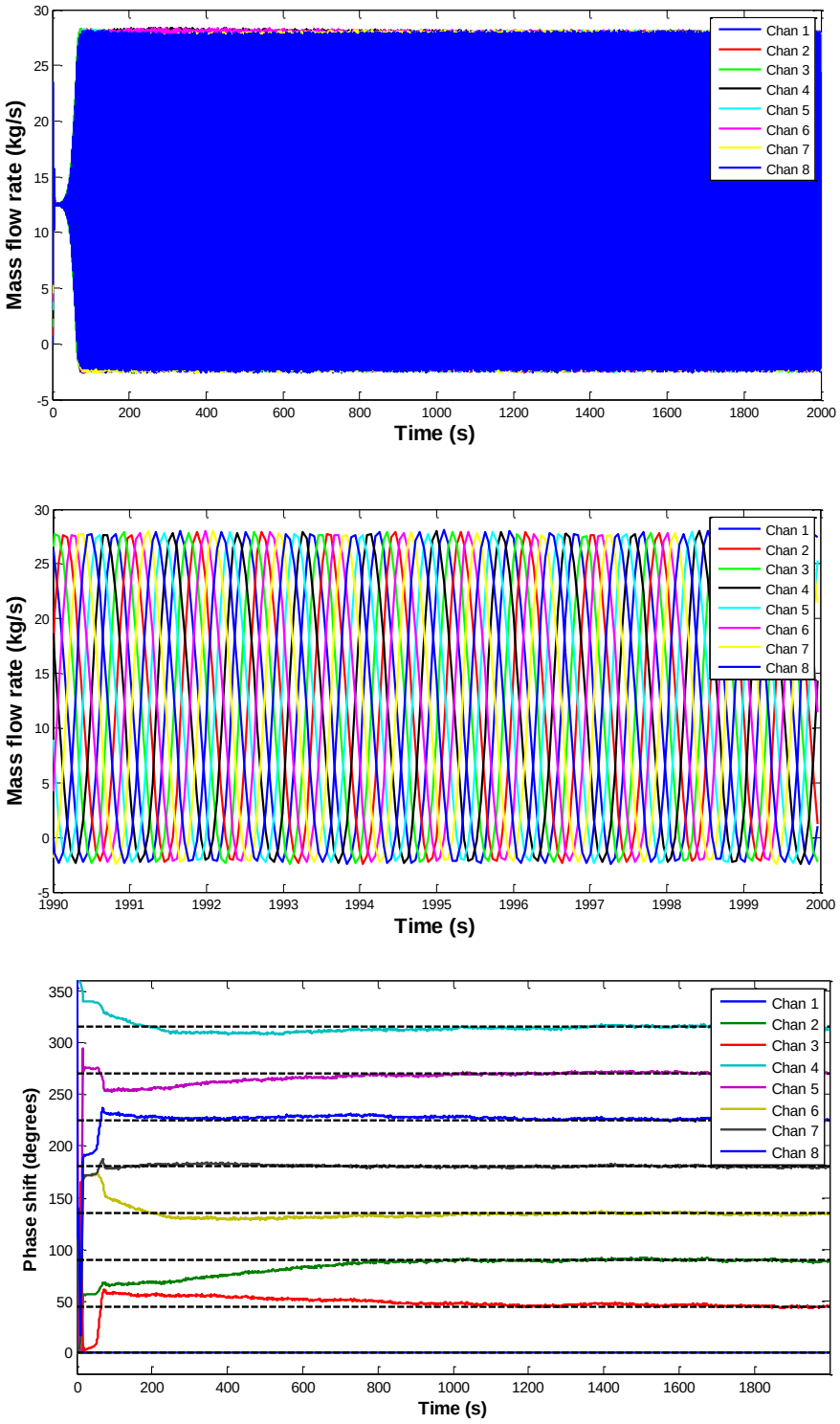

Figure 5-5 – Eight-channel TRACE model, showing channel flow rates over the entire problem time (top) and a ten-second interval during the converged limit cycle (middle), as well as the relative phase shift between Channel 1 and Channels 2-8 (bottom).

The previous section introduced an argument based on both experimental evidence and logical reasoning that, for an odd number of channels N, the phase shifts among channels will tend to be staggered by $(2\pi/N)$. However, this argument did not apply, at least in the case of linear oscillations, when N is even, due to the ability for channels to "pair up" in the fashion described above. It is somewhat surprising, then, to find that the channels in these TRACE simulations tended towards the same $(2\pi/N)$ pattern even after the channels had "paired up" and hence had already seemingly ensured a constant total flow rate regardless of phase shift between channels.

Based on this numerical result, the author hypothesizes that for finite amplitude oscillations, *i.e.* oscillations which are not purely linear, the channels will (in repeatable and non-arbitrary fashion) tend towards the $(2\pi/N)$ pattern due to some nonlinear behavior of the governing equations which cannot be determined via linear analysis alone.

Hypothetical Case to Explain Nonlinear Behavior

The full explanation of why the rotating behavior might occur is presented in detail in Chapter 7; however, in the meantime, the following subsection presents a simplified example to motivate the discussion as well as to present a good reasoning for switching to a fixed pressure drop boundary condition in future studies as opposed to the fixed total flow rate boundary condition used here.

This section will present a simple argument in an attempt to elucidate what might be causing the $(2\pi/N)$ pattern demonstrated in the previous section. It does not necessarily correspond precisely to nonlinear behavior that might actually be seen in an oscillating channel. It has been demonstrated in Chapter 2 that the linearized form of the equations governing BWR dynamics provide a perfectly sinusoidal response to some initiating perturbation (generally multiplied by a growing or dampening exponential term as well). However, it has also been shown in Chapter 2 that limit cycles – such as those shown in the previous section, where the flow rate oscillations eventually "saturate" at some fixed amplitude – occur due to nonlinear effects inherent in the governing equations.

It has also been demonstrated, for example in the large-amplitude oscillations calculated by TRACE/PARCS as shown in 0, that the oscillations themselves can become non-sinusoidal, in terms of exhibiting a wide "trough" and a narrow "peak" over the course of one oscillation period.

Therefore, one might imagine a similar shape for the flow rate behavior in, for example, a single unstable channel with a fixed pressure drop boundary condition (which is similar to the boundary condition imposed in the parallel-channel models shown above, except for the restriction of fixed total flow rate). A hypothetical flow rate trend versus time for the limit cycle case for this channel might, for the sake of argument, be something along the lines of a sine function raised to some power. A power of 4 on the sine term will prove to be convenient for this purpose, as will be seen below. The fourth order sine function with the average value and same amplitude as $f_1 = \sin(\omega t)$ is

$$f_2(\omega t) = 2\sin^4\left(\omega t/2 + \frac{\pi}{4}\right) - \frac{3}{4} \tag{5.3}$$

which can be rewritten using trigonometric identities as

$$f_2(\omega t) = \sin(\omega t) - \cos(2\omega t)/4 \tag{5.4}$$

Functions f_1 and f_2 are plotted in Figure 5-6 over two periods.

If one considers that the function f_1 (or f_2) represents the deviation in a given channel's flow rate compared to the steady-state flow rate, the total flow rate at any time in a four-channel model relative to the steady-state value would be given by the summation of four functions f_1 (or f_2), possibly with different phase shifts among the four functions.

As shown in Figure 5-7, for the case of two channels with a 0° phase shift and two with a 180° phase shift, the total flow rate remains constant using the "linear" channel oscillations according to $f_1 = \sin(\omega t)$. The same is true when two of the channels (originally at 0° and 180° phase) are shifted by an additional 45° lag (Figure 5-8) or additional 90° lag (Figure 5-9); in fact, the total flow remains constant regardless of the common lag added to these two channels. This behavior was noted in the previous two sections, where it was suggested that – for linear oscillations – two pairs of counter-phase channels could form with any arbitrary phase shift and still maintain a constant total flow rate.

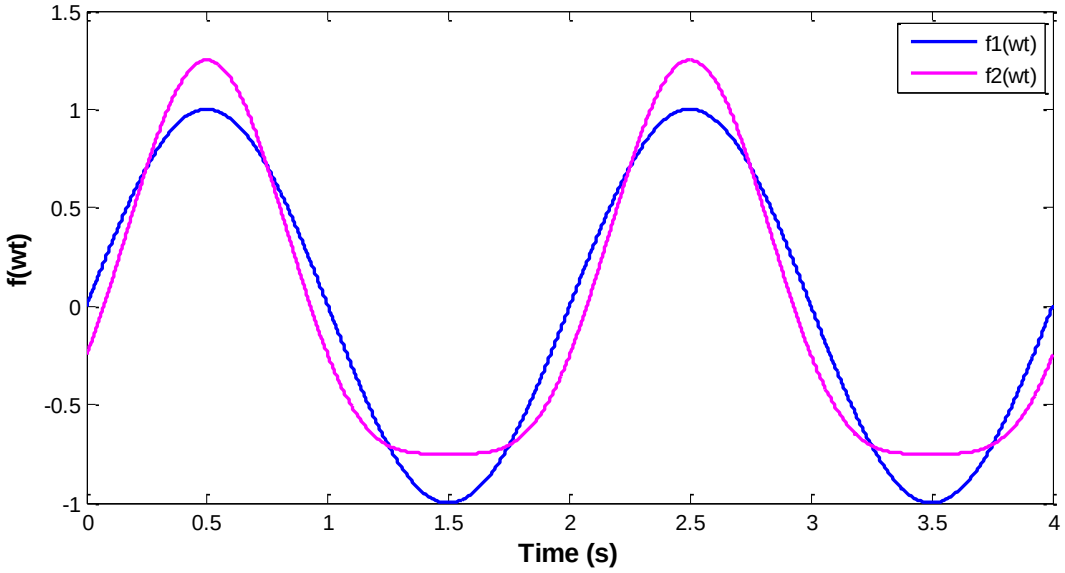

Figure 5-6 – $f_1(\omega t)$ and $f_2(\omega t)$, for $\omega = \pi$.

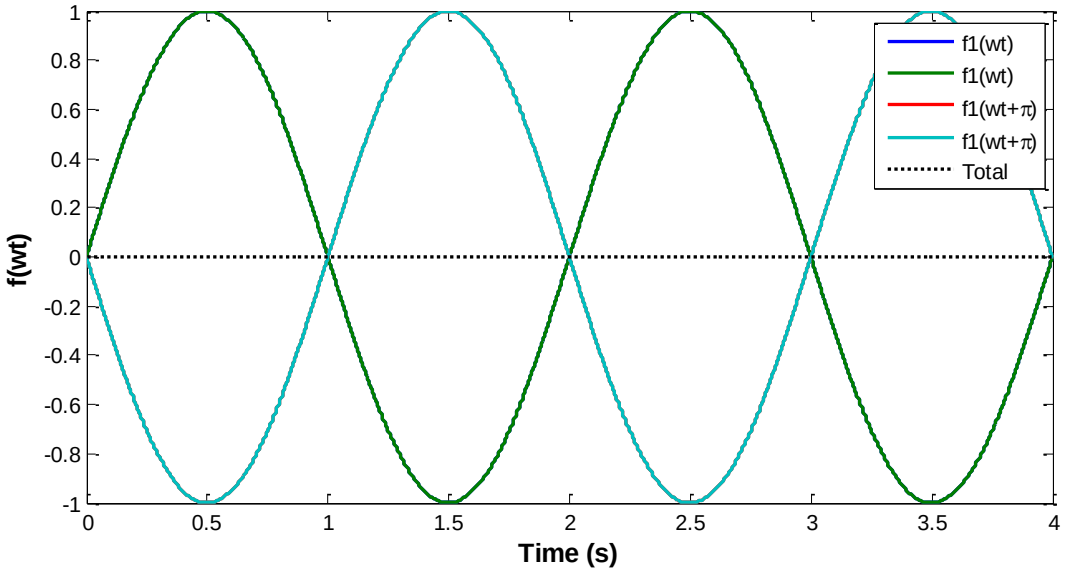

Figure 5-7 – Demonstration that the total flow rate remains constant for two duplicate pairs of counter-phase channels, using $f_1 = \sin(\omega t)$.

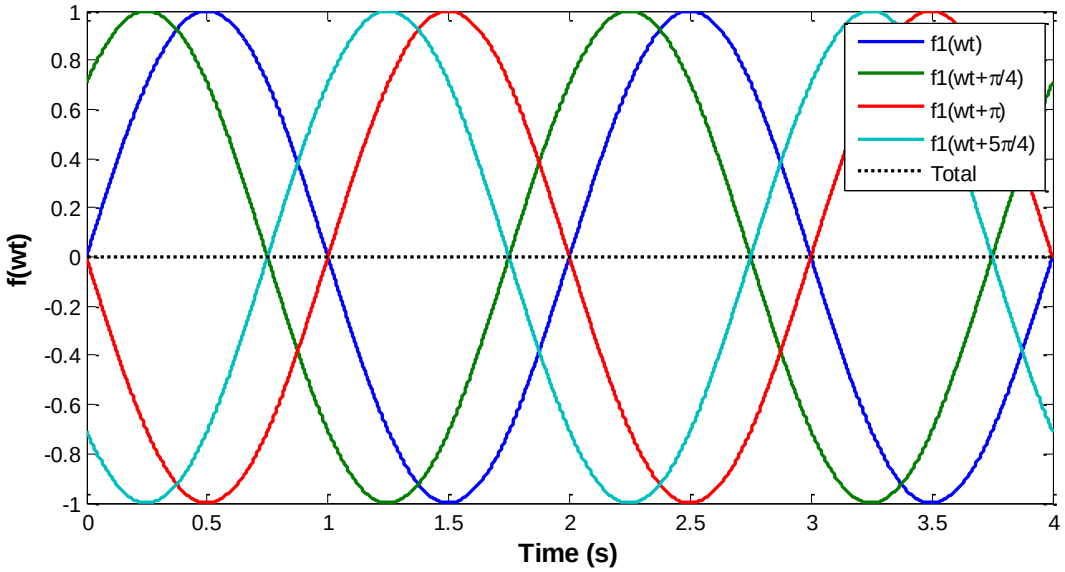

Figure 5-8 – Demonstration that the total flow rate remains constant for two pairs of counter-phase channels staggered from each other by 45°, using $f_1 = \sin(\omega t)$.

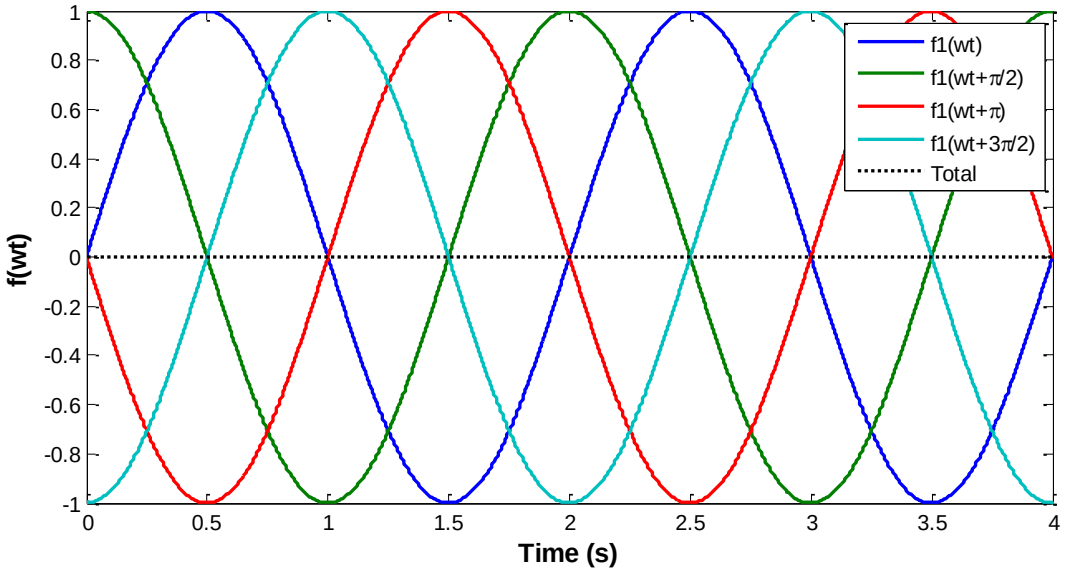

Figure 5-9 – Demonstration that the total flow rate remains constant for two pairs of counter-phase channels staggered from each other by 90°, using $f_1 = \sin(\omega t)$.

However, for the case of a general non-sinusoidal periodic variation in channel flow rates, the total flow rate in general cannot become constant for any combination of phase shifts among the channels, at least in the four-channel system shown here (the specific choice

of f_2, incidentally, does become constant for a phase shift of 90°, but for a general non-sinusoidal periodic function this will typically not be the case). However, assuming that the channels form into two pairs of counter-oscillating channels as described in the previous section, the magnitude of the variation in total flow rate across one period of oscillation in general will be highest when the two pairs are "doubled up" (*i.e.* have the same phase as each other) and lowest when the two pairs are staggered apart by 90°.

For the specific choice of f_2 given in Eq. (5.4), it can be shown that the variation in total flow rate among two pairs of channels with a relative phase shift of ϕ is equal to

$$\begin{aligned} &f_2(\omega t) + f_2(\omega t + \phi) + f_2(\omega t + \pi) + f_2(\omega t + \pi + \phi) \\ &= -\cos\phi\cos(2\omega t + \phi) \end{aligned} \tag{5.5}$$

This is a simple cosine function with half the period of the channel oscillations and with an amplitude equal to $\cos\phi$. Eq. (5.5) is shown graphically as the dotted line in Figure 5-10 through Figure 5-12, showing that the variation in total flow rate is highest for $\phi = 0$ and lowest for $\phi = \pi/2$.

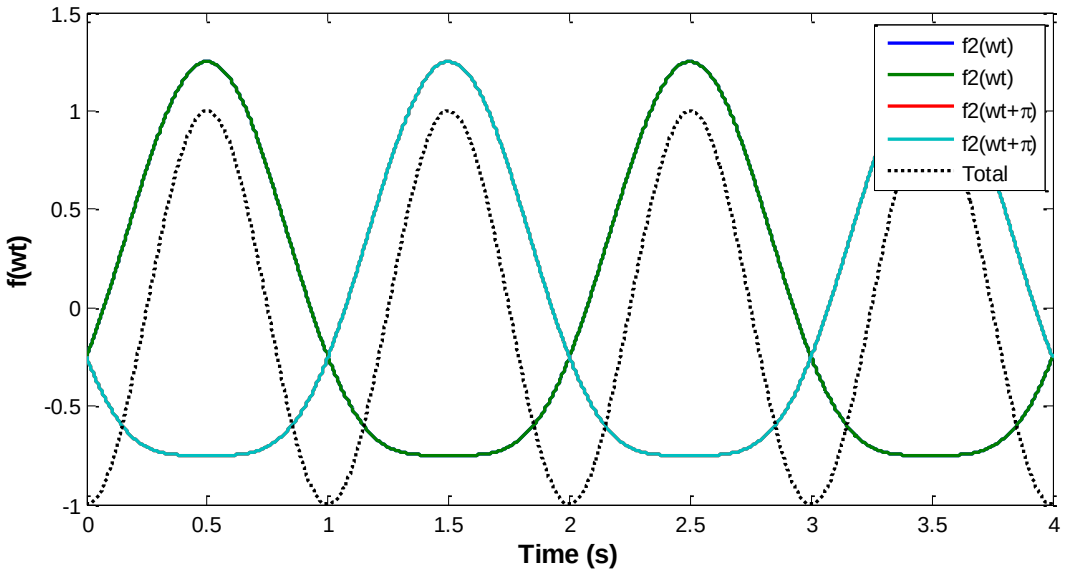

Figure 5-10 – Demonstration that the total flow rate does not remain constant for two duplicate pairs of counter-phase channels, using $f_2(\omega t)$.

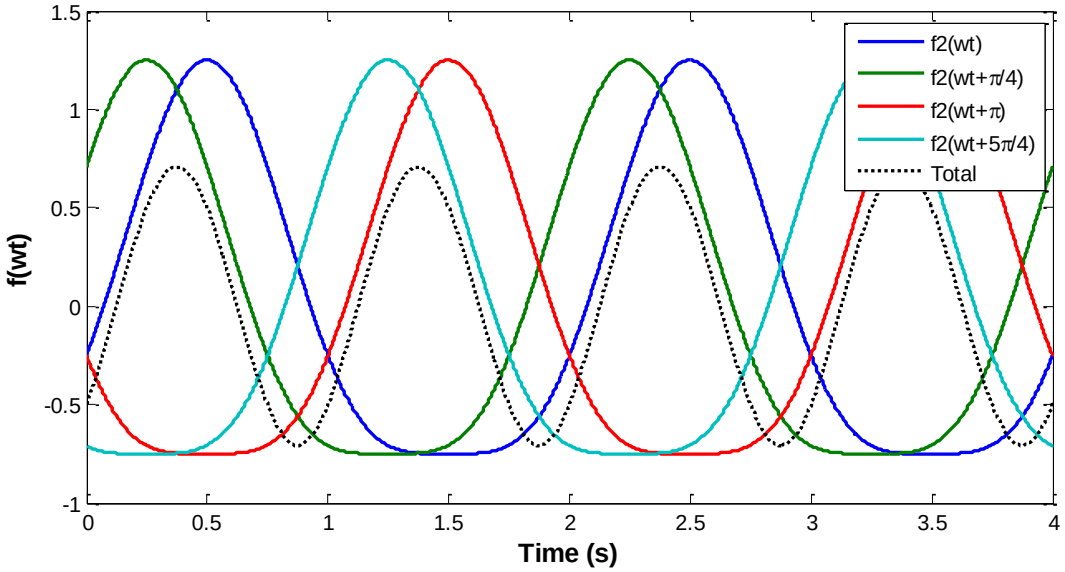

Figure 5-11 – Demonstration that the variation in total flow rate decreases as the phase shift between channel pairs increases to 45°, using $f_2(\omega t)$.

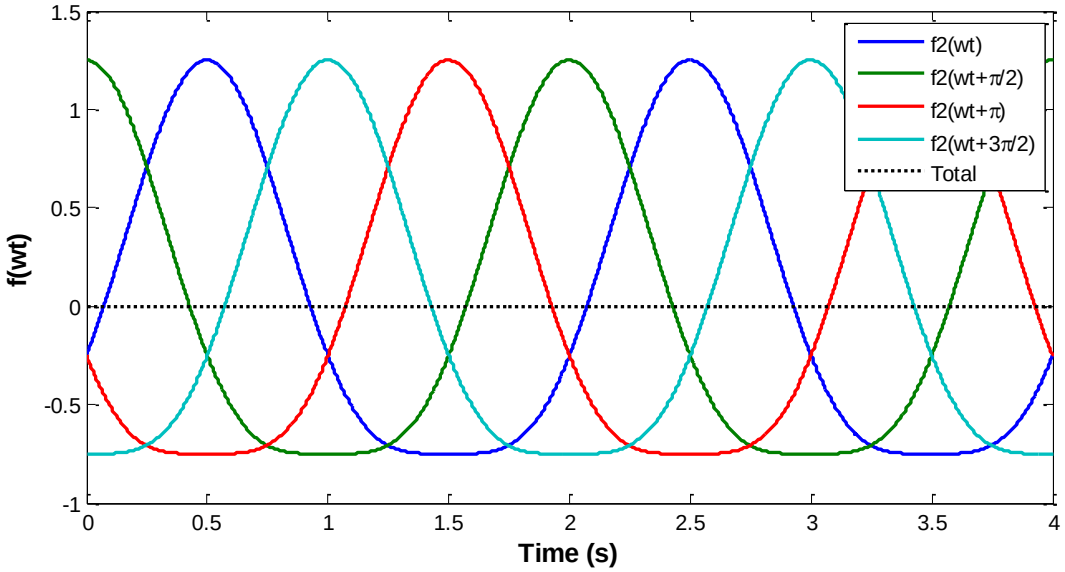

Figure 5-12 – Demonstration that the variation in total flow rate decreases further (becoming constant in this case) as the phase shift between channel pairs increases to 90°, using $f_2(\omega t)$.

It should be clarified that the individual channels in a four-channel case with a fixed total flow rate constraint are not expected to oscillate with a behavior similar to function f_2, but rather similar to function f_1 instead. A single channel case with a fixed pressure drop boundary

condition, for example, could be expected to oscillate in some "nonlinear" shape similar to f_2. However, the constraint of a constant total flow rate provides a sort of "driving force" that immediately cancels out any potential variations in total flow rate by adjusting individual channel flow rates on the fly.

One may imagine a simulation in which, due to some small perturbation, the four channels begin oscillating with the sinusoidal shape and the $(0,0,-1,-1)$ phase distribution as shown in Figure 5-7. However, as the oscillations grow (assuming the DR is greater than 1), there exists a tendency in each channel to depart from the symmetric sinusoidal behavior as in f_1 and to develop an asymmetric periodic behavior such as f_2. However, as illustrated in Figure 5-10, any non-symmetric (*i.e.* "nonlinear") shape would create a non-constant total flow rate, so the channels must continue to oscillate as perfectly symmetric sinusoids, at least as long as the $(0,0,-1,-1)$ phase distribution persists. Hence, the constant total flow restraint creates a "resistance" to the natural oscillation mode of the individual channels, whose underlying equations would normally lend themselves to the nonlinear behavior akin to f_2.

As Eq. (5.5) illustrates, this "resistance" would be lessened if one of the channel pairs were to drift away from the other pair of channels in the form of a phase lag (or lead). In other words, a "driving force" is present which pushes the phase shift ϕ higher in magnitude until the point of least resistance, $\phi = \pi/2$, is reached. This, hypothetically, would be the most "natural" state for the channels to oscillate in, as it requires the least interference from the total flow constraint mechanism on the natural oscillation of the channels.

This view is supported by the phase plot shown in, for example, Figure 5-4, where the channels start out oscillating with essentially arbitrary phase shifts but gradually evolve towards the $\left(1,-1,e^{\pi i/2},-e^{\pi i/2}\right)$ behavior (*i.e.* phase shifts of 0°, 90°, 180°, and 270°) over time.

As will be shown in Chapter 6, a fixed pressure drop boundary condition (with proper treatment of inlet and outlet pressure drops) provides a more logical and satisfying condition than the fixed total flow rate boundary condition, based on the discussion above. For the fixed ΔP case, both the in-phase and out-of-phase modes are possible; the system is not artificially forced into the out-of-phase mode due to a fixed total flow requirement. Furthermore, since the total flow rate is allowed to vary in the former case, this lends itself to an understanding of

the rotating mode in terms of *minimizing the variation in the total flow rate* directly, rather than resorting to a discussion of "resistance" as described above when the total flow rate is fixed. Thus, based on the results in this chapter, future chapters will rely on the total pressure drop condition instead.

Sensitivity Study on Limit Cycle Amplitude

If the above hypothesis is correct – namely, that the $\left(1, -1, e^{\pi i/2}, -e^{\pi i/2}\right)$ mode is caused by nonlinear effects of the individual channel flows under the constraint of a fixed total flow rate – then the channels would be expected to migrate towards this phase pattern more quickly as the limit cycle amplitude increases. This is because the nonlinear effects would increase as the oscillation amplitude increases, creating a larger impetus for the channels to adjust their phase to the $\left(1, -1, e^{\pi i/2}, -e^{\pi i/2}\right)$ mode more quickly.

This is successfully demonstrated in the following two cases, which are identical to the four-channel model as shown in Figure 5-4, except that the total power was set to 27.1 MW and 26.3 MW, respectively, for the two cases (the total power for the case given in Figure 5-4 was 26.5 MW).

Results are shown in Figure 5-13 through Figure 5-15. The 27.1 MW case with a limit cycle amplitude of roughly $\pm$15 kg/s converged to the $\left(1, -1, e^{\pi i/2}, -e^{\pi i/2}\right)$ phase behavior within 400 s. Recall from Figure 5-4 that the 26.5 MW case with a limit cycle amplitude of roughly $\pm$6 kg/s converged to the same phase behavior after 1500 s. However, the 26.3 MW case with a limit cycle amplitude of roughly $\pm$2.5 kg/s required approximately 8000 s to converge to the same phase behavior.

These cases reveal a clear trend between increasing limit cycle amplitude and decreasing time required to converge to the eventual limit cycle behavior, which is $\left(1, -1, e^{\pi i/2}, -e^{\pi i/2}\right)$ in all cases. This is in line with the argument in the previous section which postulates that this phase behavior is driven by nonlinear effects which become more significant as the oscillation amplitude increases.

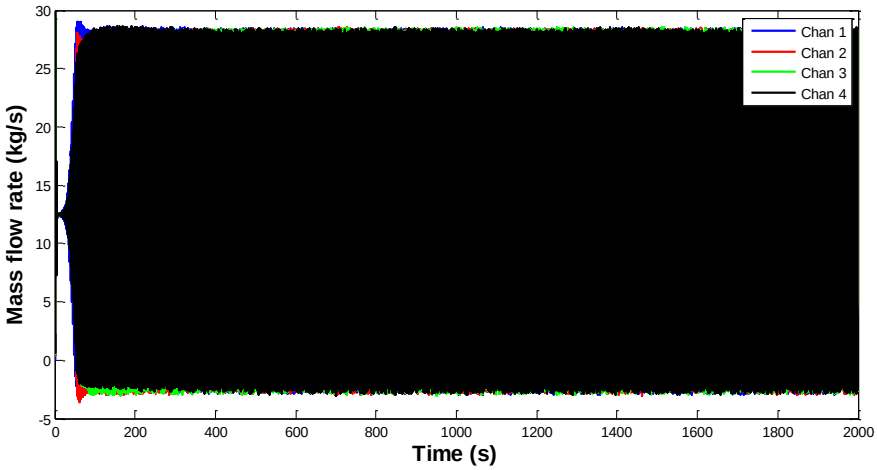

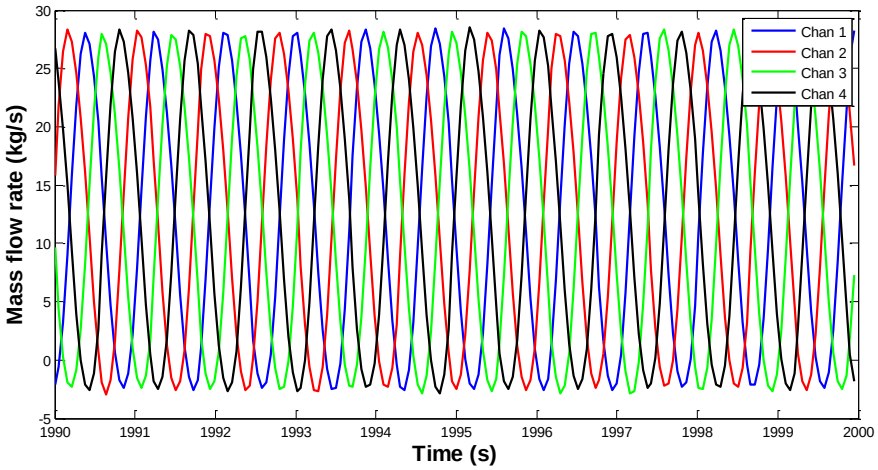

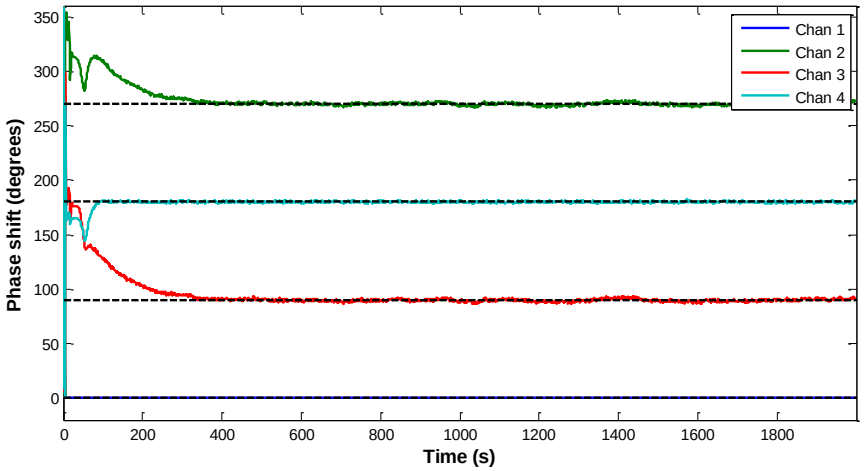

Figure 5-13 – Four-channel TRACE model with a power level of 27.1 MW, showing channel flow rates over the entire problem time (top) and a ten-second interval during the converged limit cycle (middle), as well as the relative phase shift between Chan. 1 and Chans. 2-4 (bottom).

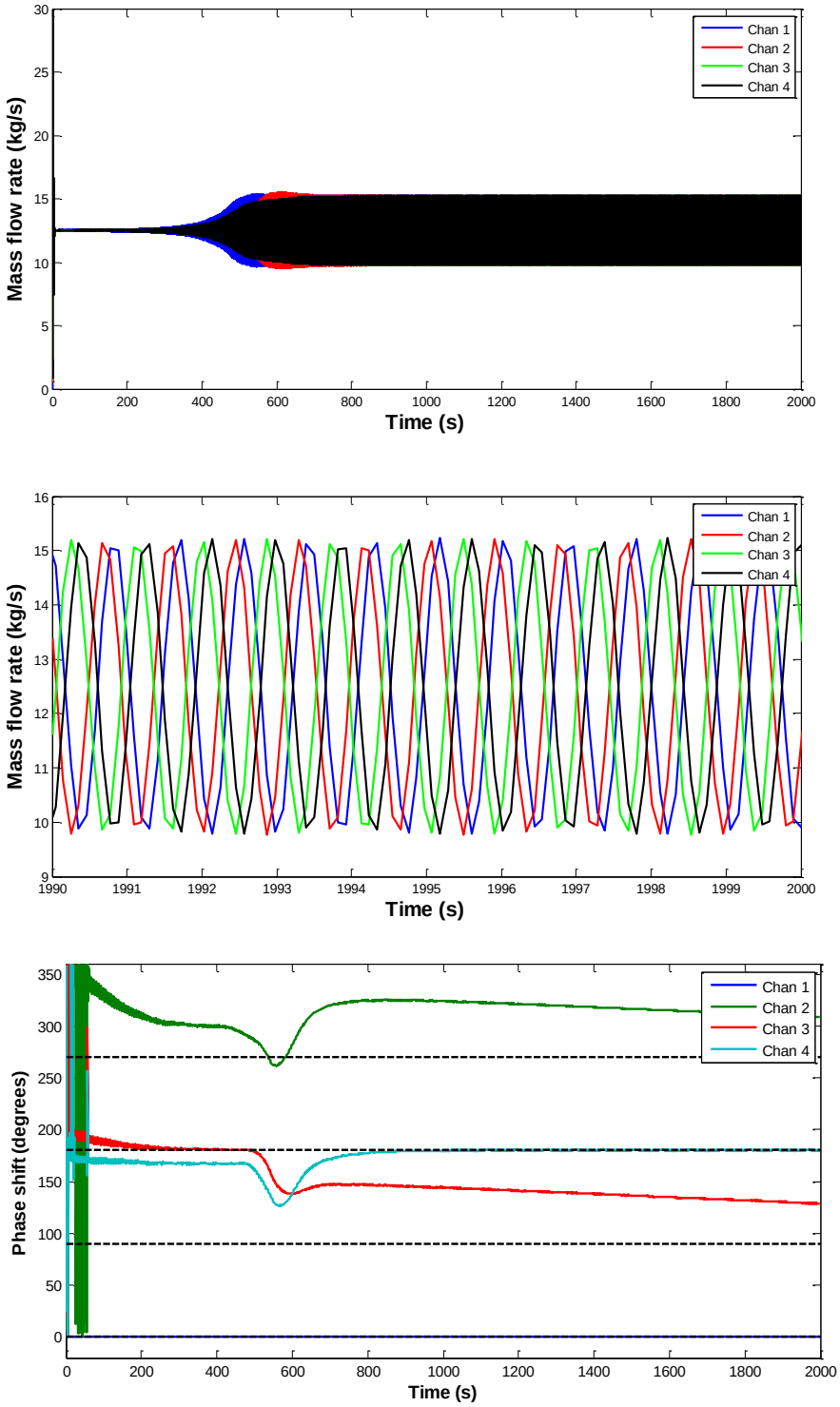

Figure 5-14 – Four-channel TRACE model with a power level of 26.3 MW, showing channel flow rates over the entire problem time (top) and a ten-second interval before the solution had converged to the limit cycle (middle), as well as the relative phase shift between Channel 1 and Channels 2-4 (bottom).

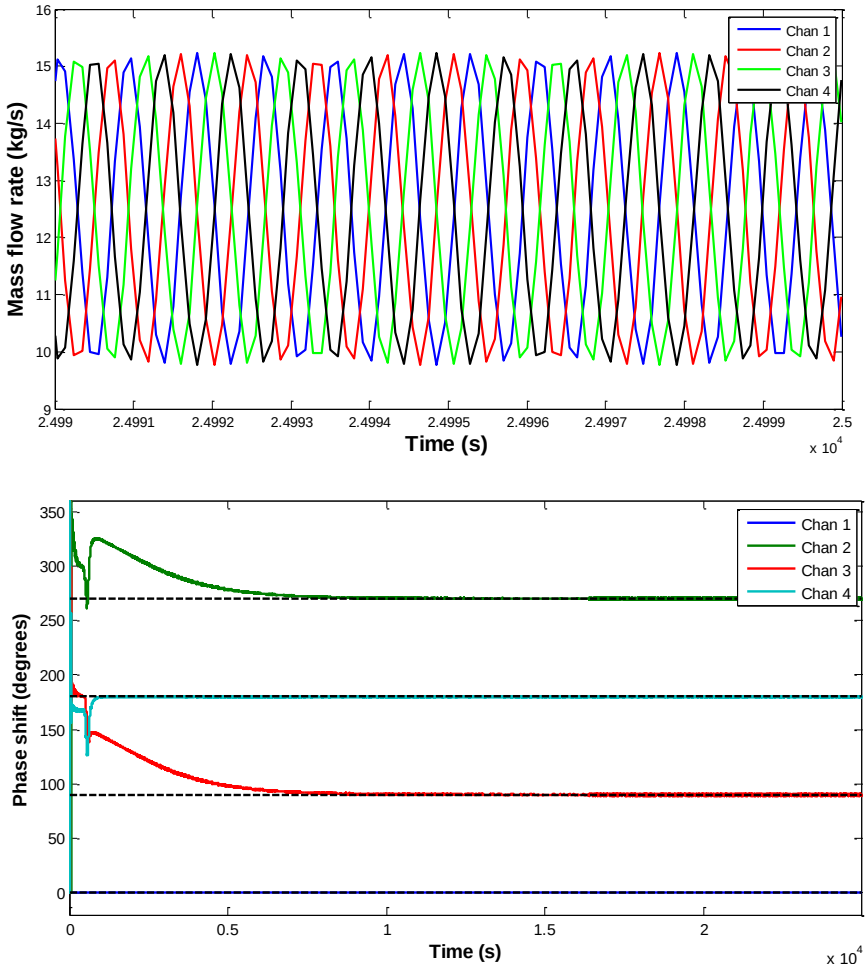

Figure 5-15 – Four-channel TRACE model with a power level of 26.3 MW, showing channel flow rates over a ten-second interval once the solution had converged to the limit cycle (top), as well as the relative phase shift between Channel 1 and Channels 2-4 over the entire 25000 s transient (bottom).

5.3 Coupled TRACE/PARCS Four-Channel Model

The four-channel TRACE model described in the previous section was coupled to a four-assembly PARCS model which included 5 active fuel nodes with the same 70 cm axial mesh spacing as the TRACE TH nodes, as well as single 10 cm reflector nodes on top and bottom. To make the model as simple as possible, all burnup and history values were set to zero, and the same cross section set was used in all axial and radial fuel nodes to ensure a homogeneous core. Additionally, it was found that using reflective boundary conditions in the radial direction gave better numerical performance compared to vacuum boundary conditions. This was likely due to the extremely steep gradients in fluxes and currents caused by the reduced radial size of the model unless reflective boundaries were used.

While the radial location of each channel was irrelevant for the previous calculations with TH only, for the coupled case the radial ordering of channels becomes important. Therefore, the radial location of each channel is given in Figure 5-16, for later reference.

1	2
3	4

Figure 5-16. Channel radial numbering scheme for the 4-channel problem.

Investigation of Eigenmodes

An initial calculation at essentially zero power was performed with the coupled model in order to verify the performance of the Arnoldi subroutine for the simplest case possible. This ensured that the coolant density and fuel temperatures were essentially constant (with only small variation in coolant density due to a pressure difference in the fluid between the inlet and outlet) and therefore the power profile would be as close to symmetric in the axial direction as possible, with the four assemblies having the same power level as well.

Table 5-2 shows the eigenvalues of the first ten modes for the coupled four-channel problem. It can be seen that the first five eigenvalues are clustered relatively close together, while eigenvalues 6 and 7 are substantially smaller. The reason for this is the difference in radial mode shapes, which is discussed below.

Figure 5-17 shows the axial profiles of the fast group flux for the first 5 eigenmodes. The radial profiles are not shown here, since they are simply flat in the radial direction (*i.e.* identical axially-averaged values in all four channels), which corresponds to the "fundamental" flux shape in the radial direction. However, the axial direction contained increasingly higher-order mode shapes. These correspond approximately to the mode shapes $\sin(n\pi z/L)$, where n is the mode number, z is the axial coordinate, and L is the total height.

Table 5-2. Eigenvalues of the first 10 modes for the coupled four-channel problem.

Mode Number	Eigenvalue
1	0.99372
2	0.98327
3	0.97052
4	0.96000
5	0.95430
6	0.65899
7	0.65899

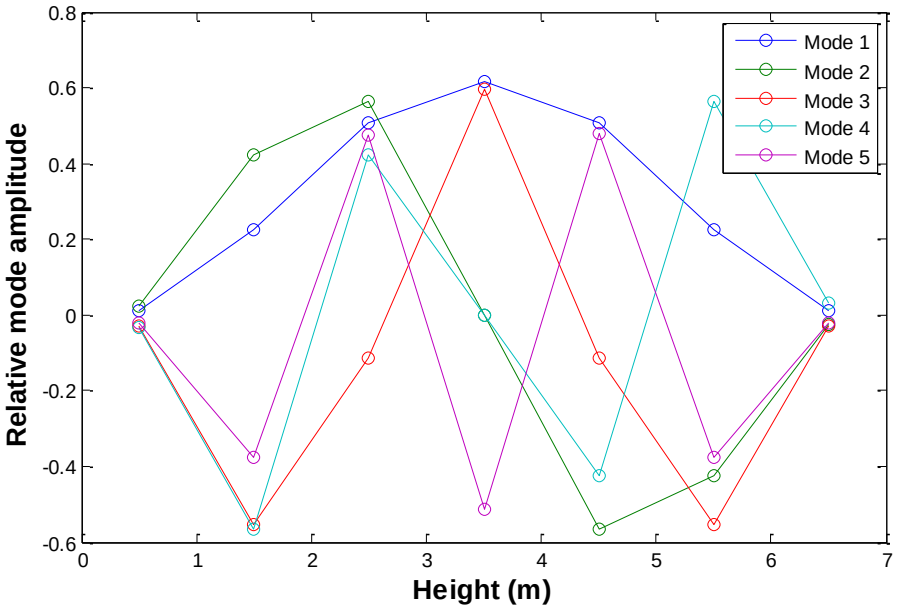

Figure 5-17 – Axial profile for modes 1-3 of the fast group flux in channel 1.

Figure 5-18 and Figure 5-19 show the radial and axial profiles, respectively, of the fast group flux for eigenmodes 6 and 7. Unlike for modes 1-5, which clearly corresponded to the fundamental radial mode shape, modes 6 and 7 correspond to what would normally be called

the first and second azimuthal modes. However, the eigenvalues corresponding to these radial modes are degenerate due to the radial symmetry of the 4-channel system.

The eigenvalue degeneracy of multiplicity two creates a two-dimensional subspace in which the two eigenvectors (or eigenmodes) corresponding to the degeneracy must reside. However, since the same eigenvalue applies to any vector in the subspace, the two degenerate eigenmodes need not be orthogonal to each other in the same way that non-degenerate eigenmodes must be. In terms of the current problem, this means that eigenmodes 6 and 7 can take on any radial orientation, with a radial "symmetry line" anywhere from 0° to 360° with respect to the x-axis, and the two need not be oriented 90° apart from each other.

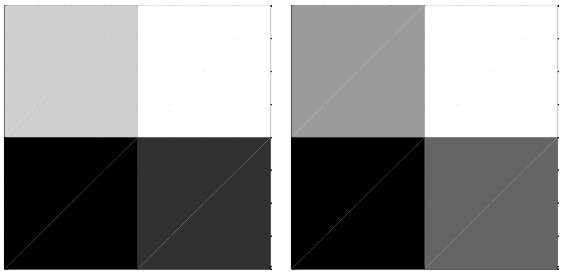

Figure 5-18 – Radial profile for modes 6-7 of the axially-averaged fast group flux, before orthogonalization.

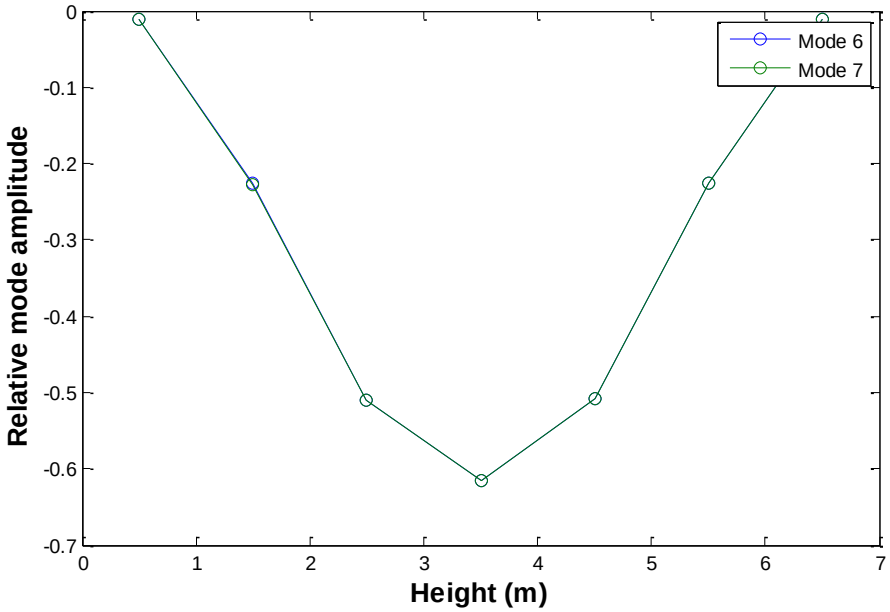

Figure 5-19 – Axial profile for modes 6-7 of the fast group flux in channel 1.

However, the case of degenerate eigenvalues can usually be rectified through a simple Gram-Schmidt orthogonalization process, in which a new eigenvector can be constructed orthogonal to one of the degenerate eigenmodes in the direction of the second degenerate eigenmode. The result of this process for the current problem is shown in Figure 5-20, in which modes 6 and 7 are seen to be properly orthogonal to each other. The axial profile of the two modes is omitted here but did not change from the ones shown in Figure 5-19.

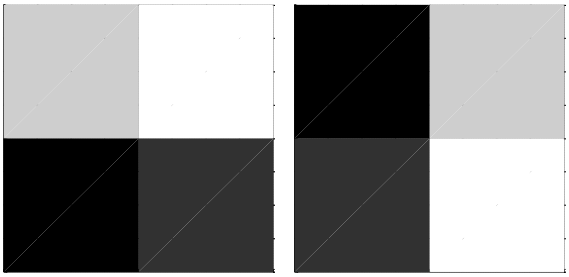

Figure 5-20 – Radial profile for modes 6-7 of the axially-averaged fast group flux, after orthogonalization.

Limit Cycle Results

For the transient calculation, the power was adjusted before each run until a limit cycle of adequate amplitude was attained. Results for flow rates are shown in Figure 5-21.

The flow rates showed nearly the same $\left(1, -1, e^{\pi i/2}, -e^{\pi i/2}\right)$ (or 0°-90°-180°-270°) phase behavior for the converged limit cycle as was seen in the standalone TRACE case, except that the second pair of channels was roughly 5° off (*i.e.* the pattern was roughly 0°-95°-180°-275°). This was likely due to numerical issues of some sort, perhaps some slight asymmetry arising somewhere in the coupled calculation (note, however, that the converged steady-state power distribution was perfectly symmetric).

Nonetheless, the qualitative behavior was as expected. Furthermore, as opposed to the N-channel standalone TRACE models which gave essentially an arbitrary ordering of channels in terms of phase shifts, the coupled model gave a definite "rotating" behavior in terms of channel ordering. Namely, the channels oscillated in the order 1-2-4-3, corresponding to x-y quadrants II, I, IV, and III, respectively.

Although further study is needed to confirm this behavior, it appears that the neutronic coupling causes a strong enough tendency, due to azimuthal flux harmonics, to order the channels in a "rotating" fashion. This is as opposed to, say, a 1-2-3-4 ordering of channels, which would not give the same rotating behavior.

The results for neutronic mode amplitudes are shown in Figure 5-22. The fundamental amplitude does not appear in the figure, but this amplitude remains almost perfectly constant at 100.0% throughout the simulation. The first two azimuthal modes (corresponding to modes 6 and 7 above) show the expected 90° relative phase shift behavior which agrees with the previous mode amplitude behavior demonstrated with the full core model in 0. However, the amplitude of oscillation in terms of neutronics was exceedingly small, merely ±0.4% of relative power.

The small amplitude of neutronic oscillation was almost certainly due to the high degree of subcriticality of the azimuthal modes in this small 4-channel problem, as shown in Table 5-2. This creates a very weak response of the azimuthal modes to changes in cross sections due to changes in moderator density and fuel temperature caused by the TH oscillations, which by comparison fluctuated by roughly ±10% flow. Additional cases with slightly higher total power levels (not shown here) showed a slightly stronger but still relatively weak neutronic response even when flow rates varied by at least ±100%.

The fact that the coupled four-channel model gives essentially the same behavior as the full-core model shown in 0, despite the much weaker neutronic feedback in the four-channel model, indicates that the rotating-mode behavior may arise primarily from nonlinearities in the TH equations, with any nonlinearities in the neutronics equations (or in the coupling of the two fields) playing only a secondary role – for example, in determining the ordering of channels as discussed above, but not necessarily in causing the 90° phase shifts themselves. Further study is needed to test this hypothesis.

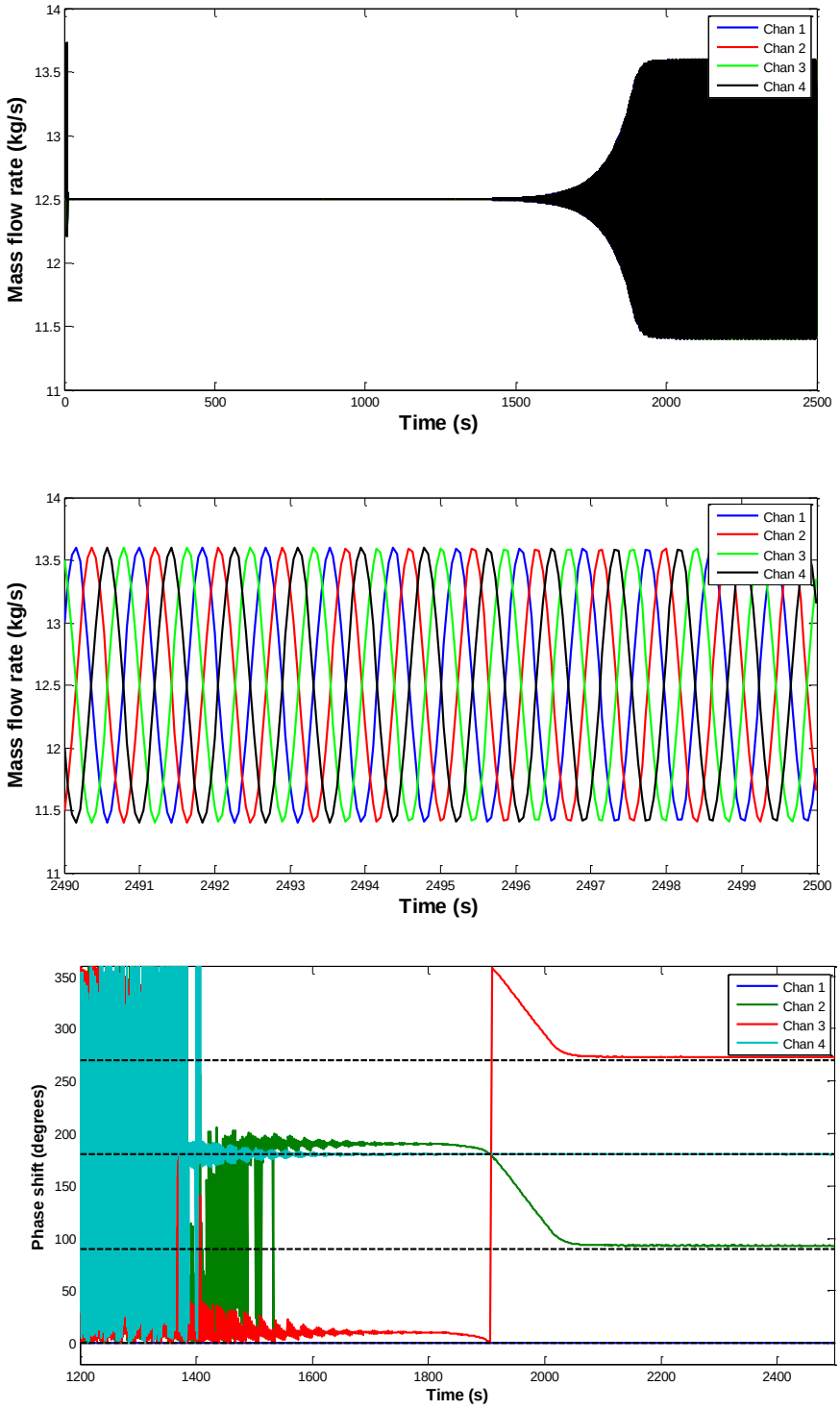

Figure 5-21 – Four-channel coupled TRACE/PARCS model with a power level of 24.6 MW, showing channel flow rates over the entire problem time (top) and a ten-second interval after the solution had converged to the limit cycle (middle), as well as the relative phase shift between Channel 1 and Channels 2-4 (bottom).

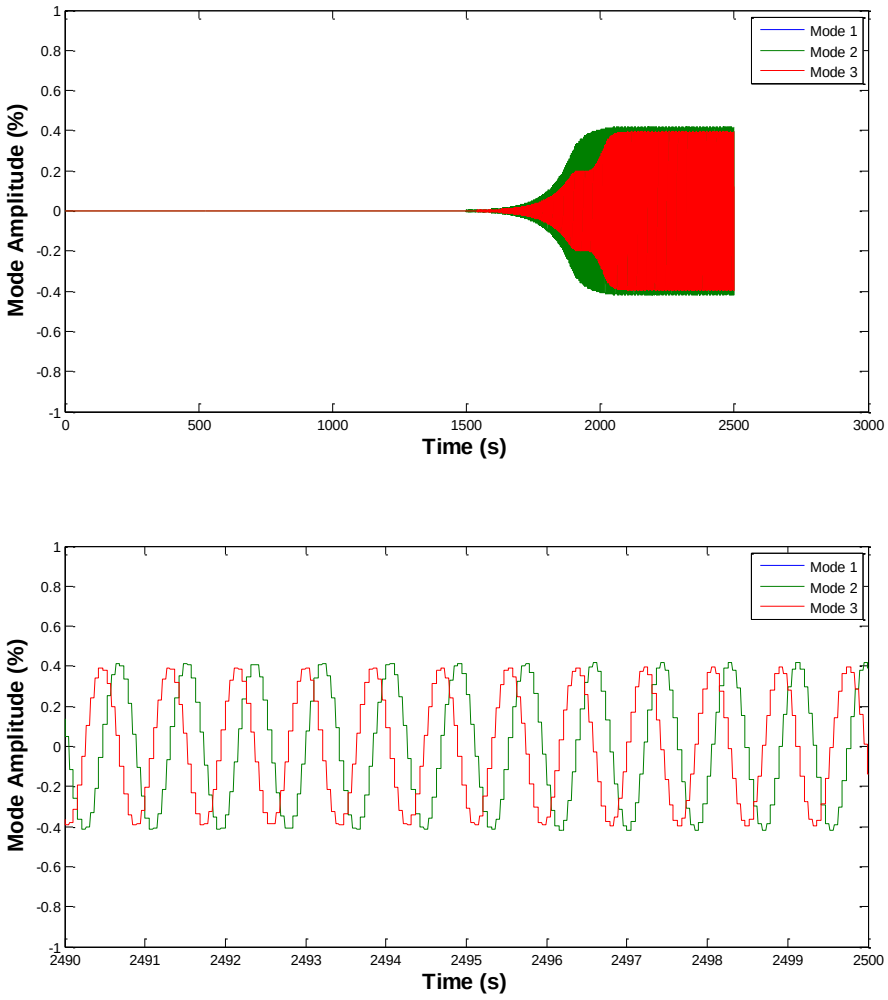

Figure 5-22 – Mode amplitudes for the four-channel coupled TRACE/PARCS model with a power level of 24.6 MW. Mode 1 is the fundamental mode (out of frame; normalized to 100% power), while modes 2 and 3 are the first two azimuthal modes.

Chapter 6. Investigation of Oscillations with a Reduced-Order Model

Detailed three-dimensional coupled codes such as TRACE/PARCS are currently the most accurate and dependable means of predicting the stability characteristics and behavior of a BWR system, able to account for important axial and radial effects, heterogeneities in core loading and geometry, etc. However, the author will now make use of an entirely different solution methodology – a so-called "reduced order model" (ROM) – for two main reasons: for independent verification of the results shown previously (especially the "rotating mode" behavior), and for the ability to gain much clearer physical insights from the ROM than is possible with complicated codes like TRACE/PARCS.

On the first point: there has been some evidence, perhaps, of a "rotating mode" behavior in real reactors, such as witnessed in the Oskarshamn-3 reactor [32]; however, the available data for this is limited and it has remained an open question whether the "rotating mode" behavior in particular is a physically real phenomenon or merely a peculiarity of the numerical tools used without basis in reality.

In an attempt to answer this question, a reduced-order model (ROM) has been employed. As will be described in the next section, ROMs employ a much different set of implemented equations and numerical assumptions than, for example, TRACE/PARCS; and, due to these differences, if the ROM is able to demonstrate the same rotating-mode behavior as TRACE/PARCS, then this grants more confidence that this behavior is indeed physical and not merely a numerical anomaly.

In addition, the ROM provides several key advantages over TRACE/PARCS in terms of developing a fundamental understanding of the physical phenomena at play. For example, in the ROM, the feedback reactivity coefficients can be freely adjusted, and in such a way that the steady-state conditions are unaffected, allowing for easy comparison between cases; whereas, with TRACE/PARCS, the reactivity coefficients are internally calculated and are not easily adjusted, and changing their values would also in general lead to, for example, a change in the

axial power profile which would make direct “apples to apples” comparisons between cases impossible.

Another key benefit of the ROM is the ability to easily construct a Jacobian matrix to linearize the system of ordinary differential equations, and then to extract the values of all eigenvalues and eigenvectors of the system. This is in contrast to TRACE/PARCS, for which only the most unstable eigenvalue can be determined directly, and requires post processing procedures (noise analysis or curve fitting) are required to find it, which introduces significant error.

It should be pointed out that, in the literature, ROMs have shown limited accuracy in terms of, for example, precise calculation of decay ratios and natural frequencies at particular operating points. However, such models have been designed specifically to capture all the relevant basic physical phenomena involved in BWR stability; therefore, the precise numerical accuracy of the ROM is of less interest than the overall qualitative behavior it demonstrates.

6.1 Theory

The ROM used in the present study was introduced by Karve et al. [27], and was selected here as being perhaps the simplest model available which still includes all the elements needed for this study. The original model described in the chapter consists of a single thermal-hydraulic channel with fuel temperature and coolant density feedback provided via a point kinetics model for neutronics. For the present study, the model has been extended to allow for multiple thermal hydraulic channels in parallel, connected via common inlet and outlet plena. In addition, an option has been added to employ higher-order modal kinetics, up to the first three neutronic modes (*i.e.* the fundamental and first two azimuthal neutronic modes).

It should be noted that extension of the Karve model to multiple channels and higher neutronic modes is not an original contribution of this work; such extensions have been implemented previously, *e.g.* by Karve [59] and Dokhane [16], among others. However, to the author's knowledge, previous analyses have been restricted to up to two thermal hydraulic channels and two neutronic modes (fundamental and first azimuthal), whereas the present study primarily employs four thermal hydraulic channels and three neutronic modes (fundamental and first and second azimuthal). In addition, as will be described below, there is an important difference in how the present study has linked the channels thermal hydraulically, via the inlet and outlet plena, as compared to the other studies mentioned, which have included either a constant total pressure drop across the core channels, or have included some treatment of the recirculation loop dynamics.

Description of the Original Karve Model

First, the original Karve model will be described, with the modifications performed for the present work described in the section to follow. A full description of the equations and assumptions for the original model is provided by Karve et al. [27]; however, a brief overview is provided here. The original model, for a single channel, consists of a system of nine nonlinear ordinary differential equations (ODEs) with the general form

$$\frac{\mathrm{d}\bar{X}(t)}{\mathrm{d}t} = F(\bar{X}(t);\kappa) \tag{6.1}$$

where $\bar{X}(t)$ is the vector of phase variables given by

$$\bar{X}(t) = \left[\mu(t), s(t), v(t), T_{1,1\phi}(t), T_{1,2\phi}(t), T_{2,1\phi}(t), T_{2,2\phi}(t), n(t), c(t)\right]^T \quad (6.2)$$

and κ is a vector of operating and design parameters. A description of each variable in $\bar{X}(t)$ is given in Table 6-1. Note that all variables contained in $\bar{X}(t)$ and κ are cast in dimensionless form for all calculations, as described in the original paper [27].

Table 6-1. Description of phase variables solved for in the original ROM by Karve

Variable	Description
$\mu(t)$	Axial location of boiling boundary
$s(t)$	Slope of quality in two-phase region
$v(t)$	Inlet velocity
$T_{k,1\phi}(t)$	kth expansion coefficient for fuel temperature in single-phase region ($k = 1,2$)
$T_{k,2\phi}(t)$	kth expansion coefficient for fuel temperature in two-phase region ($k = 1,2$)
$n(t)$	Neutron density
$c(t)$	Neutron precursor concentration

The thermal hydraulics treatment is based off of three underlying thermal hydraulics equations, to which a weighted residual method is applied to reduce the three partial differential equations (PDEs) to ODEs. Though higher-order approximations in space can and have been used for ROMs (*e.g.* by Dokhane [16]), the original Karve model used in this study relies on a first-order approximation in space for each thermal hydraulic variable.

The first ODE is derived from the single-phase energy equation, by approximating the single-phase temperature as a linear function of space and integrating from the channel inlet to the boiling boundary $\mu(t)$. A spatially-constant, time-varying heat flux $q''_{1\phi}(t)$ is assumed across this single-phase region, based on the difference of the fuel surface temperature $T_{s,1\phi}(t)$ and the average single-phase fluid temperature, multiplied by a heat transfer

coefficient based on the Dittus-Boelter correlation. The resulting expression is then solved for $\frac{\mathrm{d}\mu(t)}{\mathrm{d}t}$ in terms of the unknowns $\mu(t)$, $v(t)$ (inlet coolant velocity), and $T_{s,1\phi}(t)$.

The second ODE is derived from the mixture density equation, which is integrated from $\mu(t)$ to the channel outlet, assuming a separate (but still spatially constant) heat flux $q''_{2\phi}$ across this two-phase region, a spatially linear but time-dependent quality $x(z,t)$ defined by the expression $x(z,t) = s(t)[z - \mu(t)]$ (where z is the axial coordinate and $s(t)$ is a variable to be solved for), and with the mixture density determined based on the quality using the homogeneous equilibrium model (HEM) approximation [60]. The resulting expression is then solved for $\frac{\mathrm{d}s(t)}{\mathrm{d}t}$ in terms of the other unknowns.

The third ODE is derived by integrating the single- and two-phase momentum equations across the length of the channel and deriving expressions for gravitational, frictional, accelerational, and local pressure loss terms. Then, a fixed pressure drop boundary condition is applied by using the expression $\Delta P_{tot} = \Delta P_{ext}$, where ΔP_{tot} is the sum of all individual pressure drop components and ΔP_{ext} is a user-input value. The resulting expression is then solved for $\frac{dv(t)}{dt}$ in terms of the other variables.

The fuel temperature equations are obtained using the time-dependent cylindrical heat conduction equation with internal heat generation (treating the entire fuel pin as a single region in the radial direction). The method of variations is used, in which a functional based on the conduction equation is defined and minimized using a two-piece quadratic trial function for each region (single- and two-phase) separately. This minimization results in two ODEs in each region, in terms of the two expansion coefficients $T_{1,j\phi}(t)$ and $T_{2,j\phi}(t)$ ($j = 1$ for the single-phase region and $j = 2$ for the two-phase region) and with constant coefficients based on the fuel geometry and material properties, as well as the convective heat transfer coefficient between fuel and coolant.

The final two equations are the standard point kinetics equations using a one-delayed-group approximation, given by

$$\frac{\mathrm{d}n(t)}{\mathrm{d}t} = \frac{\rho(t) - \beta}{\Lambda} n(t) + \lambda c(t)\,, \tag{6.3}$$

and

$$\frac{\mathrm{d}c(t)}{\mathrm{d}t} = \frac{\beta}{\Lambda} n(t) - \lambda c(t)\,, \tag{6.4}$$

where all variables have their usual meaning in point kinetic theory (see, *e.g.*, Ott [19]). The reactivity term $\rho(t)$ is given by

$$\rho(t) = \rho_0^S + c_1 \Delta\alpha(t) + c_2 \Delta T_{avg}(t)\,, \tag{6.5}$$

where ρ_s^0 is a user-input external reactivity term,

$$\Delta\alpha(t) = \alpha(t) - \alpha_0\,, \tag{6.6}$$

$\alpha(t)$ is the axially-averaged void fraction, α_0 is a reference void fraction value, c_1 is the user-input void reactivity coefficient,

$$\Delta T_{avg}(t) = T_{avg}(t) - T_{avg,0}\,, \tag{6.7}$$

$T_{avg}(t)$ is the axially-averaged fuel temperature, $T_{avg,0}$ is a reference fuel temperature value, and c_2 is the user-input fuel temperature (Doppler) reactivity coefficient.

Modifications for the Present Study

For the present study, the original Karve model was implemented from scratch using MATLAB and MATLAB's symbolic toolbox. The original model was implemented as-is, except for a few key modifications for the specific application of the present study.

First, the equations and phase variables governing thermal hydraulics and fuel heat conduction were trivially extended to N channels, with each channel i being solved independently in complete analogy to the original single-channel treatment, with two exceptions: the conduction solution was reduced to a single-region problem (in the radial direction) for simplicity, and the inlet and outlet k-factor treatment was altered in a way that was unique to the multi-channel system, as discussed in the next section.

In addition, the neutron kinetics treatment was extended from simple point kinetics to multimodal kinetics, allowing for any number of neutronic modes M as specified by the user. The resulting system, the phase variables of which are shown in Table 6-2, consists of $(5N + 2M)$ equations. Note that all system parameters in vector κ remained unchanged from the single-channel case, except for the special inlet and outlet k-factor treatment, and the mass

flow rate $\dot{m}$, which is increased proportionally to N to maintain the same average flow rate per channel regardless of N. Thus, all N channels are defined with the same values (geometry, heat transfer coefficients, etc.) and have the same steady-state solution as each other.

Table 6-2. Description of phase variables solved for in the model as implemented in the current work.

Variable	Description
$\mu_i(t)$	Axial location of boiling boundary for channel i
$s_i(t)$	Slope of quality in two-phase region for channel i
$v_i(t)$	Inlet velocity for channel i
$T_{1,1\phi,i}(t)$	kth expansion coefficient for fuel temperature in single-phase region for channel i
$T_{1,2\phi,i}(t)$	kth expansion coefficient for fuel temperature in two-phase region for channel i
$n_m(t)$	Neutron density for neutronic mode m
$c_m(t)$	Neutron precursor concentration for neutronic mode m

In this chapter, all single-channel coupled cases used a single neutronic mode (fundamental), while all two-channel cases used two neutronic modes (fundamental and first azimuthal) and all four-channel cases used three neutronic modes (fundamental, first azimuthal, and second azimuthal).

Following the approach used by Dokhane [16], the equations governing the M neutronic modes are given by

$$\frac{\mathrm{d}n_m(t)}{\mathrm{d}t} = \frac{1}{\Lambda}\left[(\rho_m^s - \beta)n_m(t) + \sum_{l=0}^{M-1}\rho_{ml}(t)n_l(t)\right] + \lambda c_m(t), \quad m = 0, M-1 \tag{6.8}$$

and

$$\frac{\mathrm{d}c_m(t)}{\mathrm{d}t} = \frac{\beta}{\Lambda} n_m(t) - \lambda c_m(t), \qquad m = 0, M-1 \tag{6.9}$$

where $n_m(t)$ is the amplitude of neutronic mode m, $c_m(t)$ is the precursor concentration for neutronic mode m, ρ_m^s is the static reactivity for mode m (with $\rho_0^s = 0$), and ρ_{ml} is a reactivity term for the coupling between mode m and mode l.

Again using the notation of Dokhane [16], the reactivity coupling terms are given by

$$\rho_{ml}(t) = \sum_{i=0}^{N} WD_{ml}^{(i)} \left(c_1 \Delta\alpha_i(t) + c_2 \Delta T_{avg,i}(t) \right) \tag{6.10}$$

where

$$WD_{ml}^{i} = \frac{\langle \phi_m^*(\vec{r}), \phi_n(\vec{r}) \rangle^{(i)}}{\langle \phi_m^*(\vec{r}), \phi_m(\vec{r}) \rangle} \tag{6.11}$$

$$\Delta\alpha_i(t) = [\alpha(t)]_i - \alpha_0 \tag{6.12}$$

ϕ_m and ϕ_m^* are the shape functions for the static forward and adjoint flux, respectively, of mode m, i is the channel index, and N is the total number of channels. The notation $\langle \cdot \rangle$ denotes spatial integration over the entire domain, while $\langle \cdot \rangle^{(i)}$ denotes integration over the spatial region corresponding to the ith channel only.

For all cases performed in this work, the N channels are always assumed to be identical to each other in terms of geometry and other operating parameters; thus, considering at most 4 channels, an analogous expression for WD_{ml}^{i} can be written in terms of vector dot products without needing any detailed knowledge of the actual spatial flux shape within each assembly node. For example, for the most complicated case of $N = 4$ and $M = 2$ (four channels and three neutronic modes), one can write

$$\vec{\phi}_0 = \vec{\phi}_0^* = [1, 1, 1, 1] \tag{6.13}$$

$$\vec{\phi}_1 = \vec{\phi}_1^* = [-1, 1, -1, 1] \tag{6.14}$$

$$\vec{\phi}_2 = \vec{\phi}_2^* = [-1, -1, 1, 1] \tag{6.15}$$

and then each term of WD_{ml}^{i} can be calculated using

$$WD_{ml}^{i} = \frac{\phi_{m,i}^* \phi_{l,i}}{(\vec{\phi}_m^*) \cdot (\vec{\phi}_m^*)} = \frac{\phi_{m,i}^* \phi_{l,i}}{4} \tag{6.16}$$

where $\phi_{m,i}$ (a scalar) is the ith component of $\vec{\phi}_m$ (*i.e.* corresponding to channel i). Note that the three vectors $\vec{\phi}_m$ in Eqs. (6.13)-(6.15) are mutually orthogonal (as they must be, by definition); and, using the channel radial numbering scheme shown in Figure 6-1 (which was the same numbering scheme used in 0), one can visualize mode 0 as being the fundamental mode, mode 1 being the "east-west" mode, and mode 2 being the "north-south" mode. Note that for 1-mode, 1-channel problems, $\vec{\phi}_0 = \vec{\phi}_0^* = [1]$; while for 2-mode, 2-channel problems, $\vec{\phi}_0 = \vec{\phi}_0^* = [1, 1]$ and $\vec{\phi}_1 = \vec{\phi}_1^* = [-1, 1]$.

1	2
3	4

Figure 6-1 – Channel radial numbering scheme for the 4-channel problem.

The values for all physical and operating parameters were the same as used by Karve et al. [27]. Note that one important value (n_0, a reference neutron density value) was not provided explicitly in the original paper; however, the value was deduced from information provided by Dokhane [16] which used the same Karve model as a starting point. Using the deduced value, the steady-state results matched those of Karve et al.; thus, it was determined to be the same value Karve et al. used, as a different value of n_0 would have altered the steady-state solution.

One additional difference in the current model compared to the original Karve model involves the use of α_0 and $T_{avg,0}$, a reference void fraction and average fuel temperature, respectively, based on typical BWR operating conditions. These values, not explicitly provided by Karve et al., are used in Eqs. (6.6) and (6.7), respectively, and affect the steady-state reactivity values calculated by the model. In the original Karve model, the α_0 and $T_{avg,0}$ were set at fixed values across all cases, and the value of ρ_s^0 in Eq. (6.5) was manually input as an operating parameter which will affect the steady-state conditions. The steady-state neutron density, $\tilde{n}$, as well as the other steady state values are calculated based on the chosen values of N_{sub} and ρ_s^0.

However, since no specific values for α_0 and $T_{avg,0}$ were provided, a slightly different approach was used in the current model: ρ_s^0 was set equal to zero for all cases, $\tilde{n}$ was manually input to a pre-chosen value, and α_0 and $T_{avg,0}$ were calculated and set equal to the actual steady-state conditions calculated by the model for each case. Thus, rather than pre-defined values for α_0 and $T_{avg,0}$ and case-dependent ρ_s^0 and $\tilde{n}$ values, pre-defined ρ_s^0 and $\tilde{n}$ values and case-dependent α_0 and $T_{avg,0}$ values were used. This amounts to nothing more than a change of conventions; one could easily convert from one convention to the other with no change in steady-state or transient results – but only if one knows the values for α_0 and $T_{avg,0}$ used by Karve et al. However, not knowing these values, it is not possible to know ahead of time which values of α_0 and $T_{avg,0}$ corresponded to which values of ρ_s^0. For example, Karve et al. show plots of the stability boundary as a function of ρ_s^0 (termed ρ_{ext} in that paper) on the x-axis and N_{sub} on the y-axis, but if one changes the values of α_0 and $T_{avg,0}$ the stability boundary would shift either left or right along the x-axis; thus, it was not meaningful to directly compare results for the current model with results presented by Karve et al., since the location on the x-axis is unknown when comparing the two.

All calculations in this chapter were performed using MATLAB. Eigenvalues, eigenvectors, and steady-state solutions were obtained using the Symbolic Toolbox package in MATLAB, while numerical solutions of the system of ODEs was carried out using MATLAB's built-in *ode23* function (a one-step second-order Runge Kutta method); this was chosen above other built-in ODE solvers as it gave the best accuracy and numerical robustness for the problems calculated in this chapter. A relative tolerance of 10^{-6} was used, as any tolerances smaller than this showed no noticeable change in the solution.

One additional difference in the model as implemented in MATLAB (versus the original implementation as described by Karve et al.) was in the use of a simple limiter which set any negative values for the phase variables to zero, preventing negative solutions. This proved necessary for the problems shown in this chapter, as the limit cycles often had large enough amplitudes to give negative velocities during a portion of the oscillation period; in almost every case, this very quickly led to a solution that quickly diverged to infinity in either direction. This was most often linked to $\mu_i(t)$ becoming either less than zero or greater than unity, which

violates the assumption of a two-region problem with a boiling boundary between zero and one. Thus, the velocity (and other parameters) were prevented from going below zero, and this gave a stable solution in all cases thereafter (with $\mu_i(t)$ never exceeding unity under these conditions).

It should be noted that the use of limiters has the effect of "truncating" the limit cycle oscillations and restricting the limit cycle amplitude below what it would otherwise have been; however, as will be shown, the limit cycles still behaved qualitatively as expected, and the qualitative conclusions drawn from this study were not affected by the use of these "artificial" limiters.

Inlet and Outlet Plena Loss Factors

As will be shown in the next section, applying a fixed pressure drop boundary condition from only the inlet to the outlet of each channel prevents any coupling between channels, at least when neutronics are disabled. In a real BWR, though, the channels are coupled thermal-hydraulically through the inlet and outlet plena, which has a flow rate equal to the sum of the flow rates in all channels at the channel inlet and outlet, respectively. By including a pressure drop term which operates on the total core flow rate, a mechanism is created by which the channels may be coupled to each other.

In the present work, the pressure loss for the inlet plenum is termed ΔP_{below} and is applied as a concentrated pressure loss with a local loss factor k_{below} as given by

$$\Delta P_{below}(t) = k_{below}\rho_l v_{inlet,avg}^2(t)\,, \tag{6.17}$$

where ρ_l is the single-phase liquid density, and $v_{in,avg}(t)$ is the time-dependent average inlet velocity given by

$$v_{inlet,avg}(t) = \frac{1}{N}\sum_{i=1}^{N} v_i(t)\,, \tag{6.18}$$

where N is the total number of channels and $v_i(t)$ is the inlet velocity for channel i.

The pressure loss for the outlet plenum, termed ΔP_{above}, is also applied as a concentrated pressure loss using a local loss factor k_{above} and the expression

$$\Delta P_{above}(t) = k_{above}\rho_{above}(t)v_{above}^2(t)\,, \tag{6.19}$$

where $\rho_{above}(t)$ is the mixture density for the outlet plenum and $v_{above}(t)$ is the mixture velocity for the outlet plenum. Their values are calculated from the following expressions:

$$x_{above}(t) = \frac{\sum_{i=1}^{N}\rho_{exit,i}(t)v_{exit,i}(t)x_{exit,i}(t)}{\sum_{i=1}^{N}\rho_{exit,i}(t)v_{exit,i}(t)}, \tag{6.20}$$

$$\rho_{above}(t) = \frac{1}{1+\frac{x_{above}(t)}{N_\rho N_r}}, \tag{6.21}$$

and

$$v_{above}(t) = \frac{\frac{1}{N}\sum_{i=1}^{N}\rho_{exit,i}(t)v_{exit,i}(t)}{\rho_m}, \tag{6.22}$$

where $x_{above}(t)$ is the mixture quality in the outlet plenum, and N_ρ and N_r are dimensionless numbers given in the original model by Karve et al. [27]. These expressions for mixture qualities are derived from simple conservation of mass and energy relations for two-phase flow [60].

Note that, for this model, the *average* velocity among channels is used for calculating the inlet and outlet plenum loss terms, rather than the *sum* of the channel velocities. This is done for the sake of convenience: when ΔP_{below} is defined based on average velocities, increasing k_{below} by some amount gives the same steady-state pressure drop as increasing k_{inlet} in each channel by that same amount. This makes maintaining the same steady-state solution among cases easy, since one need only ensure that the value of $(k_{below} + k_{inlet})$ stays constant between cases to ensure that $(\Delta P_{below} + \Delta P_{inlet})$ stays constant (hence the same steady-state solution to match the same total system pressure drop). The same is true for the outlet as well. This would not be the case, however, if ΔP_{below} or ΔP_{above} were defined based on total velocities rather than average velocities, leading to a slightly less convenient requirement for maintaining the same steady-state conditions. Physically, using the average velocities is analogous to increasing the flow area of the inlet and outlet plena by a factor of N (the total number of channels), such that the steady-state inlet and outlet plena velocities are the same as the average channel inlet and outlet velocities, respectively.

Nomenclature for Case Indexing

For the ensuing sections, the following nomenclature will be used to denote cases: 'S' for standalone TH cases or 'C' for coupled neutronic-TH cases, followed by the number of channels in the model, and then a unique letter for each case within that category. For example, Case S-1A is the first single-channel standalone case presented, Case S-1B is the second single-channel standalone case presented, and so on.

6.2 Initial Coupled Results

Table 6-3 shows the steady-state values calculated for the single-channel model, named Case C-1A, with $N_{sub} = 1.5$ and $\tilde{n} = 1.69$. These values correspond exactly to the values calculated by Karve et al. [27] for the same conditions. The eigenvalues calculated for this case are shown in Table 6-4. The highest real component belonged to the pair of eigenvalues $0.263 \pm 7.840i$; as described in Section 0, this corresponds to a growing exponential with a time constant of 0.263, multiplied by a sinusoidally-varying amplitude function with frequency 7.840. Thus, this operating point was found to be unstable according to the model. Karve et al. also reported this point being unstable, albeit with a real component likely closer to 0.0 (*i.e.* near the stability boundary), though the actual value was unspecified. Note that the eigenvalue is given in dimensionless terms; if converted to dimensional form, the value becomes $(0.185 \pm 5.495i)$ s^{-1}. This imaginary component corresponds to an oscillation period of 1.14 s. The oscillation frequency at this point was unspecified by Karve et al., but a nearby point had a frequency of approximately 1.5 s. The difference in eigenvalue between the two models might possibly be accounted for by a shift brought on by a different definition of α_0 and $T_{avg,0}$, as described above, and perhaps by the use of a single radial fuel region in the current work rather than the more complicated two-region treatment used by Karve et al., which would account for some difference in transient behavior.

Table 6-3. Steady-state values for all phase variables in the single-channel model, for $N_{sub} = 1.5$

Variable	Steady-state value
$\tilde{\mu}$	0.231
$\tilde{s}$	0.350
$\tilde{v}$	0.878
$\tilde{n}$	1.69
$\tilde{c}$	2957

Table 6-4. Eigenvalues for Case C-1A and Case S-1A

Case C-1A	Case S-1A
0.264+7.840i	0.000
0.264-7.840i	-0.300
-0.112	-0.315
-0.301	-4.275-5.852i
-9.759	-4.275+5.852i
-68.020	-68.075
-199.465	-199.889

6.3 Standalone TH Results

Single-Channel Standalone TH Results

A simple change to the base single channel model was made, to convert the problem to a standalone TH problem: the feedback coefficients c_1 (moderator density feedback coefficient) and c_2 (fuel temperature feedback coefficient) were both set to zero. The steady-state neutron density $\tilde{n}$ was still set to the same value of 1.69 as before; however, with both reactivity feedback coefficients set to zero, the total reactivity will remain zero regardless of the fuel temperature or coolant density (based on Eqs. (6.8)-(6.10)). Given this, and with the initial neutron density and precursor concentration set to the proper steady-state values, $n(t)$ will remain constant over time; and therefore the heat flux to the coolant will remain at the same constant value at all times as well (since the heat generation rate in the fuel is proportional to $n(t)$, and the fuel temperature profile also remains constant over time).

This results in a standalone TH simulation with a time-invariant heat flux into the coolant. Since this heat flux is the same as for the coupled steady-state conditions, the steady state values for the standalone TH case are the same as those given in Table 6-3 for the coupled case; the only difference is in the transient behavior, reflected in the eigenvalues of the problem. For this standalone TH case, denoted Case S-1A, the maximum real component belonged to an eigenvalue of 0.000 – this eigenvalue did not occur previously, and only arose due to the fact that the TH fields no longer had any effect on neutronics, hence giving neutral stability. However, as shown in Table 6-4, the only non-real-valued eigenvalues were the complex pair $-4.275 \pm 5.853i$, which corresponded to the oscillatory mode but with a strongly negative real component, indicating a very stable system. Hence, it is seen that the neutronic feedback has a strongly destabilizing effect, since the oscillatory eigenvalue had a real component of 0.263 when neutronic feedback was included.

For the ensuing studies on standalone TH instabilities, conditions needed to be found in which the channel was unstable due to TH feedback alone. However, to maintain consistency across all cases, both standalone and coupled, it was desired to keep the same steady-state conditions for the phase variables as given in Table 6-3. In order to maintain the same steady-

state conditions while also making the system unstable, the local pressure loss factors (k-factors) k_{inlet} and k_{exit}, for the inlet ($z = 0$) and outlet ($z = 1$) of the channel, respectively, were adjusted.

As explained in Section 2.1, the stability behavior of a system is closely related to the ratio of the pressure drop in the two-phase region to the pressure drop in the single-phase region. Therefore, all other things being equal (*i.e.* maintaining the same steady-state velocities, etc.), increasing the value of k_{outlet} destabilizes the system, while increasing the value of k_{inlet} stabilizes the system, and vice versa.

In order to select suitable points on the stability boundary, a series of candidate k_{exit} values were chosen, and k_{inlet} was adjusted iteratively using the secant method until the eigenvalue pair corresponding to density-wave oscillations had a real component of zero (with a tolerance of 10^{-6}). Results are shown in Table 6-5. Note that all cases had the same steady-state values for all phase variables (as given in Table 6-3), despite the total pressure drop ΔP_{tot} being different in each case. This was achieved by setting $\tilde{v} = 0.878$ and solving for ΔP_{ext} (external pressure drop, equal to ΔP_{tot} in steady-state conditions) in the script using Matlab's symbolic toolbox, rather than imposing a fixed ΔP_{ext} and solving for $\tilde{v}$ as was done in previous cases.

The original case, using the default values of $k_{inlet} = 15.0$ and $k_{exit} = 2.5$ as provided by Karve et al., is shown first in Table 6-5, followed by the cases on the stability boundary. As can be seen in the table, and in Figure 6-2, there exists a near-linear relationship between the k_{exit} value and the corresponding k_{inlet} value needed to reach the stability boundary. Furthermore, it is seen from the figure that, for a given value of k_{exit}, an increase in k_{inlet} reduces the eigenvalue. This confirms that a decrease in the two-phase to single-phase pressure drop ratio has a stabilizing effect on the system, and vice versa.

The ratio of two-phase to single-phase pressure drop (including all friction, gravitational, accelerational, and local pressure drop components for each region) for each of the $\mathrm{Re}[eig] = 0.0$ cases is shown in Figure 6-3. It can be seen that there is not one fixed ratio governing the stability of a single TH channel using this model for all cases; rather, the ratio changes from case to case. However, the overall trend of increased stability with an increasing k_{inlet} value, and

decreased stability with an increased k_{exit} value, is observed, as a larger and larger k_{inlet} value was needed to compensate for the increasing k_{exit} values.

Ultimately, for the standalone TH studies to follow, the case highlighted in red in Table 6-5 was chosen, with a k_{inlet} value of 2.82 and k_{exit} value of 4.54; this was chosen because it gives very nearly the same total pressure drop ΔP_{tot} across the channel as for the base case of $k_{inlet} = 15$ and $k_{exit} = 2.5$. The single-channel case using a k_{inlet} value of 2.82 and k_{exit} value of 4.54 will be hereafter referred to as Case S-1B.

Table 6-5. Cases used for finding the stability boundary versus k_{inlet} and k_{exit} for the single-channel standalone TH model. The case highlighted in red is termed Case S-1B.

k_{exit}	$\mathrm{Re}[eig] = -0.3$	$\mathrm{Re}[eig] = 0.0$	$\mathrm{Re}[eig] = 0.3$
0	0.612	0.344	0.083
2.5	2.238	1.798	1.381
4.5388	**3.404**	**2.821**	**2.275**
10	6.350	5.380	4.482
20	11.567	9.881	8.332
30	16.728	14.322	12.119

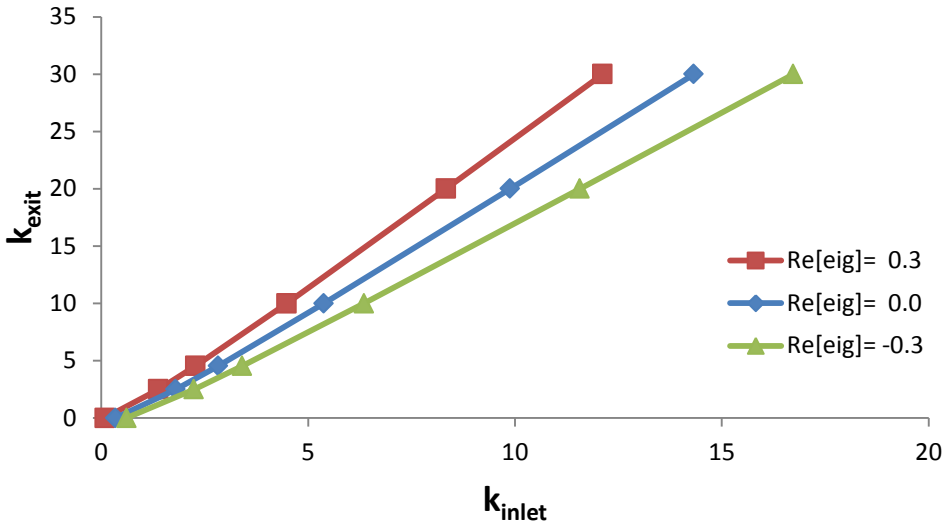

Figure 6-2 – Values of k_{exit} versus k_{inlet} needed to achieve an eigenvalue with a maximum real component of -0.3, 0.0 and 0.3, respectively, for the single-channel standalone TH model.

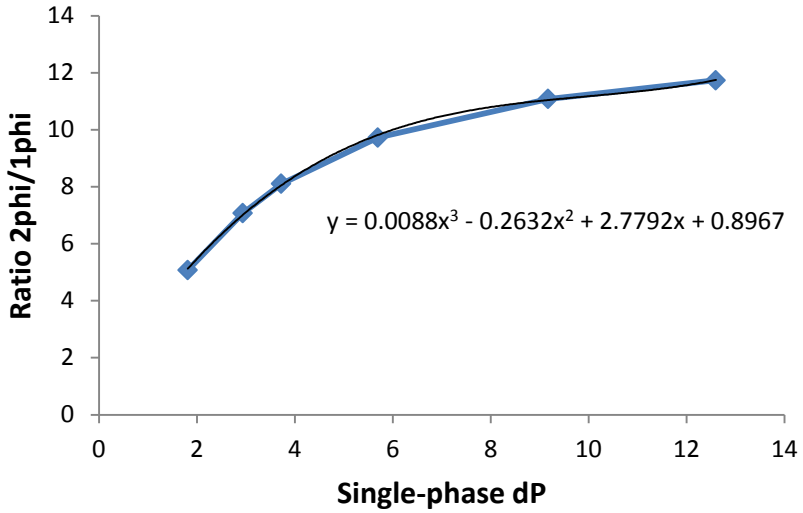

Figure 6-3 – Ratio of total pressure drop in the two-phase region to total pressure drop in the single-phase region, for different values of ΔP_{inlet} and ΔP_{exit} to give a maximum eigenvalue of 0.0 (real component).

Two-Channel Standalone TH Results

The single-channel standalone TH model used in the previous subsection was extended to a two-channel model with the same setup in each channel. That is, the two channels were identical to the previous single channel, and the total mass flow rate was doubled to give the same flow rate per channel to once again maintain the same steady-state conditions shown in Table 6-3.

Eigenvalues for the two-channel case, denoted Case S-2A, are shown in Table 6-6, along with those for the single-channel case, Case S-1B. Each eigenvalue from the single-channel case appears twice in the two-channel case. Furthermore, for each repeated eigenvalue, one eigenvector has nonzero components for the first channel variables and zeros for the second channel variables, while the opposite is true for the other eigenvector in the pair. This indicates that the two channels have the same characteristics but are completely independent from each other – any change in the values in one of the channels has no effect on the other channel.

This is shown in a numerical simulation performed for the two-channel case, in which a small perturbation from steady-state conditions is applied to Channel 1 but no such perturbation is applied to Channel 2. The results, shown in Figure 6-4, reveal that no coupling exists between Channel 1 and Channel 2; if coupling did exist, the oscillations in Channel 1 would have influenced Channel 2 and caused a departure from steady-state conditions, but this was not the case. This is to be expected because all pressure drop terms affecting Channel 1 were determined solely by Channel 1 parameters (velocity, etc.), and vice versa for Channel 2.

Table 6-6. Eigenvalue comparison for Cases S-1B and S-2A.

One Channel	Two Channels
0.000	0.000
-0.000-8.091i	0.000
-0.000+8.091i	-0.000-8.091i
-0.300	-0.000-8.091i
-0.315	-0.000+8.091i
-41.488	-0.000+8.091i
-199.889	-0.300
	-0.300
	-0.315
	-0.315
	-41.488
	-41.488
	-199.889
	-199.889

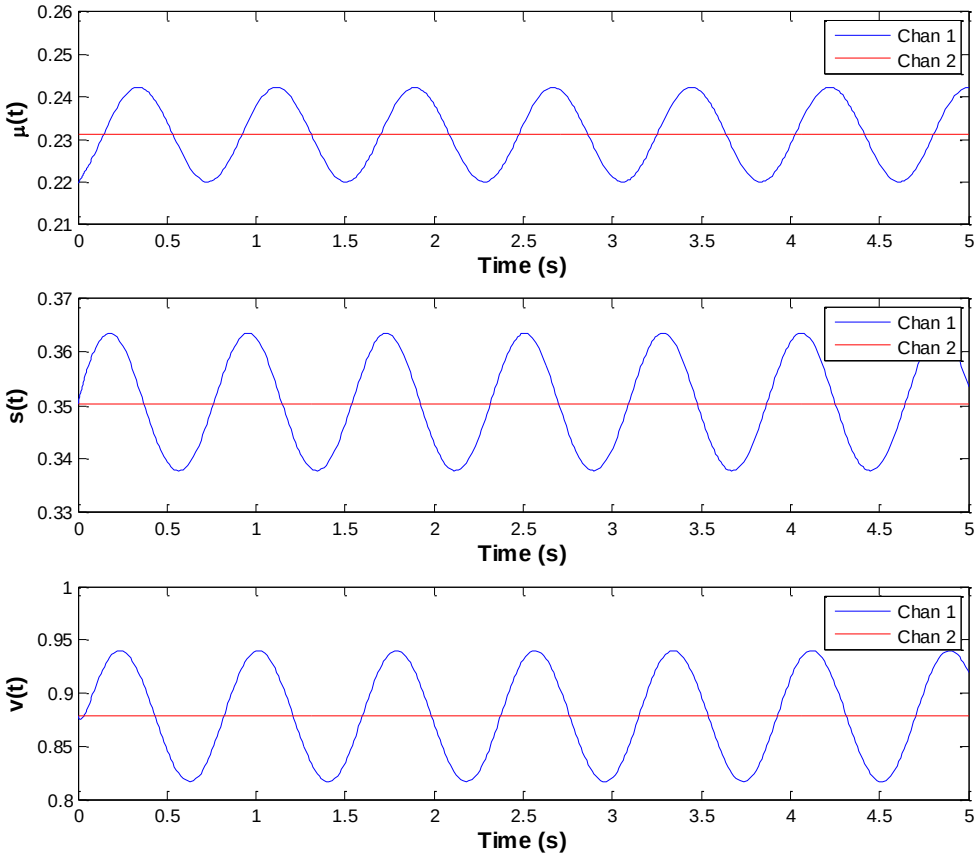

Figure 6-4 – Numerical solution for two channels with $k_{below} = k_{above} = 0$ and no initial perturbation from steady state conditions for Channel 2.

In light of these results, a new case was run, identical to Case S-2A except that k_{inlet} was decreased by 1.0 (from 2.82 to 2.72) while k_{below} was set to 1.0 (previously 0.0). Recall from the discussion around Eq. (6.17) that the steady-state solution will remain the same as long as the sum $(k_{below} + k_{inlet})$ remains constant across the different cases, which is true here. Hence, once again, the steady-state values for each channel were the same as those given in Table 6-3.

However, the redistribution of some pressure drop from ΔP_{inlet} to ΔP_{below} had an important impact on the stability characteristics of the system. The eigenvalues for this new case, shown in Table 6-7, reveal that Case S-2B has an unstable eigenvalue pair with a positive real component of 0.054, and this eigenvalue pair corresponds to out-of-phase oscillations. This was determined by recasting the eigenvectors for this eigenvalue pair in real form (as

shown in Section 0) and calculating the phase shift between the Channel 1 and Channel 2 velocity components. A phase shift of $180°$ indicates out-of-phase oscillations, while a phase shift of $0°$ indicates in-phase oscillations.

The physical reason for Case S-2B to be out-of-phase unstable, while Case S-2A was neutrally stable, is as follows. For the in-phase oscillation mode (in Case S-2B), where both channels oscillate identically, we have $v_1(t) = v_2(t) = v_{inlet,avg}(t) \equiv v(t)$. Therefore, we can write $\Delta P_{below}(t) = \frac{1}{2} k_{below} v^2(t)$ and $\Delta P_{inlet,1}(t) = \Delta P_{inlet,2}(t) = \frac{1}{2} k_{inlet} v^2(t)$; and, combining the two, we have $\Delta P_{below} + \Delta P_{inlet,i} = \frac{1}{2}(k_{below} + k_{inlet}) v^2(t)$ for $i = 1,2$. Finally, using the fact that $k_{below} + k_{inlet}$ for Case S-2B is the same as $k_{below} + k_{inlet}$ for Case S-2A, it follows that the total "inlet" pressure drop $\Delta P_{below} + \Delta P_{inlet,i}$ for Case S-2B is the same as the total inlet pressure drop $\Delta P_{inlet,i}$ for Case S-2A (with $\Delta P_{below} = 0$) for each channel i.

This means that, for the in-phase oscillation case, each channel oscillates in precisely the same fashion as for the single-channel model of Case S-1B. This is reflected in the eigenvalue pair $0.000 \pm 8.091i$ which is the same in both cases, the only difference being that this eigenvalue pair has two channels oscillating in-phase for Case S-2B but just a single channel for Case S-1B. Note that Case S-2A also had this eigenvalue pair (occurring twice), but in that case each pair corresponded to one channel or the other, not both oscillating in-phase.

Returning to Table 6-7, one finds an additional eigenvalue pair $0.563 \pm 8.106i$ which, upon extracting the phase shifts as described above, was determined to be an out-of-phase oscillation mode (the two channels being $180°$ out-of-phase with respect to each other). The key finding is that the real component of this eigenvalue pair is positive (*i.e.* larger than that of the in-phase mode).

Physically, this is due to the fact that the average inlet velocity remains constant in time for the out-of-phase oscillation mode, *i.e.* $v_{inlet,avg}(t) = \tilde{v}$ (the steady-state inlet velocity for each channel)[3]. This means that $\Delta P_{below}(t)$ remains constant in time as well, *i.e.* $\Delta P_{below}(t) = \widetilde{\Delta P_{below}}$ (the steady-state ΔP_{below} value for each channel). From an individual channel

[3] This is not strictly true for the general case of nonlinear oscillations, such as those obtained through solution of the nonlinear ODEs. However, for calculation of the eigenvalues, a linearized system is solved, and for this system the average velocity *is* strictly constant in time since the channels oscillate as simple sinusoids (growing or decaying exponentially) and the oscillations cancel each other when they have a $180°$ phase shift and are summed together.

viewpoint, this is equivalent to reducing the total channel pressure drop by an amount equal to $\Delta\widetilde{P_{below}}$ and likewise reducing k_{inlet} by an amount equal to k_{below}. In other words, the pressure drop in the single-phase region is reduced, while the pressure drop in the two-phase region is unaffected. Again, this is due to ΔP_{below} not oscillating when in the out-of-phase mode, thus it does not participate in the dynamic behavior of the system.

Since the single-phase pressure drop is reduced relative to the two-phase pressure drop (while maintaining the same steady-state conditions), the system is less stable in this mode. This is due to the phase delay added by the two-phase region, as discussed in Section 2.1 and also corroborated by the results in Figure 6-2, which shows that a decreased k_{inlet} value has a destabilizing effect and vice versa.

Table 6-7. Eigenvalues for Case S-2B

Eigenvalue	Oscillation Type
0.563+8.106i	Out-of-phase
0.563-8.106i	Out-of-phase
0.000	-
0.000	-
-0.000+8.091i	In-phase
-0.000-8.091i	In-phase
-0.300	-
-0.300	-
-0.315	-
-0.315	-
-39.150	-
-41.488	-
-199.889	-
-199.889	-

Results for the numerical simulation of Case S-2B for the first 20 seconds of the transient are shown in Figure 6-5. As for Case S-2A, the Channel 2 variables were given no initial perturbation from their steady-state values; however, unlike for Case S-2A, the Channel 2 variables for Case S-2B began oscillating visibly within the first one or two periods. This confirms that a coupling mechanism now exists between the channels, as the oscillations in Channel 1 are directly causing a change in the Channel 2 behavior. As discussed above, this is

due to a nonzero response in $\Delta P_{below}(t)$ which couples the channels by operating on the average channel velocity.

For the case, the limit cycle was achieved within approximately 7 seconds from the start of the transient. The results are qualitatively similar to those shown in, for example, Figure 5-2, which gives confidence in the basic ability of the ROM to capture the relevant limit cycle physics.

Figure 6-6 gives a zoomed-in view of the oscillations for a 5-second interval after a limit cycle has been reached, while Figure 6-7 shows the phase shift of Channel 2 relative to Channel 1 for the duration of the transient. The phase plot methodology was the same as used in 0. Note that, since the perturbations in Channel 2 were driven from the start by its response to Channel 1, the phase shift was close to the final value of $180°$ from the start.

Figure 6-8 and Figure 6-9 show the results for the same model, except with a different initial perturbation for Channel 2. As expected, the limit cycle eventually converged to the same $180°$ phase shift behavior with the same limit cycle amplitude for both cases regardless of the initial perturbation, though the behavior before that point was different. From here on out, multiple different perturbation schemes will be used, sometimes perturbing all channels in the same direction, sometimes in opposite directions (*i.e.* positive or negative), depending on what gives the clearest or most conclusive results.

It should be noted that it is theoretically possible to obtain a different limit cycle trajectory depending on the initial conditions chosen; such behavior was in fact noted by Karve et al. [27] using the same ROM upon which the current study is based. However, for most cases presented in the current study, multiple different initial conditions were attempted, but no cases were found in which the limit cycle behavior changed depending on the initial conditions. Though an attempt was made to study a wide range of cases and a range of different initial condition types, the possibility always remains that interesting or different results could be found in different points in the state space or with different initial conditions.

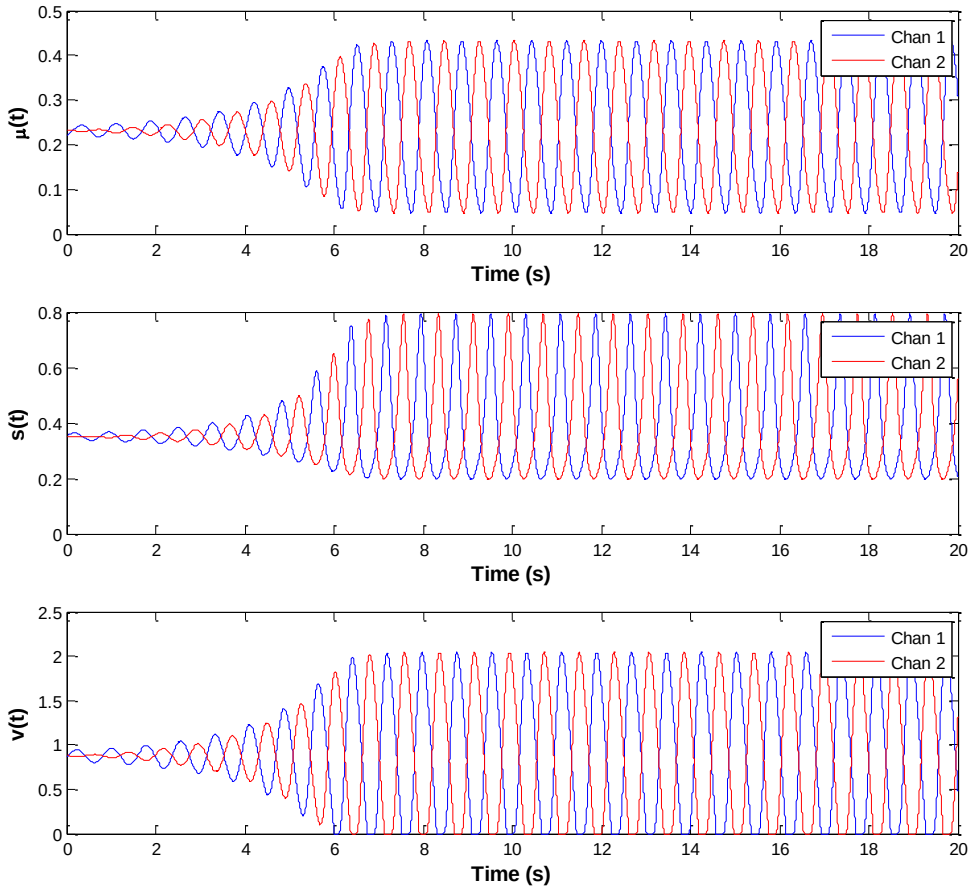

Figure 6-5 – Numerical solution from 0 seconds to 20 seconds for Case S-2B, using a +5% initial perturbation in Channel 1 (away from steady state values) and no initial perturbation in Channel 2.

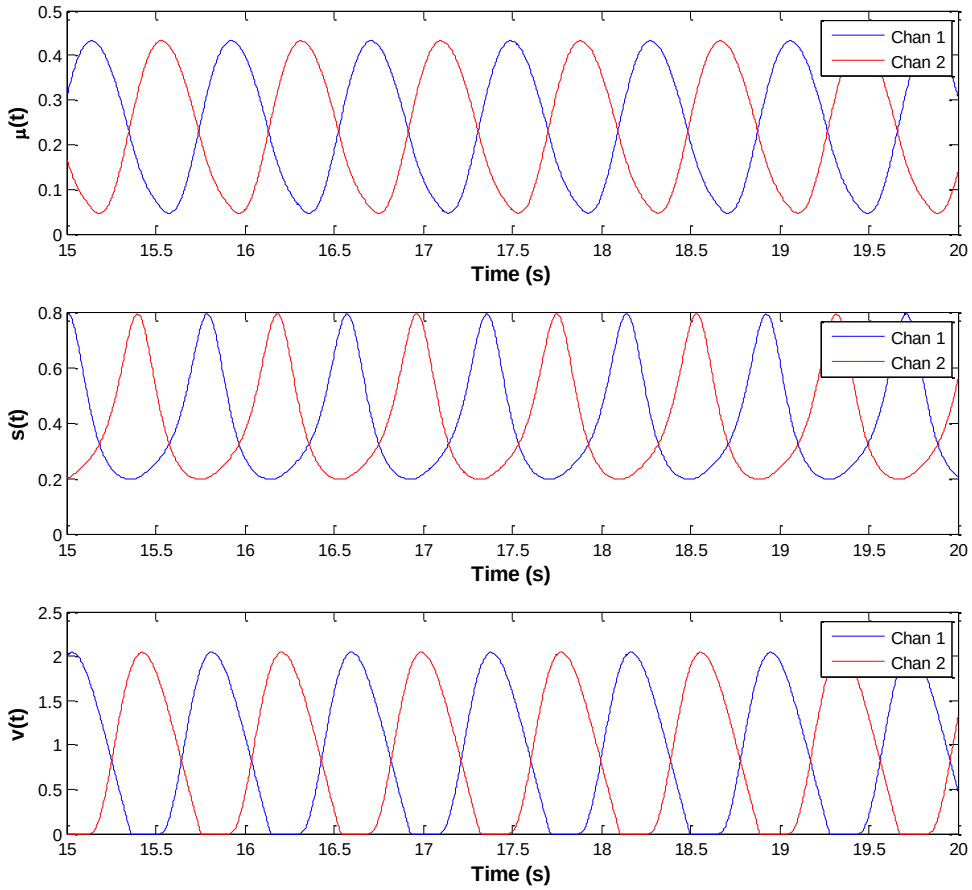

Figure 6-6 – Numerical solution from 15 seconds to 20 seconds for Case S-2B using a +5% initial perturbation in Channel 1 (away from steady state values) and no initial perturbation in Channel 2.

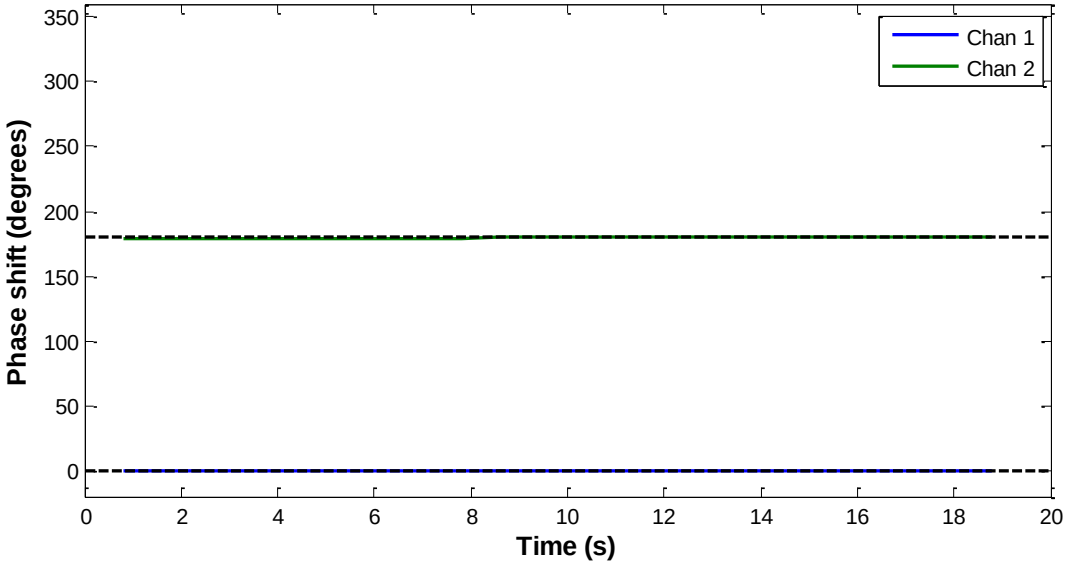

Figure 6-7 – Phase shift plot for Case S-2B.

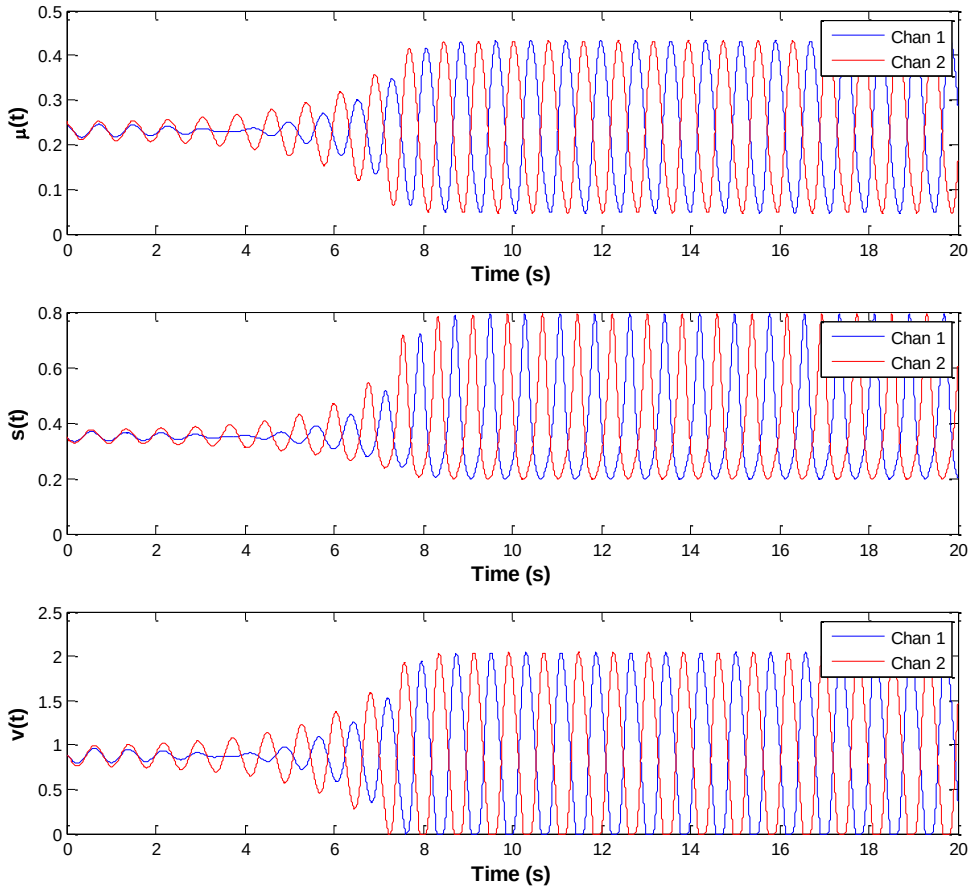

Figure 6-8 – Numerical solution from 0 seconds to 20 seconds for Case S-2B using a +5% initial perturbation in Channel 1 (away from steady state values) and a +7% initial perturbation in Channel 2.

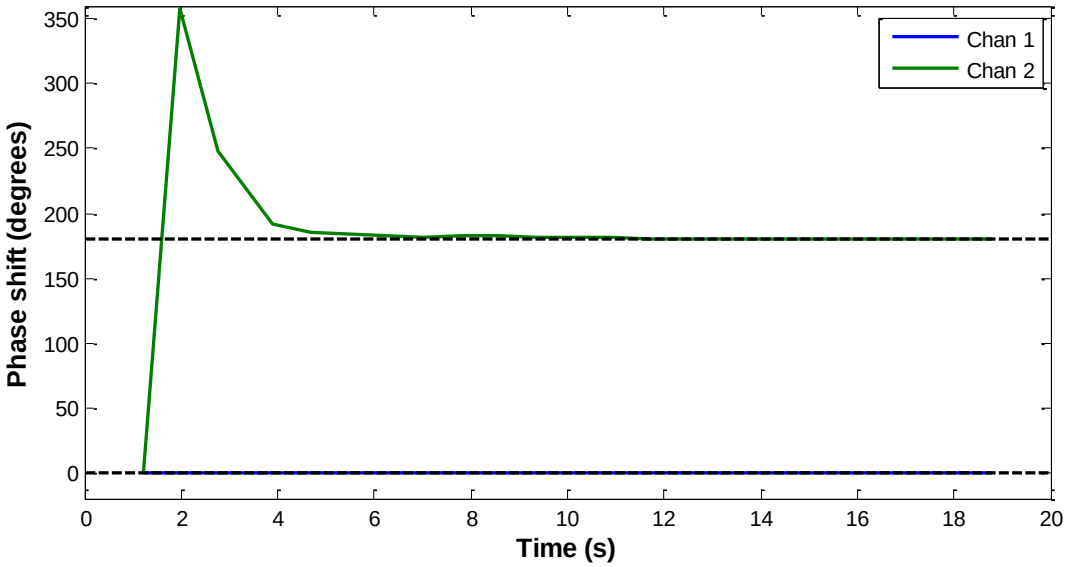

Figure 6-9 – Phase shift plot for Case S-2B, using a +5% initial perturbation in Channel 1 (away from steady state values) and a +7% initial perturbation in Channel 2.

A third 2-channel TH standalone case, Case S-2C, was run, in which k_{below} was set to 0 and k_{above} set to 1.0. As shown in Table 6-8, the out-of-phase mode now has a lower real eigenvalue component than the in-phase mode; this is explained by similar reasoning in terms of the single-phase and two-phase pressure drops as in Case S-2B. Specifically, for Case S-2C, setting k_{above} to 1.0 and decreasing k_{exit} by the same amount means that the two-phase pressure drop in the out-of-phase oscillation mode is decreased (since $\Delta P_{above}(t)$ does not oscillate in the out-of-phase mode). Thus, the two-phase pressure drop is decreased relative to the single-phase pressure drop, and a more stable system (*i.e.* smaller real eigenvalue component) results. Once again, the in-phase eigenvalue is unaffected, since $\Delta P_{above}(t)$ oscillates in-phase with $\Delta P_{exit}(t)$ and their sum is equal to the value of $\Delta P_{exit}(t)$ if k_{above} were set to 0.0 and k_{exit} were set to its full value (*i.e.* as in case S-1B or S-2A).

The numerical solution of Case S-2C is shown in . As expected, the system converged to an in-phase oscillatory behavior, with the out-of-phase mode decaying away over time. Not, however, that this case does **not** converge to a limit cycle over the 200 s duration of the transient; it merely appears to do so, since the dominant eigenvalue has a real component of -0.000002. In the long run, this slightly-negative eigenvalue would cause the system to

converge to a stable (non-oscillatory) state. The case is only shown here to confirm that the system does indeed tend toward in-phase oscillations; if the real component of the in-phase eigenvalue were positive, it would converge to an in-phase limit cycle.

Table 6-8. Eigenvalues for Case S-2C.

Eigenvalue	Oscillation Type
0.000	-
0.000	-
-0.000+8.091i	In-phase
-0.000-8.091i	In-phase
-0.289-7.929i	Out-of-phase
-0.289+7.929i	Out-of-phase
-0.300	-
-0.300	-
-0.315	-
-0.315	-
-37.445	-
-41.488	-
-199.889	-
-199.889	-

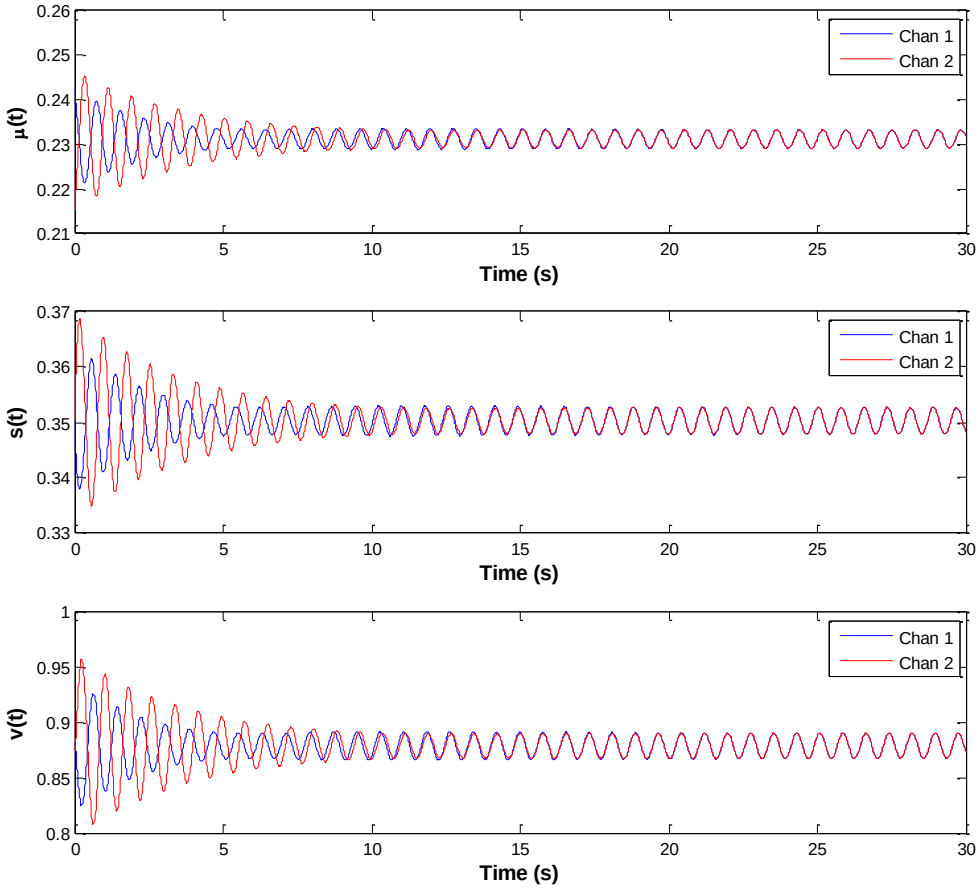

Figure 6-10 – Numerical solution from 0 seconds to 30 seconds for Case S-2C using a +5% initial perturbation in Channel 1 and a -7% initial perturbation in Channel 2.

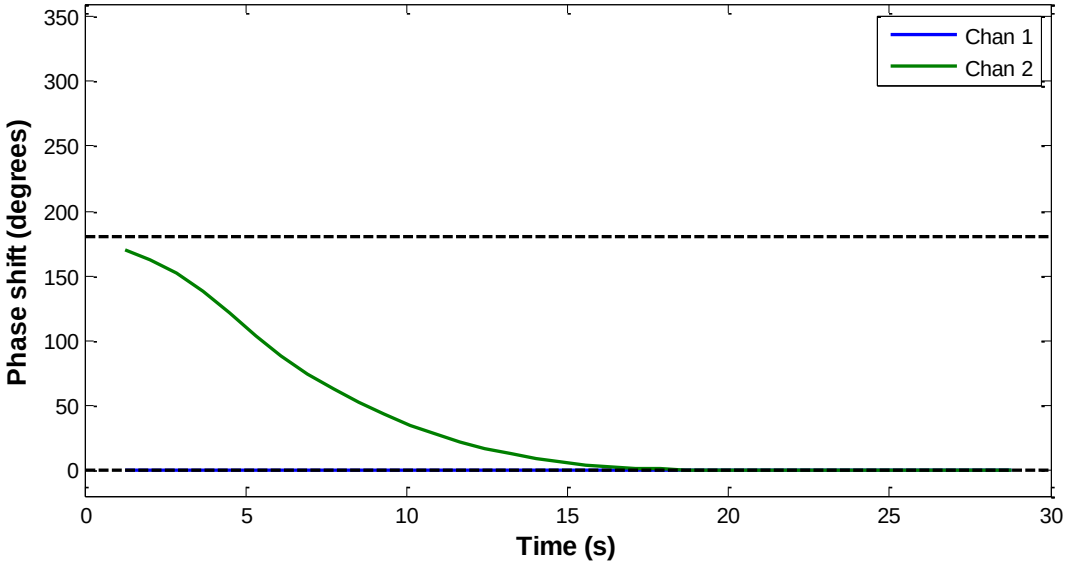

Figure 6-11 – Phase shift plot for Case S-2C, using a +7% initial perturbation in Channel 1 and a -5% initial perturbation in Channel 2.

Mathematically, one may also select negative values of k_{below}, k_{above}, or both. While not physically realistic, nonetheless it provides a useful check to see whether the physical reasoning explained above still holds. In Case S-2D, k_{below} was set to -1.0 while k_{inlet} was increased by 1.0 from the normal value; while in Case S-2E, k_{above} was set to -1.0 while k_{exit} was increased by 1.0 from the normal value. As expected, Case S-2D had a lower out-of-phase eigenvalue (real component) than in-phase, while Case S-2E had a higher out-of-phase eigenvalue (real component) than in-phase; the same reasoning can be applied as for cases S-2B and S-2C, respectively, albeit in reverse. The time-dependent plots for Cases S-2D and S-2E are omitted for brevity, as they show only the expected behavior (akin to Cases S-2C and S-2B for in-phase and out-of-phase, respectively).

An attempt was made to characterize the relationship between the value of k_{below} versus k_{above} (or $\Delta\widetilde{P_{below}}$ versus $\Delta\widetilde{P_{above}}$) needed to cross over from in-phase unstable to out-of-phase unstable. In other words, if $k_{below} = k_{above} = 0$, the in-phase and out-of-phase modes have the same real eigenvalue component; but if k_{below} (or $\Delta\widetilde{P_{below}}$) is increased, one wishes to know how much must k_{above} (or $\Delta\widetilde{P_{above}}$) be increased to maintain this same real eigenvalue component (0.000 in this case).

Table 6-9. Eigenvalues for Cases S-2D and S-2E.

Case S-2D		Case S-2E	
Eigenvalue	Oscillation Type	Eigenvalue	Oscillation Type
0.000	-	0.235+8.224i	Out-of-phase
0.000	-	0.235-8.224i	Out-of-phase
-0.000+8.091i	In-phase	0.000	-
-0.000-8.091i	In-phase	0.000	-
-0.300	-	-0.000+8.091i	In-phase
-0.300	-	-0.000-8.091i	In-phase
-0.315	-	-0.300	-
-0.315	-	-0.300	-
-0.503-8.032i	Out-of-phase	-0.315	-
-0.503+8.032i	Out-of-phase	-0.315	-
-41.488	-	-41.488	-
-43.947	-	-45.424	-
-199.889	-	-199.889	-
-199.889	-	-199.889	-

The results of this study are shown in Table 6-10 and Figure 6-12. A second-order polynomial curve fit revealed that the relationship between $\left(\frac{\Delta\widetilde{P_{above}}}{\Delta\widetilde{P_{2\phi}}}\right)$ versus $\left(\frac{\Delta\widetilde{P_{below}}}{\Delta\widetilde{P_{1\phi}}}\right)$ (where $\Delta\widetilde{P_{1\phi}}$ and $\Delta\widetilde{P_{2\phi}}$ are the overall pressure drop in the single-phase and two-phase regions, respectively) needed to balance to in- and out-of-phase modes was not precisely linear, though it was relatively nearly so. In other words, for small values of k_{below} and k_{above}, the stability threshold between the in- and out-of-phase modes for this particular case can be expressed roughly as

$$\left(\frac{\Delta\widetilde{P_{above}}}{\Delta\widetilde{P_{2\phi}}}\right) \approx C\left(\frac{\Delta\widetilde{P_{below}}}{\Delta\widetilde{P_{1\phi}}}\right) \tag{6.23}$$

where C in this case takes on the value 1.5. However, this value is certainly case-dependent, and operating conditions far from these would likely give a significantly different value of C. Thus, Eq. (6.23) is written more for qualitative understanding of the physical phenomena, rather than a precise quantitative prescription. At the very least, one can say with confidence that the value of C is positive – it follows from the discussion above that an increase in $\Delta\widetilde{P_{below}}$ must be matched by an increase in $\Delta\widetilde{P_{above}}$ to maintain equal stability for the in- and out-of-phase modes.

Table 6-10. Value of k_{below} versus k_{above} needed to achieve the same in-phase and out-of-phase real eigenvalue components (both 0.000), using Case S-2A as a starting point.

k_{below}	$\left(\frac{\Delta\widetilde{P_{above}}}{\Delta\widetilde{P_{1\phi}}}\right)$	k_{above}	$\left(\frac{\Delta\widetilde{P_{above}}}{\Delta\widetilde{P_{2\phi}}}\right)$	$\mathrm{Re}[eig]$
0.000	0.000	0.000	0.000	0.000
0.493	0.102	1.000	0.153	0.000
1.003	0.208	2.000	0.306	0.000
2.125	0.440	4.000	0.613	0.000

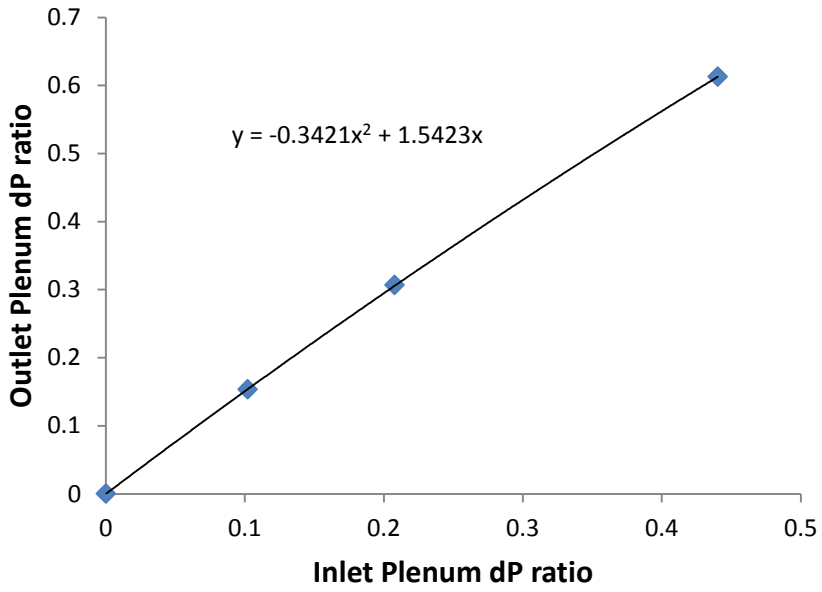

Figure 6-12 – Value of $\left(\frac{\Delta\widetilde{P_{above}}}{\Delta\widetilde{P_{2\phi}}}\right)$ versus $\left(\frac{\Delta\widetilde{P_{below}}}{\Delta\widetilde{P_{1\phi}}}\right)$ needed to achieve the same in-phase and out-of-phase real eigenvalue components, using Case S-2A as a starting point.

Four-Channel Standalone TH Cases

The same conditions in Case S-2B were extended to a four-channel model, Case S-4A, the only difference being that the total flow rate was doubled (to keep the same flow rate per channel). Once again, k_{below} was set to 2.0 and k_{above} to 0.0.

Eigenvalues, shown in Table 6-11 6-11, were as expected, with all the same eigenvalues from Case S-2B being present in Case S-4A, except most of them being repeated additional

times. For example, the eigenvalues 0 and -199.889 were each of multiplicity 3, reflecting the 3 neutronic modes which were enabled by default (though, once again, with $c_1 = c_2 = 0$, the neutronic modes had no effect on the solution); whereas four total pairs of eigenvalues with nonreal (oscillatory) components appeared in Case S-4A, versus two pairs in Case S-2B, based on four channels being present instead of two. Note that only a single pair of in-phase eigenvalues were present in each case, with the remaining pairs (either a single pair or three pairs, depending on N) constituted the out-of-phase mode(s).

The numerical simulation for Case S-4A was carried out to 500 seconds, by which point a stable limit cycle had been achieved (and nearly so by 250 s), as shown in Figure 6-13 and Figure 6-14. The channels unmistakably evolve toward a "rotating-mode" behavior, in the same manner as was observed using the TRACE code in 0. Also in similar fashion to the TRACE results, the channels formed quickly into two pairs of channels oscillating $180°$ apart, with the phase shift between the pairs much more slowly converging to $90°$.

The fact that two independent codes, using very different solution methodologies (*e.g.* TRACE using a finite volume approach and a detailed two-fluid solution, and the ROM using a weighted residual method and a simple HEM void formulation) gives added confidence that the observed rotating behavior is something based on real physical effects and not merely the result of some particular anomaly caused by the numerical methods or other assumptions used.

As mentioned at the beginning of this chapter, one important distinction between the TRACE results of 0 and the results shown here is that the current results were obtained using a fixed pressure drop boundary condition, while the TRACE results were obtained using a fixed total inlet flow rate boundary condition (and fixed outlet pressure). This also gives added confidence in the results, as it appears not to depend on the choice of boundary condition either (as long as it is one of the two choices used here).

A detailed explanation of why the "rotating mode" behavior is favored over a "side-to-side" oscillation pattern, or other possible configurations, is provided in Chapter 7 to follow[4].

[4] Strictly speaking, the terms "rotating" and "side-to-side" only make sense when dealing with coupled cases in which the radial location of each channel is relevant; however, this terminology will be used for standalone TH cases as well, in which the channels oscillate in a $(0°, 90°, 180°, 270°)$ or $(0°, 0°, 180°, 180°)$ pattern, respectively.

Table 6-11. Eigenvalues for case S-4A.

Eigenvalue	Oscillation Type
0.563+8.106i	Out-of-phase
0.563+8.106i	Out-of-phase
0.563+8.106i	Out-of-phase
0.563-8.106i	Out-of-phase
0.563-8.106i	Out-of-phase
0.563-8.106i	Out-of-phase
0.000	-
0.000	-
0.000	-
-0.000+8.091i	In-phase
-0.000-8.091i	In-phase
-0.300	-
-0.300	-
-0.300	-
-0.300	-
-0.315	-
-0.315	-
-0.315	-
-0.315	-
-39.150	-
-39.150	-
-39.150	-
-41.488	-
-199.889	-
-199.889	-
-199.889	-

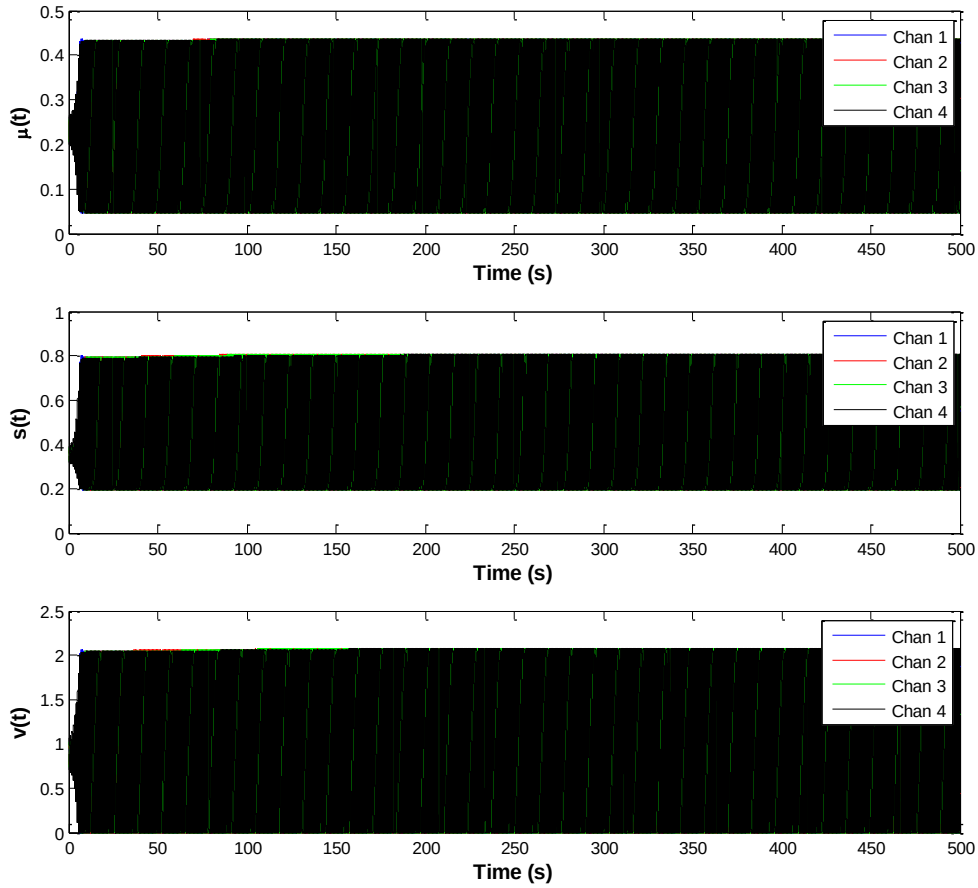

Figure 6-13 – Numerical solution from 0 seconds to 100 seconds for Case S-4A.

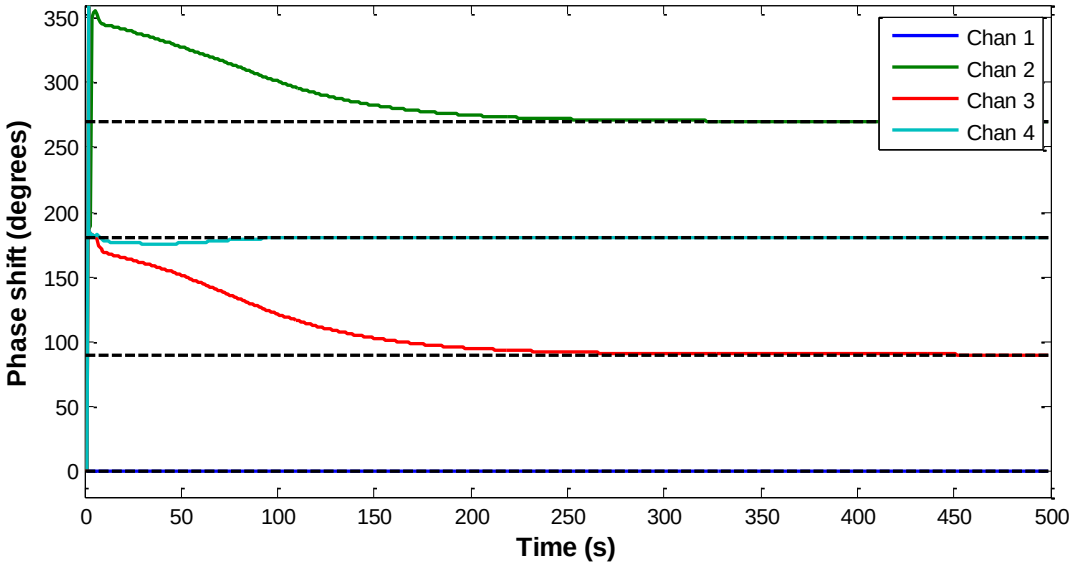

Figure 6-14 – Phase shift plot for Case S-4A.

6.4 Coupled Results

Single-Channel Coupled Cases

Recall that, for the standalone TH cases above, c_1 (void reactivity coefficient) and c_2 (fuel temperature reactivity coefficient) were set to 0 to eliminate any neutronic feedback from the dynamic behavior of the system. In other words, the neutron concentration $n(t)$ (equal to $\tilde{n}$ in this case) still determined the rate of heating of the coolant, but $n(t)$ remained constant and the system behaved as a TH channel with a fixed heat flux entering the coolant.

In order to determine the individual effects of c_1 and c_2 on the stability of the system, Case C-1A (which used the nominal values of c_1 and c_2) was modified such that c_1 and c_2 were set to zero separately. The results are shown in Table 6-12. The terms "c_1 multiplier" and "c_2 multiplier" refer to value by which the original c_1 and c_2 values, respectively, are multiplied; thus, a c_1 multiplier of 1.0 gives the original value of $c_1 = -0.15$ (*i.e.* $-150\ \mathrm{pcm}/\ \%\ \mathrm{void}$) as defined by Karve et al., and likewise for c_2 (with a nominal value of $-2\ \mathrm{pcm/K}$ before nondimensionalizing). Note that the "real eigenvalue component" referred to in Table 6-12 is only for the eigenvalue pair with an imaginary component; other eigenvalues might have a larger real component in some cases but these are not shown since only the oscillatory mode is of interest.

Based on Table 6-12, an increase in c_1 has a strong destabilizing effect on the system, while an increase in c_2 has a weak stabilizing effect (at least in terms of the nominal values of c_1 and c_2 cited by Karve et al.).

Recall that the reactivity coefficients c_1 and c_2 are defined as a change in the neutronic k_{eff} eigenvalue for a given change in void fraction or fuel temperature, respectively. Therefore, it might seem counterintuitive at first that c_1 is negative yet it has a positive effect on the eigenvalue in Table 6-12; however, in fact, the eigenvalues reported here are not defined in the same way as the k_{eff} eigenvalue. The k_{eff} eigenvalue describes the behavior of the neutronics field only, at a specified TH condition; therefore, it doesn't include the full system stability effects as do the eigenvalues presented here (for example, the time delay feedback mechanism

associated with the density wave). Thus, it is possible for c_1 to be negative but its effect on the overall eigenvalue to be positive.

Table 6-12. Effect of c_1 and c_2 on the stability of the single-channel system.

k_{inlet}	k_{exit}	c_1 Multiplier	c_2 Multiplier	Real Eig. Component
15.0	2.5	0.0	0.0	-4.275
15.0	2.5	1.0	0.0	0.386
15.0	2.5	0.0	1.0	-4.283
15.0	2.5	1.0	1.0	0.264

The numerical solution of Case C-1A, which uses the nominal c_1 and c_2 values, is shown in Figure 6-15 and Figure 6-16. In addition to the TH variables shown in previous cases, neutronic variables are now shown as well: the neutron density, precursor concentration, and the fuel temperature expansion coefficient in each region (single- and two-phase regions).

The system was unstable due to the eigenvalue pair $0.264 \pm 7.840i$; however, in the nonlinear regime the system also shows a simple bifurcative behavior in which the oscillations alternate between two different peak amplitudes from one peak to the next. This behavior has been well-documented in previous studies (*e.g.* [24], [61]), and is not surprising for ROMs such as the one used here.

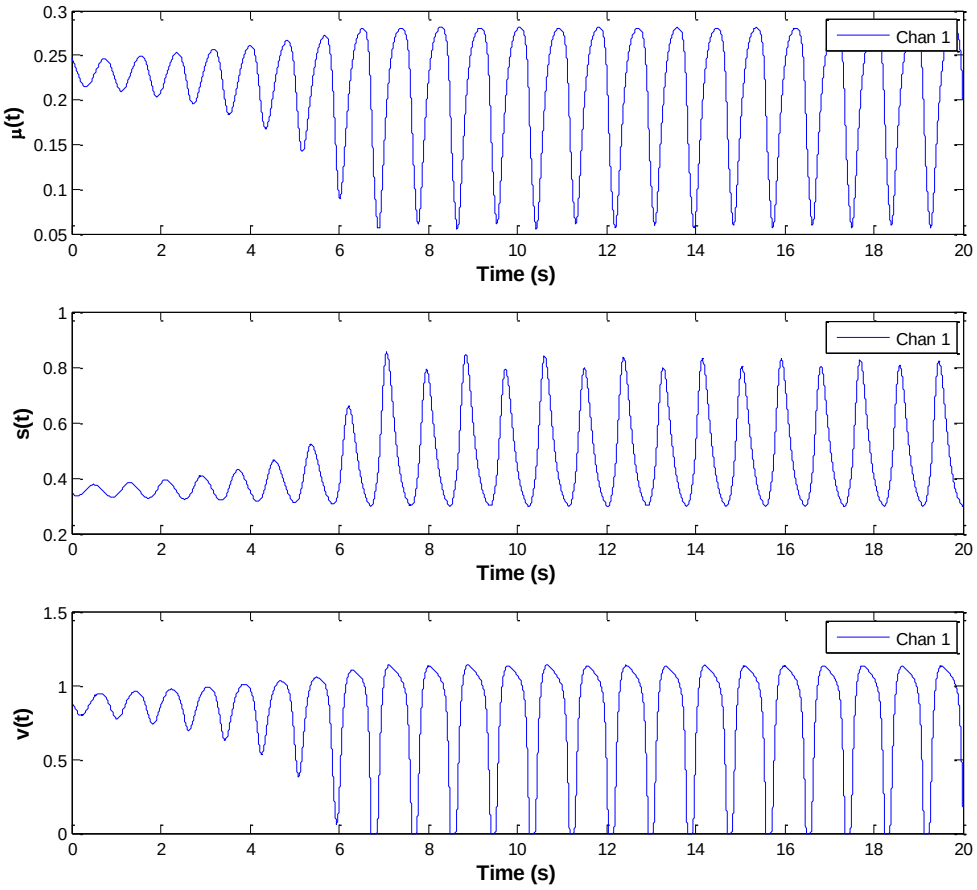

Figure 6-15 – Numerical simulation for Case C-1A from 0 to 20 seconds (TH variables).

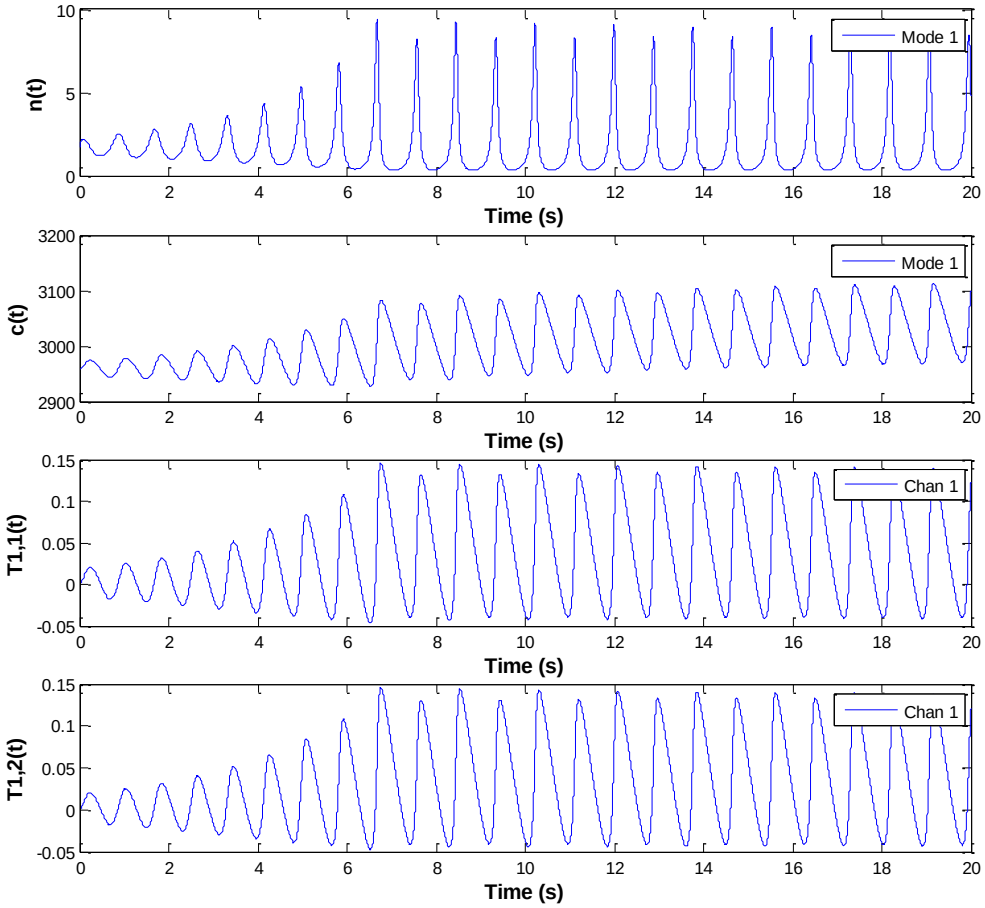

Figure 6-16 – Numerical simulation for Case C-1A from 0 to 20 seconds (neutronic variables).

Two-Channel Coupled Cases

A new case, C-2A, with two TH channels and two neutronic modes was set up in analogy to Case C-1A, in the same manner as done previously for the two-channel standalone TH cases. Once again, all steady state solutions are the same across each channel and across all cases. In addition, Case C-2A assumes a static reactivity of 0.0 for the first azimuthal mode, *i.e.* $\rho_1^s = \rho_0^s = 0.0$.

Eigenvalues for Case C-2A are shown in Table 6-13. All eigenvalues from Case S-1A (Table 6-4) also appear for Case C-2A, with each of them simply repeated a second time. Note also that the 0 eigenvalues for the standalone TH cases no longer appear, since those

eigenvalues were only 0 because the neutronic variables were decoupled from the TH variables.

For the results to follow, only the oscillatory eigenvalues (*i.e.* the ones forming complex conjugate pairs) will be shown, with the understanding that the other eigenvalues are still present but remain the same from case to case.

Table 6-13. Eigenvalues for Case C-2A

Eigenvalue	Oscillation Type
0.264+7.840i	N/A
0.264+7.840i	N/A
0.264-7.840i	N/A
0.264-7.840i	N/A
-0.112	-
-0.112	-
-0.301	-
-0.301	-
-9.759	-
-9.759	-
-68.02	-
-68.02	-
-199.465	-
-199.465	-

Three additional cases were created for illustrative purposes. Each highlights the effect of a different parameter on the stability characteristics. The three cases are identical to Case C-2A except for the differences shown in Table 6-14. Note that the "c_1, c_2 Multiplier" column refers to both c_1 and c_2, which were always given the same multiplier within each case (*i.e.* $c_1 = c_2 = 0.9$ or $c_1 = c_2 = 1.0$). The values shown in the table were arbitrarily chosen; the conclusions would remain the same if other values were to be chosen instead.

Table 6-14. Differences between Cases C-2A through C-2D

Case	k_{below}	ρ_1^s	c_1, c_2 Multiplier
C-2A	0	0	1
C-2B	1	0	1
C-2C	0	-0.0004	1
C-2D	0	0	0.9

Eigenvalues for the four cases C-2A through C-2D are shown in Table 6-15 in condensed form, with the other eigenvalues from Table 6-13 omitted for brevity (note that these other eigenvalues remained unchanged across all four cases).

Comparing Case C-2B to Case C-2A, it is clear that the results for the standalone TH cases still hold for the coupled cases: namely, that the addition of a positive k_{below} term has a destabilizing effect in the out-of-phase mode, but no effect at all on the in-phase mode (note that, as in previous cases, k_{inlet} was reduced accordingly, to yield the same steady-state solution as Case C-2A).

Case C-2C reveals that a negative value for the static reactivity ρ_1^s (where the 1 refers to "Mode 1", the azimuthal or out-of-phase neutronic mode) has a stabilizing effect on the out-of-phase mode, but no effect on the in-phase mode. This is because the reactivity terms driving the changes in $n_1(t)$ (neutron density for Mode 1) depend solely on the *difference* in void and fuel temperature perturbations between the two channels (whereas the fundamental mode, Mode 0, depends on the *average*, or total, of the perturbations in the two channels), as can be deduced from Eqs. (6.10) and (6.16). Hence, Mode 1 is completely inactive for in-phase oscillations (in which the *difference* in perturbations between channels is zero, at least in the linear case) whereas Mode 0 is completely inactive for out-of-phase oscillations (in which the *average* of the perturbations is zero, in the linear case). Therefore, ρ_1^s which affects the reactivity of Mode 1 has no effect on the in-phase eigenvalues but has a direct effect on the out-of-phase eigenvalues.

Finally, Case C-2D illustrates that the reactivity feedback coefficients c_1 and c_2 affect both the in- and out-of-phase eigenvalues equally, with an overall stabilizing effect as c_1 and c_2 are decreased in tandem (since the effect of c_1 is stronger than that of c_2, as seen in Table 6-12). In Eq. (6.10), c_1 and c_2 appear in the reactivity feedback terms for both neutronic modes, thus they affect the stability of both modes to the same extent.

Understanding the individual effects of each of these terms – k_{below}, ρ_1^s, and the c_1 and c_2 multipliers – will allow for a clearer understanding of the four-channels cases shown in the subsection below.

Table 6-15. Eigenvalues for Cases C-2A through C-2D

	In-Phase	Out-of-Phase
Case C-2A	0.264±7.840i	0.264±7.840i
Case C-2B	0.264±7.840i	0.380±7.923i
Case C-2C	0.264±7.840i	0.141±7.691i
Case C-2D	0.088±7.605i	0.088±7.605i

Four-Channel Coupled Cases

To examine the possible rotating mode behavior of the four channel coupled system, it was necessary to create a series of out-of-phase unstable cases. Based on the previous subsection, this will occur as long as k_{below} is sufficiently large relative to the magnitude of ρ_1^s (assuming k_{below} is positive and ρ_1^s is negative). For simplicity, ρ_1^s was taken to be 0 (which would be true, for example, for an infinitely large reactor in the radial direction) and various positive k_{below} values were chosen.

However, increasing k_{below} also increases the out-of-phase eigenvalue; so, in an attempt to maintain consistency between cases, the c_1 and c_2 multiplier was adjusted in each case to yield a real component of 1.0 for the leading (*i.e.* out-of-phase) eigenvalue. This allowed the oscillations to grow and develop at similar rates, and with similar limit cycle amplitudes; more importantly, it also allows one to gradually adjust the strength of the neutronic channel coupling versus the strength of the TH channel coupling (via the c_1 and c_2 multiplier, and k_{below}, respectively).

Results for the series of cases are shown in Table 6-16. The values of k_{below} were adjusted over the range of 11.0 to 13.5, which required c_1 and c_2 multipliers ranging from 0.388 to 0.121, respectively, to maintain an out-of-phase real eigenvalue component of 1.0. Thus, Case C-4A with $k_{below} = 11.0$ gave the weakest TH channel coupling and the strongest neutronic channel coupling, while Case C-4J with $k_{below} = 13.5$ gave the strongest TH channel coupling and the weakest neutronic channel coupling. If the k_{below} values were extended further, one would reach a point at which c_1 and c_2 would be zero, giving a TH standalone case with no neutronic feedback at all, and (as shown previously) such a case would give a rotating-mode behavior.

The final columns of Table 6-16 show the asymptotic phase shifts between channels after running each case numerically and converging to the final, fully-converged limit cycle. Detailed numerical results are shown for Cases C-4C, C-4E, and C-4G in Figure 6-17 – Fully-converged limit cycle results for Case C-4C (TH variables). In all three figures, the Chan 1 and Chan 2 lines overlap, and the Chan 3 and Chan 4 lines overlap.Figure 6-17 through Figure 6-25.

For all cases of the present cases with $k_{below} \geq 12.25$, the simulation converged to the $(0°, 90°, 180°, 270°)$ rotating limit cycle behavior. However, the ordering of channels in terms of phase shift was no longer arbitrary (*i.e.* based solely on initial conditions) as in the standalone TH cases; rather, in the limit cycle, the channels were forced to oscillate in either a clockwise or counterclockwise pattern due to the addition of neutronic coupling. Due to the shape of the azimuthal neutronic modes – one divided into "east" and "west" halves, and the other into "north" and "south" halves – a "NW-SE-NE-SW" ("NW"="Northwest", etc.) oscillation pattern would be strongly damped, while either a "NW-NE-SE-SW" pattern (*i.e.* a clockwise pattern, or "1-2-4-3" in terms of the channel numbering) or a "NW-SW-SE-NE" pattern (counterclockwise or "1-3-4-2") would be favored.

This is the behavior seen here, and recall that the same behavior was also seen using TRACE/PARCS in Chapter 5. To verify that either a clockwise or counterclockwise pattern would be equally possible, a separate case was run based on C-4J except with a different set of initial conditions, and this resulted in the identical limit cycle behavior shown in Table 6-16 except with Channels 2 and 4 switching places in (*i.e.* clockwise rather than counterclockwise). For no set of initial conditions was a "1-3-4-2" or "1-2-3-4" pattern (*i.e.* neither clockwise nor counterclockwise) observed.

However, for the cases with $k_{below} \leq 11.75$, the simulation converged to a $(0°, 0°, 180°, 180°)$ side-to-side limit cycle behavior instead of the $(0°, 90°, 180°, 270°)$ rotating limit cycle behavior. Since the only parameters that changed between the cases were k_{below}, c_1, and c_2, it is apparent that the behavior (rotating versus side-to-side) depends directly on the relative strength of the channel coupling due to neutronics (via c_1 and c_2) compared to the channel coupling due to TH (via k_{below}). Specifically, a relatively stronger neutronic channel

coupling apparently favors the side-to-side mode, while a relatively stronger TH channel coupling favors the rotating mode.

For the three cases that were run within the range $11.75 < k_{below} < 12.25$, the simulation converged to a limit cycle behavior of $(0°, \phi, 180°, \phi + 180°)$, where ϕ was some value between $90°$ and $180°$ (*i.e.* partway between the purely rotating case and the purely side-to-side case). For these three cases, ϕ increased monotonically as k_{below} decreased. If enough cases were run in the range $11.75 < k_{below} < 12.25$, a precise value would presumably be found at which ϕ "breaks away" from $90°$ and moves toward $180°$ (this would occur somewhere between Cases C-4G and C-4F); likewise, a value would presumably be found at which ϕ "breaks away" from $180°$ and moves toward $90°$ (somewhere between Cases C-4C and C-4D). Also, presumably, ϕ would change monotonically between these two "breakaway" points.

Table 6-16. Final limit cycle phase shift depending on the relative strength of neutronic versus TH channel coupling. In each case, the real component of the out-of-phase eigenvalue pair was 1.00000.

					Final Phase Shift (degrees)			
Case	k_{below}	k_{above}	c_1 Multiplier	c_2 Multiplier	Chan. 1	Chan. 2	Chan. 3	Chan. 4
C-4A	11.000	0	0.388	0.388	0.0	0.0	180.0	180.0
C-4B	11.500	0	0.336	0.336	0.0	0.0	180.0	180.0
C-4C	11.750	0	0.310	0.310	0.0	0.0	180.0	180.0
C-4D	11.875	0	0.297	0.297	0.0	329.6	149.6	180.0
C-4E	12.000	0	0.284	0.284	0.0	318.1	138.1	180.0
C-4F	12.125	0	0.271	0.271	0.0	305.8	125.8	180.0
C-4G	12.250	0	0.258	0.258	0.0	270.0	90.0	180.0
C-4H	12.500	0	0.231	0.231	0.0	270.0	90.0	180.0
C-4I	13.000	0	0.177	0.177	0.0	270.0	90.0	180.0
C-4J	13.500	0	0.121	0.121	0.0	270.0	90.0	180.0

Initially, Cases C-4D through C-4F were run out to a simulation time of 200 seconds, and based on the results it was believed that they were simply not converged by that time, *i.e.* had not been run out to a long enough time to allow the asymptotic limit cycle behavior to be reached (since only the $(0°, 0°, 180°, 180°)$ and $(0°, 90°, 180°, 270°)$ behaviors had been seen up to this point in the thesis). Therefore, Cases C-4D through C-4F were each run again, to a

much longer simulation time (4000 s, as in Figure 6-22), but the final phase shift behavior remained as shown in Table 6-16. It is interesting to note that, in Figure 6-20, Channels 1 and 4 oscillate with a different amplitude in the limit cycle than Channels 2 and 3 do. This was only true for the "transition" cases, Cases C-4D through C-4F; for the cases with either fully side-to-side or fully rotating behavior, the oscillation amplitude of all four channels were identical. The occurrence of uneven amplitudes among the channels in the final limit cycle appears to be related somehow to the "transition" behavior; however, no satisfactory explanation for the uneven amplitudes or the "transition" behavior is known at this time.

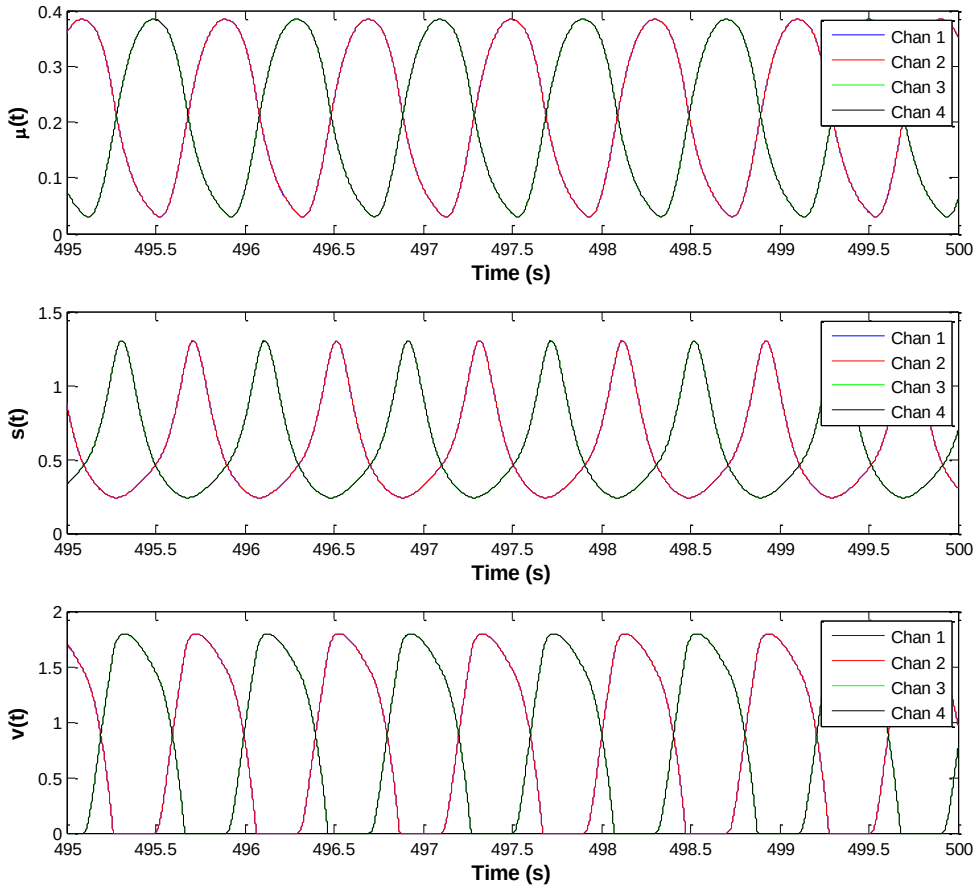

Figure 6-17 – Fully-converged limit cycle results for Case C-4C (TH variables). In all three figures, the Chan 1 and Chan 2 lines overlap, and the Chan 3 and Chan 4 lines overlap.

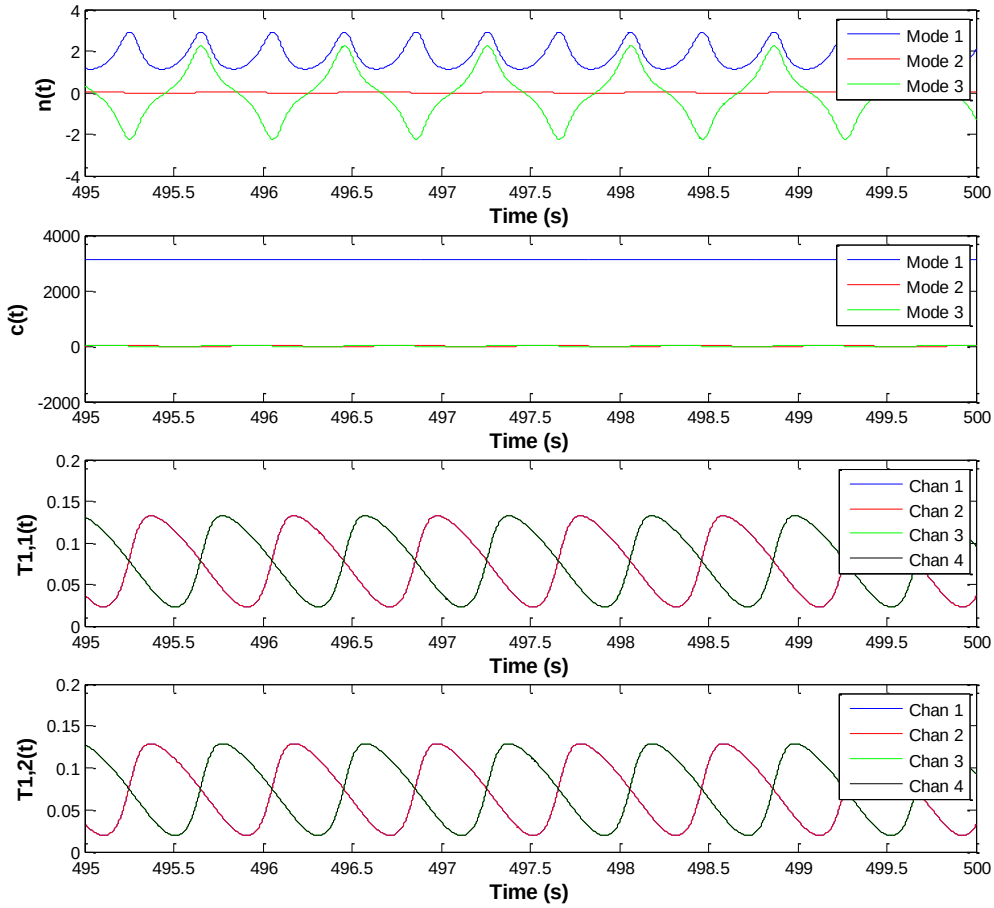

Figure 6-18 – Fully-converged limit cycle results for Case C-4C (neutronic variables). In the bottom two figures, the Chan 1 and Chan 2 lines overlap, and the Chan 3 and Chan 4 lines overlap.

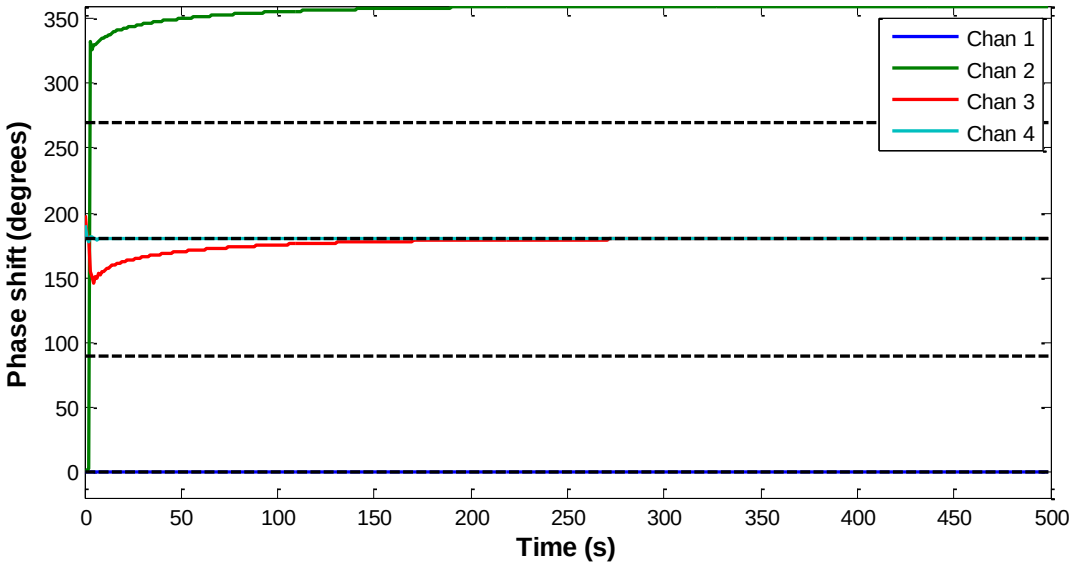

Figure 6-19 – Phase shift plot for Case C-4C

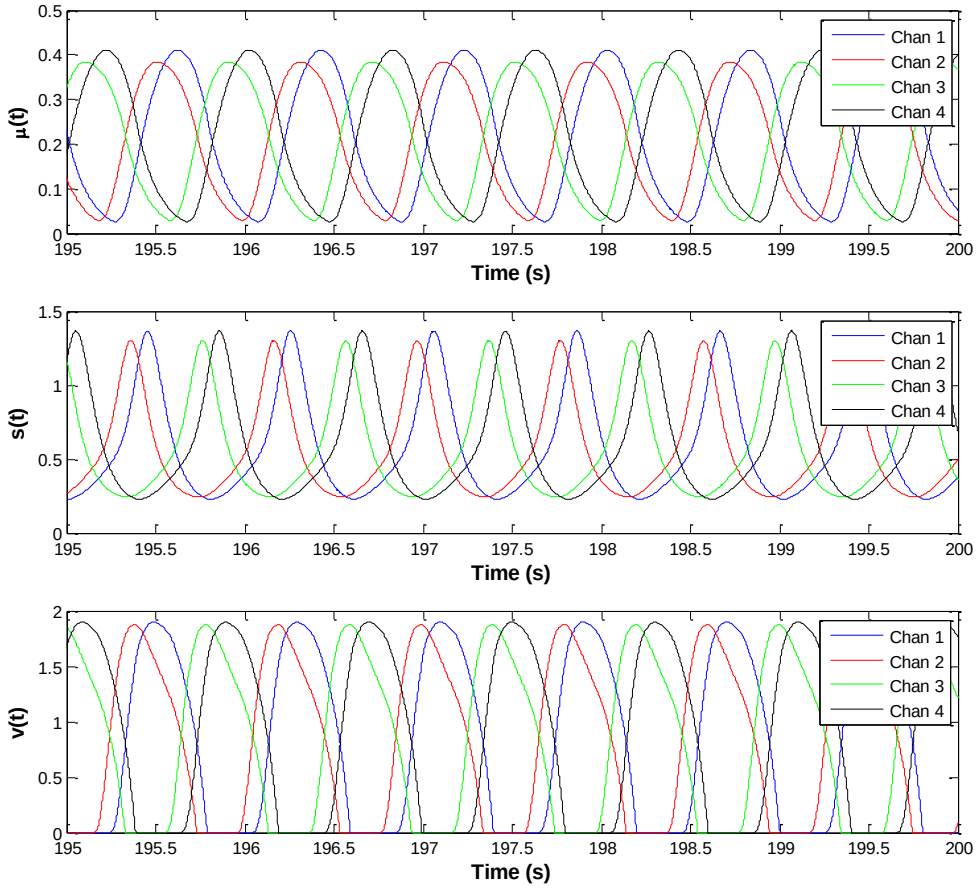

Figure 6-20 – Fully-converged limit cycle results for Case C-4E (TH variables)

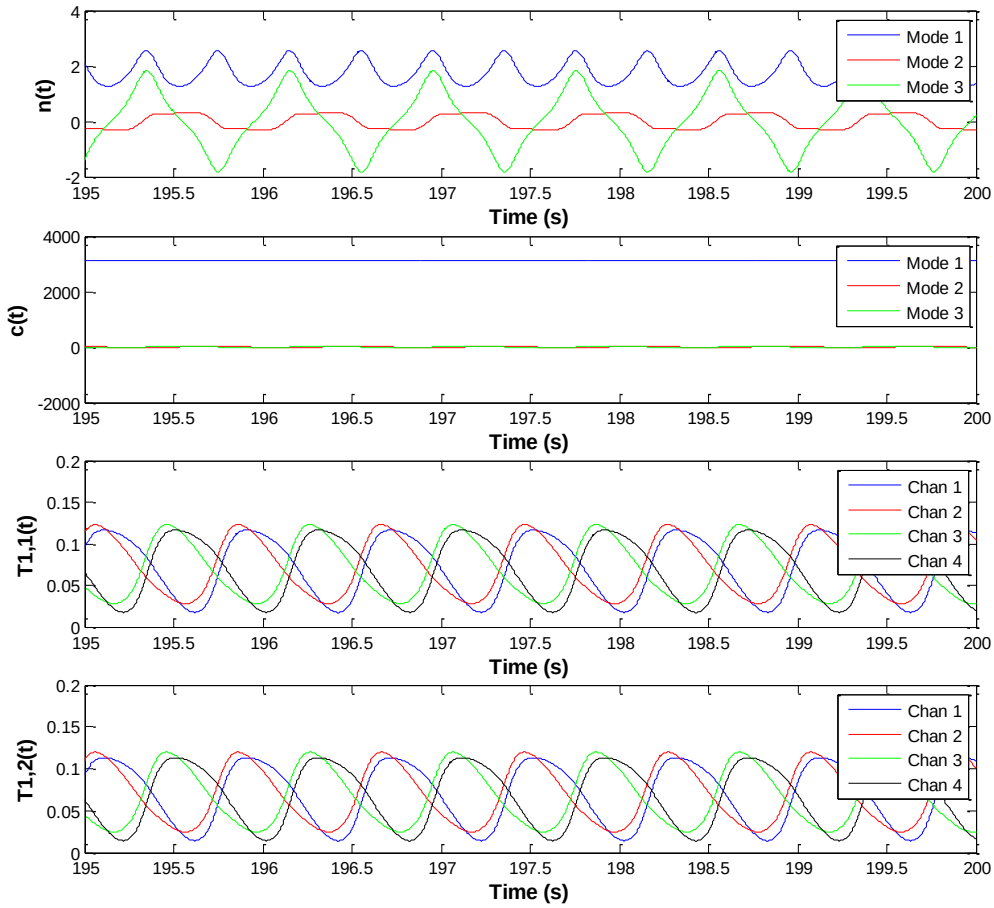

Figure 6-21 – Fully-converged limit cycle results for Case C-4E (neutronic variables).

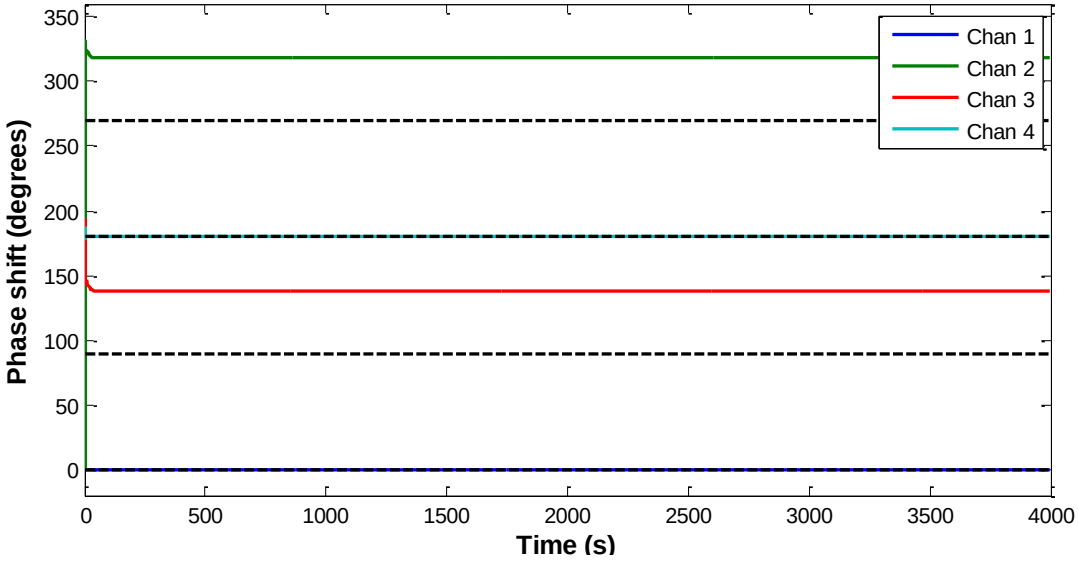

Figure 6-22 – Phase shift plot for Case C-4E

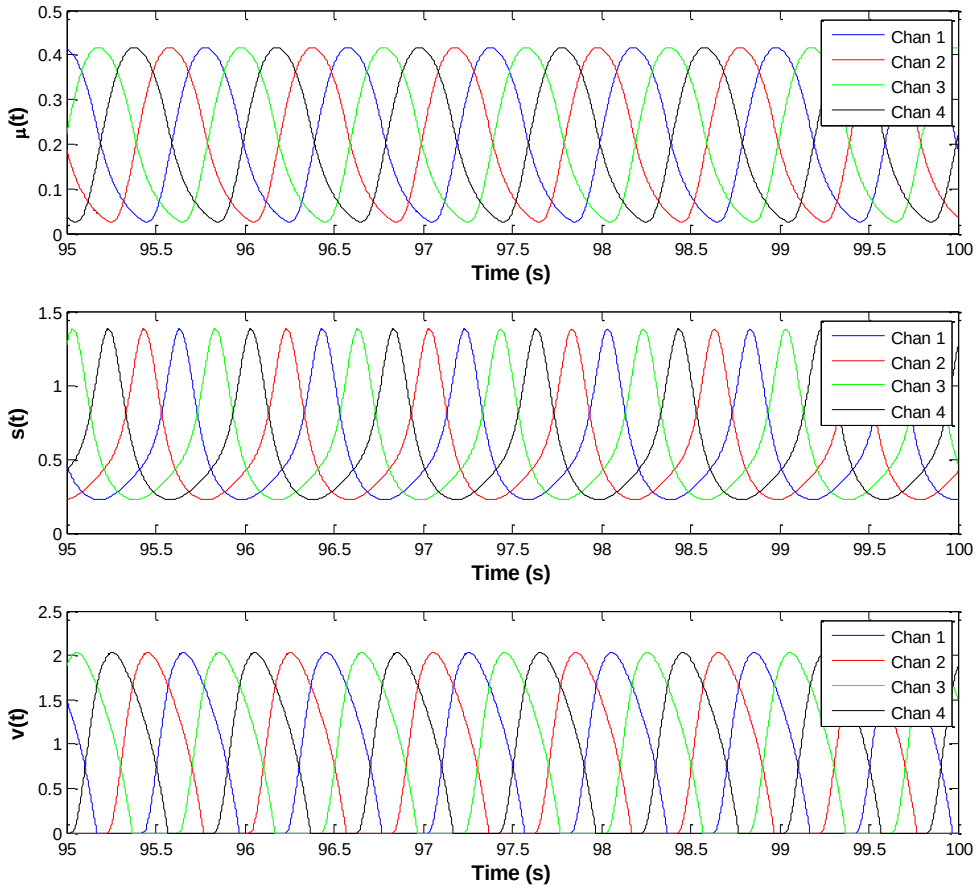

Figure 6-23 – Fully-converged limit cycle results for Case C-4G (TH variables).

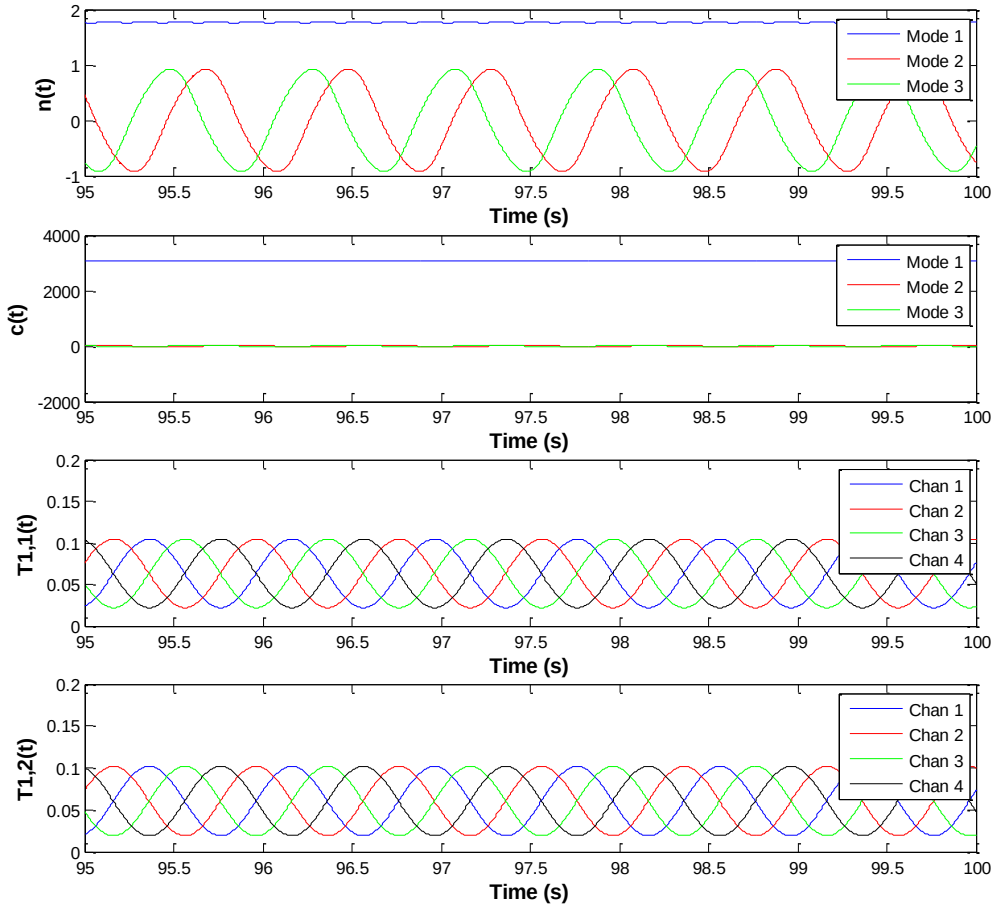

Figure 6-24 – Fully-converged limit cycle results for Case C-4G (neutronic variables).

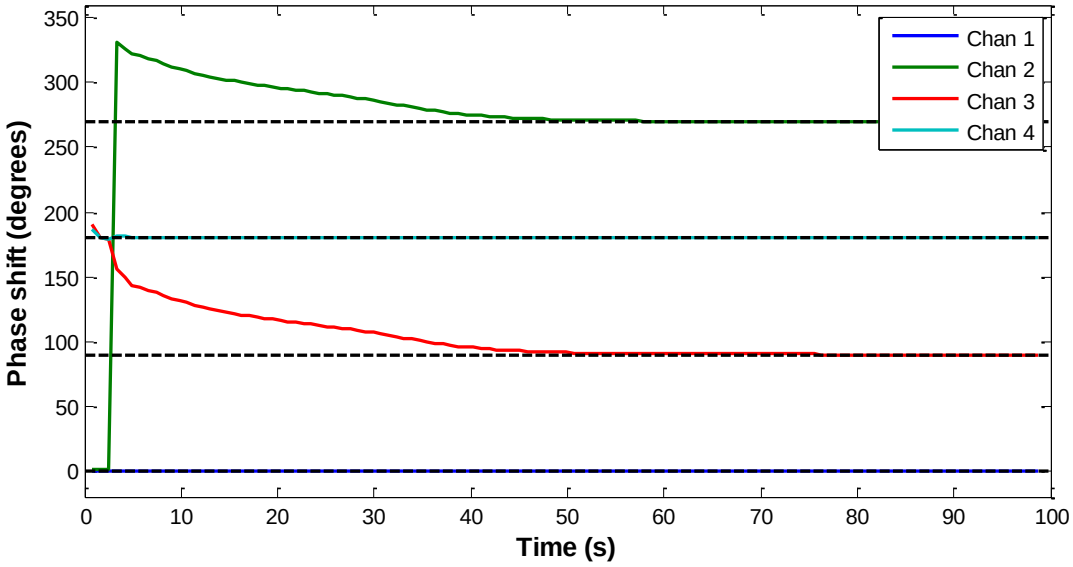

Figure 6-25 – Phase shift plot for Case C-4G

Chapter 7. Physical Explanation For Rotating-Mode Behavior

The following section will present a physical explanation of why the rotating mode is favored over the side-to-side mode for 4-channel limit cycle oscillations, from the standpoint of TH. As indicated by the results shown in the previous subsection, certain coupled cases appear to favor the side-to-side mode or some intermediate behavior in between the rotating and side-to-side modes; however, no clear physical explanation has yet been developed to explain those behaviors, so the current discussion will restrict itself to the case of standalone TH.

The logical steps behind the explanation presented here for the rotating behavior is as follows:

1) Under certain conditions, show that the four-channel system is most unstable when the variation in the total core inlet flow rate is minimized.
2) Show that the rotating mode minimizes the variation in the total core inlet flow rate (compared to the side-to-side mode or any other pattern) for typical nonlinear TH oscillations.

If both of these conditions hold, it follows that the rotating mode gives the most unstable oscillation pattern, hence it is the mode toward which the limit cycle will tend towards.

Note that, for the current chapter, whenever the term “flow rate” or “velocity” is used, specifically the *inlet* flow rate or velocity is being referred to. Additionally, the discussion will be in terms of the *average* inlet flow rate among channels (for mathematical convenience), but the conclusions remain unchanged if the *total* flow rate among channels is considered instead.

7.1 Systems Which Prefer a Minimal Variation in Total Flow Rate

Recall from Section 0 that a standalone TH system with a positive value for k_{below} and a k_{above} equal to 0 will have an out-of-phase mode as the dominant oscillation mode[5]. This was explained by considering the pressure drops in the single- and two-phase regions. For the in-phase case, the $\Delta P_{below}(t)$ term participates in the oscillations and contributes fully to the single-phase pressure drop. However, in the out-of-phase case, the $\Delta P_{below}(t)$ term is constant and non-oscillatory (at least for linear oscillations), hence this contribution is eliminated from the single-phase pressure drop in the oscillations, and the result is a system oscillating with a smaller single-phase pressure drop compared to the in-phase case (with the two-phase pressure drop remaining unchanged). This yields a more unstable system in the out-of-phase mode than the in-phase mode, precisely because the total core inlet flow rate remains constant for the out-of-phase mode (hence eliminating $\Delta P_{below}(t)$ from the oscillations).

Unlike for the linear case, though, in the case of nonlinear oscillations the total flow rate, in general, can never be completely constant. This is due to the presence of higher frequency terms in the Fourier expansion which are not canceled out in the case of out-of-phase oscillations (as will be described in detail in the next subsection). However, the same argument given above still applies for nonlinear oscillations: any oscillation pattern that minimizes the variation in the total flow rate will minimize the variation in $\Delta P_{below}(t)$, and this will lead to the most unstable conditions (again, due to minimizing the single-phase oscillatory ΔP relative to the two-phase oscillatory ΔP).

[5] Alternatively, k_{above} could be positive but sufficiently smaller than k_{below}. However, we will restrict our consideration the the case of $k_{above} = 0$ for the present discussion, for simplicity, as both cases yield the same conclusion.

7.2 Oscillation Pattern Which Minimizes the Variations in the Total Flow Rate

The following section will demonstrate that the rotating mode minimizes the variation in the total flow rate over each oscillation period in the four-channel model. Two time signals were chosen as starting points for this analysis: the Channel 1 time signal from the four-channel standalone TRACE calculation shown in Figure 5-4 (called Signal A), and the Channel 1 time signal from Case C-4G using the reduced-order Karve model as shown in Figure 6-23 (called Signal B). These time signals were each chosen from the fully-converged limit cycle portion of the transients, taking the final five periods of oscillation as data for curve fitting. The choice of Channel 1 was arbitrary; all four channels in each case were identical and the results of this analysis would be the same regardless of which channel was selected. Figure 7-1 shows the time signals used, where the initial time used here was reset to 0 for convenience (though, again, they were taken from later on in the transients).

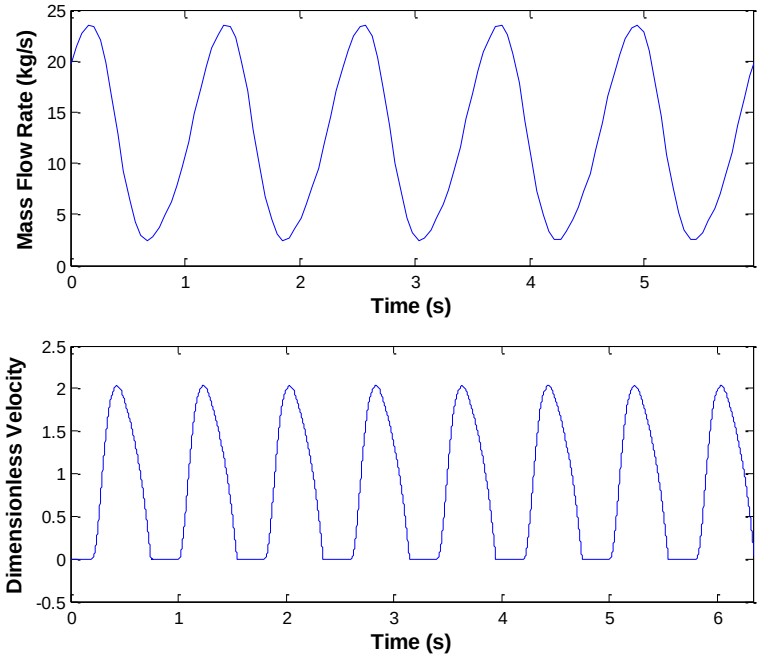

Figure 7-1 – Converged limit cycle oscillation pattern from Channel 1 for the 4-channel TRACE case (Signal A, top) and the 4-channel ROM case C-4G (Signal B, bottom)

Fourier Expansion of the Time Signals

A Fourier expansion was performed to decompose the time signals into separate frequency components. This was done using the built in MATLAB function '*fit.m*' using the option '*fourier8*', which uses an eighth-order Fourier decomposition of the form

$$f_1(t) = a_0 + \sum_{n=1}^{8} (a_n \cos(\omega n t) + b_n \sin(\omega n t)) , \tag{7.1}$$

where $f_1(t)$ is the time signal shown in Figure 7-1 (used as an input for the *'fit.m'* function), $a_n$and b_n are expansion coefficients, and n is the component index.

Eq. (7.1) can be also be written in the form

$$f_1(t) = a_0 + \sum_{n=1}^{8} A_n \sin(\omega n t + \phi_n) , \tag{7.2}$$

where A_n is the amplitude of mode n and ϕ_n is the phase shift. The two forms are related by

$$A_n = \sqrt{a_n^2 + b_n^2} \tag{7.3}$$

and

$$\phi_n = \tan^{-1}\left(\frac{a_n}{b_n}\right). \tag{7.4}$$

The analysis and results shown below will use the form in Eq. (7.1); however, the mode amplitude A_n will be used in tables as well, as a convenient means of comparing relative magnitudes of frequency components.

Results for the curve fit for both signals are tabulated in Table 7-3 through Table 7-4, with the overall approximation to $f_1(t)$ shown in Figure 7-2. From visual inspection, the 8th order expansion is more than adequate to give agreement for Signal A, while for Signal B the 8th order expansion still has slight difficulty capturing the discontinuous derivatives caused by the use of limiters preventing negative velocity values.

A visualization of the normalized mode amplitudes for both signals is given in Figure 7-3. Overall, Signal B had significantly larger contributions from higher-frequency components (*i.e.* beyond $n = 1$) than did Signal B; this was almost certainly due to the discontinuous derivatives in Signal B.

Table 7-1. Fitting coefficients a_0 and ω for the Fourier expansion for Signal A

a_0	ω
12.5000	5.2820

Table 7-2. Fitting coefficients for the sine and cosine terms for Signal B

n	a_n	b_n	Mode amp. (normalized)
1	8.0590	6.6040	1.0000
2	-1.0000	0.8161	0.1239
3	0.1101	-0.2614	0.0272
4	0.0576	-0.1079	0.0117
5	-0.0554	-0.0051	0.0053
6	0.0005	-0.0319	0.0031
7	0.0053	0.0123	0.0013
8	-0.0042	0.0094	0.0010

Table 7-3. Fitting coefficients a_0 and ω for the Fourier expansion for Signal B

a_0	ω
0.8413	7.8520

Table 7-4. Fitting coefficients for the sine and cosine terms for the Fourier expansion for Signal B

n	a_n	b_n	Mode amp. (normalized)
1	-0.9315	-0.5742	1.0000
2	0.1472	0.0929	0.1591
3	-0.1028	0.1222	0.1459
4	-0.0152	-0.0022	0.0140
5	0.0316	0.0198	0.0341
6	0.0116	0.0206	0.0216
7	0.0094	0.0013	0.0087
8	0.0075	-0.0068	0.0093

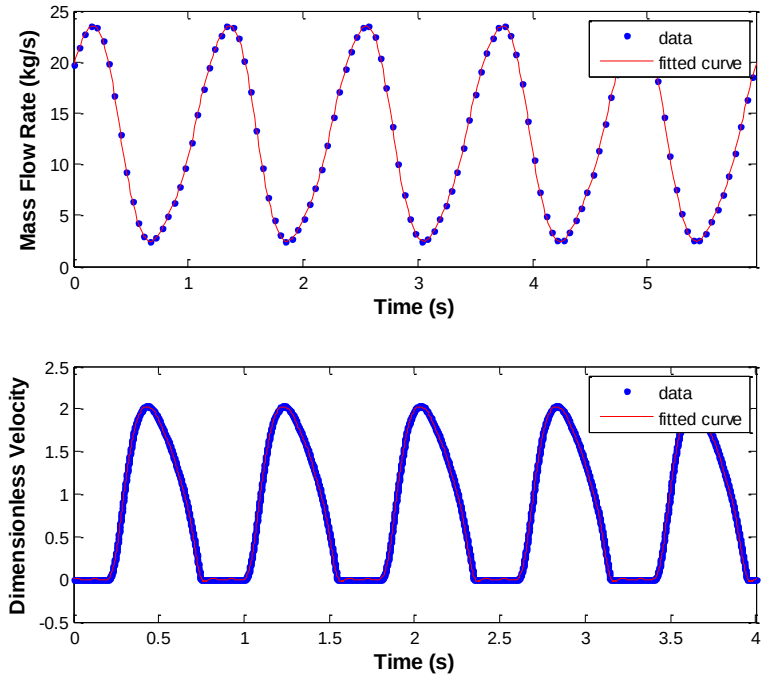

Figure 7-2 – Curve fit for Signal A (top) and Signal B (bottom)

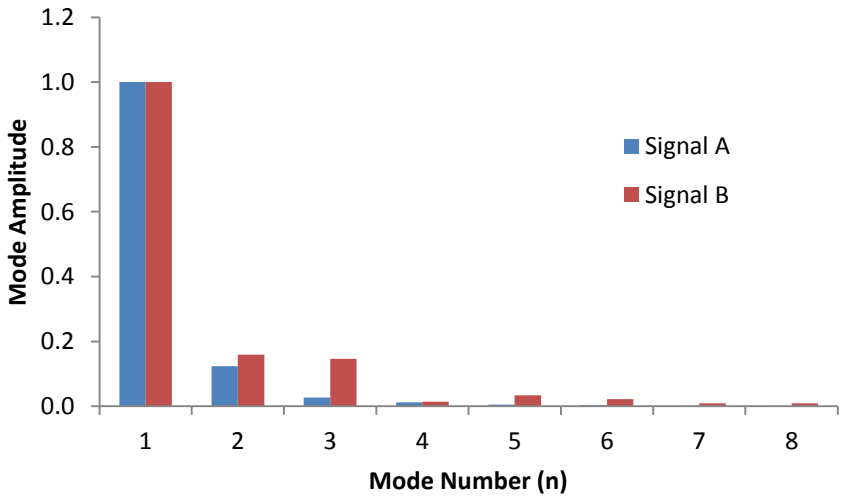

Figure 7-3 – Amplitudes of frequency modes (A_n) for both signals (normalized to give $A_1 = 1.0$)

Fourier Components of the Average Velocity – Two-Channel Case

The task now is to find an expression for the average inlet flow rate among N channels, defined as

$$g(t) = \frac{1}{N}\sum_{i=1}^{N} f_i(t) \tag{7.5}$$

where $f_i(t)$ is the inlet flow rate in channel i. First, consider the case of two identical channels with an arbitrary phase shift ϕ_2 between the channels. Using the expression for $f_1(t)$ in Eq. (7.1) with a frequency of ω, the expression for $f_2(t)$ is then simply

$$f_2(t) = f_1\left(t + \frac{\phi_2}{\omega}\right) \tag{7.6}$$

which can be substituted into Eq. (7.1) to find an explicit expression for $f_2(t)$ in terms of a summation of sine and cosine functions and the unknown quantity ϕ_2. Plugging the expressions for $f_1(t)$ and $f_2(t)$ into Eq. (7.5), one finds that the average flow rate between the two channels is given by

$$\begin{aligned} g(t) = a_0 + \sum_{n=1}^{8} \cos\left(\frac{n\phi_2}{2}\right)\Bigg[a_n \cos\left(\omega n t + \frac{n\phi_2}{2}\right) \\ + b_n \sin\left(\omega n t + \frac{n\phi_2}{2}\right)\Bigg] \end{aligned} \tag{7.7}$$

The case of $\phi_2 = 0°$ corresponds to an in-phase oscillation between the two channels, while $\phi_2 = 180°$ corresponds to out-of-phase oscillations. The individual terms in the summation of $g(t)$ for each of these cases is given in Table 7-5. Note that the out-of-phase case cancels out all odd n components in $g(t)$, while having no effect on the even n components (*i.e.* returning the same values from the original single-channel case). Therefore, all components in the out-of-phase case are less than or equal to those in the in-phase case in magnitude, and so the resulting function $g(t)$ will experience smaller oscillations in the out-of-phase case. A visual comparison of the component amplitudes for the in- and out-of-phase cases is given in Figure 7-4. It is clear that the out-of-phase case ($\phi_2 = 180°$) will give a much smaller variation in the average flow rate, primarily due to eliminating the $n = 1$ component which is the dominant term in $f_1(t)$.

Table 7-5. Terms of $g(t)$ for two channel in- and out-of-phase cases.

n	Two channels, $\phi_i = (0°, 0°)$ (in-phase)	Two channels, $\phi_i = (0°, 180°)$ (out-of-phase)
0	a_0	a_0
1	$a_1 \cos(\omega t) + b_1 \sin(\omega t)$	0
2	$a_2 \cos(2\omega t) + b_2 \sin(2\omega t)$	$a_2 \cos(2\omega t) + b_2 \sin(2\omega t)$
3	$a_3 \cos(3\omega t) + b_3 \sin(3\omega t)$	0
4	$a_4 \cos(4\omega t) + b_4 \sin(4\omega t)$	$a_4 \cos(4\omega t) + b_4 \sin(4\omega t)$
5	$a_5 \cos(5\omega t) + b_5 \sin(5\omega t)$	0
6	$a_6 \cos(6\omega t) + b_6 \sin(6\omega t)$	$a_6 \cos(6\omega t) + b_6 \sin(6\omega t)$
7	$a_7 \cos(7\omega t) + b_7 \sin(7\omega t)$	0
8	$a_8 \cos(8\omega t) + b_8 \sin(8\omega t)$	$a_8 \cos(8\omega t) + b_8 \sin(8\omega t)$

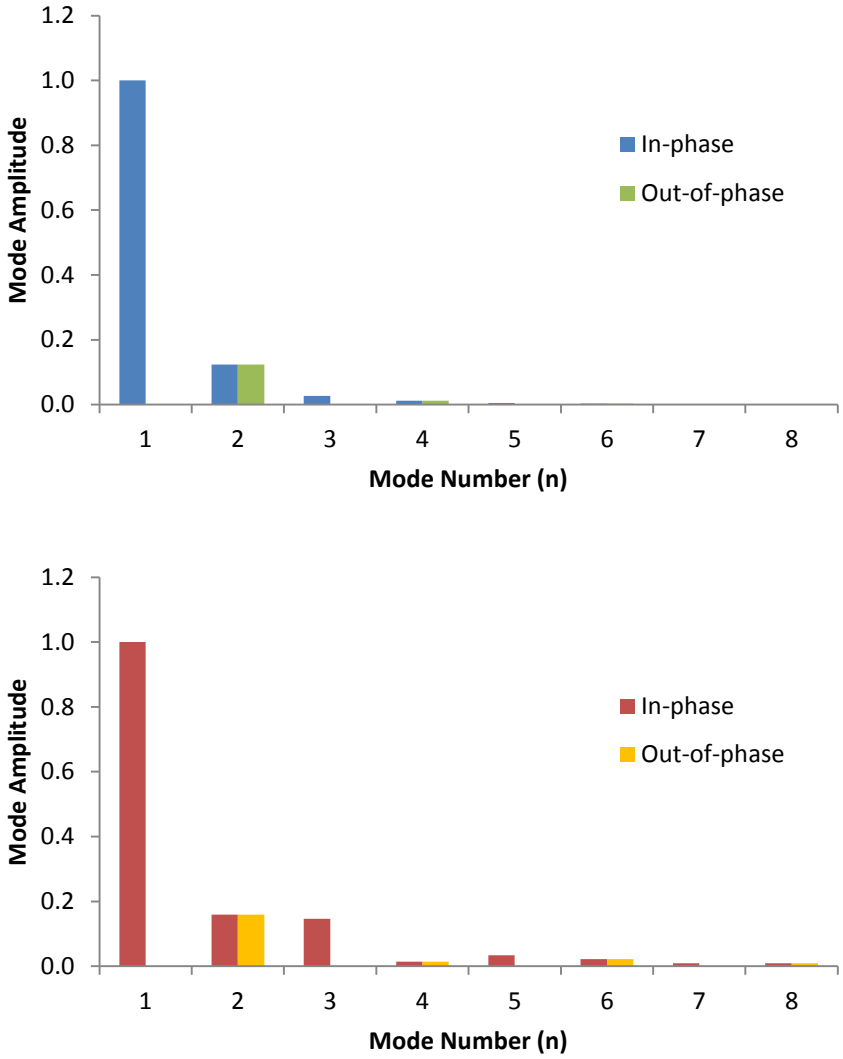

Figure 7-4 – Amplitudes of frequency modes (A_n) for the average flow rate ($g(t)$) for the two-channel in-phase and out-of-phase cases, based on the normalized values for Signal A (top) and Signal B (bottom), respectively

However, for completeness, the term "smaller variation in average flow rate" must be more precisely defined. This is because $g(t)$ can in principle exhibit complicated behavior, *e.g.* multiple local maxima and minima with different y-locations within a single period of oscillation; hence, it is difficult to define a single "amplitude" of oscillation in the same way as one would for a simple sine function.

Therefore, in order to quantify the amount of variation in the average flow rate over time, three different norms will be used: the L^1-norm, L^2-norm, and L^∞-norm of $(g(t) - \tilde{g})$,

over a single oscillation period, where $\tilde{g}$ is the steady-state average flow rate (equal to a_0 in the Fourier expansion). These norms are defined as

$$\|g(t) - \tilde{g}\|_b = \left(\int_0^{2\pi/\omega} |g(t) - \tilde{g}|^b dt \right)^{\frac{1}{b}} \tag{7.8}$$

where $\|g(t) - \tilde{g}\|_b$ is the L^b-norm of $(g(t) - \tilde{g})$, and $(2\pi/\omega)$ is a single oscillation period. The L^∞-norm thus reduces to the maximum absolute value of $(g(t) - \tilde{g})$ over the oscillation period; however, the L^1-norm and the L^2-norm are integral quantities that take into account the average flow variation along the entire time interval. These latter quantities are preferred in this analysis because, physically speaking, the stability of the system depends on the average flow rate behavior across the *entire* oscillation period, not merely the maximum variation.

Mathematically, for a completely arbitrary starting function $f_1(t)$, the case of $\phi_2 = 180°$ does *not* guarantee the minimum variation in average flow rate in terms of these norms. For example, consider a case where the starting time signal $f_1(t)$ has very small expansion coefficients a_n and b_n for odd n (including $n = 1$), and larger coefficients for even n. Then the cancellation of odd-n terms for the out-of-phase case (Table 7-5) would have only a minimal effect on $g(t)$ (since the odd-n terms in $f_1(t)$ are so small to begin with in this scenario). Additionally, the even-n terms would actually be *reduced* if ϕ_2 moved away from $180°$, due to the $\cos\left(\frac{n\phi_2}{2}\right)$ factor in front of each frequency component in Eq. (7.7). The result is that $\phi_2 = 180°$ (and $\phi_2 = 0°$) could actually be the *worst*-case scenario (*i.e.* give the *maximum* flow variation), and some intermediate value (likely $\phi_2 = 90°$) would give the minimum flow variation in this case.

However, the case given above is highly unrealistic for TH channel oscillations. As shown in Figure 7-3, the a_1 and b_1 terms (or the amplitude A_1) are by far the dominant terms in the two nonlinear limit cycle velocity profiles used in this section, and it is implausible that they would ever *not* be the dominant terms for any realistic case. Recall that for linear oscillations, the $n = 1$ terms are the *only* terms that appear, and as the oscillations grow in amplitude the $n > 1$ terms gradually increase in amplitude relative to the $n = 1$ terms. However, even with limit cycle oscillations of more than $\pm 100\%$ in Signal B (as well as an artificial discontinuous

derivative), the $n > 1$ terms are *still* much smaller than the $n = 1$ terms. And, based on Table 7-5, the $n = 1$ terms (and other odd-n terms) are the ones that truly favor the out-of-phase behavior.

To confirm the above conclusions, $g(t) = f_1(t) + f_1\left(t + \frac{\phi_2}{\omega}\right)$ was evaluated (using the original Signal A and Signal B, respectively, rather than the truncated 8th-order Fourier approximations) for ϕ_2 values ranging from $0°$ to $360°$. Then, then the L^1-norm, L^2-norm, and L^∞-norm were calculated as shown in Eq. (7.7)(7.8) for each value of ϕ_2. The results are plotted in Figure 7-5. As expected, $\phi_2 = 180°$ gave the minimum variation in the average flow rate, in terms of all three norms. This successfully demonstrates that the out-of-phase pattern in a 2 channel system will give the minimum variation in average flow, at least for realistic cases where the velocity signal is dominated by the $n = 1$ frequency mode.

As a side note, the two "plateaus" in the L^∞-norm for a small range of ϕ_2 values for Signal B were due to the flat portion of the signal (where $v = 0$); at these ϕ_2 values, the flat portions of both channels must have overlapped such that the maximum value of $(g(t) - \tilde{g})$ remained constant over that range. However, these effects were smoothed out by the other two norms due to the integration over the whole time interval.

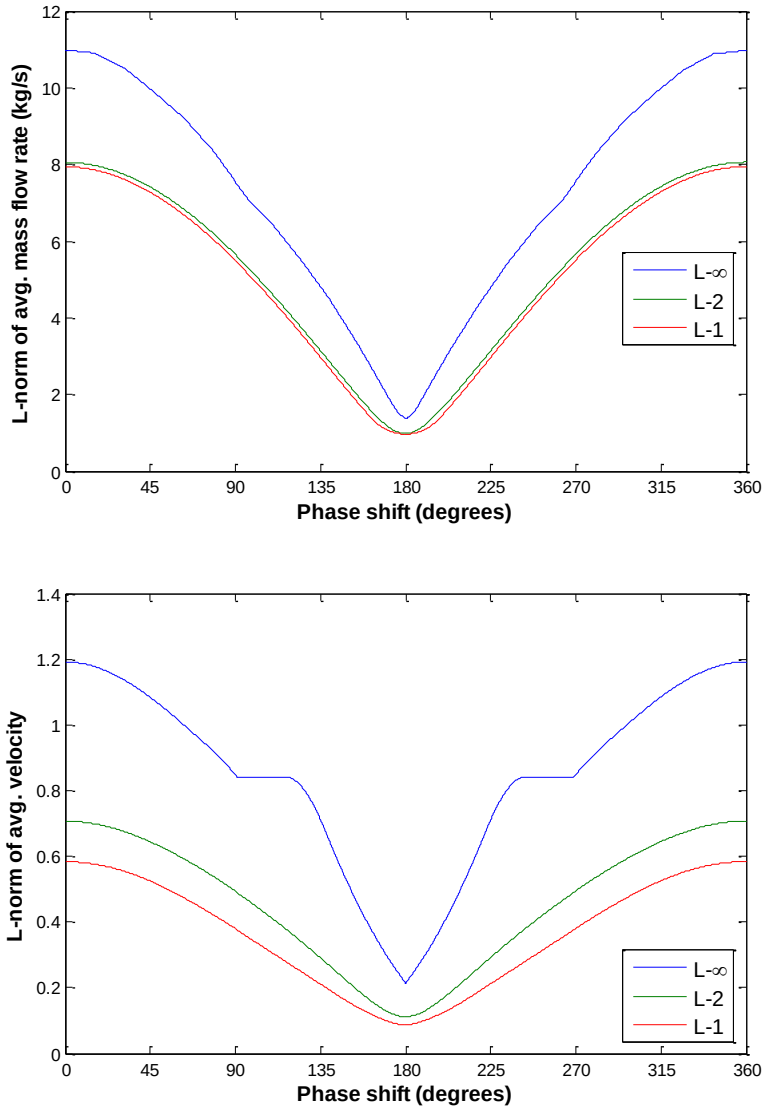

Figure 7-5 – L-norms of the variation in average flow rate as a function of ϕ_2 over the range $(0°, 360°)$ for the two-channel case, for Signal A (top) and Signal B (bottom)

Fourier Components of the Average Velocity – Four-Channel Case

The previous analysis on two-channel cases will now be extended to the case of four identical channels. In principle, the four channels could be governed by three distinct phase shifts ϕ_2, ϕ_3, and ϕ_4 (for channels 2-4 with respect to channel 1), and one could seek to minimize the L-norm of $(g(t) - \tilde{g})$ in the three-dimensional space $\{\phi_2, \phi_3, \phi_4\}$. However, if one takes any two channels in the four channel system, those two channels between themselves will strongly favor a $\phi_2 = 180°$ behavior (as shown

above), mainly because it eliminates the very large a_1 and b_1 components from the signal; therefore, it is highly unlikely that the optimum case would involve anything other than two pairs of channels oscillating $180°$ out-of-phase within each pair. This tendency has been demonstrated repeatedly in every four-channel numerical simulation performed in this thesis – namely, two pairs of counter-phase channels form very rapidly; then, over (usually) a much longer time scale, the phase shift between Pair 1 and Pair 2 gradually drifts toward a final value (see, *e.g.*, Figure 5-4 and Figure 6-14).

Therefore, this analysis will reduce the four-channel problem from three degrees of freedom (ϕ_2, ϕ_3, and ϕ_4) to just a single degree of freedom ϕ, with $f_1(t)$ given by (7.1),

$$f_2(t) = f_1\left(t + \frac{\phi}{\omega}\right), \tag{7.9}$$

$$f_3(t) = f_1\left(t + \frac{180°}{\omega}\right), \tag{7.10}$$

$$f_4(t) = f_1\left(t + \frac{\phi + 180°}{\omega}\right), \tag{7.11}$$

and ϕ being the phase shift between the first pair of channels (channels 1 and 3) and the second pair (channels 2 and 4).

The analysis is carried out in precisely the same fashion as before, except that $g(t)$ in Eq. (7.5) is now a summation of four channels rather than two. After inserting the above expressions for $f_i(t)$ into Eq. (7.5) and simplifying, the resulting expression is

$$g(t) = \begin{cases} 0\ , & n \text{ odd} \\ a_0 + \sum_{n=1}^{8} \cos\left(\frac{n\phi}{2}\right)\left[a_n \cos\left(\omega n t + \frac{n\phi}{2}\right) + b_n \sin\left(\omega n t + \frac{n\phi}{2}\right)\right]\ , & n \text{ even} \end{cases} \tag{7.12}$$

This is the same expression as in Eq. (7.7), except with every odd term equal to zero.

At first glance, this may appear to be no better than the two-channel case, since the two-channel case had already managed to eliminate all odd terms when $\phi_2 = 180°$, and the even terms are the same as in the two-channel case as well. In fact, when $\phi = 180°$ in the four-channel problem, the four phase shifts are $(0°, 0°, 180°, 180°)$ (the side-to-side oscillation pattern) and the average velocity is identical to the two-channel case with phase shifts of $(0°, 180°)$, which appears to once again minimize variations in $g(t)$.

However, upon further inspection, it becomes apparent that this scenario does *not* in fact give the minimum variation in $g(t)$. The key distinction is that the odd terms are *always* zero for the four-channel case, not just when $\phi = 180°$ as in the two-channel case. Effectively, this allows the system to

select some other value of ϕ with no "penalty." In other words, the two-channel system needed to have $\phi = 180°$ in order to eliminate the dominant $n = 1$ terms; but the four-channel system has eliminated these "automatically" (*i.e.* thanks to the two-channel pairing scheme discussed above).

Therefore, the system is now "free" to choose a different ϕ to eliminate some of the other modes that remain, without a penalty associated with the odd modes. The best way to do this is to choose $\phi = 90°$, which eliminates *half* of the remaining modes. One can imagine the problem being divided in half (*i.e.* half the interval for ϕ and double the frequency): $\phi = 90°$ eliminates the $n = (2,4,6, \dots)$ modes over the interval $(0°, 180°)$ in the same way that $\phi_2 = 180°$ eliminates the $n = (1,2,3, \dots)$ modes over the interval $(0°, 360°)$ in the two-channel problem.

This result is shown in Table 7-6, where the $\phi = 90°$ case has eliminated all modes except when n is a multiple of 4. Figure 7-6 gives a graphical representation of the differences in the remaining $g(t)$ terms for each case ($\phi = 180°$ versus $\phi = 90°$). Note that the scale of the vertical axis has been reduced compared with Figure 7-4; this is because most of the contributions to $g(t)$ had already been eliminated by eliminating A_1 (which was done automatically by the four-channel model), and the remaining terms were significantly smaller. And, as with the choice of $\phi_2 = 180°$ in the two-channel case, the choice of $\phi = 90°$ in the four-channel case eliminated the large majority of the remaining contribution to $g(t)$ (in this case, by eliminating the A_2 term).

Table 7-6. Terms in $g(t)$ for four channels and two different phase shift patterns.

n	Four chans., $\phi_i = (0,0,180°,180°)$ (side-to-side case)	Four chans., $\phi_i = (0,90°,180°,270°)$ (rotating mode case)
0	a_0	a_0
1	0	0
2	$a_2 \cos(2\omega t) + b_2 \sin(2\omega t)$	0
3	0	0
4	$a_4 \cos(4\omega t) + b_4 \sin(4\omega t)$	$a_4 \cos(4\omega t) + b_4 \sin(4\omega t)$
5	0	0
6	$a_6 \cos(6\omega t) + b_6 \sin(6\omega t)$	0
7	0	0
8	$a_8 \cos(8\omega t) + b_8 \sin(8\omega t)$	$a_8 \cos(8\omega t) + b_8 \sin(8\omega t)$

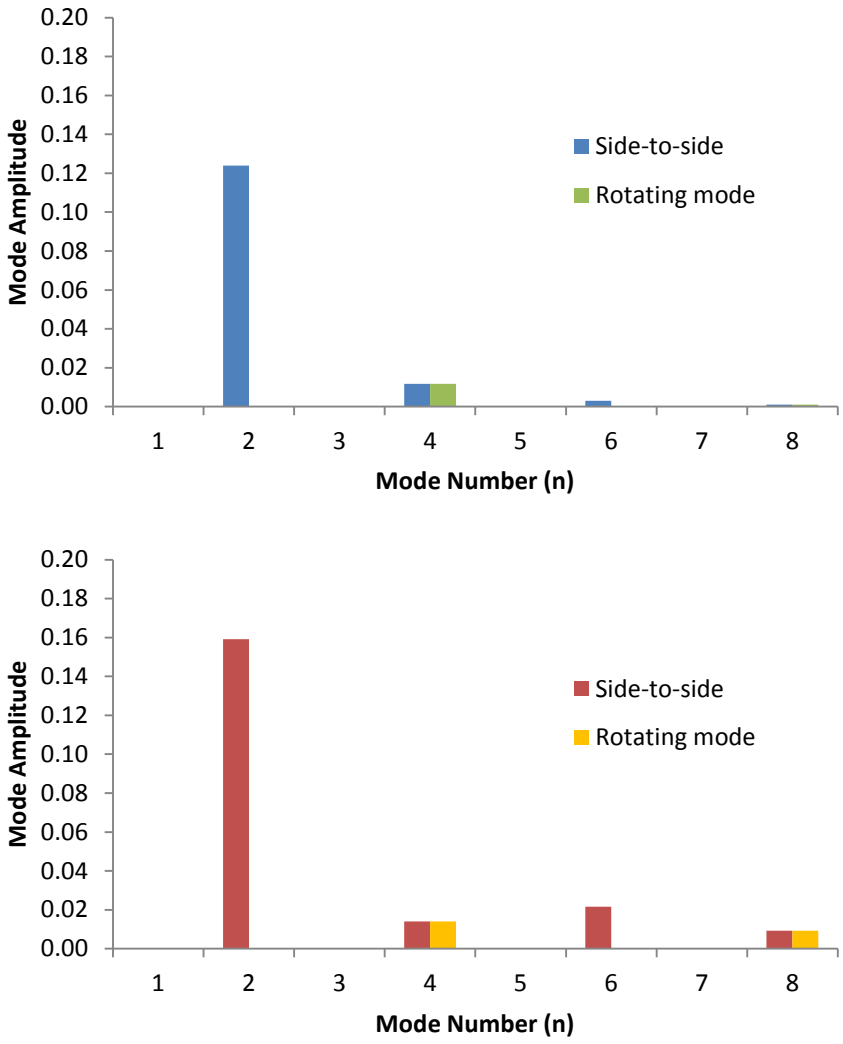

Figure 7-6 – Amplitudes of frequency modes (A_n) for the average flow rate ($g(t)$) for the four-channel side-to-side and rotating mode in-phase and out-of-phase cases, based on the normalized values for Signal A (top) and Signal B (bottom), respectively

Figure 7-7 shows the L-norms of $(g(t) - \tilde{g})$ for the four-channel case as a function of ϕ. In principle, ϕ only needed to be varied over the range $(0°, 180°)$, but it was varied over the range $(0°, 360°)$ in the figure in order to make the relationship with the two-channel case easier to understand (*i.e.* the "dividing in half" of the ϕ interval as discussed above). Note that some slight asymmetries appear in the L^{∞}-norm for Signal A; this was merely a result of the coarse timestep size of the original signal (see Figure 7-2), which meant that small differences in the signal from one period to the next were present due to numerical discretization error. If this was not the case, the portion of the

curve from $(0°, 180°)$ in Figure 7-7 would have been completely identical to the curve from $(180°, 360°)$.

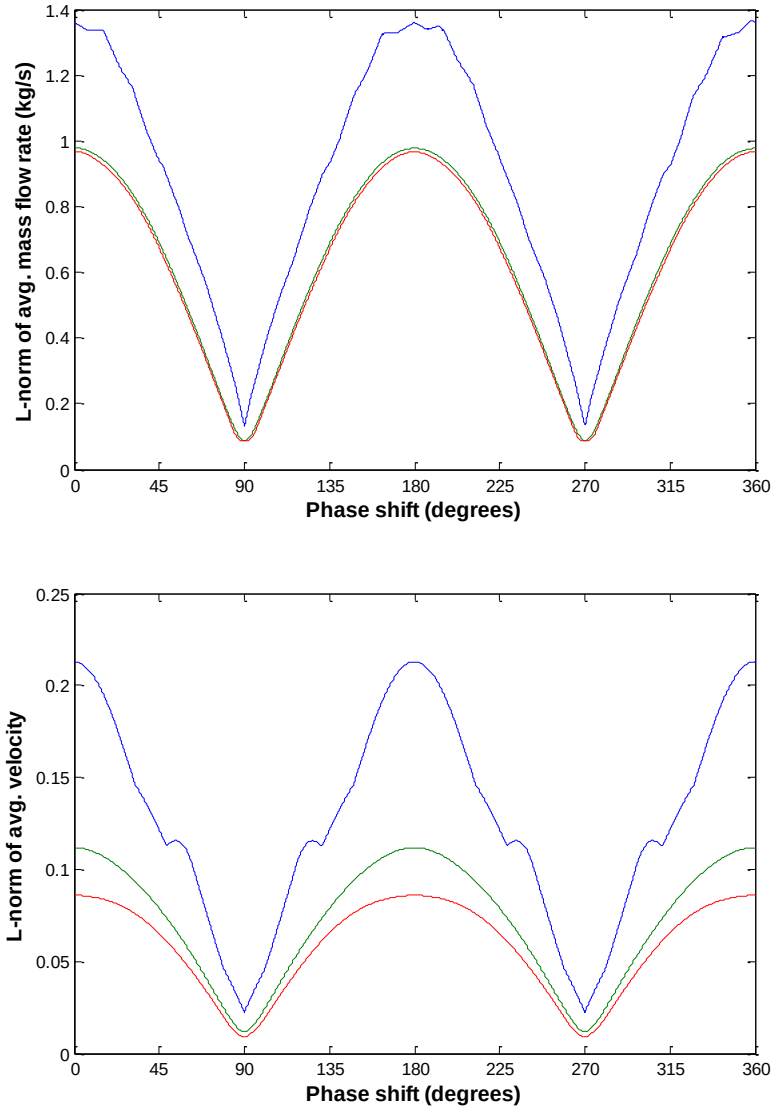

Figure 7-7 – L-norms of the variation in average flow rate as a function of ϕ_2 over the range $(0°, 180°)$ for the four-channel case, for Signal A (top) and Signal B (bottom)

It is important to note that the *maximum* value of each L-norm in the four-channel case was equal to the *minimum* value of each L-norm in the two-channel case. As discussed above, the four-channel case essentially starts from where the two-channel case ends, in terms of eliminating additional $g(t)$ components and minimizing the variation in the average flow rate.

Explanation of Behavior Seen in Phase Plots

In addition to the *asymptotic* limit cycle behavior (*e.g.* the final $(0°, 90°, 180°, 270°)$ behavior), the Fourier analysis shown above also sheds light on the transient behavior of the four-channel system leading up to the asymptotic results.

In particular, recall the phase shift plots from previous four-channel simulations, *e.g.* Figure 6-25, that two pairs of channels always form first (with a $180°$ phase shift within each pair), followed by a much more gradual change in the phase shift between Pair 1 and Pair 2 to eventually the $(0°, 90°, 180°, 270°)$ behavior.

The reason for this behavior is the following. Based on Figure 7-3, the lowest-frequency mode of the original signal has by far the largest amplitude; therefore, for arbitrary initial phase shifts between channels, the $n = 1$ mode will create by far the largest fluctuations in the average flow rate. This will create a very large driving force for the system to attempt to eliminate those fluctuations (since the system prefers no average flow fluctuations, as discussed in Section 7.1).

As a result, two pairs of channels will quickly form due to this large driving force, in order to eliminate the biggest source of average flow variation, the $n = 1$ mode. And, since the remaining terms are smaller in amplitude and therefore cause much smaller fluctuations in the average flow rate, there is much less of a driving force to eliminate those components, hence they are eliminated much more slowly (*i.e.* the phase shift ϕ between the channels slowly moves towards $90°$ to eliminate the $n = 2$ mode and others).

This is borne out in Figure 7-5 and Figure 7-7, which show that the initial selection of $\phi_2 = 180°$ (within each channel pair) allows the L^2-norm of the average flow fluctuations to decrease from approximately 8.0 to 1.0, a decrease of about 7.0, while the follow-up adjustment in ϕ (between the two pairs) only decreases this same norm from 1.0 to about 0.1, a decrease of 0.9. In other words, the ϕ_2 adjustment was about 7 times more effective than the ϕ adjustment, and one would perhaps expect the ϕ_2 adjustment to occur roughly a factor of 7 times quicker than the ϕ adjustment as well.

In fact, this was roughly what was observed in Figure 5-4: once the oscillation amplitudes had saturated, it took roughly 200 seconds (t=200 s to t=400 s) for the channels to form into pairs, but roughly 1300 seconds (t=200 s to t=1500 s) for the final rotating behavior to be established – a rough factor of 6.5 difference.

This further increases the confidence that the rotating-mode behavior is indeed explainable by the approach shown in this chapter, and that the physical intuitions shown here correctly describe the behavior of the system.

Extension to N-Channel Systems

One could easily extend this analysis to 3-channel systems, or systems with 5 or more channels. It is expected that such an analysis would lead to the conclusion that the minimum average flow variation would be achieved with a $(2\pi/N)$, or $(360°/N)$, phase pattern, *i.e.* the N channels oscillating with phases spaced $(360/N)$ degrees apart. This is an extension of the rotating mode behavior, and it was the behavior found in the TRACE simulations in Section 0 for all values of N that were attempted ($N = 2, 3, 4, 5$ and 8).

For the cases where N is prime, assuming that all channels have the same oscillation amplitude, the $(360°/N)$ behavior will be preferred, since this is the only configuration that will ensure that the $n = 1$ mode is eliminated from $g(t)$[6]. Therefore, a Fourier analysis of this case would be expected to yield the same $(360°/N_1)$ result as long as the $n = 1$ mode is the dominant mode in $f_1(t)$.

However, when N is not prime, the $(360°/N)$ behavior is no longer the only pattern that eliminates the $n = 1$ mode from $g(t)$. For example, when $N = 4$, two pairs of channels can form, such that the $n = 1$ mode is eliminated regardless of the value of ϕ between each pair.

Therefore, a piecewise approach would be required for the general case of determining the optimal phase shift pattern based on Fourier expansion analysis for arbitrary N. This approach is summarized as follows:

1. Find the prime factorization of N such that $N = N_1^a N_2^b N_3^c \ldots$, with $N_1 < N_2 < N_3$.

[6] This is analogous to the discussion in Section 0, which discussed this in the context of eliminating the flow variations for the case of linear oscillations (which, again, consist only of an $n = 0$ oscillatory mode and no higher modes).

2. Perform the analysis for a system with N_1 channels first[7]. Find that the optimal phase shift behavior is $\phi = (360°/N_1)$ between channels, which eliminates the A_1 mode amplitude term (and possibly others).
3. If $a > 1$, consider a system with number of channels $N^* = N_1^2$, with N_1 groups of channels with each group containing N_1 channels in a $(360°/N_1)$ pattern. The Fourier analysis should determine that a $\phi = (360°/N_1^2)$ behavior is optimal, as it eliminates the A_2 amplitude term.
4. Repeat step 3 until $N^* = N_1^a$, with N_1 groups containing $(a-1)$ levels of subgroups, each subgroup level containing N_1 of the subgroup level below it. In the end of step 4, a value of $\phi = (360°/N_1^a)$ will be found as the optimal one, with each level successively eliminating the leading component of $g(t)$ that remains.
5. Consider a system with $N^* = N_1^a N_2$ channels, with N_2 groups containing all a levels of subgroups from part 4. A value of $\phi = (360°/N_1^a N_2)$ will be optimal.
6. Repeat in the same manner until $N^* = N_1^a N_2^b N_3^c$ and the total number of levels of nested subgroups is $(a+b+c)$, each level having the corresponding number (N_1, N_2, or N_3) of subgroups associated with it. The final step will have an optimal value of $\phi = \left(360°/N_1^a N_2^b N_3^c\right)$, *i.e.* $\phi = (360°/N)$.

Step 6 will have completed the analysis, resulting in an optimal configuration of N channels, each with different phase shifts spaced apart by $(360°/N)$. Of all the possible combinations of phase shifts between the N channels, this configuration *should* be the one that provides the minimum possible variation in the average flow rate.

However, this conclusion rests on one main assumption: in the original $f_1(t)$ signal, the amplitude of each frequency mode should, *on average*, decrease substantially from one mode to the next as n is increased. As seen in the previous subsection, not *every* mode amplitude has to be less than the one before it in order for the $(360°/N)$ behavior to be favored; however,

[7] The smallest factor seems likely to be the one that will drive the limit cycle behavior first; hence, it may be best to start with that factor first. For example, for $N = 6$, the limit cycle would likely gravitate towards 3 sets of 2-channel groups more readily than 2 sets of 3-channel groups. However, this is based only on intuition at this point. Regardless of which factors are chosen for analysis first, the results should be the same.

this is the general trend that must be followed, if the $(360°/N)$ behavior is to hold for larger and larger values of N. For example, in the $N = 4$ system in the previous subsection, the two pairs of channels only formed into a $90°$ behavior with each other because the A_2 mode amplitude was much larger than the other remaining ones (A_4, A_6, etc.). If that were not the case, the $(360°/N)$ behavior would have been less strongly favored over other possibilities, and might not have even been the optimal one overall. Similarly, as more and more groups and subgroups of channels are nested together in the above analysis for general N, if for some reason there were enough high-frequency components that were relatively stronger than the next lower frequency components somewhere down the line, the $(360°/N)$ might not be optimal. Certainly, too, in a real system which would exhibit a degree of noise and small-scale fluctuations in the operating conditions, the driving force for a precise $(360°/N)$ phase shift between channels would simply not be strong enough once N gets large enough and the subgroups of channels get too numerous; thus, the analysis in this section is largely academic in nature, and is not expected to be easily verifiable experimentally.

Chapter 8. Conclusions and Future Work

8.1 Conclusions

The following conclusions have been made regarding the use of the TRACE/PARCS code system for stability analysis:

- The TRACE/PARCS code was successfully able to reproduce the stability behavior of the Ringhals-1 BWR, showing good agreement with the measured data for both in-phase and out-of-phase stability points.
- An in-phase stability event in the Oskarshamn-2 BWR was successfully reproduced with a full-core TRACE/PARCS model, able to capture not only linear stability characteristics (decay ratio, natural frequency) but also the behavior for large-amplitude, nonlinear oscillations with amplitudes of roughly $\pm$50% rated power.
- Numerical diffusion was found to be an important source of error for stability calculations using first-order discretization methods such as in TRACE. However, an approach was developed which uses an optimized selection of (nonuniform) axial node spacing, timestep size, and discretization method, in order to minimize the numerical diffusion, leading to a more accurate predictive capability for stability analysis using TRACE/PARCS.

The following conclusions have been made regarding the use of TRACE/PARCS for limit cycle calculations:

- The TRACE/PARCS simulations were extended to the analysis of limit cycle oscillations using a modified form of the original validated Ringhals model. Both in-phase and out-of-phase models were successfully established in the simulations.

- A new subroutine was implemented into the PARCS code to calculate the eigenvalues and eigenvectors for the higher λ-modes of the neutron flux, in order to gain physical insights into the system.
- Additionally, the functionality was added to decompose the time-dependent 3D power shape in terms of the eigenvectors of the static neutron flux, yielding time-dependent amplitude values for each mode which could be used to extract useful information for out-of-phase oscillations.
- An interesting behavior was observed in certain out-of-phase limit cycle simulations, in which the power level rotates azimuthally over time with a more or less steady rate of rotation. This behavior was then described in terms of a $90°$ phase shift between the first two azimuthal modes of the neutron flux. It was found that this phase shift persisted even if the two azimuthal modes had different natural frequencies, indicating that a particular nonlinear coupling mechanism was at play, leading to the "rotating mode" behavior.
- However, in a separate simulation with a similar full-core model, rather than a rotating mode limit cycle behavior with a $90°$ phase shift between azimuthal modes, a "side-to-side" limit cycle behavior was observed which showed a preference for a $0°$ phase shift between azimuthal modes.
- The practical importance of the side-to-side mode versus the rotating mode was explored by examining the maximum power level reached in each channel during each type of oscillation pattern. It was found that the rotating mode gave a larger "ring" of hot channels during the oscillations, compared to the side-to-side mode in which only a few channels experienced the maximum power level. This was related to safety and fuel performance considerations, as a greater number of hot channels would yield a greater number of expected fuel failures.
- An additional study demonstrated the importance of introducing a small source of artificial noise into the system to excite *both* the in-phase and out-of-phase modes during stability simulations; failure to do so could lead to mistaken conclusion that

the in-phase mode is the most unstable when in reality the out-of-phase mode was instead, or vice versa, if an insufficiently long simulation time is taken.

The following conclusions were made regarding the simplified N-channel TRACE model:

- A simplified N-channel TRACE model was created to develop physical insights into the behavior observed in the full-core model. The new model used a simplified VESSEL component and a fixed total flow rate boundary condition, with the flow divided among the N identical channels in parallel. This resulted in out-of-phase limit cycle oscillations, for which the phase shifts between channels were plotted and analyzed.
- For odd N, the results agreed with the results from previous studies in the literature – namely, the N channels oscillate with evenly-spaced phase shifts of $(360°/N)$, in order to maintain a constant total flow rate.
- However, for even N, the results found here contrasted with those found in previous studies, which claimed only that the channels would form into $N/2$ pairs, with a phase shift of $180°$ within each pair. In contrast, the results found in this thesis for nonlinear limit cycle oscillations indicated a specific preference for the $(360°/N)$ behavior, with two pairs of counter-oscillating channels forming first, then a gradual approach towards a $90°$ phase shift between the two pairs.
- In the standalone TH case (TRACE), the ordering of channels was arbitrary; however, a coupled case (TRACE/PARCS) was run which found the same phase shift pattern except with the channels forced to oscillate in clockwise or counterclockwise order (depending on initial conditions). This rotating behavior was directly analogous to the behavior seen in the full-core model (in terms of the first two azimuthal modes with a relative phase shift of $90°$).

The following conclusions were made regarding the reduced-order model:

- A reduced order model was implemented which allowed for N parallel channels and (optionally) up to M neutronic modes. The model used a fixed pressure drop boundary condition across the core.
- For a single-channel model, steady-state results matched the previously reported values from the original study from which the model originated. Transient results (*i.e.* linear stability characteristics) appeared to agree as well.
- For multi-channel standalone TH cases, in order to promote either out-of-phase or in-phase instability, it was necessary to include two additional pressure drop terms which operated on the core average inlet and outlet flow rates, respectively. The reason why these terms affected the mode of oscillation was explained in detail, in terms of the relative magnitudes of the single-phase and two-phase pressure drops and the dynamic behavior of each under different oscillation modes.
- For standalone TH cases with four channels, the system was once again found to prefer the rotating-mode behavior in the limit cycle, with a $90°$ phase shift between channels.
- However, for cases with four TH channels and three neutronic modes, different behaviors were observed depending on the relative magnitude of the inlet plenum pressure loss coefficient and the reactivity feedback coefficients, which affect the strength of the TH channel coupling and neutronic channel coupling, respectively. For cases with strong TH coupling, the rotating mode was favored, with an asymptotic phase shift pattern of $(0°, 90°, 180°, 270°)$, but for cases with strong neutronic coupling, the "side-to-side" mode was favored, with an asymptotic phase shift pattern of $(0°, 0°, 180°, 180°)$. This was analogous to the behavior seen with the full-core TRACE/PARCS models, which showed either a rotating or side-to-side behavior, depending on the model.

The conclusions regarding a physical explanation for the rotating mode behavior were as follows:

- For standalone TH cases, it was shown that, for a particular set of system configurations, the most unstable oscillation pattern is the one which minimizes the variation in the total (or average) flow rate. Namely, this is true for systems in which the out-of-phase mode is the dominant mode.
- Separately, a mathematical analysis was performed to determine the behavior of the average flow rate for four-channel systems under different oscillation patterns. This analysis expressed the individual channel flow rates using Fourier expansions and determined the effect of different phase shifts between channels on the average flow rate in terms of the individual Fourier mode amplitudes.
- It was found that the side-to-side mode eliminates all odd-numbered Fourier modes from the average flow rate, while the rotating mode eliminates the odd modes plus modes 2, 6, 10, etc. Hence, under normal circumstances, the rotating mode was found to give the minimum possible variation in the average (or total) flow rate
- This conclusion was confirmed by using two specific inlet velocity profiles $v(t)$ from limit cycle simulations performed earlier; these were decomposed into Fourier modes, showing that the signal was dominated by the lowest-frequency mode, with diminishing contributions in general for each successive mode.
- As a result, it was found that the side-to-side oscillation pattern eliminated on the order of 90% of the variation in average flow, by eliminating the dominant ($n = 1$) term; while the rotating mode eliminated on the order of 99% of the variation in average flow, due to eliminating the next-most dominant ($n = 2$) term as well.
- Furthermore, a connection was made to the original limit cycle simulation for this case, which found that the time required for the channels to form into pairs (thus eliminating the $n = 1$ term) was roughly one-tenth the time required for the eventual rotating behavior to be established (thus eliminating the $n = 2$ term), and this was attributed to the fact that the latter case had a roughly ten times stronger effect on reducing the variation in average flow rate (thus creating a ten times

stronger “driving force” for the system to eliminating that mode from the average oscillations). This provided clear evidence to support the physical explanation for why the rotating mode is preferred, as mentioned above.

- In general, this analysis indicates that the larger the limit cycle amplitude is, the more quickly the system will converge to the rotating behavior. This is because larger-amplitude oscillations will have larger contributions from higher-frequency Fourier components (i.e. the oscillations are more nonlinear) than small-amplitude oscillations which behave nearly linearly. Therefore, larger-amplitude oscillations benefit more from the rotating behavior, in terms of having larger overall variations in total flow rate, thus a stronger driving force for establishing the rotating behavior.

One additional conclusion is made which ties together conclusions from multiple sections above:

- The above conclusions on the observed four-channel limit cycle behavior, as well as the Fourier analysis of the average flow rate, lead to the possible additional conclusion that the rotating mode might be favored for larger BWR cores (with more channels), while the side-to-side mode might be favored for smaller cores. This is because, as the reduced order model indicated, the neutronic coupling between channels seems to favor the side-to-side mode; however, as the (radial) size of the core is increased, the core becomes increasingly decoupled in terms of neutronics, meaning that the strength of neutronic coupling among channels would probably weaken compared to the TH coupling among channels. Additionally, in terms of TH, having a larger number of channels might cause the rotating mode to become even *more* favorable than in the four channel case, since the channels can more and more evenly distribute themselves in terms of phase shift in order to eliminate more and more Fourier components from the average flow rate signal. This would create an even *greater* advantage for the rotating mode versus the side-to-side mode; and, along with the neutronic decoupling of the core, the result would likely be that the

rotating mode becomes increasingly favored over the side-to-side mode as the size of the core (and number of channels) increases.

8.2 Future Work

The following additional recommendations for future work are provided which would further extend the understanding of out-of-phase limit cycle behavior in BWRs using the reduced order model:

- An effort should be made to better understand why the neutronic field appears to favor the side-to-side out-of-phase oscillation mode while the TH field favors the rotating oscillation mode. A more in-depth study should be performed in an attempt to explain the side-to-side or transition behavior in terms of simple physical insights, as was accomplished for standalone TH in explaining the rotating mode.
- The possibility discussed above – that the rotating mode might be favored for larger cores and the side to side mode favored for smaller cores – should be investigated with the reduced order model first. For example, a 9-channel or 16-channel system with neutronic coupling could be set up in the same manner as the 4-channel system, and a detailed study could reveal whether a slightly greater neutronic coupling versus TH coupling is needed to give the side-to-side behavior instead of the rotating. Eventually, if this proves fruitful, the study could be extended to full-core models, and/or using TRACE/PARCS.
- Additional boundary conditions for the reduced order model could be investigated, such as inclusion of some simple recirculation loop dynamics as has been performed by other authors. This could potentially prove interesting for the study of rotating versus side-to-side limit cycle oscillations, to determine whether similar conclusions hold for these other boundary condition types as well. Such a boundary condition treatment would relate more closely to the behavior of real BWRs.
- Additional work should be done to more precisely quantify the conditions under which a four-channel model will experience in-phase or out-of-phase oscillations, in terms of the inlet/outlet plenum loss factors, the reactivity feedback coefficients, the azimuthal mode subcriticality, etc.. This understanding could be

used to inform future studies with a full-core TRACE/PARCS model using a more realistic treatment of recirculation loop dynamics and 3-D core effects, which could ultimately lead to a more robust prediction of whether a core will be in-phase or out-of-phase unstable.

- For the reduced order model, additional cases could be run in which not all four channels are identical. For example, if one azimuthal mode was only *slightly* more unstable than the other, how much eigenvalue separation would be tolerated before the behavior switched from a rotating mode to a side-to-side mode favoring the dominant eigenvalue? Such a question would have important implications for real BWR cores for which the first two azimuthal modes are typically not identical.

The following recommendations for future work are suggested for extending the application of the TRACE/PARCS code system to the understanding of out-of-phase instabilities:

- The simplified four-channel TRACE model should be extended to include a fixed pressure drop boundary condition (unlike the fixed flow rate boundary condition currently used). This would allow for both the in-phase and out-of-phase modes to occur, and would allow one to examine whether the conclusions drawn from the reduced-order model would apply to TRACE as well – for example, whether the inlet and outlet plenum loss factors determine the in- and out-of-phase behavior in the same way, and likewise for the rotating mode behavior versus side to side behavior.
- Using the existing full-core TRACE/PARCS model, finding an out-of-phase unstable case proved highly difficult and time-consuming. To give more predictable and repeatable results in terms of in- versus out-of-phase oscillations, the simplified 1-D VESSEL component with no bypass flow (used originally in the four-channel TRACE model) could be used with a full-core model instead. This could lead to similar studies as were performed with the reduced order model, only with a more representative BWR core.

Finally, the following specific recommendation for future work is provided regarding the physical explanation for the rotating behavior given in Chapter 7:

- The analysis in Chapter 7 was performed for just two nonlinear oscillation shapes based on particular simulations that were performed. However, for completeness, the mathematical analysis should be extended to include all possible nonlinear oscillation shapes that might be encountered during any limit cycle oscillations in a TH channel. Such an analysis might, for example, place restrictions on the maximum possible amplitude of particular higher-frequency Fourier components for realistic cases; and then the mathematical analysis could be performed to ensure that the $\phi = 90°$ (*i.e.* rotating mode) behavior minimizes the total flow variation (hence is the favored mode) for the entire broader range of cases.

Works Cited

[1] F. D'Auria, "The BWR stability issue," in *THICKET*, 2008.

[2] J. March-Leuba and J. M. Rey, "Coupled thermohydraulic-neutronic instabilities in boiling water reactors: a review of the state of the art," *Nuclear Engineering and Design*, vol. 145, pp. 97-111, 1993.

[3] P. Balestra, C. Parisi, E. Negrenti and M. Sepielli, "Modeling by RELAP5-3D system code of the instability transient occurred on 25th February 1999 at the Oskarshamn-2 BWR," *Energia, Ambiente e Innovazione,* vol. 6, 2013.

[4] J. Blomstrand, "The KKL core stability test, conducted in September 1990," ABB-Report BR91-245, 1992.

[5] C. Demaziere and I. Pazsit, "On the possibility of the space-dependence of the stability indicator (decay ratio) of a BWR," *Annals of Nuclear Energy,* vol. 32, pp. 1305-1322, 2005.

[6] R. Miro, D. Ginestar, D. Hennig and G. Verdu, "On the regional oscillation phenomenon in BWR's," *Progress in Nuclear Energy,* vol. 36, no. 2, pp. 189-229, 2000.

[7] F. Zinzani, C. Demaziere and C. Sunde, "Calculation of the eigenfunctions of the two-group neutron diffusion equation and application to modal decomposition of BWR instabilities," *Annals of Nuclear Energy,* vol. 35, pp. 2109-2125, 2008.

[8] D. Hennig, "A study on boiling water reactor stability behavior," *Nuclear Technology,* vol. 126, pp. 10-31, 1999.

[9] A. Dokhane, D. Hennig, Rizwan-uddin and R. Chawla, "Interpretation of in-phase and out-of-phase BWR oscillations using an extended reduced order model and semi-analytical bifurcation analysis," *Annals of Nuclear Energy,* vol. 32, pp. 271-287, 2007.

[10] L. S. Tong, Boiling Heat Transfer and Two-Phase Flow, New York: John Wiley and Sons, Inc., 1965.

[11] J. A. Boure, "Review of Two-Phase Flow Instability," *Nuc. Eng. Des.*, pp. 165-192, 1973.

[12] A. E. Bergles, P. Goldberg and J. S. Maulbetsch, "Acoustic Oscillations in a High Pressure Single Channel Boiling System," in *EURATOM Report, Proc. Symp. on Two-phase flow dynamics*, Eindhoven, Netherlands, 1967.

[13] H. Firstenberg, K. Goldmann and J. H. Hudson, "Boiling Songs and Associated Mechanical Vibrations," NDA-2131-12, 1960.

[14] W. Ambrosini, P. Di Marco and J. C. Ferreri, "Linear and nonlinear analysis of density wave instability phenomena," 2001.

[15] G. Verdu, D. Ginestar, V. Vidal and R. Miro, "Modal decomposition method for-BWR stability analysis," *Nuc. Sc. and Tech.*, vol. 35, no. 8, pp. 538-546, 1998.

[16] A. Dokhane, "BWR stability and bifurcation analysis using a novel reduced order model and the system code RAMONA," Lausanne, 2004.

[17] K. Hashimoto, "Linear modal analysis of out-of-phase instability in boiling water reactor cores," *Ann. Nuc. En.*, vol. 20, no. 12, pp. 789-797, 1993.

[18] J. L. Munoz-Cobo, R. B. Perez, D. Ginestar, A. Escriva and G. Verdu, "Nonlinear analysis of out of phase oscillations in boiling water reactors," *Annals of Nuclear Energy*, vol. 23, pp. 1301-1335, 1996.

[19] K. O. Ott, Introductory Nuclear Reactor Dynamics, La Grange Park, Illinois: American Nuclear Society, 1985.

[20] J. Guckenheimer and P. Holmes, Nonlinear oscillations, dynamical systems and bifurcations of vector fields, New York: Springer Verlag, 1983.

[21] D. G. Zill and M. R. Cullen, Advanced Engineering Mathematics, Sudbury, MA: Jones and Bartlett Publishers, 2006.

[22] J. March-Leuba, "Dynamic behavior of boiling water reactors," Knoxville, Tennessee, 1984.

[23] T. van der Hagen, R. Zboray and W. de Kruijf, "Questioning the use of the decay ratio in BWR stability monitoring," *Ann. Nuc. En.*, vol. 27, pp. 727-732, 2000.

[24] J. March-Leuba, D. G. Cacuci and R. B. Perez, "Nonlinear dynamics and stability of boiling water reactors: Part 1 - Qualitative analysis," *Nuc. Sci. and Eng.*, vol. 93, pp. 111-123, 1986.

[25] J. L. Munoz-Cobo and G. Verdu, "Application of Hopf bifurcation theory and variational methods to the study of limit cycles in boiling water reactors," *An. Nuc. En.*, vol. 18, no. 5, pp. 269-302, 1991.

[26] M. Tsuji, K. Nishio and M. Narita, "Stability analysis of BWRs using bifurcation theory," *J. Nuc. Sci. and Tech.*, vol. 30, no. 11, pp. 1107-1119, 1993.

[27] A. A. Karve, Rizwan-uddin and J. J. Dorning, "Stability analysis of BWR nuclear coupled thermal-hydraulics using a simple model," *Nuc. Eng. and Des.*, vol. 177, pp. 155-177, 1997.

[28] C. Lange, D. Hennig and A. Hurtado, "An advanced reduced order model for BWR stability analysis," *Prog. Nuc. En.*, vol. 53, no. 1, pp. 139-160, 2011.

[29] Rizwan-uddin, "Turning points and sub- and supercritical bifurcations in a simple BWR model," *Nuc. Eng. and Des.*, vol. 236, pp. 267-283, 2006.

[30] C. Lange, D. Hennig and A. Hurtado, "A novel result in the field of nonlinear stability analysis of boiling water reactors," *International Journal of Bifurcation and Chaos*, vol. 22, no. 2, 2012.

[31] A. Dokhane, H. Ferroukhi and A. Pautz, "On out-of-phase higher mode oscillations with rotation and oscillation of symmetry line using an advanced integral stability methodology," *Ann. Nuc. En.*, vol. 67, pp. 21-30, 2013.

[32] S. Andersson and M. Stepniewski, "RAMONA-3B calculations of core-wide and regional power/flow oscillations - comparison with Oskarshamn 3 natural circulation test data," in *Proceedings of the OECD/CSNI International Workshop on Boiling Water Reactor Stability*, Brookhaven, Holtsville NY, 1990.

[33] J. Spore, "LA-UR-00-910 TRAC-M/FORTRAN 90 Theory Manual," Los Alamos National Laboratory, Los Alamos, NM, 2000.

[34] T. Downar, V. Seker and A. Ward, "PARCS: Purdue Advanced Reactor Core Simulator," in *Proceedings of the ANS Reactor Physics Topical Meeting PHYSOR 6*, Vancouver, BC, 2006.

[35] J. March-Leuba, "Time-space nodalization issues in BWR stability calculations," in *NURETH-15*, Pisa, Italy, 2013.

[36] F. Odar, C. Murray, R. Shumway, M. Bolander, D. Barber and J. Mahaffy, "TRACE/RELAP Advanced Computational Engine (TRACE) V5.0 User Manual," US NRC, 2009.

[37] "TRACE V5.0 Theory Manual: Field Equations, Solution Methods, and Physical Models," U.S. NRC, 2008.

[38] C. A. de Moura and C. S. Kubrusly, The Courant-Friedrichs-Lewy (CFL) Conditon: 80 Years After Its Discovery, Birkhauser, 2013.

[39] "Thermophysical Properties of Fluid Systems," NIST, [Online]. Available: http://webbook.nist.gov/chemistry/fluid/. [Accessed 5 May 2014].

[40] Y. Xu, T. Downar, K. Ivanov, J. Vedovi, A. Petruzzi and J. Staudenmeier, "Analysis of the OECD/NEA Ringhals instability benchmark with TRACE/PARCS," in *ANS Mathematics and Computation Meeting*, Avignon, 2005.

[41] Y. Xu, T. Downar, R. Walls, K. Ivanov, J. Staudenmeier and J. March-Leuba, "Application of TRACE/PARCS to BWR stability analysis," *Annals of Nuclear Energy*, vol. 36, pp. 317-323, 2009.

[42] S. L. Marple, Digital Spectral Analysis with Applications, Englewood Cliffs: Prentice Hall, 1987.

[43] J. L. Munoz, G. Verdu and C. Pereira, "Dynamic reconstruction and lyapunov exponents from time series data in boiling water reactors," *Ann. Nuc. En.*, vol. 19, p. 223, 1992.

[44] K. Ivanov, T. Beam, A. Baratta, A. Irani and N. Trikouros, "PWR MSLB Benchmark. Volume 1: Final Specifications," NEA/NSC/DOC(99)8.

[45] J. Solis, K. Ivanov, B. Sarikaya, A. Olson and K. Hunt, "BWR TT Benchmark. Volume I: Final Specifications," NEA/NSC/DOC(2001)1.

[46] B. Ivanov, K. Ivanov, P. Groudev, M. Pavlova and V. Hadjiev, "VVER-1000 Coolant Transient Benchmark (V1000-CT). Phase 1 - Final Specification," NEA/NSC/DOC(2002)6.

[47] L. A. Carmichael and R. O. Niemi, "Transient and Stabilty Tests at Peach Bottom Atomic Power Station Unit 2 at End of Cycle 2," EPRI NP-564, 1978.

[48] T. Lefvert, "Ringhals 1 stability benchmark specifications," NEA/NSC/DOC(94), 1994.

[49] G. Verdu, "Forsmark 1 & 2 Boiling Water Reactor Stability Benchmark, Time Series Analysis Methods for Oscillation during BWR Operation - Final Report," NEA/NSC/DOC(2001)2.

[50] T. Kozlowski, "BWR Stability Event Benchmark based on Oskarshamn-2 1999 Feedwater Transient. Final Draft.," NEA/NSC/DOC(2013).

[51] J. March-Leuba, C. G. Thurston and T. L. Huang, "Time-space nodalization issues in BWR stability calculations," in *NURETH-15*, Pisa, Italy, 2013.

[52] Y. Xu and T. Downar, "GenPMAXS, Code for Generating the PARCS Cross Section Interface File PMAXS," Purdue University, PU/NE-00-20 (Rev. 9).

[53] T. Kozlowski, S. Roshan, T. Lefvert, T. Downar, Y. Xu, A. Wysocki, K. Ivanov, J. Magedanz, M. Hardgrove, C. Netterbrant, J. March-Leuba, N. Hudson, O. Sandervag and A. Bergman, "TRACE/PARCS validation for BWR stability based on OECD/NEA

Oskarshamn-2 Benchmark," in *The 14th International Topical Meeting on Nuclear Reactor Thermohydraulics*, Toronto, 2011.

[54] P. L. Woodfield, M. Monde and Y. Mitsutake, "Improved analytical solution for inverse heat conduction problems on thermally thick and semi-infinite solids," *International Journal of Heat and Mass Transfer,* vol. 49, pp. 2864-2876, 2006.

[55] I. Gajev, W. Ma and T. Kozlowski, "Space-time convergence analysis on BWR stability using TRACE/PARCS," *Ann. Nuc. En.*, vol. 51, 2013.

[56] J. March-Leuba and E. D. Blakeman, "A mechanism for out-of-phase power instabilities in boiling water reactors," *Nuclear Engineering and Design,* vol. 107, pp. 173-179, 1991.

[57] G. M. Grandi and K. S. Smith, "BWR stability analysis with SIMULATE-3K," in *Proc. of International Conference on the New Frontiers of Nuclear Technology Safety and High Performance Computing (PHYSOR-2002),* Seoul, Korea, 2002.

[58] S. Nakanishi, M. Ozawa and S. Ishigai, "The Modes of Flow Oscillation in Multi-Channel Two-Phase Flow Systems," in *Advances in Two-Phase Flow and Heat Transfer*, vol. II, S. Kakac and M. Ishii, Eds., Boston, Martinus Nijhoff Publishers, 1983, pp. 709-724.

[59] A. A. Karve, "Nuclear-coupled thermal-hydraulic stability analysis of boiling water reactors," University of Virginia, 1998.

[60] N. E. Todreas and M. S. Kazimi, Nuclear Systems I: Thermal Hydraulic Fundamentals, New York: Taylor and Francis Group, 1990.

[61] J. D. Lee and C. Pan, "The complex nonlinear dynamics in the multiple boiling channels coupling with multi-point reactors with constant flow rate," *An. Nuc. Energy,* vol. 71, pp. 174-189, 2014.

[62] D. F. D'Arcy, "An experimental investigation of boiling channel flow instability," in *Proc. Symp. Two-Phase Flow Dynamics*, Eindhoven, Netherlands, 1967.

[63] J. Borkowski, "SIMULATE-3K simulation of the Ringhals 1 BWR stability measurements," in *PHYSOR96*, Mito, Japan, 1996.

[64] T. Dinh, "Understanding the ill-posed two-fluid model," in *NURETH-10*, Seoul, Korea, 2003.

[65] A. Hotta, M. Zhang and H. Ninokata, "BWR regional instability analysis by TRAC/BF1-ENTREE II: application to Ringhals unit stability test," *Nuc. Tech.*, vol. 135, no. 1, pp. 17-38, 2001.

[66] T. Kozlowski and T. Downar, "Analysis of the OECD/NEA PWR main steam line break benchmark with TRAC-M/PARCS," *Nucl. Tech.*, 2004.

[67] T. Lefvert, "Ringhals 1 stability benchmark, final report," NEA/NSC/DOC(96)22, 1996.

[68] J. H. Mahaffy, "A stability-enhancing two-step method for fluid flow calculations," *J. Comp. Phys.*, vol. 46, pp. 329-341, 1982.

[69] J. H. Mahaffy, "The advantages and limitations of the SETS method," in *International Conference on Numerical Methods in Nuclear Engineering*, Montreal, 1983.

[70] J. H. Mahaffy, "Numerics of codes: stability, diffusion, and convergence," *Nuc. Eng. and Des.*, vol. 145, pp. 131-145, 1993.

[71] R. Taleyarkan, "MAZDA-NF - A parallel channel stability analysis code for BWR fuel assemblies," WCAP-11146 Westinghouse Nuclear Energy Systems, 1986.

[72] Y. Xu, T. Downar, K. Ivanov, A. Petruzzi, F. Maggini, R. Miro and J. Staudenmeier, "Methodologies for BWR stability analysis with TRACE/PARCS," in *ANS Mathematics and Computation Meeting*, Avignon, 2005.

[73] T. Kozlowski, "TRACE/PARCS Validation for BWR Stability Based on OECD/NEA Oskarshamn-2 Benchmark," in *NURETH-14*, Toronto, Canada, 2011b.

[74] J. L. Munoz-Cobo, M. Z. Podowski and S. Chiva, "Parallel channel instabilities in boiling water reactor systems: boundary conditions for out of phase oscillations," *Annals of Nuclear Energy*, vol. 29, pp. 1891-1917, 2002.